Universitat Autònoma de Barcelona

Doctorat en Biotecnologia
Departament de Genètica i Microbiologia – Facultat de Biociències

Nanophotonic Biosensors for Deciphering Cell Regulation Pathways

Doctoral Thesis – 2016

César Sánchez Huertas

Author

Prof. Laura M. Lechuga

Director

Prof. Antoni Villaverde

Tutor

CSIC
Consejo Superior de Investigaciones Científicas

ICN2
Institut Català de Nanociència i Nanotecnologia

Excelencia Severo Ochoa

Abstract

This Doctoral Thesis focuses on the development of innovative biosensor devices as alternative analytical techniques for the evaluation of different gene regulating pathways in order to obtain a more informative and accurate diagnosis and follow-up therapy of cancer. We propose the use of a novel nanophotonic biosensor for a rapid, highly sensitive and direct analysis of these regulating routes without the need of labeling or amplification steps.

Different genetic and epigenetic disorders associated with cancer appearance and progression are studied taking advantage of circulating nucleic acids as target biomarkers. For the label-free detection and evaluation of these biomarkers, we have employed two different optical biosensors: (i) the well-known Surface Plasmon Resonance (SPR) biosensor, and (ii) a novel nanotechnology-based interferometric device, the Bimodal Waveguide (BiMW) biosensor. First, an in-depth study of different biofunctionalization strategies on both platforms is presented. Several surface chemistry procedures have been optimized for an efficient immobilization of nucleic acids as biorecognition elements that ensure a highly sensitive target detection with maximum selectivity and reproducibility, especially for the direct analysis of complex human samples such as urine or serum. The optimized strategies were applied for the evaluation of specific and clinically relevant gene regulation pathways, such as RNA alternative splicing events, micro-RNA regulation, or DNA methylation processes. All the developed methodologies have been assessed in terms of selectivity, sensitivity and reproducibility, and in some cases, they have been validated with real samples. The obtained results overcome some of the critical drawbacks of the current methodologies employed for the analysis of such processes and offer standardized protocols for a highly sensitive and selective detection with minimal sample manipulation.

The work in this Thesis has opened a new Research line in our Group and combines our wide knowledge in the development of powerful photonic biosensor technology with our bioanalytical expertise in order to offer advanced analytical tools for the direct and effective evaluation of gene regulating pathways as new solutions for cancer diagnosis and follow-up therapy.

Resumen

La presente Tesis Doctoral se centra en el desarrollo de metodologías analíticas de carácter innovador para el estudio de diferentes rutas de regulación genética. Éstas nuevas técnicas de análisis se presentan como una atractiva alternativa para conseguir un diagnóstico y seguimiento de terapia del cáncer más precisos e informativos. Se propone el uso de un nuevo biosensor basado en tecnología nanofotónica como una plataforma ideal para el análisis rápido, directo y altamente sensible de dichas rutas, evitando el uso de marcadores o procesos de amplificación.

Diferentes trastornos genéticos y epigenéticos asociados con la aparición y el progreso de cáncer han sido estudiados empleando ácidos nucleicos como marcadores biológicos. Para ello, se han empleado dos tipos de biosensores ópticos: (i) el conocido biosensor basado en Resonancia de Plasmón Superficial (*SPR*), y (ii) una nueva plataforma nanotecnológica altamente sensible basada en señales interferométricas producidas en guías de onda bimodal (biosensor *BiMW*). En primer lugar se ha llevado a cabo un estudio en profundidad de diversos procesos de biofuncionalización en ambas plataformas biosensoras. Se han optimizado diferentes procedimientos químicos de funcionalización de superficie de tal forma que aseguren una eficiente inmovilización de oligonucleótidos como elementos de biorreconocimiento. Esto ha permitido la detección de las secuencias diana de forma muy selectiva, ofreciendo la máxima sensibilidad y reproducibilidad posibles, especialmente para el análisis de muestras humanas complejas como son la orina o el suero. Una vez optimizadas las estrategias de biofuncionalización, se han evaluado diferentes rutas de regulación genéticas clínicamente relevantes como son los procesos de *splicing* alternativo, la regulación de micro-ARNs o los procesos de metilación de ADN. Todas las metodologías desarrolladas han sido evaluadas en términos de selectividad, sensibilidad y reproducibilidad, siendo validadas finalmente con el análisis de muestras reales. Las metodologías desarrolladas eluden inconvenientes críticos a los que se enfrentan normalmente las tecnologías convencionales empleadas para el estudio de estos procesos, ofreciendo protocolos más estandarizados que permiten una detección muy sensible, selectiva y con una mínima manipulación de la muestra.

Este trabajo constituye el nacimiento de una nueva línea de investigación en nuestro grupo de investigación y combina nuestro amplio conocimiento en el desarrollo de innovadoras tecnologías biosensoras con nuestra gran experiencia en bioanalítica, ofreciendo finalmente herramientas de análisis muy avanzadas para la evaluación directa y efectiva de rutas de regulación genética como nuevas soluciones en el diagnóstico de cáncer y seguimiento de terapias.

Agradecimientos

Después de poco más de cinco meses escribiendo este manuscrito y tantos años de esfuerzo y trabajo, no sería justo cerrar esta etapa sin agradecer a todas esas personas que, de forma directa o indirecta, han ayudado a hacer posible que concluya esta gran experiencia.

En primer lugar, me gustaría dar las gracias a Laura Lechuga. Gracias por ofrecerme la oportunidad de realizar el doctorado en tu grupo. Me siento un privilegiado de haber podido trabajar contigo y haber aprendido tanto durante este tiempo. Gracias por tu exigencia, por la gran confianza que has depositado sobre mí y por compartir tus puntos de vista, que me han ayudado a seguir en la buena dirección.

Quería agradecer a la gran familia NanoB2A, que sin duda ha sido un lujazo trabajar con todos vosotros y compartir tantos momentos memorables. Aún recuerdo con añoranza recorrer el larguísimo pasillo de la ETSE para hablar de los últimos resultados con Laurita que, aunque fueran desastrosos, siempre me inundaba con nuevas ideas y grandes dosis de motivación. Entrar en el laboratorio y pasar de pies puntillas por la mesa de David Regatos, no vaya a ser que le moviera alguna de sus requeteordenadas piezas de su mesa. Pelearme con Silvia por quién cogía primero la pipeta de 100 cuando aún solo había un juego, o esquivar a Elena porque siempre se le acumulaban experimentos de última hora. Las escapadas al cuarto oscuro, donde estaban Bert y Borja, para evadirme cuando el laboratorio de sensores se convertía en un gallinero. Y ahora, en el nuevo edificio, las risas con Jesús en el laboratorio entre medida y medida. O el verano de locura de experimentos con Daphne, que me dio tantos dolores de cabeza. Me río aun con las genialidades de Ana, sin duda, el alma del grupo, y todas las fiestas que hemos disfrutado en el patio de su casa. Los momentos míticos de algunas *NanoB2A productions*, como el patinaje artístico sobre ruedas con Sam, la detención de la inocente Blanca, la declaración de amor de Gerardo, o los negocios oscuros de Daniel…¿Y las innumerables veces que Mar y Fari me han sacado de más de un lío arreglándome el sensor? ¡mil gracias! También agradezco a M. Carmen y Sonia, por resolverme las dudas de última hora. A Rebe, por los momentos de terapia bio, y a Toni por tener siempre alguna buena idea que aportar. Ha sido un placer volver a cruzarme con Adrián, que me vio como estudiante de máster y ha vuelto ahora que ¡casi soy doctor!

A los que nos han visitado algún tiempo y nos han dejado tan buenos momentos. Siempre recordaré los bomboncillos de café de Jhonattan a los que me he convertí en adicto… Las barbacoas truncadas en casa de Adrián y su encantadora esposa Mane. Y, sobre todo, la eterna sonrisa de mi gran Meli, sin duda una amiga para toda la vida. A mis innumerables alumnos (ya casi pierdo la cuenta…) que he tenido el honor de supervisar a lo largo de todos estos años y que me han hecho crecer como profesional: Alejandra, Marta, Mª Cruz, Sebastian, Anna y Santos. Gracias por vuestra paciencia y esfuerzo y, sobre todo, por ayudarme con mi trabajo. También a mi medio paisana Patricia, que aunque no estabas a mi cargo, me ha encantado ayudarte en lo que he podido y descubrir ese corazón tan gran grande que tienes. A las nuevas incorporaciones, Cristina y a Nuria, aunque no he tenido el placer de compartir mucho con vosotras os doy mucho ánimo y suerte en vuestros proyectos.

Me llevo un recuerdo muy especial de mis niñas Stef, Iraís y Maria, a las que quiero con locura y cuyo apoyo ha sido imprescindible. En estos últimos meses he echado de menos los momentos de desahogo en el *coffee break* o las cervecitas los viernes en el *underground* para dar la bienvenida al fin de semana. Y en particular, los abrazos de mi Stef, sus prisas por bajar a fumar un cigarrillo y su empeño en hacerme entender los dichosos armónicos… A mi pequeña mexicana, Iraís, muy dura por fuera pero con un corazón inmenso. No habría sido lo mismo sin nuestros momentos de risas por nuestras idas de olla en el despacho. Pero sobre todo a mi inseparable Maria. Sin duda, esto no lo habría conseguido sin ti. Hemos compartido tanto que todo lo que escriba se quedará corto… Has sido una compañera excepcional y una amiga incondicional que siempre ha estado a mi lado incluso cuando ni me lo he merecido. Gracias por ser así y darme ese huequito tan privilegiado en tu vida.

Gracias también a mi grupo adoptivo del CRG por acogerme tan cálidamente durante los meses que estuve allí y hacerme sentir uno más. A Juan Valcárcel por su entrega y compromiso que ha sido imprescindible en el desarrollo de esta tesis. A Villy y sus pastelitos, que echo tanto de menos. Y, sobre todo, a mi ángel de la guarda Elías, que siempre está cuando más lo necesito.

Tampoco sería justo irme sin mencionar a toda esa gente que ha formado parte de los momentos extra-oficiales de la tesis y con la que he tenido el placer de convivir todos estos años. Esto no hubiera sido lo mismo sin ellos.

A mi tita Juli y mis primas Bea, Olga y, sobre todo, a Esther, por acogerme y hacer mi adaptación a Barcelona mucho más fácil. Nunca olvidaré las locas reuniones familiares atiborrándonos de majares que me han hecho sentir como en casa.

A mi comunidad andaluza… ¿Qué hubiera hecho yo sin Sofía todos estos años? Empezamos juntos esta experiencia sin tener ni idea de lo que nos iba a deparar… Hemos compartido risas, llantos y muchísimas alegrías y, sin darnos cuenta, nos hemos convertido en imprescindibles el uno para el otro. Gracias por ayudarme a sacar la mejor versión de mí mismo. ¿Y mi Villa? A la que agradezco la acogida tan grande que nos hiciste y por demostrarme que siempre estás ahí, con esa gran generosidad, fuerza y afán de superación. A mi Clarita, que me alegro de haberte redescubierto aquí en Barcelona porque me encanta tu sinceridad, tus locuras y tu energía positiva. Y a la galleguiña adoptada Mariki, mi andaluza de corazón, porque siempre me demuestras que en todo momento se puede sacar una sonrisa y disfrutar de cada pequeño detalle de la vida. A ellas, y a los que ya se fueron y he echado tanto de menos, como Cristina, Toñi, Mariajo, Carlos y Luisa… gracias por haber formado parte de esta gran familia.

A mis tres mosqueteros Ardi, Enric y Rubén, que habéis sido como mis hermanos. Gracias por tantos momentos divertidos y tantas locuras vividas en los últimos años, en los que a veces la realidad han superado a la ficción. No hubiera sido igual sin los planes sin fin organizados por Ardi, o los consejos y curiosas experiencias de Enric. Y, sobre todo, ha sido imprescindible el apoyo de Rubén en esta última etapa llena de momentos de amargura y que parecía que esto no iba a acabar nunca. Gracias por haber estado ahí, eres una de mis personas favoritas y un amigo excepcional.

Y, de vuelta a mi tierra, a mis amigos de toda la vida mis dueños del circo, porque a pesar de todos los años que llevo fuera, os sigo sintiendo con el mismo cariño y amistad de siempre. Por esos cafés torero interminables que acaban pasándonos factura, y por todos los momentos de tapeo, con cervecita en mano, poniéndonos al día de nuestras vidas.

Finalmente a mi familia. Gracias por estar a mi lado y por confiar en mí. Por haberme inculcado tantos valores y demostrar ese amor que nos une tanto en los buenos como en los malos momentos. Gracias por regalarme esos momentos de reseteo que necesitaba cuando pensaba que no podría más… A mis hermanas, por permitirme volver a ser el hermano pequeño y olvidarme un poco de tantas obligaciones. Y a mi sobrinita Julia, que aunque no sea ahora muy consciente, me ha servido de motivación para conseguir lo mejor de todo esto. Pero sobre todo quería agradecérselo a mis padres, por todos los consejos que me habéis dado, por escucharme en los momentos de más desesperación y por el apoyo incondicional que he recibido siempre por vuestra parte. A vosotros os debo todo lo que soy y lo que he conseguido. Os quiero muchísimo.

Gracias a todos.

Contents

Abstract i

Resumen iii

Agradecimientos v

Abbreviations and Acronyms 1

Motivation and Objectives 5

1. Introduction 9

1.1. Deciphering gene regulation pathways for cancer diagnosis 10

1.2. Analytical techniques for deciphering gene regulating pathways study 12

1.3. Nucleic acid-based biosensors 13

1.3.1. Nucleic acids as biorecognition elements 14

1.3.2. Nucleic acid-based biosensors for clinical applications 15

1.4. Surface Plasmon Resonance biosensor 17

1.5. Bimodal waveguide interferometer biosensor 23

2. DNA-functionalization of the sensor surface 35

2.1. The biorecognition layer 35

2.1.1. Oligonucleotide-based probe design 36

2.2. DNA immobilization strategies for gold surfaces. 38

2.2.1. Thiol-chemistry based strategies 38

2.2.2. Optimization of a monolayer with antifouling properties 48

2.2.3. PolyA based strategy 56

2.2.4. Conclusions 61

2.3. Biofunctionalization of the Si_3N_4 sensor area 62

2.3.1. Surface modification using an amino-terminated silane (APTES) 63

2.3.2. Application of the biofunctionalization protocol using APTES to the BiMW device 72

2.3.3. Si_3N_4 surface recycling 73

2.3.4. Conclusions and future perspectives 76

2.4. Materials & Methods 76

2.4.1. Chemical Reagents and Buffers Composition 76

2.4.2. DNA/RNA sequences 77

2.4.3. Gold surface biofunctionalization 79

2.4.4. BiMW sensor chip and Si_3N_4 surface biofunctionalization 80

2.4.5. Surface characterization 81

2.4.6. DNA/RNA Hybridization 82

3. Quantitative evaluation of alternatively spliced mRNA isoforms by label-free real-time biosensing 85

3.1. Introduction 85

3.1.1. Mechanism and regulation of alternative splicing 86

3.1.2. Alternative Splicing as a biomarker 87

3.2. *Fas* gene alternative splicing and strategy design 88

3.2.1. Strategy 1: Two-step selective recognition of alternative splicing isoforms 89

3.2.2. Strategy 2: One-step selective detection of alternative splicing isoforms.....................92
3.2.3. Strategy 3: Direct and specific quantification of alternative splicing isoforms 94
3.3. Experimental validation of *Fas* alternative splicing with HeLa cells 100
3.4. Conclusions 112
3.5. BiMW biosensing of mRNA splicing isoforms 112
3.6. Conclusions and future perspectives..114
3.7. Materials and Methods 114
3.7.1. DNA sequences 114
3.7.2. HeLa cell mRNA samples..115
3.7.3. DNA-probes immobilization...117
3.7.4. Isoforms hybridization and biosensor regeneration...117
3.7.5 Data analysis...117

4. Profiling micro-RNA levels by amplification-free and label-free biosensing... 121
4.1. Introduction..121
4.1.1. Biogenesis and functions of miRNAs 121
4.1.2. MiRNAs as a cancer biomarker 123
4.1.3. State-of-the-art in miRNA analysis...123
4.2. miRNA-181a detection in SPR biosensor 124
4.2.1. miRNA-181a as biomarker..124
4.2.2. Optimization of the selective detection of miR-181a..125
4.2.3. SPR Antibody-DNA-RNA signal amplification..130
4.2.4. Detection of miR-181a in biological samples by SPR..135
4.2.5. Conclusions..137
4.3. BiMW: highly sensitive detection of miRNAs 138
4.3.1. miR-181a specific detection by BiMW 138
4.3.2. Detection of circulating miR-181a in urine samples by BiMW.................................140
4.3.3. Conclusions and future perspectives..142
4.4. Materials and Methods 143
4.4.1. miRNA sequences...143
4.4.2. SH-MiR-181a probe immobilization...144
4.4.3. Detection conditions. 144
4.4.4. Urine samples...144

5. DNA methylation profiling for cancer diagnosis 147
5.1. Introduction..147
5.1.1. DNA methylation mechanism...147
5.1.2. DNA methylation and cancer...148
5.1.3. Determining the cancer DNA Methylome 149
5.2. Assessment of CpG island quantification in *PAX-5* gene promoter..........................150
5.3. Conclusions and future perspectives 154
5.4. Materials and Methods 155
5.4.1. DNA sequences 155
5.4.2. SH-*PAX-5* probe immobilization..156
5.4.3. Target hybridization...156
5.4.4. MBD capture 156

General Conclusions and Future Perspectives 157

A. Sensitive and Label-Free Detection of miRNA-145 by Triplex Formation 163
A.1. Introduction 163
A.2. SPR detection of miRNA-145 using parallel clamps 164
A.3. Conclusions and future perspectives 167
A.4. Materials & Methods. 168
A.4.1. Synthesis of Oligonucleotides 168
A.4.2. Experimental Procedure for Detection Using the SPR Biosensor 169
Publications 171
List of Figures 173
List of Tables 181
Bibliography 0

Nanophotonic Biosensors for Deciphering Cell Regulation Pathways

Abbreviations and Acronyms

A	Adenine
AGO	Argonaute
AH	6-amino-1-hexanol
Akt	Protein kinase B
APTES	3-aminopropyltriethoxy silane
ATR	Attenuated Total Reflection
BiMW	BiModal Waveguide
BSA	Bovine Serum Albumin
C	Cytosine
CV	Coefficient of Variability
CV	Coefficient of Variation
Cy3	Cyanine 3
DIPEA	Diisopropylethylamine
DMF	Dimethylformamide
DMF	Dimethylformamide
DNA	Deoxyribonucleic acid
ds-RNA	Double-stranded RNA
DTT	Dithiothreitol
EDC	1-Ethyl-3-(3-dimethylaminopropyl)carbodiimide
EM	Electromagnetic
FA	Formamide
G	Guanosine
HEPES	4-(2-hydroxyethyl)-1-piperazineethanesulfonic acid
HEPES	4-(2-hydroxyethyl)-1-piperazineethanesulfonic acid
LOC	Lab On Chip
LOD	Limit of Detection

LOQ	Limit of Quantification
LSPR	Localized Surface Plasmon Resonance
MCH	6-Mercapto-1-hexanol
MES	2-(N-morpholino)ethanesulfonic acid
MES	2-(N-morpholino)ethanesulfonic acid
MHDA	Mercaptohexadecanoic acid
MHDA	Mercaptohexadecanoic acid
miRNA	micro-RNA
mRNA	messenger RNA
MUOH	11-Mercaptoundecanol
ncRNA	non-coding RNA
NCS	Isothiocyanate
O/N	Over Night
ORF	Open Reading Frame
PBS	Phosphate Buffered Saline
PCR	Polymerase Chain Reaction
PDITC	p-Phenylene diisothiocyanate
PEG	Polyethylene Glycol
PLL	Poly-L-Lysine
POC	Point of Care
PTEN	Phosphatase and Tensin homolog
RISC	RNA-induced silencing complex
RIU	Refractive Index Unit
RNA	Ribonucleic acid
RT-qPCR	quantitative Reverse-Transcription PCR
s-NHS	sulfo-N-Hydroxysuccinimide
SAM	Self-Assembled monolayer
SD	Standard Deviation

SDS	Sodium Dodecyl Sulfate
SNP	Single Nucleotide Polymorphisms
snRNA	small-nuclear RNA
SP	Surface Plasmon
SPP	Surface Plasmon Polariton
SPR	Surface Plasmon Resonance
SSC	Saline Sodium Citrate
ssDNA	single-stranded DNA
Sulfo-GMBS	N-(γ-Maleimidobutyryloxy) sulfosuccinimide ester
T	Thymine
TCEP	Tris(2-carboxyethyl)phosphine
TE	Transverse-electric
TIR	Total Internal Reflection
TM	Transverse-magnetic
TMAC	Tetramethylamonium chloride
U	Uracile
UTR	Untranslated Region
UV	Ultra Violet
XPS	X-ray photoelectron spectroscopy

Motivation and Objectives

Cancer research has led to a massive development of knowledge about the cellular mechanisms involved in the onset of tumorigenic processes. Why, when and where the cancer is taking place are the main questions that researchers keep trying to answer to elaborate early and efficient diagnostic tools and to develop more effective and less invasive therapies.

Gene regulating pathways have shown to play important roles during cell development and equilibrium maintenance. Their study has helped to elucidate the different shortcuts that cancer cells take by shifting these regulating routes in favor to their outliving and proliferation over normal cells. The specific reversion of these routes shows great potential in cancer therapy in order to return the cells to their normal state, without implying invasive chemotherapies and post-treatment side effects.

For that reason, there is an urgent need for the development of more effective diagnostic tools for the monitoring of gene regulating pathways. New highly sensitive and selective strategies are needed to achieve rapid and reliable analyses. In this regard, optical biosensors have profiled themselves as robust and efficient analytical tools offering fast, simple and ultra-sensitive detection of disease-related biomarkers. They also show interesting miniaturization and integration capabilities to build Lab-on-a-Chip (LoC) systems, representing a potential alternative to develop Point-of-Care (PoC) devices. However, their implementation for complex biochemical analysis has not been yet fully accomplished.

The analysis of the regulating pathways not only includes the detection of the nucleic acids involved but also the subtle shifts in their expression that lead to aberrant cancerous cells. Sequence similarities and very low concentrations are the main constraints that impede a proper study of these routes. Intensive effort must be directed to develop and optimize biofunctionalization and detection procedures for the reliable and accurate analyses of these relevant biomarkers directly in biological fluids involving minimal sample manipulation. The development of versatile and fully optimized biosensor methodologies for deciphering gene regulating pathways might signify a breakthrough in cancer diagnosis and therapy.

This PhD Thesis constitutes a brand-new research line in our group combining two current topics in research: Epigenetics and Nanobiotechnology. The goal of this work is aimed at designing and evaluating novel biosensor methodologies for the analysis of gene regulating pathways as potential tools for early cancer diagnosis and therapy monitoring with a user-friendly technology. In particular, the main objectives outlined for the work involve:

1) Design of novel analytical methodologies for genomic and epigenomic biomarker detection for deciphering the regulatory routes taken by cancerous cells;

2) Assessment and optimization of the biofunctionalization and detection conditions that enhance the analytical parameters of the assay in terms of sensitivity, selectivity and accuracy for the analysis of real samples.

3) Implementation of the developed analytical methodologies into a novel and powerful nanotechnological device, the Bimodal Waveguide biosensor, to achieve reliable Lab-on-a-Chip portable platforms.

Chapter 1· Introduction

This chapter describes the high regulation presented in eukaryotic cell genome through the interplay of different and complex pathways, which are mainly governed by Epigenetics. The importance of their analysis due to their direct implication in cancer development is highlighted and the drawbacks presented in the current methodologies for their study are underlined. Biosensors are introduced as suitable platforms for their analysis and their employment as diagnostic tools in the clinical environment. Special attention is given to optical biosensors and, especially, evanescence wave biosensors are underscore as suitable platforms for cell regulation pathways evaluation, pointing out their advantages and limitation in the clinical practice.

1. Introduction

The discovery of DNA and its function in living beings has led to an impressive development in the knowledge of life science. The idea that DNA stores the information that configures what we are, transcribes it into a messenger RNA (mRNA) molecule that is translated into a protein bearing a specific function, constitutes the basis of the central dogma of molecular biology[1] (**Figure 1.1**). However, continuing research has shown that the production of proteins from DNA is far more complex than originally thought.[2]

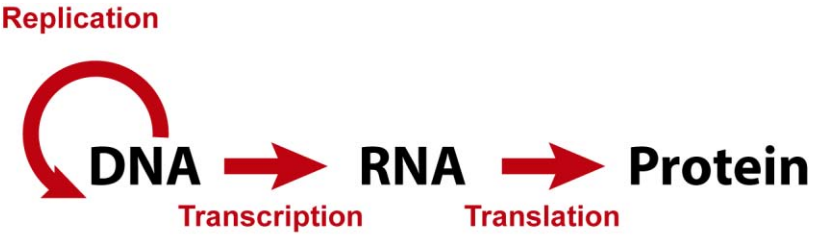

Figure 1. 1 Central Dogma of Molecular Biology.

Ever since Charles Darwin (12 February 1809 – 19 April 1882, England) exposed his theory of evolution,[3] molecular biology has centered the explanation of the new findings based on the unbreakable Darwinian laws. The laws support the idea of natural selection, which states that the evolution is due to the outliving of those individuals with characters that better suited the surrounding circumstances, conferring them with advantages over those individuals not carrying such characters. It was generally accepted that these acquired characteristics could be inherited only through direct mutation of the DNA contained in germ cells (sperm and eggs). This version of evolution has triggered an explosive development and progress in biological sciences. Recently, a new revolution in molecular biology is emerging supported by controversial cutting-edge studies in biology and genetics that cannot be explained by the traditional evolutionary theories. Little by little, Lamarckism inheritance is gaining more support. Jean-Baptiste Lamarck (1 August 1744 – 18 December 1829, France) postulated that acquired characteristics could be transmitted from one generation to the next. Such hypothesis was buried down by strong religion beliefs in the nineteenth century, which supported better the Fixism whose ideas matched more with the Creationist doctrine. But the idea that species evolve thanks to behavioral attributes in the parents is now becoming more apparent. We are entering now in the Epigenetic era.[4]

Epigenetic (literally, *outside* or around *genetics*) inheritance refers to any heritable trait which is not derived from the sequence of DNA. The mechanism by which these characteristics are inherited is extraordinarily unique. They are transmitted to offspring in the form of subtle chemical modifications to DNA and DNA-associated proteins and exert their effects by modifying the gene expression. These modifications play an important role in cell decision-making, providing the cells with a powerful capability to readily change their genome through sensing and signaling processes in order to survive and reproduce faithfully in ever changing environments. However, it requires the simultaneous contribution of hundreds of thousands of genes which are expressed and work in concert in order to assure the cell's function, fitness and survival. In this way, each gene must be expressed at the proper time and in the suited quantities for an appropriate functional outcome. For some genes, their regulation and expression are highly robust, being controlled by invariable expression programs. However, the expression of other genes is more stochastic, showing different levels from cell to cell and from individual to individual. This flexibility in gene regulation provides the cells with many advantages and it is highly beneficial in the physiological responses to outside signals and stresses.

1.1. Deciphering gene regulation pathways for cancer diagnosis

There are many regulatory mechanisms that serve the cells to overcome environmental changes successfully and they occur at different expression levels, constituting a complex gene regulatory network highly structured. Thus, the cell can decide whether to translate or not one concrete gene by reorganizing its chromatin structure through epigenetics modifications such as DNA methylation or histone acetylation;[5] or to express one protein isoform or another with completely different functions by an alternative edition of a common mRNA at the post-transcriptional level.[6] In addition, gene expression can be epigenetically regulated by a complex network of interfering small non-coding RNA (nc-RNA) molecules, such as micro-RNAs, through their interaction with mature mRNAs[7] (**Figure 1.2**).

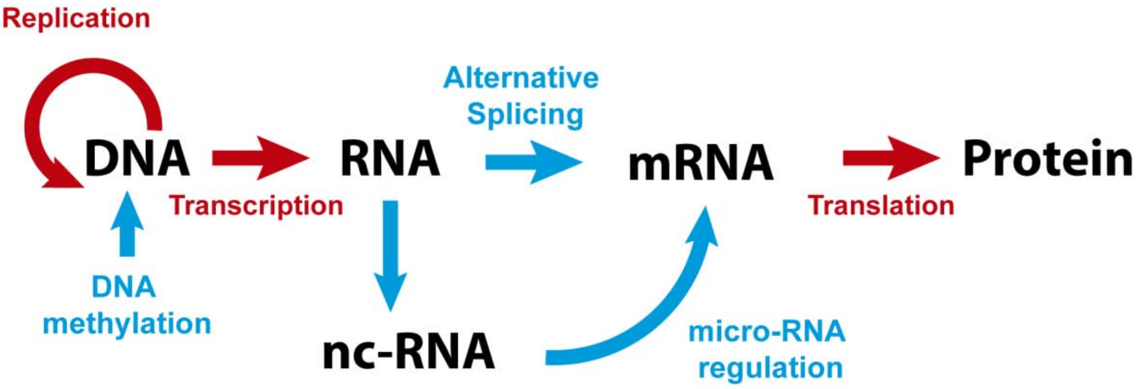

Figure 1. 2 Scheme of the different alterations in gene regulation pathways which can take place inside the cell.

Gene regulation pathways have an important role in every process of life, including cell differentiation, metabolism, cell cycle and signal transduction. The alteration of such processes may alter the fate of the cells and its consequences can be devastating, resulting in the origin of grave diseases. For example, aberrant DNA methylation produces the silencing of tumor suppressor genes leading to the generation of cancer. This process is even more common in human tumor than gene mutations (nucleotide changes, deletions, recombinations) or cytogenetic abnormalities.[8] Also, most cancers are associated with a switch in the splicing pattern of specific isoforms that provides them with proliferative capacity and survival properties.[9] The regulation of key cancer-related pathways, such as cell cycle control and the

DNA damage response, among others, is carried out by micro-RNAs, whose aberrant expression can lead to tumorigenic processes.[10]

Deregulation of gene expression can be considered therefore as a hallmark of many malignancies, including cancer. Current diagnostic approaches are focused on the detection of overexpressed cancer protein blood biomarkers. However, their number and clinical use are limited, requiring a large population of cancer patients with well-defined clinical staging and outcomes. Deciphering gene regulation pathways may be more informative, specific and accurate than the analysis of protein biomarkers by the determination of not only the cancer itself, but also the mechanisms by which it is generated. In addition, aberrant DNA methylation, alterations in mRNAs isoform ratio or changes in nc-RNAs patterns can be associated to concrete tumorigenic profiles and can be used as specific cancer marks. Recent studies indicate that there exist collaborative activities between these gene regulating pathways resulting in a common outcome[11] (**Figure 1.3**).

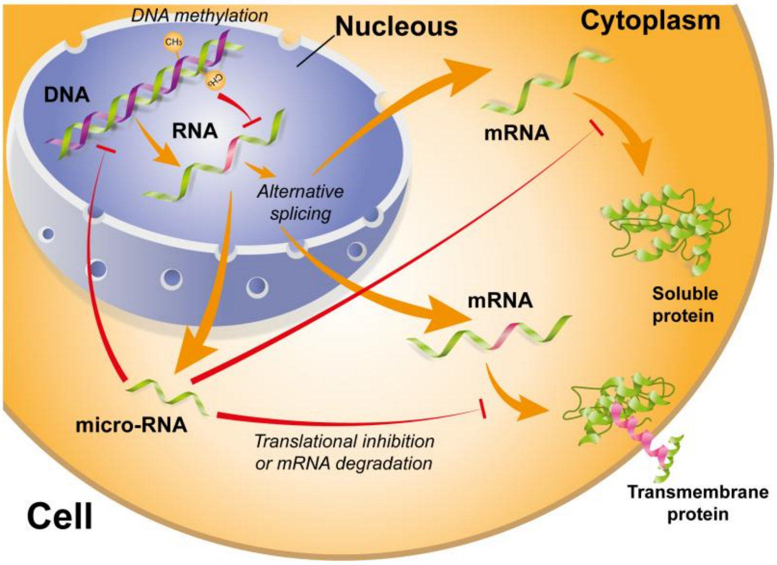

Figure 1. 3 Interplay between gene regulating pathways inside the cell.

Understanding the dynamics of these networks can shed light on the mechanisms of the development of many types of cancer which may occur when these cellular processes are deregulated. It will contribute to a more efficient management of cancer patients, providing an early diagnosis, determining precise tumor staging, and monitoring the subsequent treatment.

Because of their dynamic nature and potential reversibility, gene regulation pathways constitute appealing therapeutic targets in cancer treatment. Therapies focused on reversion of the altered process to its normal state would abate the cancer progression in a less invasive manner than current chemotherapies. Various compounds that alter DNA methylation and histone modification patterns are currently being examined in clinical settings as single agents in combination with other drugs.[12, 13] Likewise, different approaches for mRNA expression control are being developed as well as different therapies for the control of nc-RNAs under- or overexpression.[14-18] Thus, a better knowledge of the cell decision-making in concrete illnesses can be better exploited for a real personalized medicine development.

1.2. Analytical techniques for deciphering gene regulating pathways study

In recent years, the interest for nucleic acid testing has been growing. The development of different approaches allowing DNA/RNA detection is motivated by applications in many fields: diagnostics,[19] gene analysis,[20] fast detection of biological warfare agents,[21] and forensic applications.[22] However, the study of gene regulation pathways implies not only the detection and quantification of the nucleic acid molecules that participate in such processes, i.e. the methylated DNA, mRNA isoforms generated by alternative splicing or micro-RNA regulators, but also the recognition of the epigenetic marks such as the 5-methylcytosines in DNA, or the shifted expression of RNA molecules with very similar sequences which, in some cases, are close to the mismatch level. In a physiological context, subtle changes in these gene regulation pathways occur at very low concentrations. Therefore, ideal diagnostic tools for deciphering gene regulation pathways should have high sensitivity and specificity to be able to reveal minimal changes in biomarker concentration in the samples for an early and accurate diagnosis.

Traditional nucleic acid detection methods involve gel electrophoresis and Southern and Northern blotting.[23-25] However, these techniques employ large quantities of sample input, and their results are available after a few days or even weeks. In contrast, Polymerase Chain Reaction (PCR) based techniques has allowed the examination of small quantities of material within hours, which has greatly promoted the clinical analysis of DNA and RNA.[26] The success is more evident since the developments on real-time PCR,[27] as results can be obtained in a matter of a few minutes, or DNA microarrays which can interrogate thousands of DNA/RNA sequences simultaneously in one sample.[28] Next-generation DNA sequencing technologies have expanded for genome-wide scale screening and have achieved a resolution to single base precision.[29] The combinatorial use of these methodologies has reinforced the notion of the disruption of gene regulation pathways as a signature of human diseases. However, the diversity of protocols and reagents currently in use for these techniques impedes the comparison of data from different laboratories, making difficult the standardization of assays, such as isolation technologies, standards, assay conditions, specificity and sensitivity. They also can be time consuming and the interpretation of the results can be very confusing and complicated. Therefore, the analysis needs to be more robust, consistent, comparative and informative.

An interesting alternative for the study of such regulating pathways is the employment of biosensor devices, which hold enormous potential as technological solutions for rapid and reliable biomedical analysis.[30] Biosensors can be designed to provide quantitative analytical information with elevated accuracy in few minutes, using low sample volumes and minimum pretreatment. They are promising analytical tools for the efficient clinical diagnosis as well as for better understanding of the complex molecular mechanisms of the pathophysiology, which will build the basis to identify novel biomarkers and to design new and more suitable treatments. Moreover, the ability to miniaturize and integrate different functional components (e.g. microfluidics, electronics, etc.) in a single platform allows for the fabrication of smaller, cheaper and easy-to-use devices that can accelerate the real implementation of Point-of-Care (PoC) biosensors in the clinical practice. The enormous possibilities provided by nucleic acid-based biosensors for employing DNA/RNA molecules as biomarkers for early diagnosis of illnesses and for designing personalized therapies have led to a remarkable development of different biosensor methodologies for clinical usage.[31]

1.3. Nucleic acid-based biosensors

A biosensor is a self-contained integrated device capable of providing specific quantitative or semi-quantitative analytical information using a biological or biomimetic recognition element which is in direct spatial contact with a transducer. The biorecognition layer is specifically designed to interact with the target compound in a sample. When the biochemical interaction occurs, a series of physicochemical changes in the medium or the surface are detected by the transducer and converted into discrete or continuous signals (**Figure 1.4**).

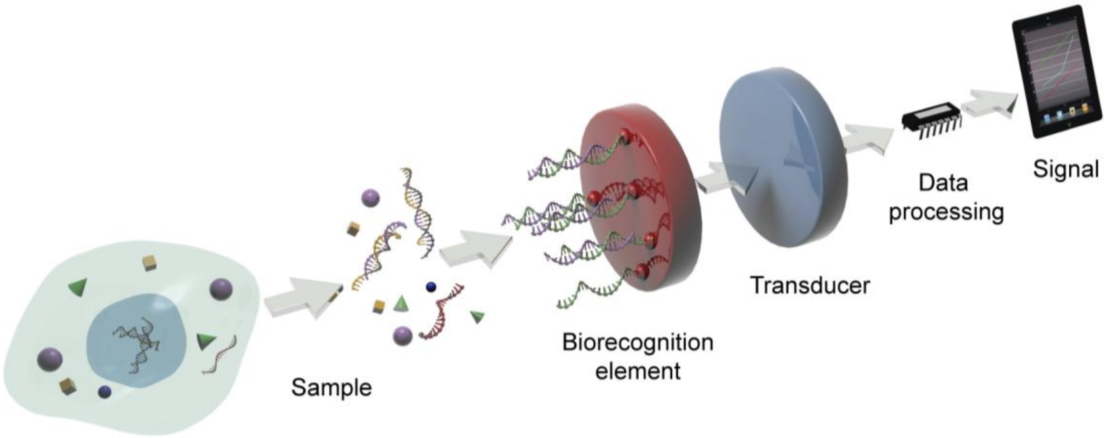

Figure 1. 4 Schematic representation of a biosensor including the heterogeneous sample, the specific biological receptor, the transducer, the data processing system and the final signal.

The design and integration of biosensors offer unique features to improve current analytical methods. The combination of the bioreceptor layer with the transducer in a single device confers the ability to detect the target analyte with high sensitivity and selectivity in a fast way. Moreover, biosensors could ideally overcome important disadvantages of conventional techniques such as the need for prior analyte extraction or purification or the use of additional equipment for signal read-out (e.g. UV-VIS spectrometer, microscope, etc.) which is usually operated by specialized personnel. Biosensors can also monitor biological interactions in real time allowing the evaluation of the affinity and kinetics of the interaction and, thereby, helping in elucidating the biochemical mechanisms involved, for example in a concrete disease. Biosensors also benefit from great versatility, being possible to measure a wide range of analytes just by selecting the appropriate biological receptor. Recent advances in nanofabrication further provide interesting opportunities for biosensor miniaturization, high-throughput and low-cost production.[32] Biosensor platforms have shown exceptional capabilities to turn into portable and user-friendly devices which can be used at doctor’s office or patient’s home.[33, 34]

The biorecognition element in a biosensor can be an enzyme, a nucleic acid (DNA or RNA), an antibody, a cell, or a tissue, which should specifically recognize and react with an analyte, and which may have the possibility to return to its initial stage without significant decrease of its activity (**Figure 1.5**). An ideal biosensor must be highly specific for the analysis purpose, should be stable under normal storage condition and must show reliable and reproducible results over a large number of assays.

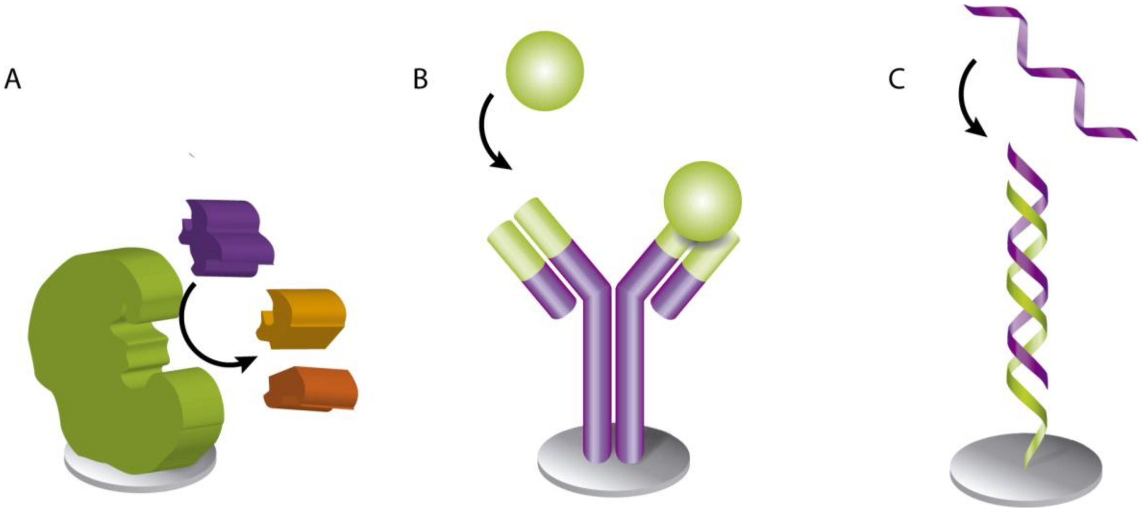

Figure 1. 5 Main types of biosensors depending on the biorecognition element: **(A)** enzymatic biosensor (catalytic), **(B)** immunosensor (affinity) and **(C)** DNA biosensor (affinity).

1.3.1. Nucleic acids as biorecognition elements

The use of nucleic acid as recognition layer in biosensor design is a booming and exciting area in analytics.[35] Nucleic acids have unique molecular recognition properties, i.e. hybridization of complementary nucleotide sequences into the double helix according to Watson-Crick base pairing. From a chemical point of view, nucleic acid strands are linear biopolymeric molecules formed by a chain of nucleotides bond by a sugar-phosphate backbone (**Figure 1.6**). The four nucleotides (adenine, A; guanine, G; cytosine, C; tyrosine/uracile, T/U) of the DNA/RNA sequence display internal amino-groups that are involved in the complementary base-pairing hybridization. Therefore, these molecules can be easily captured by a complementary sequence.

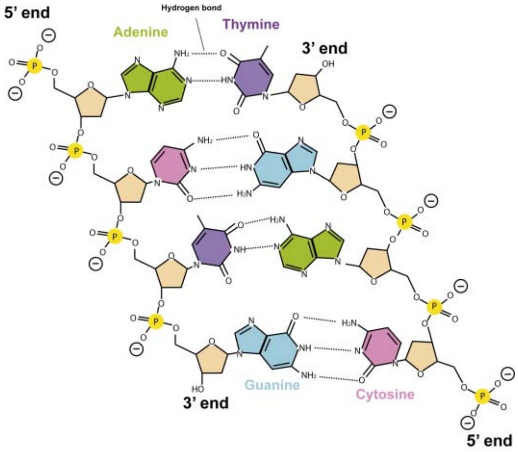

Figure 1. 6 DNA backbone scheme.

In nucleic acid-based biosensors, the biorecognition element is preferred to be a single-stranded DNA (DNA probe) with a specific sequence of nucleotides of around 9-50 bases, which is able to capture its specific target, i.e. a DNA or RNA molecule. Unlike enzymes or antibodies, DNA is an easily synthesizable biological recognition element ant it is highly stable and reusable after a simple melting process of the DNA duplex. Current biotechnological methods permit the production of synthetic nucleic acids with the desired sequence in large amounts and with a high degree of purity. Furthermore, they can be easily tailored by introducing different modifications in both the 5’ and the 3’ ends to generate probes with different characteristics depending on their application. Therefore, structural end-modifications can be introduced in the DNA probe sequence for their immobilization over different types of inorganic materials or their conjugation with other biomolecules, generating functional surfaces for nucleic acid detection at a very low manufacturing cost. Furthermore, the possibilities in DNA probe production are numerous and great advances have been made recently in order to improve target capture efficiency by developing new synthetic oligonucleotide-based receptors such as peptide nucleic acids (PNA),[36] PNA derivatives,[37] locked nucleic acids (LNAs),[38] and triplex-based nucleic acid receptors.[39] These new receptor configurations improve hybridization efficiencies and increase the selectivity for the target, largely contributing to the avoidance of cross-hybridization of non-specific targets. Functional nucleic acids (FNAs)[40] such as aptamers have also been developed using a combinatorial method called SELEX (systematic evolution of ligands by exponential enrichment), making possible to evolve nucleic acids in test tubes to bind to a diverse range of analytes beyond DNA or RNA with high affinity and specificity. They are considered as a viable alternative to antibodies due to their rapid discovery in vitro, their smaller molecular size and their relatively inexpensive generation. However, the widespread use of monoclonal antibodies has slowed down their development in worldwide laboratories. They still show less affinity to their targets compared to their antibody counterpart.[41] Due to their structure, they are more narrowly confined than antibodies and the overall oligo is very hydrophobic and negatively charged. Such characteristics make their binding to hydrophobic or acidic proteins very challenging.

1.3.2. Nucleic acid-based biosensors for clinical applications

In the last few decades, nucleic acid-based biosensors have gained much interest in detection and monitoring of various clinical manifestations, such as inherited diseases and pathogenic infections.[42] Such interest has promoted the development of new nucleic acid-based biosensors employing different types of transducers, like electrochemical, mechanical or optical.

Electrochemical biosensors

Electrochemical nucleic acid biosensors have fast response time, require simple instrumentation, and can be efficiently fabricated at low cost. In these devices DNA is immobilized onto an electrode which measures electrochemical changes (e.g. current, potential, impedance, or conductance) in the medium caused by the hybridization reaction.[43] The emergence of solid electrodes has enhanced the applicability of electrochemical methods for nucleic acid analysis.

Mechanical biosensors

In mechanical biosensors the biochemical interaction is measured as changes of mass on the surface of the transducer.[44] We can distinguish between acoustic-wave biosensors or nanomechanical biosensors. In acoustic-wave devices, also referred to as piezoelectric biosensors, the transducer is a microbalance composed of a quartz crystal without center of symmetry sandwiched between two electrodes delivering an alternating electrical field.[45] A stretch of nucleotide sequence with a few hundred base pairs possesses a measurable molecular weight. The increment of mass due to hybridization of a target with its complementary probe immobilized on the surface of a piezoelectric quartz crystal will lead to a variation in the resonance frequency of the crystal, which is transduced to measurable signals. It has allowed detecting point mutation in a human gene,[46] or the simultaneous detection and genotyping of 16 strains of the human papilloma virus by using a degenerate probe.[47]

On the other side, nanomechanical biosensors detect changes of mass by employing micro or nanocantilevers as transducers.[48] The biological interaction occurring on the surface of the cantilevers may either produce a nanomechanical deflection or changes in the vibration frequency that can be measured and quantified. Mechanical biosensors have attractive features such as label-free detection, multiplexing capabilities and thermal stability.[49] A cantilever array has permitted multiple binding assays in parallel for measuring DNA sequences in a solution.[50] However, the mechanical nature of the sensing mechanism is a main constraint for sample handling or when working in liquid environments.[51]

Optical biosensors

Optical biosensors are the most commonly used biosensors for nucleic acid detection.[42] They detect a biological interaction by measuring variations of the optical properties of the light, such as intensity, wavelength, refractive index or polarization.[52, 53] Optical sensors can be divided in two types: bio-optrodes and evanescent wave sensors. In the bio-optrodes light is guided (generally with an optic fiber) to the evaluation chamber where the biomolecular interaction produces a change in the properties of the light (absorption, fluorescence, refractive index, bioluminescence or dispersion). These sensors usually employ optical labels, such as dyes or fluorescent molecules. Hybridization between a DNA probe and its specific target has been detected by ethidium bromide by measuring internal reflection in an optical fiber, which was proportional to the total amount of this intercalated fluorescent marker.[54] Fluorescence emission from molecular beacons[55] and quantum dots[56] have also been employed for single-molecule DNA detection.

On the other hand, evanescent wave biosensors exploit the possibility of confining the electromagnetic field in certain dielectric and/or metal structures, which can result in either a localized or propagating electromagnetic mode. Part of the electromagnetic mode extends into the external medium, originating a so-called *evanescent field*. Variations in the refractive index of the external medium will cause a change of the optical properties of the excited optical mode through this evanescent tail, resulting in a variation of its effective refractive index. This relative change allows a quantitative measurement of the analyte involved in a given biomolecular interaction. Due to the exponential decay of the evanescent field in the external medium (usually few tens to a few hundreds of nanometers), only changes occurring in close proximity to the interface will be sensed, with a natural filtering of background from the surrounding medium. As a consequence, biosensors relying on the evanescent field principle are seen as ideal candidates for affinity-related analyte detections without the need for any molecular marker, allowing on-chip label-free detection.[57] **Figure 1.7** shows the two main configurations employed in evanescent wave sensors: those based on conventional dielectric waveguides (left panel) and those based on surface plasmon resonance (right panel).

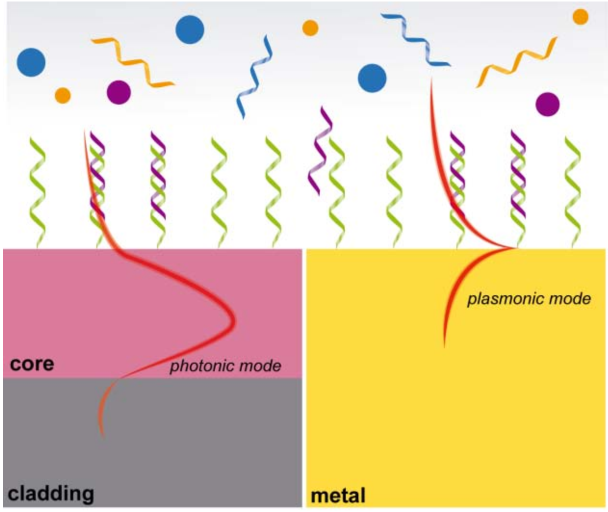

Figure 1. 7 Evanescent wave sensor configurations for conventional dielectric waveguides (*left*) and surface plasmon (*right*).

Interferometers, resonators or plasmonic biosensors are typical examples of evanescent wave biosensors.[58, 59] These devices achieve high detection sensitivities with short response times. They do not suffer from electromagnetic or mechanical interferences and have a strong potential for miniaturization and multiplexing. For that, many evanescent wave biosensors have been employed to address the various types of nucleotide probes like DNA, RNA and aptamers with potential applicability in diagnosis.[42, 60] This thesis is especially focused on the study of gene regulation pathways through evanescent wave biosensors. Here we will describe in more detail the *Surface Plasmon Resonance* (SPR) biosensor and the *BiModal Waveguide* (BiMW) interferometer.

1.4. Surface Plasmon Resonance biosensor

SPR biosensors represent the most advanced and mature label-free optical biosensor technology.[60] They offer significant advantages over conventional techniques enabling analysis with high sensitivity and excellent reproducibility in few minutes and have become a widespread tool for the study of any type of biochemical interactions. SPR sensing shows excellent properties for its application in different fields, such as environmental monitoring, food quality and safety analysis, diagnostics and biomedicine, biological engineering, drug discovery, etc.[61] Moreover, it represents a user-friendly and robust analytical tool for the analysis of oligonucleotides in minimally-processed samples as previously demonstrated by detection of DNA targets[62, 63] with a specificity up to single mismatches,[64] and various RNA types, such as micro-RNAs,[65-68] triplex-forming RNAs,[39] ribosomal-RNA[69, 70] as well as other RNA sequences.[71-73]

Surface plasmons are special electromagnetic modes that may exist at the interface of a metal and a dielectric. SPR biosensors employ propagating surface plasmons (referred to as propagating *surface plasmon polaritons*, SPP) that oscillate collectively on a planar metal-dielectric interface and behave like a quasi-free electron plasma (**Figure 1.8A**). The SPP is a transverse-magnetic (TM) wave whose magnetic field is perpendicular to the direction of propagation and parallel to the plane of the interface. It is characterized by the *propagation vector* (k_x^{SPP}) and the electromagnetic field distribution. The propagation vector of an SPP can be defined as:

$$k_x^{SPP} = k_0 \sqrt{\frac{\varepsilon_m \varepsilon_d}{\varepsilon_d + \varepsilon_m}} \tag{1.1}$$

where k_o is the wavevector of the light in vacuum: $k_0 = \omega \;\; c = 2\pi/\lambda$. ε_m represents the frequency-dependent and complex dielectric function of the metal ($\varepsilon_m = \varepsilon_m' + i\varepsilon_m''$) and ε_d is the dielectric constant of the medium, which can be directly related to the refractive index ($\varepsilon_d = n_d^2$). For the SPP excitation and propagation, the real part of the ε_m must be negative and its absolute value smaller than ε_d. In the visible and near-infrared regions of the spectrum, this condition is fulfilled for several metals. Gold, silver and aluminum are the most commonly used in plasmonics. Due to the relatively small imaginary part of the refractive index of these metals, they show strongly suppressed plasmonic attenuation when compared to other materials, thus minimizing propagation losses.

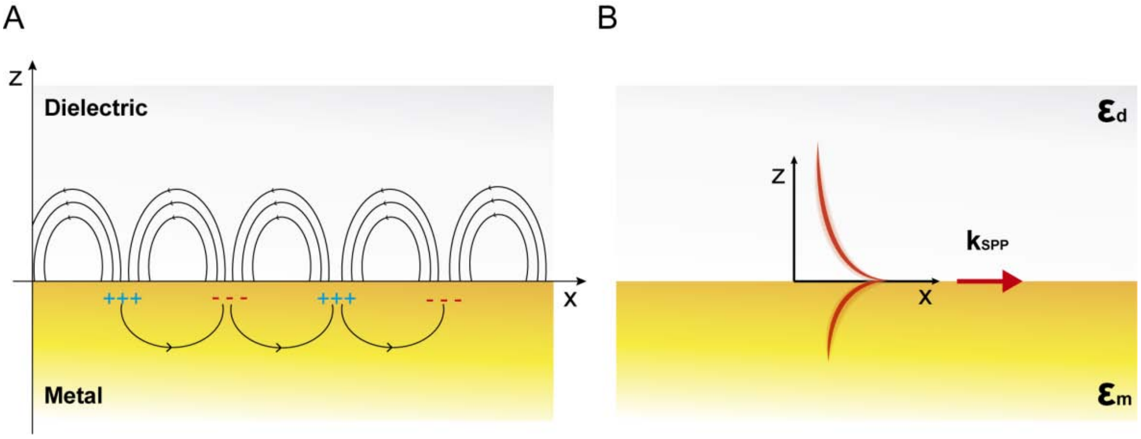

Figure 1. 8 Schematics of a SPP at the interface of a metal and a dielectric showing: (**A**) the collective charge oscillation at the surface and (**B**) the transversal evanescent field distribution.

The electromagnetic field of the SPP is confined at the metal-dielectric interface and decays exponentially into both media in the direction perpendicular to the metal-dielectric interface, generating an evanescent field (**Figure 1.8B**). The field is distributed in a highly asymmetric fashion and most of it is concentrated in the dielectric (in SPR sensors, this is typically an aqueous medium) close to the surface, showing a typical penetration depth that depends on the wavelength and the dielectric constants (ε) of the materials involved. Owing to that asymmetric distribution, the propagation constant is extremely sensitive to changes in the refractive index of the dielectric. Penetration depth into the dielectric for a surface plasmon propagating along the interface of a gold layer and a dielectric with refractive index n_d = 1.32 increases with wavelength and ranges from 100-600 nm when working in visible or near infrared regions.[74] This means that only biomolecular interactions occurring at the metal surface and within the evanescent field penetration depth would produce changes in the surface plasmon and would be detected.

The excitation of the SPP is achieved by coupling a light wave to the surface plasmons. This is only possible if the wavevector of the incoming light (k_x^{Ligh}), parallel to the interface, matches the propagation vector of the SPP:

$$k_x^{Light} = \frac{2\pi}{\lambda} \quad \overline{\varepsilon_d} \sin\theta = k_x^{SPP} \tag{1.2}$$

Generally, k_x^{SPP} is considerably larger than k_x^{Light}. Therefore, surface plasmons cannot be excited by direct illumination with light. Several techniques can be employed to promote the excitation of the surface plasmons, such as prism coupling, waveguide coupling and grating coupling. Of these, the most common approach to the excitation of surface plasmons is through the use of a prism coupler via the Attenuated Total Reflection method (ATR).[75] In the so-called Kretschmann configuration (**Figure 1.9**), light passes through a high refractive index prism with dielectric constant (ε_p) higher than the one of the dielectric. If the metal layer is thin enough ($h <$ 100nm at λ in the visible and near-infrared), light penetrates to the metal/dielectric interface and couples to the SPP. The excitation of the surface plasmon generates an evanescent wave and gives rise to a drop in the intensity of the reflected light. This evanescent wave propagates along the interface with a certain propagation vector (k_{spp}) that can be adjusted to match that of the SPP by controlling the angle of incidence (Θ).

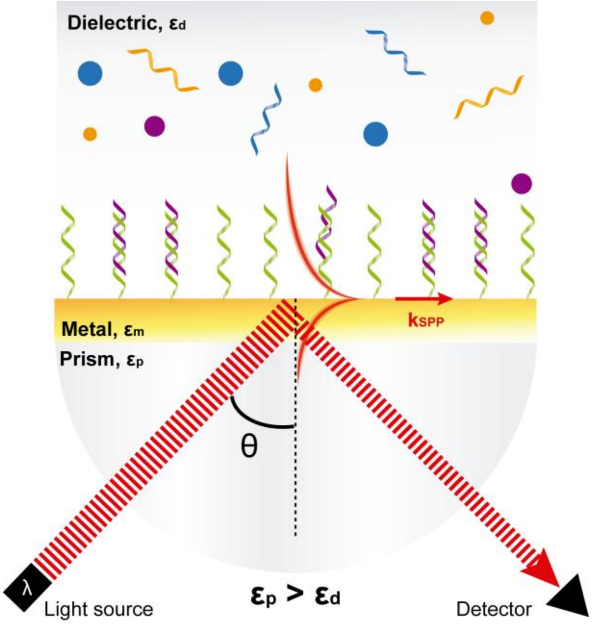

Figure 1. 9 Schematics of a SPR biosensor employing a Kretschmann configuration.

The resulting SPR is characterized by the appearance of a spectral reflectivity dip, which strongly depends on the refractive index of the dielectric but also on the properties of the metal film. Although silver has shown most efficient SPR excitation (i.e. deeper and sharper peaks) and it is quite versatile for functionalization, it is also very susceptible to surface oxidation on exposure to the atmosphere or liquid aqueous environments.[76] Thus, the biofunctionalization and the assay performance become more complicated and require careful protection of the surface and accurate conditions of analysis to avoid or minimize degradation. On the contrary, gold is very resistant to oxidation and other atmospheric contaminants as well as it can be readily modified for surface biofunctionalization procedures (e.g. thiol-gold chemistry). This makes gold the most practical and efficient metal for SPR biosensors. The thickness of the gold film is also a determining factor. For Kretschmann configurations in particular, the thickness should be around 50 nm. Above this thickness the dip in the reflective light becomes shallow while below 50 nm the peak becomes broader, worsening the sensitivity of the biosensor.[77]

An SPR biosensor generally consists of (i) an optical system for excitation and interrogation of propagating SPP, that is, the light source (either mono-chromatic or broadband) and the detector (intensity- or phase-based); (ii) the plasmonic transducer, which usually consists of a thin film (≈ 50 nm) of gold that incorporates the biomolecular recognition element on its surface; and (iii) a fluidic system comprising one or more flow cells for sample confinement at the sensing surface and a flow delivery system for sample injection and delivery.

When working at a fixed θ with broadband light source, the detection is performed by spectral analysis of the reflected light. The reflectivity spectrum shows a dip located at λ_{SPP}, which is subjected to lateral (spectral) displacements induced by changes of refractive index. Spectral interrogation of λ_{SPP} translates changes of refractive index into a measurable quantity that can be extracted as a function of time (**Figure 1.10A** and **C**). On the other hand, with a monochromatic source (i.e. fixed wavelength) the reflected light is measured as a function of the incident angle θ. At a certain angle denoted as θ_{TIR}, the Total Internal Reflection (TIR) sets in. As the angle increases, the reflected intensity exhibits a strong decrease, until a minimum value is reached. It is at this angle (θ_{SPP}), called resonance angle, where the light wavevector matches the SPP wavevector, yielding to the excitation of the SPP. When a biomolecular interaction takes place within the evanescent field of the SPP, a local refractive index change is induced altering the SPP wavevector and its excitation condition. Changes in the SPP can be observed as changes in the properties of the light. These can be detected by time-dependent monitoring of the entire curve, or by fixing θ at the point where the slope of the SPP resonance curve is maximum, after which the intensity changes of the reflected light are monitored as a function of time (**Figure 1.10B** and **D**). Our research group has a strong experience in developing complete SPR biosensor platforms based in Kretschmann configuration employing both the monochromatic source and the broadband light source approaches for the excitation of the SPP and measuring the intensity changes of the reflected light working at fixed angle. Working in either two schemes, biochemical interactions can be directly monitored in real time allowing the evaluation of the affinity and kinetic studies in a simple, rapid and label-free manner.

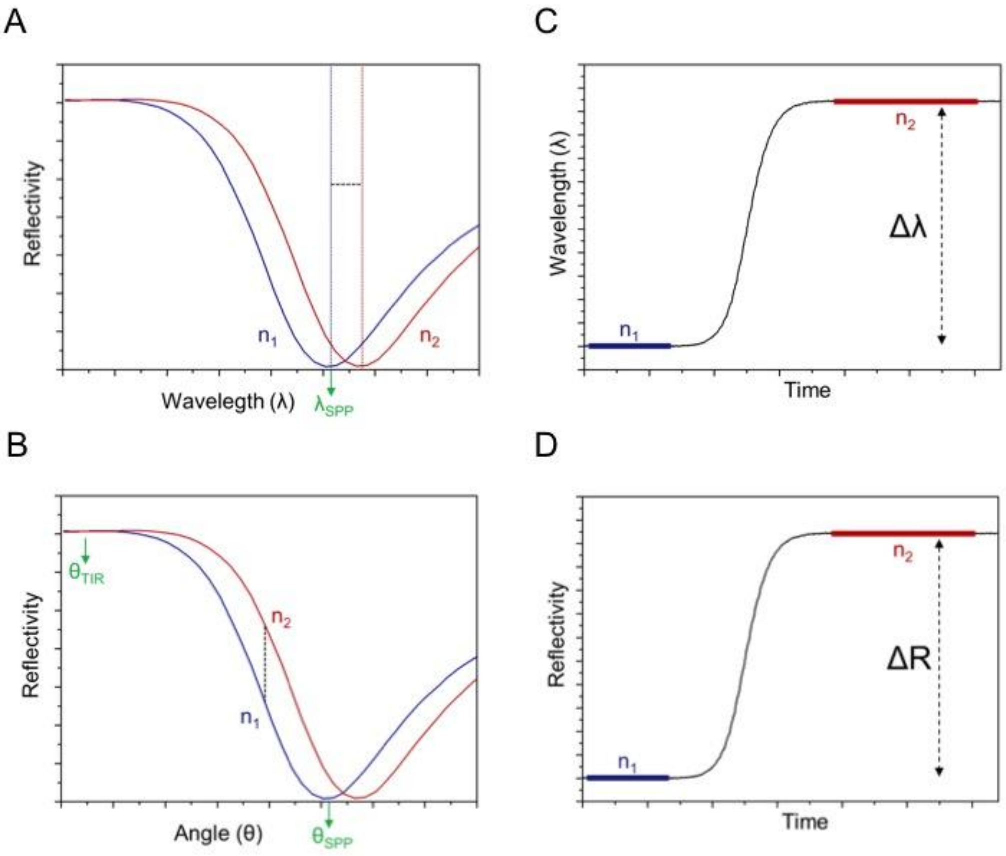

Figure 1. 10 Representative SPR curves for **(A)** λ-interrogated and **(B)** θ-SPR sensors, together with their corresponding real-time tracking of curve displacements via the monitoring of **(C)** shifts of the resonance wavelength, λ_{SPP}, and **(D)** changes of the reflectivity, R.

It is worth mentioning that the changes of the local refractive index are directly related to mass changes on the surface (i.e. an increase or decrease of the coverage of the surface with molecules of a particular size and density will alter the overall local refractive index). Therefore, the smaller the captured molecule is, the lower refractive index change will be induced, compared to an analyte with a higher molecular weight in the same concentration. These biosensors reach a relative change in the index of refraction (bulk sensitivity) between 10^{-5}-10^{-7} RIU and mass detection limits of 1-5 pg/mm^2). [74, 78]

SPR biosensor is nowadays a mature technology offering direct, rapid and systematic analysis of any type of biochemical interaction. Currently, their employment is widespread and a large variety of instruments, from miniature SPR-based devices to robust laboratory units, are commercially available to meet special requirements of a multitude of applications.[61, 79, 80] Biacore (GE Healthcare)[81] was the first commercial system launched in 1990. Since then, more than 20 companies worldwide have been offering different SPR instruments, such as Texas Instruments,[82] XanTec Bioanalytics,[83] Horiba Scientific[84] or Biosuplar,[85] among others.

The SPR biosensor employed in this thesis was developed in our Group in 2004 and was commercialized by the spin-off company Sensia S.L.,[86] which currently belongs to Mondragon Corporation (www.mondragon-corporation.com). The SENSIA SPR biosensor is integrated in a reduced platform and can be employed as a portable and user-friendly device (**Figure 1.11A**). The sensor platform is based on the Kretschmann configuration with a real-time monitoring of the intensity of the reflected light at a fixed angle of incidence. The laser beam (λ = 670 nm) is divided in two identical intensity beams using a light splitter (5 mm/side cube) to enable the simultaneous evaluation in two independent channels. The laser beams pass through a glass-coupling prism (n = 1.52), reaching the backside of the gold sensor chip *via* a refractive index matching oil (n ≈ 1.515) (**Figure 2.1B**).

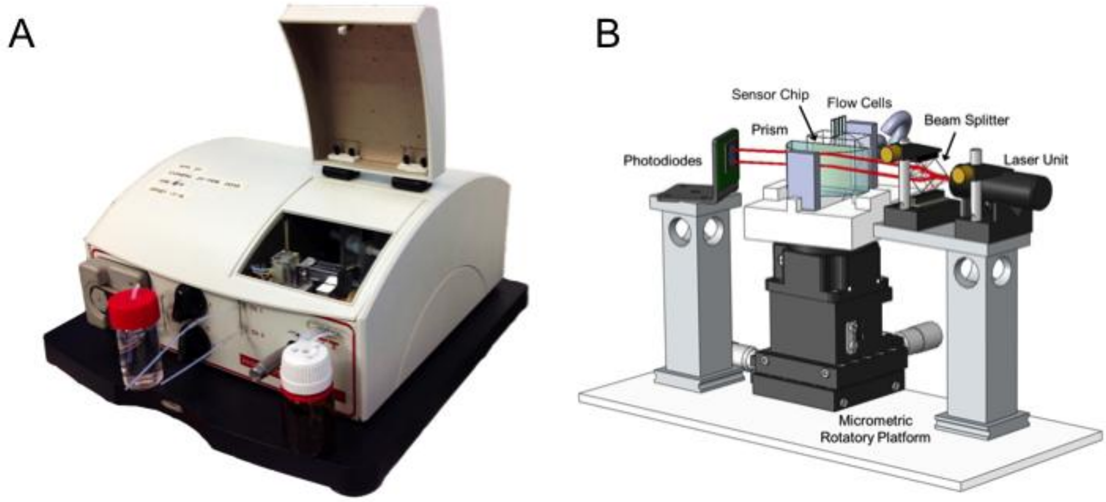

Figure 1. 11 SPR biosensor. **(A)** SENSIA SPR Biosensor device. **(B)** Schematic representation of the sensor module of the SENSIA SPR Biosensor.

The gold sensor surface where the biomolecular interaction takes place is in contact with two identical flow cells of approximately 300 nL volume each one. Biological events occurring at the sensor surface are detected as changes in the reflected light intensity (ΔReflectivity (%), ΔR (%)) by a multielement photodiode. This part of the setup is mounted on a rotary platform in order to select the optimum incidence angle that maximizes the changes of reflected light intensity. The platform also incorporates all electronics and fluidics components necessary to operate autonomously. The fluidic system consists of a peristaltic pump which keeps a continuous flow and a set of tubing and valves for the sample handling and injection to the flow cuvette. A custom-made software in LabVIEW controls the flow rate and injection of the sample as well as the monitoring of the binding events.

Due to their simplicity and versatility, SPR biosensors have profiled themselves as a routine analytical instrument whose scope has spread into a wide range of applications. The label-free detection and the real-time monitoring of biochemical interactions permit the determination of any target analyte and the affinity or kinetic studies of the reaction in a simple and reliable way. SPR-based kinetic analysis permits the monitoring of both weak and strong interaction (KD ranging from 1 mM to 1 pM)[87, 88] and typically requires lower amount of reagents than traditional biophysical techniques (titration calorimetry, ultracentrifugation, stopped flow or column chromatography). The sensitivity of refractometric SPR sensors usually ranges between 10^{-6} and 10^{-7} refractive index units (RIUs) and a limit of detection (LOD) in the pM-nM range, if an optimal biofunctionalization has been previously achieved and high-quality biological reagents are employed.[61, 89] These sensitivities are good enough for a great variety of real diagnostic applications, but become a critical factor for the direct determination of small analytes at very low concentrations or for single-molecule detection. In addition, SPR biosensor has reduced multiplexing capabilities making difficult the simultaneous detection of several targets in the same sample, which in some cases is a requisite such in the micro-RNA regulation study. Researchers are exploiting the exceptional properties offered by recent advances in nanotechnology. New biosensors based on nanoplasmonics or silicon-based photonics are being developed. They offer improved sensitivity levels and represent a step forward to the development of lab-on-a-chip devices with multiplexed capabilities.

1.5. Bimodal waveguide interferometer biosensor

A *waveguide* is a structure of conductive or dielectric material used to guide high-frequency waves, such as electromagnetic waves in the case of *optical* waveguides. They enable the light to propagate with minimal loss of energy by restricting its expansion to one-direction or two. The simplest example of an optical waveguide structure is a planar waveguide (**Figure 1.12**). It is constituted by a high refractive index material (n_1) surrounded by two media of lower refractive index (n_2 and n_3), satisfying the condition $n_1 > n_2 \geq n_3$. If $n_2 = n_3$ the waveguide is symmetric. Light can propagate in such structure in the form of *guided modes*, which are characterized by a unique field distribution and propagation velocity that depend on the waveguide geometry (core thickness, *d*, and refractive indices, n_1, n_2 and n_3) and on the working wavelength, λ.

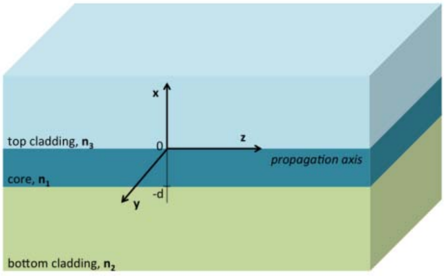

Figure 1. 12 Scheme of an asymmetric slab waveguide.

Guided modes are characterized by their effective refractive index (N_{eff}), which is related to the propagation constant β through:

$$\beta \equiv k_o N_{eff} \tag{1.3}$$

where k_0 is the wavevector. The wavevector is given by: $k_o \equiv \frac{2\pi}{\lambda_0} = \frac{\omega}{c}$, where λ_0 is the wavelength of the light in the free space, related to the angular frequency by $\omega=2\pi c/ \lambda_0$.

The condition for the propagation constant for a guided mode is given by:

$$k_0 n_2 < \beta < k_0 n_1 \tag{1.4}$$

which can be rewritten as a function of the effective refractive index as:

$$n_2 < N_{eff} < n_1 \tag{1.5}$$

Therefore, each mode is defined by their propagation constant, β_m. Waveguides admitting only one solution for the propagation constants β_m are called single-mode, while structures supporting more than one mode are referred to as multi-mode waveguides. In case that no modes can propagate the waveguide is said to be in cut-off for a given wavelength.

Depending on the light polarization, there are two types of modes, *transverse electric* (TE) and *transverse magnetic* (TM) modes, as illustrated in **Figure 1.13**. For TE modes, the electric field exhibits only a component perpendicular to the incidence plane (E_x, $E_z = 0$ and $E_y \neq 0$), while in the case of TM polarization, the modes are characterized by an electric field vector parallel to the incident plane (E_x, $E_z \neq 0$ and $E_y = 0$).

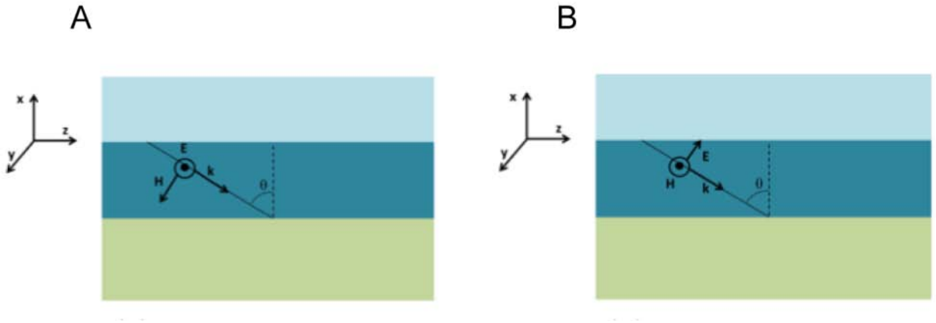

Figure 1. 13 Propagation of **(A)** TE and (**B**) TM modes in an asymmetric planar waveguide.

The confinement offered by a planar waveguide is not sufficient for many applications and the light has to be confined in a more localized region of space, directing the optical power and the related information to the region of interest, such as the sensor area in the case of biosensors. For these reasons, three-dimensional (3D) structures have been designed to allow for light confinement along two directions. The most common configurations are the raised strip, the embedded strip or the rib waveguide, as shown in **Figure 1.14**.[90] All of them consist of a 3D-structure confined between cladding layers, forcing the light to propagate along a more restricted space.

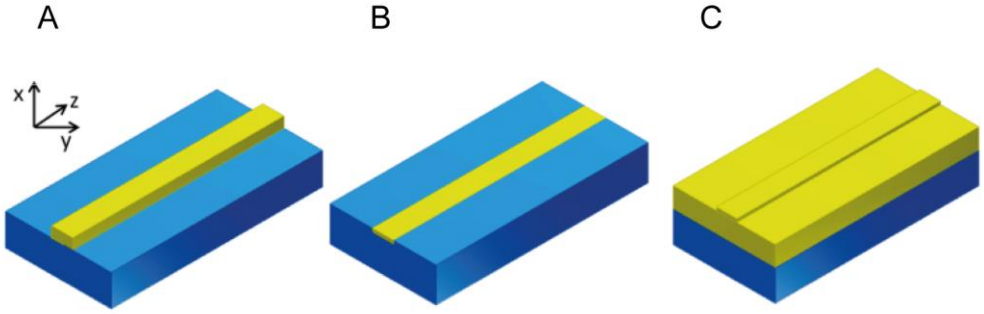

Figure 1. 14 Main types of 3D-waveguides: (**A**) raised strip waveguide, (**B**) embedded and strip and (**C**) rib waveguide.

3D optical waveguides are normally used in integrated optical circuits but can be employed also as high sensitive transducers in biosensors devices. In such biosensors, the light is confined by Total Internal Reflection (TIR) into a high refractive index 3D waveguide (the core), surrounded by mediums of lower index (the claddings). A variation of the refractive index medium over the core will be translated into a variation of the effective refractive index of the propagating mode, which can be detected at the sensor output through different working principles. In the last years, several integrated optical devices have been implemented for biosensing. Grating couplers,[91] optical resonators[92] and interferometric arrangements constitute the most important ones.

Interferometers based on optical waveguides typically have one or even two orders of magnitude better detection limit for surface mass density and refractive index changes than microring resonators and grating coupler sensors.[93] The most common configurations are the Mach-Zehnder Interferometer (MZI)[94, 95] and the Young Interferometer (YI),[96, 97] which have been implemented as totally integrated, i.e. light beam splitting and recombination take place on the same device, or hybrid configurations, i.e. bulk external optical components are required. In their basic configurations, both MZI and YI have an input single-mode waveguide which originates two arms after a Y-junction: one of the two arms is exposed to the external medium to be sensed, while the other is employed as a reference. In the case of MZI (see **Figure 1.15A**) the two arms are recombined through a second Y-junction into a single output waveguide, while in the case of YI (**Figure 1.15B**) the intensity distributions originated from the two waveguides are superposed over a screen, resulting in both cases in an interference pattern with a determined number of fringes with a certain amplitude (visibility factor) depending on their sensitivity. Due to their geometry involving two spatially separated arms, they are often referred to as double-path interferometers. Such geometry difficult their fabrication processes, which can result in asymmetric splitting of the light or in a difficult light recombination leading to unreliable output signals.

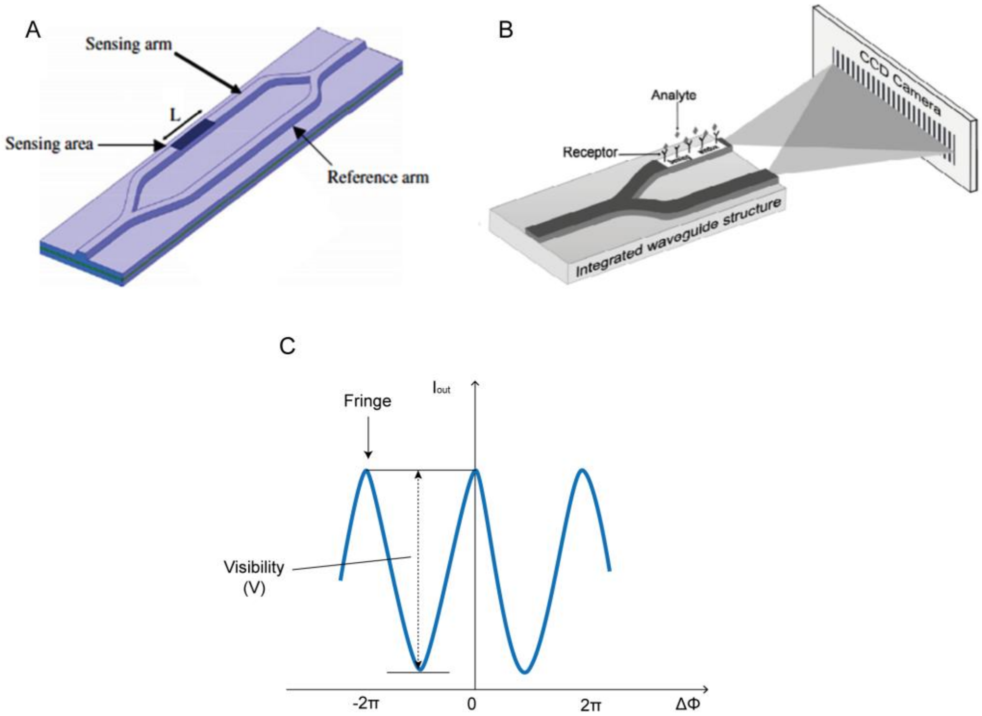

Figure 1. 15 Dual-path interferometric biosensors: (**A**) Mach-Zehnder[98] and (**B**) Young.[99] (**C**) Typical interference signal originated by interferometric biosensors.

As an alternative to these configurations, a novel interferometric arrangement that avoids light beam splitting and recombination was recently proposed in our group,[100] the BiMW device. In this interferometer, the two beams propagating into separate arms of the MZI are replaced by two modes of different orders propagating along a single straight channel (i.e. a waveguide). This results into a device with improved tolerance to fabrication variations and a smaller footprint, opening the possibility to fabricate more devices in the same area, with consequent increased of the reproducibility and reliability of the sensing evaluations.

The BiMW interferometer consists of a symmetric 3D optical rib waveguide fabricated with standard microelectronic technology, including photolithography and etching processes. This kind of fabrication allows for wafer-level packaging, producing numerous sensors in the same process with accurate precision and reproducibility, reducing the time and the manufacturing costs (**Figure 1.16A**). The BiMW biosensor miniaturized size allows for multiplexed array formats and are compatible with complementary metal-oxide-semiconductor (CMOS) fabrication processes, emerging as a promising candidate for Lab-on-Chip implementation (**Figure 1.16B**). In our standard production process at Clean Room facilities, sixteen interferometers of 31 mm total length are fabricated over a silicon substrate. A scheme of one chip containing 16 devices is shown in **Figure 1.16C**.

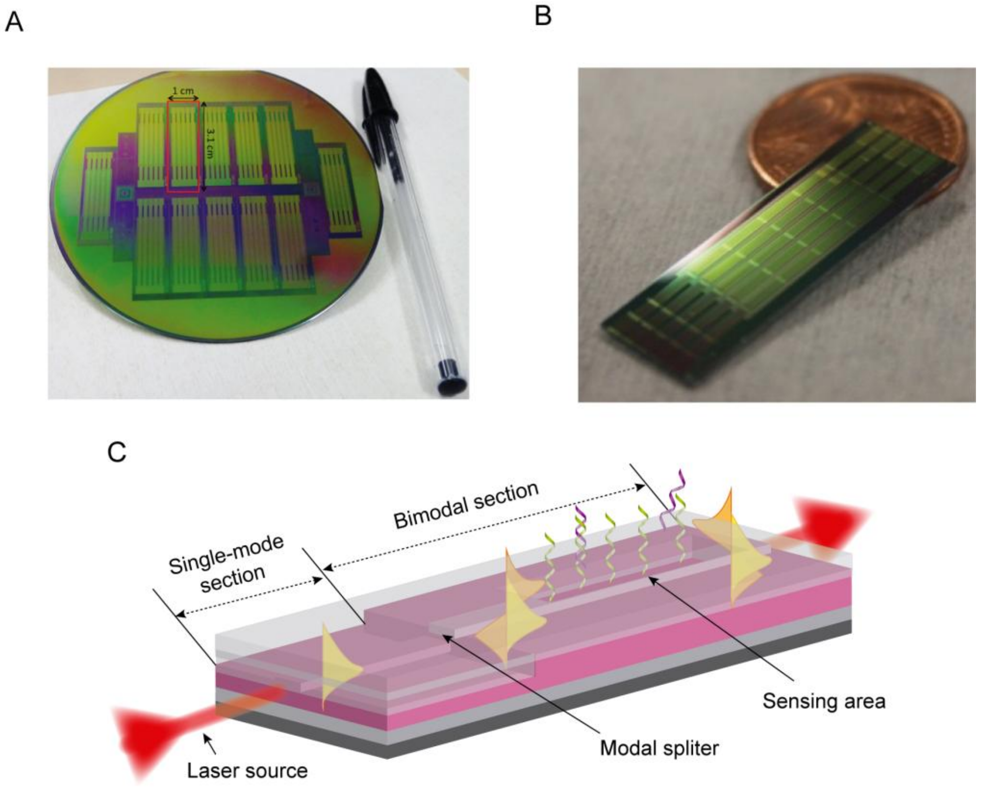

Figure 1. 16 BiMW device. (**A**) Photograph of a processed 4-inches wafer with 12 BiMW chips, resulting in a total of 192 sensors. (**B**) BiMW chip containing 16 sensors. (**C**) Scheme of the working principle of a Bimodal Waveguide interferometer. Light is injected in the single-mode input waveguide and after a modal splitter two modes are excited and propagate until the device output.

Figure 1.17 represents the cross section (**A**) and longitudinal view (**B**) of a BiMW interferometer. In order to meet the requirements for light confinement and propagation, the waveguide is constituted by a core layer of silicon nitride (Si_3N_4) of high refractive index (n_{core} = 2.00). This core layer is embedded between two silicon dioxide (SiO_2) cladding layers of smaller refractive index (n_{cladd} = 1.46) that permit the propagation of the light through the core layer. At the sensing window (section C in **Figure 1.17B**), the SiO_2 cladding layer is removed and replaced with a dielectric medium as cladding layer (in case of water, n_{H_2O} = 1.33), leaving the Si_3N_4 core layer in contact with the external medium for sensing.

Due to their transparency over a broad spectral range (~200 − 2000 nm), SiO_2 and Si_3N_4 are excellent material candidates for the fabrication of sensor devices operating at visible wavelengths. The high refractive index contrast between both materials can render in optimal structures for sensing applications.[94] Moreover, Si_3N_4 is not only appropriated as a core layer due to its high refractive index but also by its chemical properties such as high density and chemical inertness that make it resistant to ion species, oxygen, and moisture permeation.[101] Additionally, silicon microelectronic fabrication processes ensure a high homogeneity of the waveguide material and the possibility of multiplexed and final integration in complete portable platforms.

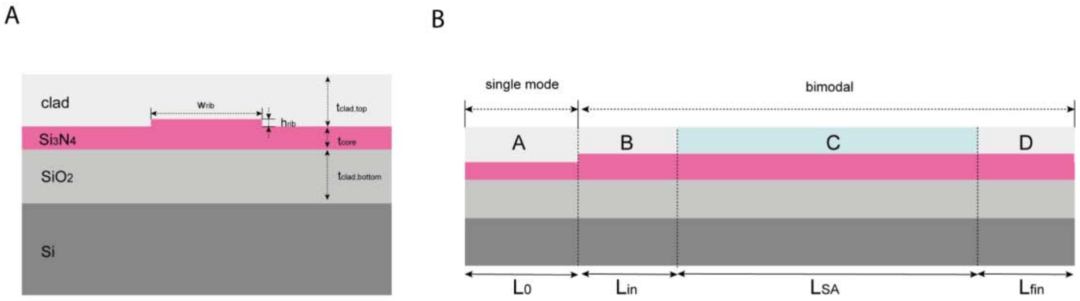
A
clad
w_{rib}
h_{rib}
$t_{clad,top}$
Si_3N_4
t_{core}
SiO_2
$t_{clad,bottom}$
Si
B
single mode
bimodal
A
B
C
D
L_0
L_{in}
L_{SA}
L_{fin}

Figure 1. 17 Bimodal Waveguide interferometers cross section (**A**) and longitudinal view (**B**).

In the BiMW device, TE-polarized light (λ_0= 660 nm) is first confined into the nanometric height rib waveguide (4 µm width x 1.5 nm height) designed to support a single transversal mode (150 nm thickness). After some distance, this fundamental mode is coupled into a vertically bimodal section (300-350 nm thickness) through a step junction, i.e. a modal splitter. At the step junction, due to the abrupt increase of the height of the waveguide core, it splits in two modes, the fundamental and the first order modes. These two modes propagate until the end of the device, resulting in an intensity distribution which depends on the phase difference between the two modes accumulated along the propagation length. A sensing window is opened along the bimodal section of the waveguide, so that the evanescent field is in contact with the external medium and it is sensitive to variations of the refractive index of the environment. By placing the BiMW sensor in a custom-made fluidic cell the desired solution can be loaded and injected to interact with the device sensing area (**Figure 1.18**).

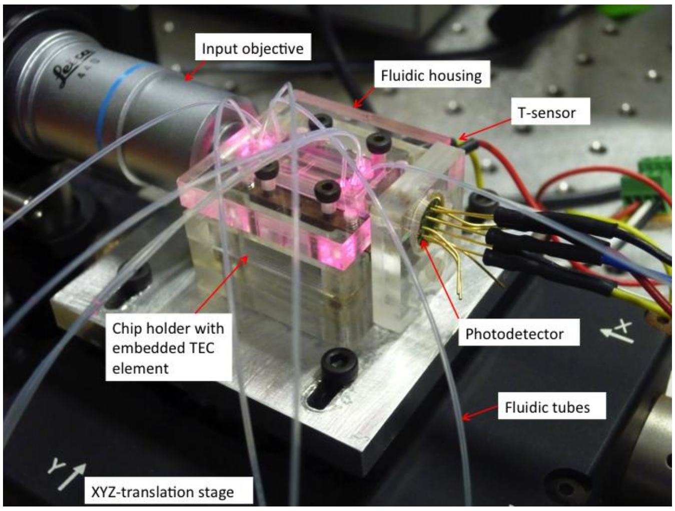
Input objective
Fluidic housing
T-sensor
Chip holder with embedded TEC element
Photodetector
Fluidic tubes
XYZ-translation stage
X
Y

Figure 1. 18 Photograph of the BiMW set-up.

Due to the different confinement factors of the propagating modes, the first order mode is the main responsible for the sensing of changes occurring on the device surface, while the fundamental mode can be considered as a virtual reference. The superposition of these two modes results in an intensity distribution whose variations can be related to the amount of stimulus variation. On the sensor surface, when a biorecognition event occurs between a biorecognition layer of refractive index n_0 and its concomitant target, the refractive index of the biosurface changes (n_0'), as shown in **Figure 1.19**.

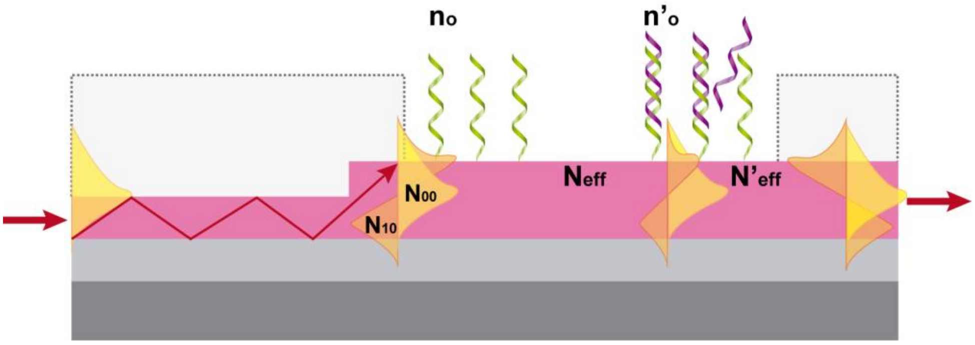

Figure 1. 19 Sensing principle of a BiMW biosensor.

This variation of the external refractive index affects the effective refractive index of the propagating modes (N_{00} for fundamental mode and N_{10} for first order mode), producing a phase change ($\Delta\Phi$):

$$\Delta\Phi = 2\pi \frac{L_{SA}}{\lambda} (\Delta N_{10} - \Delta N_{00}) \tag{1.6}$$

where L_{SA} is the length of the sensor area and λ is the working wavelength. As can be appreciated, L_{SA} is a parameter that is linearly dependent to the phase change and strongly affects to the final sensitivity of the biosensor. Therefore, a value of 15 mm has been adopted to ensure a high sensitivity while keeping a reasonable homogeneous length of the BiMW device (L_0 = 3mm, L_{in} = 4.5 mm and L_{fin} = 8.5 mm; L_{total} = 31 mm).

Changes in the refractive index generated by a biorecognition event in the sensor area will affect differently to each mode, generating an interference pattern at the output of the waveguide which is recorded by a two-section photodetector and that is directly related to the concentration of the target analyte. The phase shift induced by the biomolecular interaction taking place on the sensor surface is quantified from the variation of the output intensity distribution, by monitoring the signal S_R:

$$S_R = \frac{I_{up} - I_{down}}{I_{up} + I_{down}} \tag{1.7}$$

where I_{up} and I_{down} are the intensities collected by the upper and lower sections of the detector, respectively, and S_R is usually expressed as a percentage. The signal S_R is related to the refractive index change occurring in the sensing area of the device by:

$$S_R \propto V \cos(\Delta\Phi\ \ t\ \ ) \tag{1.8}$$

where V is the fringe amplitude (visibility factor). This factor corresponds to the amplitude of the S_R oscillation (interference fringes) and is defined as:

$$V = \frac{S_{R,max} - S_{R,min}}{2} \tag{1.9}$$

Equation 1.8 is the fundamental equation used for the quantification of the experimental data when the device is operated in standard conditions, i.e. with monochromatic light excitation. The quantity $\Delta\Phi$ is deduced from the analysis of the output intensity interference pattern: a complete oscillation of S_R, or a fringe, corresponds to a 2π phase variation. **Figure 1.20** shows the time evolution of the I_{up} and I_{down} signals during a refractive index variation $\Delta n = 9 \times 10^{-4}$ induced by flowing a solution of HCl (**A**) and the corresponding S_R signal (**B**). This last one is the typical interferometric response of a BiMW biosensor for a homogeneous variation in the refractive index of the medium in contact with the sensing area. S_R signal starts from a constant level (corresponding to water) and varies when HCl reaches the sensing area ('HCl on' in **Figure 1.20A**); then stabilizes and returns to the starting level when milli-Q water arrives again to the sensor area ('HCl off'). The phase shift induced by the refractive index variation occurring in the sensing area is determined by counting the number of fringes described during the evaluation, according to the equivalence between a complete fringe oscillation and a phase change $\Delta\Phi = 2\pi$.

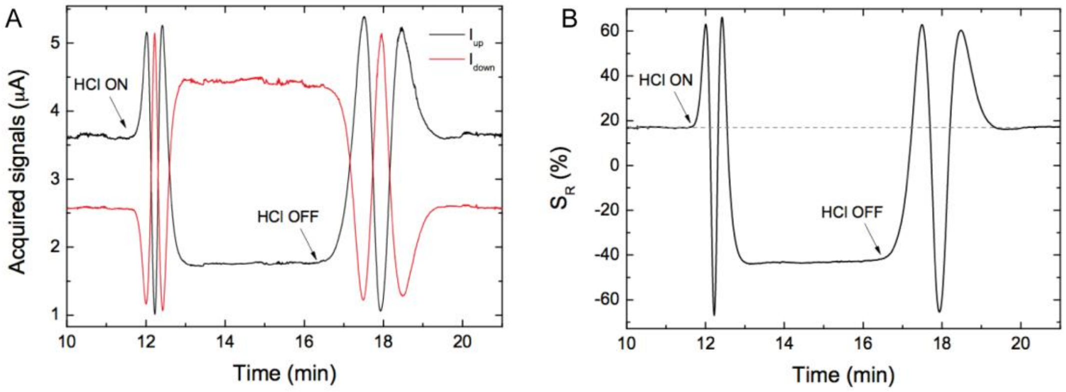

Figure 1. 20 Typical BiMW sensor signals. (**A**) Acquired I_{up} and I_{down} signals and (**B**) corresponding S_R during the detection of a refractive index change $\Delta n = 9 \cdot 10^{-4}$.

The BiMW signal is limited by the periodicity of the output signal with the phase variations, which impede a direct and non-ambiguous read-out. This has prevented their successful technological transfer for commercialization and its application in the clinical practice. In order to solve these limitations a simple, reliable and cost-effective phase modulation system has been incorporated to provide directly a linear output signal. It is based on the modulation of the incident wavelength and Fourier transform deconvolution, transforming such interferometric read-out into a real-time linear signal[102] (**Figure 1.21**).

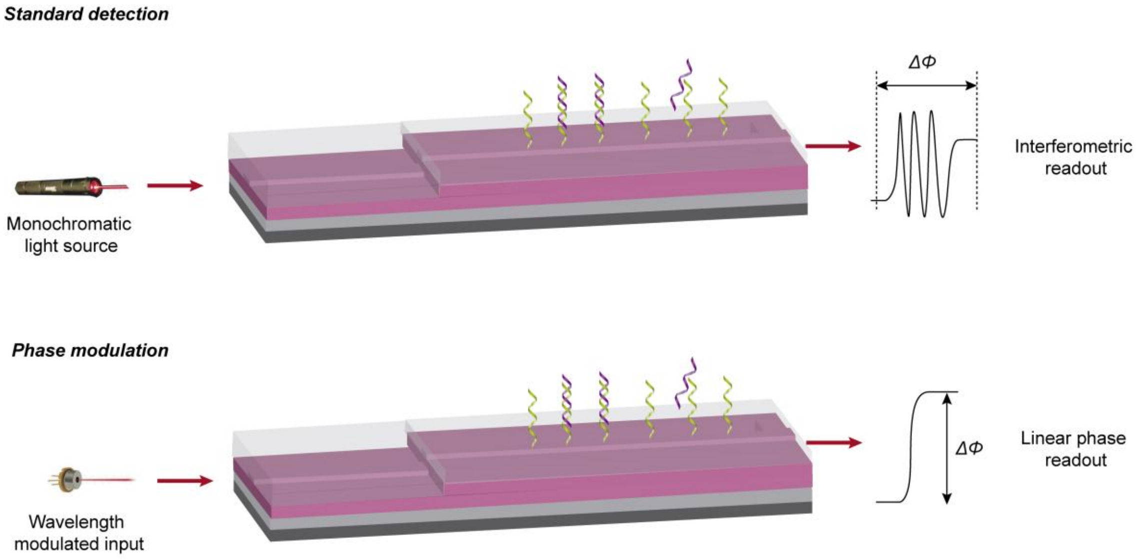

Figure 1. 21 Schematic comparison of standard monochromatic approach with sinusoidal output (*up*) and wavelength modulated sensor with linear phase read-out (*down*).

The BiMW interferometers has demonstrated bulk sensitivity detection limits in the order of **4 x 10^{-7} RIU**, making them competitive with the most sensitive optical detection methods (**Table 1.1**).[100] Their high sensitivity together with their miniaturized size and their multiplexed format, make this analytical technology a very promising candidate for Lab-on-Chip implementation and PoC development[103] (**Figure 1.22**). BiMW sensors represent an ideal platform for the direct and multiple screening of biomarkers during the analysis of complex samples avoiding pre- and post-amplification steps with minimal sample input, thus saving time and resources. Recently, our patented BiMW technology[104] has been transferred to Promax Electrónica, SL whose efforts are specially focused on the complete development and integration of this biosensor to be promptly commercialized as functional Lab-on-a-chip devices for PoC testing.

Table 1. 1 Integrated optical biosensors compared in terms of architecture and detection limits

Device configuration	Refractive index detection limit (RIU)	Mass detection limit (pg/mm^2)
SPR	$10^{-5} – 10^{-7}$	1 – 5
Gratings	10^{-6}	0.3 – 5
Ring resonators	$10^{-5} – 10^{-7}$	0.3 – 3
Interferometers	$10^{-7} – 10^{-8}$	0.02 – 1

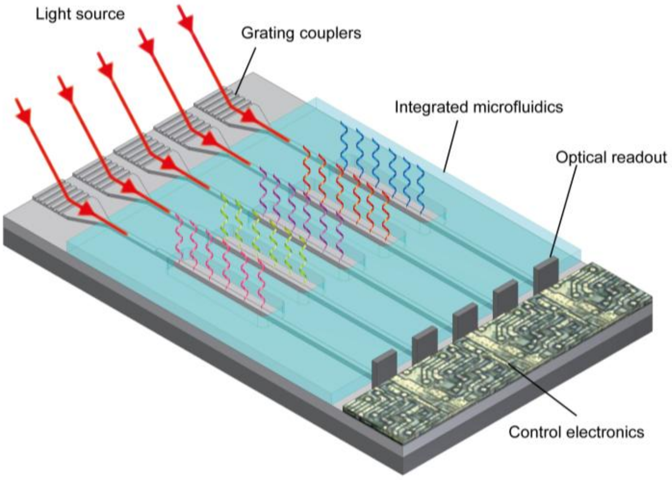

Figure 1. 22 Array of Nanophotonic sensors incorporating grating couplers for light source coupling, optical readout and control electronic, integrated on chip for Point-of-care development.

A previous proof-of-concept immunoassay of the biomarker C-reactive protein demonstrated the applicability of the BiMW device for highly sensitive and label-free biosensing.[105] Different concentrations of specific antibody solutions in the range of 0.5-5 μg/ml were successfully evaluated, achieving a limit of detection < 1ng/mL. However, although its feasibility has already been demonstrated, the development of clinical applications for diagnostic purposes has not yet been fully completed. Particularly, this sophisticated technology has not ever been applied for the detection of nucleic acid molecules. Immobilization strategies and optimization of the methodologies has to be undertaken in order to demonstrate the BiMW device as a valuable and sensitive tool for illness prognosis and follow-up therapies.

Chapter 2·DNA-functionalization of the sensor surface

This chapter focuses on the design and optimization of different functionalization procedures for DNA-probe immobilization on the sensor surface. The biofunctionalization strategies are analyzed in terms of hybridization efficiency, stability and selectivity. An exhaustive study to minimize nonspecific adsorptions onto the different sensor surfaces is also presented and evaluated with biological fluids, such as urine or blood serum. Finally, different approaches for surface recycling are explored to guarantee the reusability of the biosensor without compromising the biosensor performance.

2. DNA-functionalization of the sensor surface

2.1. The biorecognition layer

In optical biosensors, the biorecognition layer tethered at the surface of the transducer is of paramount importance. The final sensitivity and specificity of the biosensor are directly related to the activity of the immobilized molecules and the accessibility of their specific targets. In the development of nucleic-acid based biosensor there are two key steps: (i) the DNA probe design, responsible of the system selectivity; and (ii) the surface functionalization chemistry, which should allow for both, proper accessibility of the target to its complementary probe and avoidance of undesired adsorption of nonspecific molecules present in biological fluids.

The DNA probe must provide to the biosensor with the sufficient affinity and specificity for the selective capture of the target molecule avoiding non-specific hybridization from other nucleic acid molecules present in the same sample. In some cases, the selectivity needs to be very high to distinguish between single-point mutations, to discriminate between homologous sequences or to avoid cross-hybridization from nucleic acids showing half-complementarities in their sequences. On the other hand, the probe must be immobilized to the sensor inorganic surface, a crucial step to achieve a highly sensitive and selective biosensor. The control of this process is essential and is expected to address two issues: (i) the robust and reproducible grafting of probes in well-oriented and accessible positions and (ii) the creation of a low-fouling background. Different mechanisms for the attachment of the probe can be employed, such as physical adsorption or covalent immobilization. The former one is the simplest immobilization method, because it does not require any nucleic acid modification taking advantage of intermolecular forces such as electrostatic, hydrophobic and/or polar interactions.[106] This adsorption is solely governed by physical attractive forces between the biomolecule and the surface, so that the amount of adsorbed DNA probes cannot be controlled and may vary along the surface, constituting an important drawback for the biosensor performance. In addition, flow-through assays or changes in the pH or buffer composition can lead to easily desorption of the biomolecules,[107] causing a loss of the signal and possible cross-contamination of the surface. Furthermore, the interaction of the DNA nucleobases with the surface can difficult its accessibility for the target. It has been reported that DNA molecule become totally inaccessible for hybridization when only 3% of its bases are involved in the linkage.[108]

The covalent immobilization approach involves chemical reactions to link the biomolecules to the sensor surface by means of a covalent bond. It generally requires the modification of the oligonucleotide probe during the synthesis process with a functional group in order to facilitate the chemical bonding. This strategy provides the most suitable conditions to achieve a controlled grafting of the probes and ensure their proper orientation. Chemical grafting avoids the probe release to the solution, surpassing one of the main drawbacks of physical adsorption and guaranteeing a better reproducibility leading to a more robust methodology. Likewise, it can reduce the background signal coming from nonspecific adsorption because optimized surface chemistry can be implemented for that purpose.

Another important aspect in biofunctionalization is related to the surface regeneration. The removal of the target nucleic acid after the detection step, without altering the immobilized probe, provides a reusable biosensor, making possible to repeat analyses under the same conditions. This also permits the assessment of the variability of the methodology by evaluating the reproducibility and robustness of the bioactive surface. Therefore, the selection of a correct regeneration protocol with the mildest possible conditions is necessary to assure the stability and integrity of the probe monolayer.

In this chapter different oriented immobilization approaches of DNA probe grafting have been proposed. First, we have focused our attention on the evaluation of three different biofunctionalization strategies on gold surface for SPR biosensor analyses. They have been evaluated in terms of sensitivity, selectivity and stability. Likewise, we tested the fouling properties of each strategy and explored new surface coatings for the development of non-specific adsorption resistant biorecognition layers for the detection of nucleic acid targets in complex matrices for real samples analysis, such as blood serum or urine. On the other hand, we have established a DNA probe immobilization strategy on silicon nitride (Si_3N_4) surfaces for BiMW interferometers. The approach has been fully optimized and evaluated to ensure a reliable and ultra-sensitive analysis of nucleic acids with this innovative biosensor technology.

2.1.1. Oligonucleotide-based probe design

The probe design is an important step since it is the main responsible for the system selectivity and target specificity. In this chapter we focus on the design of ssDNA chains as biorecognition elements.

In the design of ssDNA probes three factors have to be considered: (i) the functional group (linker) that will allow the attachment of the probe to the sensor surface; (ii) a vertical spacer to improve accessibility, and most importantly (iii) the sequence itself (**Figure 2.1**).

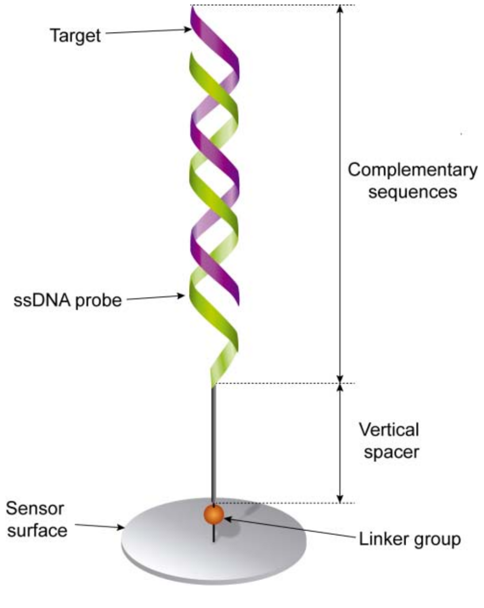

Figure 2. 1 Standard ss-DNA probe employed as bioreceptor in biosensors.

Depending on the chemistry used for the covalent grafting of the DNA probes to the surface, they can be end modified to introduce a site-specific group for covalent and oriented attachment. A wide variety of linkers are available for synthetic oligonucleotides depending on the surface chemistry required. Short DNA strands (oligonucleotides) modified by amino, thiol, hydrazide, phosphorothioates or biotin linkers are commonly used for DNA immobilization.[106] In particular, we used two different functional linkers: the thiol (SH-) group and the amine (NH_2-) group for different immobilization strategies discussed below.

End modification of DNA probes not only introduces a site-specific group for the oriented covalent attachment of the probes, but also can insert a spacer link between the nucleic acids probes and the surface. This vertical spacer is intended to improve the mobility of the immobilized probes and their accessibility by the complementary target sequences. They also move away the DNA probe from the surface, reducing the adsorption and steric effects produced by the surface. Different vertical spacers can be introduced, such as a simple carbon chain[109] or poly-thymine ($polyT_m$) sequences[64, 110] which acts as a vertical spacer due to the low affinity of thymine bases for gold surfaces.[111] From our studies, due to their easiness in synthesis and their better stability, we selected a sequence of 15 thymines ($polyT_{15}$) between the nucleic acid probes and the functional group attached to the surface.

For the selection of the probe sequence there are available many commercially codes that help to tailor the probe-target stability of a given application.[112] One major problem in the design of oligonucleotide probes for DNA/RNA capture is the presence of regions that can assume conformations by self-hybridization and may hide the binding site of interest, i.e. by formation of secondary structures such as hairpins or loops (**Figure 2.2**). In order to avoid this self-hybridization or secondary structures, it is very important to take into account the length of the probes and the C-G base content. It has been studied that probes containing between 15 to 25 bases for the recognition of their targets permit a strong hybridization while avoiding self-complementarities and reducing the likelihood of cross-hybridization from undesired off-target molecules.[112] At the same time, an adequate content of C-G bases promote a stronger hybridization due to higher contribution of stacking interactions during hybridization, hence contributing to the stability of the formed hybrid.[113] However, excess in the CG content may lead to non-specific hybridization of other sequences bearing also a high quantity of these nucleotides. The preferred composition varies from at least 40% to 60% to stabilize the hybrid on the surface.

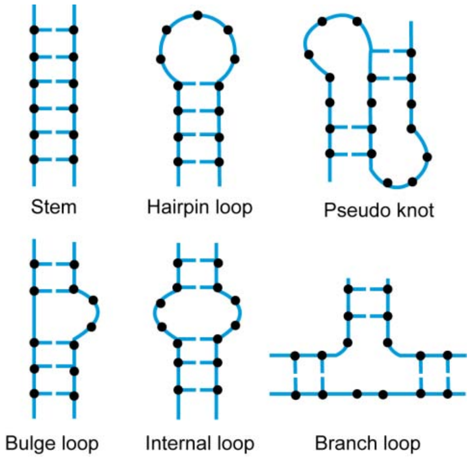

Figure 2. 2 Different DNA secondary structures that can be formed in single stranded nucleic acids.

Additional requisites should be considered depending on the application. In some cases the design of the probes is restricted to a limited sequence of the target or the target sequence is too short, making difficult to adjust the parameters discussed above and, therefore, putting into risk the sensitivity of the biosensor. This difficulty becomes even more challenging when dealing with target presenting different isoforms or homologous sequences showing differences up to the single mismatch, hence hampering the selective detection. These problems narrow down the possibilities in the probe design and in the hybridization conditions applied during the detection and should be finely tuned in order to compensate for such issues.

2.2. DNA immobilization strategies for gold surfaces.

As mention in **Chapter 1**, gold surfaces are the most employed in SPR biosensors. Two of the most widely used approaches for immobilization of probes on gold surfaces are the direct chemical grafting of DNA probes via a thiol linker[114] and the covalent binding on a previously functionalized sensor surface.[115] Other strategies make use of affinity linkers, such as biotinylated probes, which can be efficiently immobilized on avidin/streptavidin modified surfaces.[62, 116] In addition, a new immobilization strategy has been recently proposed based on the affinity of poly-adenine (polyA) sequences to the gold surface.[117] All of these approaches give rise to an ensemble of properly oriented probes attached by only one end-point. They also allow tuning the grafting density, which in turn influences the hybridization efficiency of the targets.

2.2.1. Thiol-chemistry based strategies

Chemical adsorption (i.e. chemisorption) of thiolated molecules on metals, and particularly on gold, is the most widely used immobilization approach due to its easy preparation from gas phase or from solution. It takes advantage of the strong affinity of thiol atoms towards gold surfaces.[118] The immobilization strategy relies on the arrangement of the thiolated molecules for the formation of a secondary and more complex structure with fewer degrees of freedom called *self-assembled monolayer* (SAM).[119] The generated monolayers exhibit molecular order, and are relatively stable in ambient conditions. Typical SAM precursors can be divided in three different parts: the *head* (linking group), that provides chemisorption to the substrate (i.e. thiol group for gold surfaces); the *spacer*, that makes significant contribution to the mechanical properties of the SAM; and the *terminal functional* group, providing the surface with the desired physical and chemical properties (**Figure 2.3A**). The head links the biomolecule to the surface through a covalent bond and the van der Waals forces between neighbor molecules stabilize the structure of the monolayer. The formation of SAMs on gold surfaces with organosulfur compounds follows two distinct steps. The first corresponds to a very fast step where adsorption of the molecules from solution to the surface takes place. Secondly, the monolayer organizes into a well-order state in a slower second step[120] (**Figure 2.3B**).

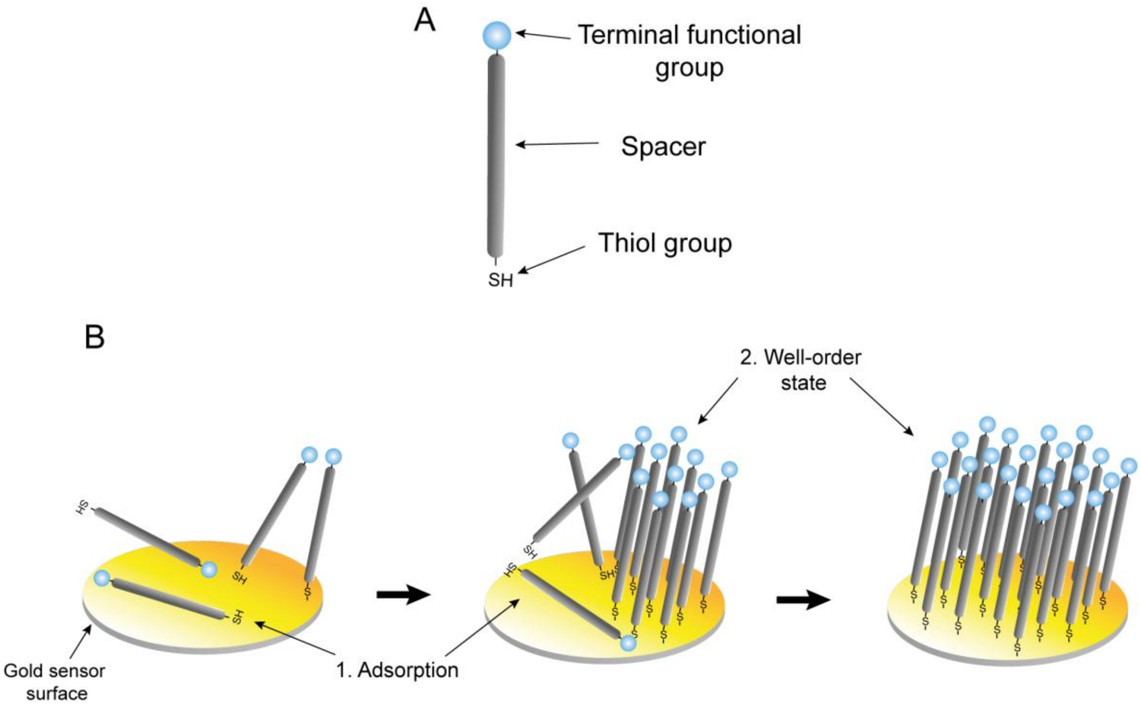

Figure 2. 3 SAM formation on gold surfaces.

Direct DNA probe-surface chemisorption through thiol-chemistry

Chemisorption of DNA probes modified with a thiol linker, i.e. SH-DNA probes, is the most straightforward approach for the development of nucleic acid biosensors. This type of immobilization generates SAMs carrying directly the probe sequence that will hybridize the desired nucleic acid sequence. The grafting density of thiolated probes is high compared to those obtained using other immobilization methods[121, 122] and it can be tuned by changing the length of the probe,[110] pH,[123] or the concentration of ions in the immobilization buffer.[124] However, in a densely packaged DNA monolayer hybridization may be hindered because of steric and electrostatic factors leading to lower accessibility and loss of detection signal.[114] Hybridization signal can be improved with a careful optimization of the DNA coverage and surface properties by the use of certain small-molecules that can act as both, lateral spacers and blocking agents, such as 6-mercapto-1-hexanol (MCH),[114, 124] longer alkanethiols[122] or thiolated oligoethileneglycols.[125] These molecules also promote the orientation of the probes,[124] reduce their density and improve the resistance to the non-specific adsorption of nucleic acids to the surface[122] (**Figure 2.4**).

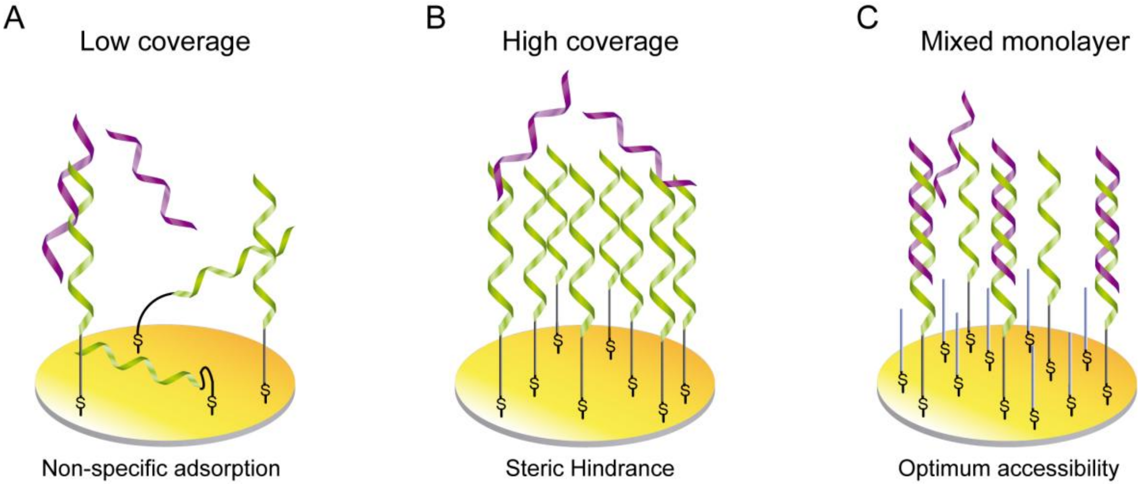

Figure 2. 4 Scheme of the target accessibility at different gold sensor surface coverages. (**A**) Low DNA-probe coverage with poor SAM packaging and bad DNA-probe orientation. (**B**) High DNA-probe coverage with high steric hindrance forces leading to poor probe accessibility that prevent target hybridization. (**C**) Lateral spacing by blocking agents providing good probe orientation and optimum accessibility.

Optimization of the immobilization of SH-DNA probes on gold surfaces

SAMs based on thiolated probes can be generated by two ways: *ex-situ* and *in-situ* procedures. *Ex-situ* immobilization is performed outside the sensor apparatus by putting in contact the gold sensor chip with the solution containing a convenient concentration of the SH-DNA probe. On the other hand, *in-situ* immobilization is carried out with the gold sensor chip placed in the sensor apparatus and flowing the DNA-probe solution at a determined rate. *Ex-situ* immobilization has been demonstrated to be highly reproducible.[64] It involves longer times of immobilization (from 3 hours to over-night) than *in-situ* immobilization, which enhances the possibilities of obtaining a more compact and better ordered SAM. However, *in-situ* immobilization facilitates the functionalization of each SPR sensor channel with different probes for the simultaneous detection of independent target sequences. Some studies demonstrated that performing the immobilization in flow led to SH-DNA monolayers similar to those obtained by *ex-situ* methods at long immobilization times.[126] **Figure 2.5** illustrates a model SPR sensogram from an *in-situ* immobilization of a SH-DNA probe with its subsequent hybridization cycle. The sensogram represents changes in the intensity of the reflected light (ΔR, %) due to variations in the refractive index of the medium close to the gold sensor surface. A change in the refractive index can be observed after injection of the SH-DNA probe, changing the position of the baseline due to the covalent adsorption of biomolecules. Subsequently, hybridization of the complementary nucleic acid target produces another refractive index change directly related to its concentration in the analyzed sample. Finally, the hybridization can be interrupted by a regeneration solution, liberating the biosensor surface for further analyses with the same sensor. Therefore, binding events lead to positive changes of the baseline while unbinding events lead to negative variations. As can be appreciated, in some cases, the change in the refractive index is not only related to the interaction of the targets with the immobilized probes, but also influenced by the difference in the refractive index of the injected solution and the running buffer. For that reason, our analyses relied only on final variation (in equilibrium) in the light reflectivity evidenced by a shift in the baseline at the end of the monitored measurement.

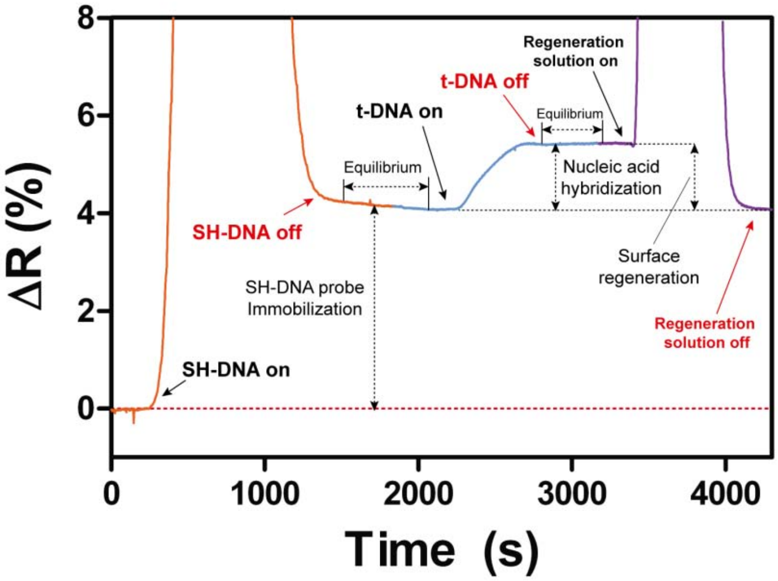

Figure 2. 5 Typical sensogram for *in-situ* immobilization of SH-DNA probes and their subsequent hybridization/regeneration cycle.

To study the gold sensor surface coverage by SH-DNA probes via *in-situ* immobilization, we explored several parameters to ensure a proper surface coverage for minimizing non-specific adsorption and to provide a good probe density for an adequate accessibility of the target. We tested different DNA_1-probe (**section 2.4. Materials & Methods**, **Table 2.3**) concentrations (0.15, 0.25, 0.5, 1 and 2 µM) at fixed conditions of flow-rate (10 µL/min) and exposition time (25 min). We employed a highly saline buffer PBS 50 mM (pH 7), which ensured a maximum immobilization efficacy. Previous studies demonstrate that immobilization depend strongly on solution ionic strength.[109] High ionic strength solutions reduce the electrostatic repulsions between probe molecules promoting a higher coverage. The surface coverage was evaluated by the SPR response to each of the concentrations tested. As can be observed from **Figure 2.6**, SPR immobilization signals gradually increased with increasing DNA probe concentration. Concentrations over 0.5 µM presented similar sensor response meaning that an almost complete coverage of the surface is achieved by employing a concentration of probe of 1 µM or higher.

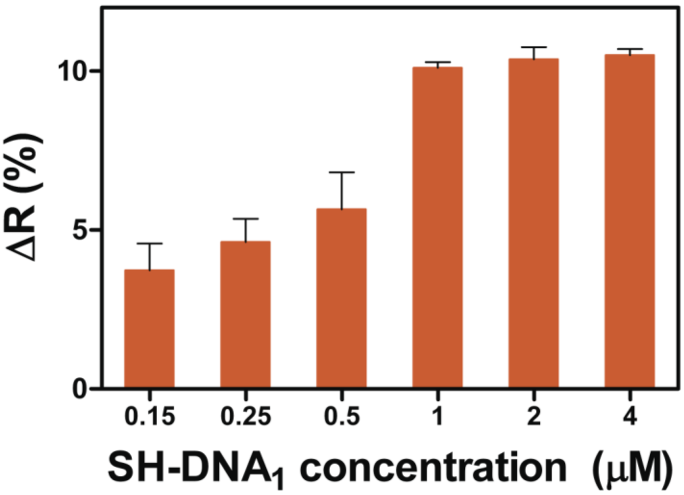

Figure 2. 6 SPR responses of different DNA probe concentrations.

However, optimum coverage not only depends on a sufficient amount of immobilized probes but also on the probe density for the subsequent accessibility for target hybridization. To assess the more convenient probe density, several detection cycles of the complementary target were carried out for the different probe concentrations. As can be appreciated in **Figure 2.7**, the hybridization signal decreased as the probe concentration was increased, suggesting that accessibility was hampered by steric and electrostatic hindrances for too tightly packed surface bound DNA strands. Thus, a SH-DNA probe concentration of 1 μM produced the most convenient SAM on the gold surface during the *in-situ* immobilization, providing a suitable surface coverage while maintaining a good accessibility for the target recognition.

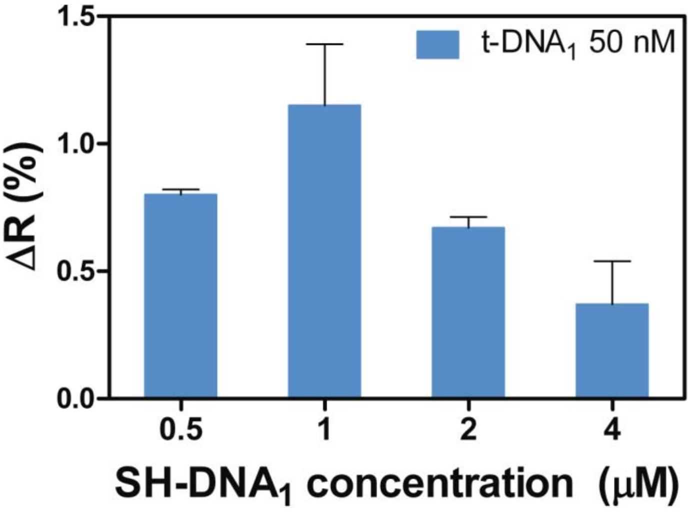

Figure 2. 7 Target hybridization efficiency for different probe densities.

For further improvement of the monolayer accessibility, we tested the influence of the introduction of a horizontal spacer in the SAM formation. Concretely we used mercaptohexanol (MCH), a commonly used lateral spacer of 6C chain that competes with the thiolated DNA molecules, reducing the probe density and, therefore, minimizing steric hindrance effects.[64] To evaluate the effect of this lateral spacer, several probes: SH-DNA$_1$, SH-DNA$_2$, SH-DNA$_3$ and SH-DNA$_4$ (**Table 2.3**) at different SH-DNA/MCH molar ratios (1:0, 20:1 and 10:1) were immobilized at a total concentration of 1 µM. Each condition was tested by several hybridizations with their respective complementary targets at a 50 nM concentration.

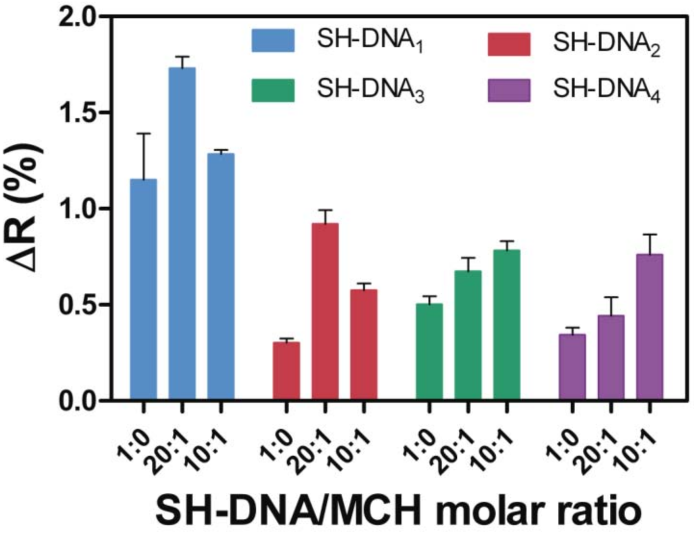

Figure 2. 8 MCH effect in target hybridization efficiency with different DNA probes.

As can be appreciated from **Figure 2.8**, all the probes tested showed an increase in the target signal in the mixed SAMs containing the MCH spacer, corroborating its influence in target accessibility. The difference in target capture efficiency among the SH-DNA probes employed can be explained by the different probe sequences. As mention before, the hybridization efficiency strongly depends on the contribution of the different bases of the probe in both, their content and their sequence order.

Surface regeneration

The subsequent experiments consisted in the optimization of the dehybridization of the double stranded oligonucleotides to obtain the former single-stranded state of the tethered probes, which can be further rehybridized. For a good biosensor performance it is necessary to find the most suitable regeneration solution for a complete removal of the target that allows reusing the biosensor surface in subsequent analyses. A complete regeneration should be carried out under working flow-rate conditions to permit a fast and reliable analysis. Normally, the double-stranded conformation of nucleic acids is favorable over the single-stranded one, being necessary the use of some destabilizing conditions to disrupt the stability of the duplex. Some nucleic acid detection techniques such as the PCR technique rely on high temperatures for destabilizing nucleic acid hybrids. Other destabilizing compounds are used to reduce the melting temperature (i.e. the temperature corresponding to the midpoint in transition from helix to random coil) of the hybridization, not being necessary to induce high temperatures for the dehybridization. Among them, formamide (FA) and urea in aqueous solutions are suitable compounds that reduce the melting temperature, destabilizing the bonds between the two strands.[127, 128] Also, changes in the pH can favor the duplex destabilization. Mild concentrations of sodium hydroxide (NaOH) or hydrochloric acid (HCl) solutions are usually employed for that purpose in nucleic acid biosensing.[129, 130] Therefore, we tested three different approaches for target/probe destabilization: H_2O (100ºC), FA 35% and HCl 2 mM. We carried out three different regeneration cycles applying the different regeneration solutions at 16 µL/min after target/probe hybridization.

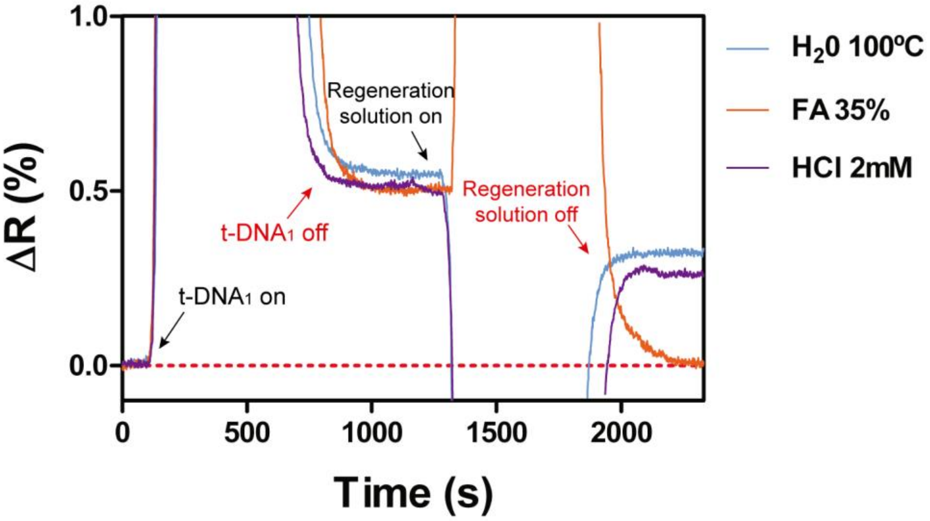

Figure 2. 9 Surface regeneration for the SPR biosensor.

Surface regenerations for each tested condition are shown in **Figure 2.9**. All regeneration solutions were able to remove part of the hybridized t-DNA$_1$ (i.e. the baseline after surface regeneration was lower). However, only the FA 35% solution achieved a complete surface regeneration with the assay condition tested, i.e. the baseline got back to the same level than before hybridization. Neither H_2O (100ºC) nor HCl 2 mM were able to remove 100 % of the hybridized targets, suggesting that these approaches needed longer exposition times for a complete surface regeneration. Therefore, FA 35% was the most suitable regeneration solution for a rapid surface regeneration and it was employed for subsequent experiments.

To demonstrate the robustness of this immobilization approach at the optimized conditions, we assessed the signal reproducibility in several hybridization/regeneration cycles. We determined the Coefficient of Variability (CV) of the signal for a given target concentration (20 nM). Target detection maintained a stable response through more than 100 regeneration cycles with no notable signal loss compared to initial values, showing a variation of 4 %, well-below the maximum variability recommended for analytical methods (~15%)[131] (**Figure 2.10**).

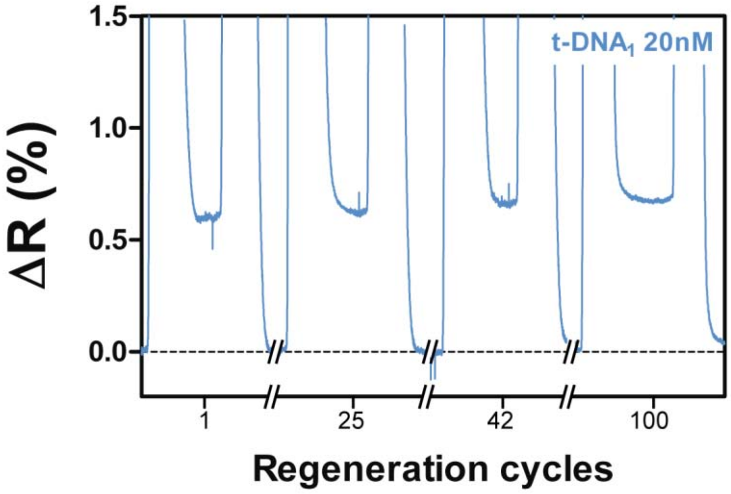

Figure 2. 10 Detection cycles after consecutive interactions of t-DNA$_1$ (20 nM) with its specific probe (SH-DNA$_1$) and subsequent surface regenerations with FA35%.

Covalent immobilization of DNA probes to a functional layer

The surface of an SPR sensor can also be modified with a functional layer that carries various functional end-groups, such as maleimide,[132] amine[133] or carboxyl[115] groups for the subsequent covalent immobilization of the probes. The functional layer can either allow for the immobilization of probes on the surface of the layer (e.g. SAM of alkanethiols) or in a three-dimensional matrix (e.g. carboxymethylated dextran). Due to a greater number of reactive sites, the 3D matrix permits the immobilization of a larger number of probes. However, the efficiency and selectivity of hybridization may be decreased due to lower accessibility of the probes and slower diffusion of the target through the matrix.[134]

Surface functionalization with carboxyl groups

We optimized a DNA probe immobilization based on the formation of long-chain alkanethiol SAMs functionalized with carboxyl groups (-CO_2H). Long-chain alkanethiols, i.e. more than 10 atoms of carbon, leads to dense and well-ordered SAMs similar to crystalline structures. The employment of carboxyl groups usually involves amine-modified DNA probes (NH_2-DNA probes) for the covalent attachment. This covalent coupling consists of an amide bond formed between the primary amine (-NH_2) group of the DNA probe and the -CO_2H group of the alkanethiol, which is previously activated. DNA probes are selectively tethered by their amino terminus because the terminal primary amino groups are much more reactive than the internal amino-groups of the DNA bases, resulting in an oriented immobilization.[135, 136] We selected the mercaptohexadecanoic acid (MHDA) as the SAM unit. Likewise, we studied the combination of the MHDA with a shorter non-reactive alkanethiol carrying a hydroxide (OH-) group, the mercapto-undecanol (MUOH), allowing the control of probe density and the reduction of steric hindrance effects and, therefore, promoting the enhancement of the target detection. For the NH_2-DNA probe covalent bonding, carboxyl groups were activated by the well-known carbodiimide-mediated chemistry, employing 1-Ethyl-3-(3-dimethylaminopropyl)-

carbodiimide/ N-hydroxysuccinimide (EDC/NHS). This reaction produces a NHS-ester intermediate highly reactive to primary amines. This chemical procedure is well established and it generates highly stable amide bonds. After binding, non-reacted NHS-ester groups are deactivated by flowing an ethanolamine solution to prevent nonspecific binding (**Figure 2.11A**). **Figure 2.11B** shows a typical SPR sensogram monitoring the different steps of this procedure in real time.

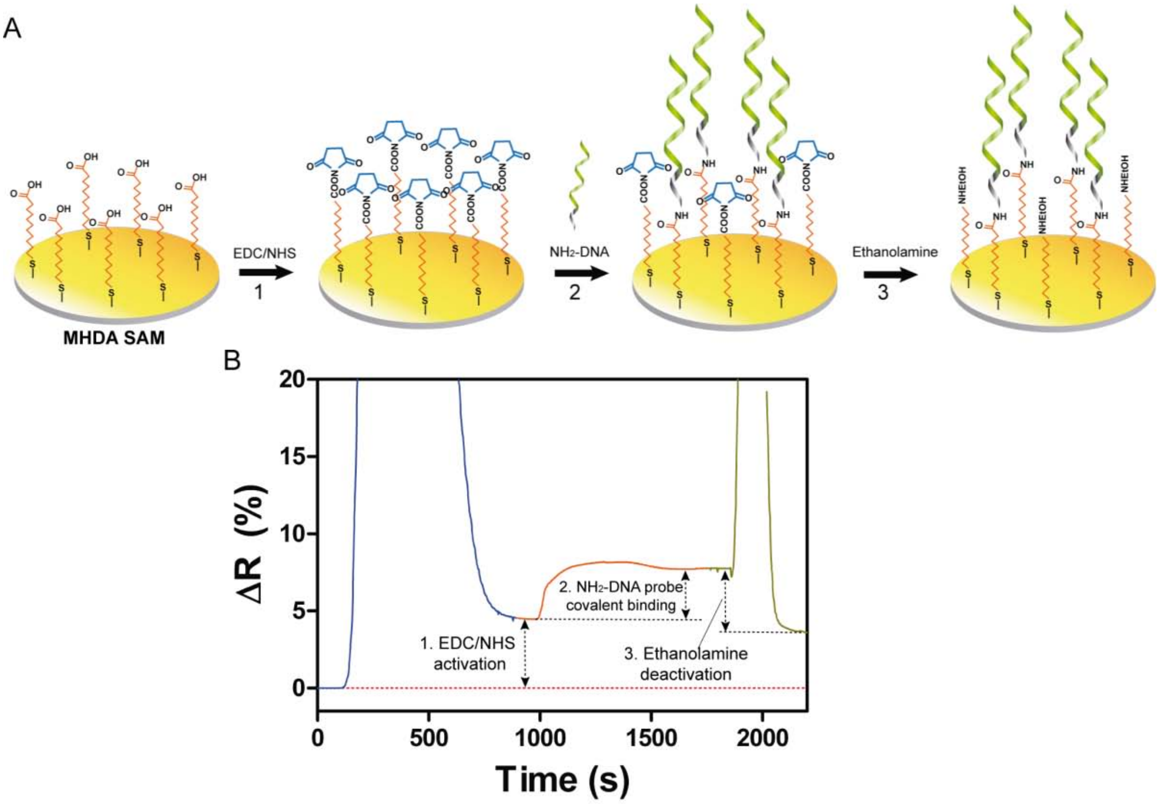
A
MHDA SAM
EDC/NHS
1
NH2-DNA
2
Ethanolamine
3
OH
COON
NH
NHEtOH
S
B
ΔR (%)
Time (s)
0
5
10
15
20
0
500
1000
1500
2000
1. EDC/NHS activation
2. NH2-DNA probe covalent binding
3. Ethanolamine deactivation

Figure 2. 11 Scheme (**A**) and real-time SPR sensogram (**B**) of the covalent immobilization of NH_2-DNA probes in a MHDA SAM mediated by EDC/NHS activation.

The alkanethiols were *ex-situ* immobilized at a concentration of 250 µM at different MHDA/MUOH molar ratios (1:0, 1:5, 1:10 and 1:20). After the functionalization, gold sensor chips were placed in the sensor device. EDC/NHS solution was flowed *in-situ* over the sensor area, activating the carboxyl groups. Subsequently, a concentration of 1 µM of NH_2-DNA probes in PBS 1x buffer was flowed for the covalent coupling of the amine groups to the activated SAM. The different molar ratios were tested, evaluating their hybridization performances by monitoring in real-time with the SPR biosensor.

As can be seen in **Figure 2.12**, immobilization signals from the NH_2-DNA probes decreased when decreasing the concentration of the MHDA molecules due to a decrease of the number of the active groups. Surprisingly, this coupling was poorer in the monolayer containing only MHDA units (ΔR (%) = 2.97) compared to the 1:5 molar ratio (ΔR (%) = 3.5), suggesting an electric repulsion of the active molecules on the surface to the negatively charged DNA sequences.

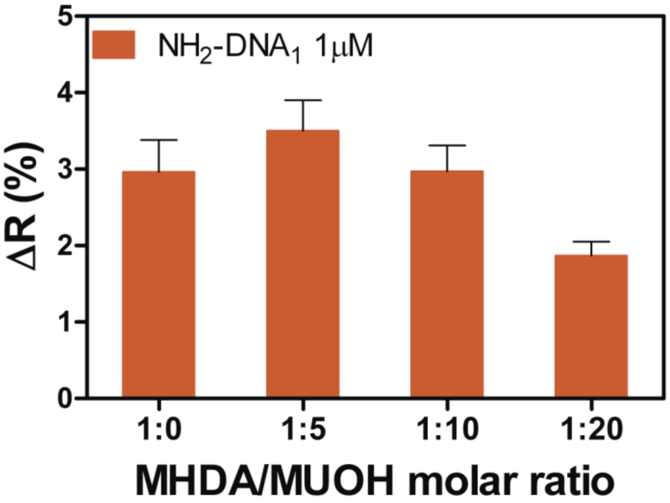

Figure 2. 12 Immobilization signals of 1 µM NH2-DNA$_1$ on different MHDA/MUOH monolayers.

In fact, a notorious improvement of the target detection was achieved in the mixed monolayers in comparison with the pure MHDA SAM (**Figure 2.13).** A high steric hindrance effect was evidenced in this monolayer by a target signal close to the background noise level (ΔR (%) = 0.035) even at high target concentrations (30 nM). Molar ratio of 1:10 showed the highest hybridization efficiency (ΔR (%) = 0.34), corroborating the enhancement of target detection by the reduction of the steric hindrance effect.

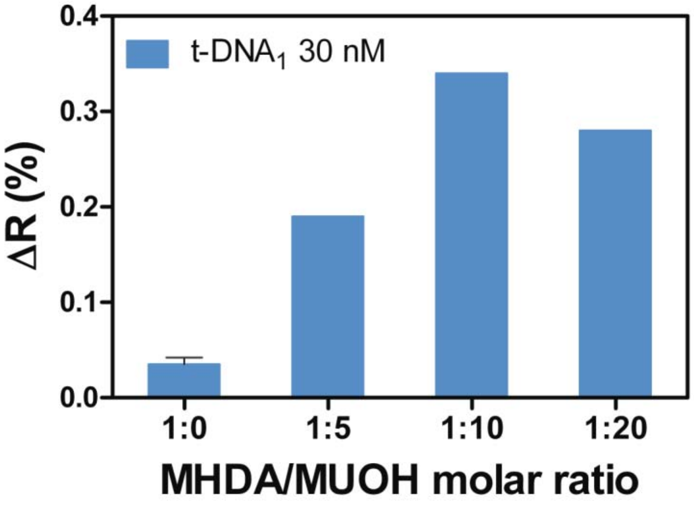

Figure 2. 13 Target hybridization SPR signals for the different MHDA/MUOH monolayers.

Next, we decided to exploit the employment of an amino functional 6-C chain (i.e. 6-amino-1-hexanol (AH)) as competing lateral spacer during the probe attachment to the carboxylic groups at the SAM surface. It will act as the MCH spacer in the direct SH-DNA probe immobilization. This incorporation adds a second-layer of horizontal spacing as well as may help the proper vertical orientation of the probes, positively contributing to the target accessibility and the SAM stability. We compared three different molar ratios of NH_2-DNA probe/AH (1:0, 20:1 and 10:1). As can be seen in **Figure 2.14**, moderate addition of AH spacer (20:1 molar ratio) clearly improved the accessibility of the target to the probe in 179 % (ΔR (%) = 0.61) compared with SAMs with no AH (ΔR (%) = 0.34). The highest concentration of AH tested (10:1 molar ratio) produced a SAM with a better accessibility than in the absence of the spacer but with lower target signal, probably due to a poorer probe density.

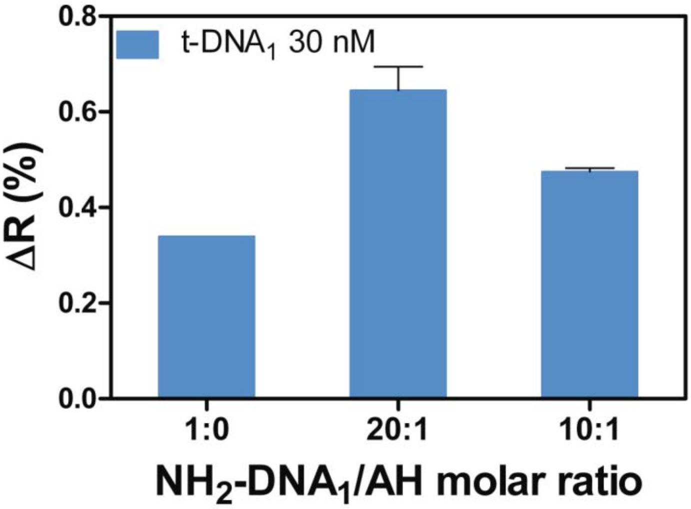

Figure 2. 14 Effect on the hybridization efficiency after the employment of different molar ratios of NH_2-DNA_1/AH during the immobilization.

This hybridization efficiency was maintained until 15 hybridization/regeneration cycles, showing a 9% CV. These results evidence a less stable monolayer than the one achieved with the SH-DNA probes. Although this covalent functionalization of DNA probes allows for a second layer of horizontal spacing and better-controlled surface coverage, the monolayers generated show less stability than the direct DNA chemisorption on gold. In addition, the overall methodology implies more steps and longer times for the DNA functionalization of gold surfaces, making the whole process more challenging.

2.2.2. Optimization of a monolayer with antifouling properties

Label-free optical biosensors enable a direct observation of interactions among biomolecules in real time, providing a rapid detection tool for chemical and biological species. However, because they are based on the evaluation of refractive index changes caused by the binding of target molecules to biorecognition elements immobilized on the sensor surface, their performance may be compromised by interfering effects that produce refractive index changes unrelated to the analyte binding, referred to as fouling effects.[137] When the target molecules are contained in a complex solution, the specific response due to their capture may be concealed due to the adsorption of non-target molecules. In consequence, these “fouling” effects may be particularly severe during the analysis of complex real samples such as blood plasma, serum or urine. There are many nonspecific interactions between the surface and the complex matrix components such as hydrogen bonds, hydrophobic, electrostatic and/or polar interactions making the reduction of the background signal a difficult task.

For the particular case of circulating DNA/RNA, they are present in very low concentrations compared to other biomolecules (e.g. proteins, lipids, etc), further hindering their specific detection in real samples. Previous purification steps could be a solution but they may compromise their detection due to a possible loss of sample input as well as distort the final analysis and leading to an inaccurate quantification. Therefore, the development of biosensor strategies for the analysis of complex solutions directly without the need for any purification steps is on demand.

Antifouling effect in serum samples

The most widely explored biofluid for circulating biomarkers is blood. Cancer cells secrete several molecules within which are mixed circulating DNA, micro-RNAs or mRNAs that reach the circulating blood, increasing their concentration and serving as biomarkers of disease onset. However, direct evaluation of undiluted serum (and especially whole blood) remains challenging and is still a not well-solved problem in direct label-free evaluation. The high amounts of proteins and lipids present in blood (**Figure 2.15**) can adsorb onto the sensor surface and usually can lead to high background signals obscuring the specific signal of the target; in addition they can also hamper their recognition.

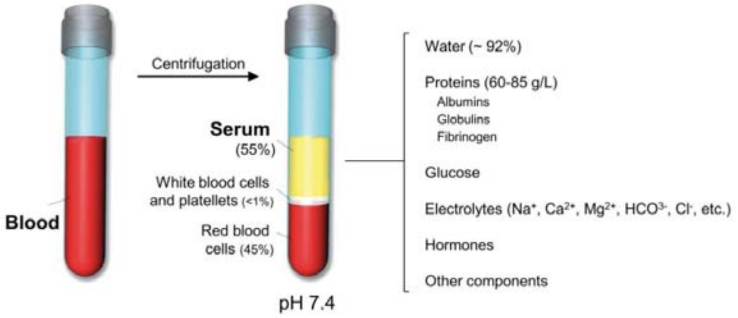

Figure 2. 15 General composition of the most commonly used human clinical samples for diagnostics: blood and serum.

A common approach to reduce the fouling effects is the addition of different surfactants (e.g. Tween), protein-based additives (including BSA or casein), or non-protein reagents. They minimize any hydrophobic and/or electrostatic attractions between the complex matrix and the functionalized surfaces. Unfortunately, they have limited antifouling properties.[138, 139] Therefore, to suppress nonspecific adsorption to the sensor surface, functionalization methods enabling the immobilization of biorecognition elements while also providing a low-fouling background in complex solution have to be implemented. Most of the anti-fouling strategies are based on the generation of surfaces with highly hydrophilic functional groups. Herein, low-fouling surfaces based on poly(ethylene glycol) (PEG) and its derivatives have been used widely.[140, 141] In addition, recent advances in polymer chemistry have led to the development of various polymer coatings (e.g. zwitterionic and non-ionic polymer brushes) with high resistance to fouling from complex biological fluids.[142]

PLL-PEG modified layer

In order to minimize the undesired adsorption, an optimization study was carried out consisting of: (i) evaluating surface blocking with poly-L-lysine PEG (PLL-PEG) (**Figure 3.13**), and (ii) changing the buffer composition employed to dilute the serum and to reduce the non-specific interaction of other biomolecules present in the samples. Such dilution must be minimal in order to maintain the analyte concentration as close as possible to the initial value in the sample to procure the maximum sensitivity.

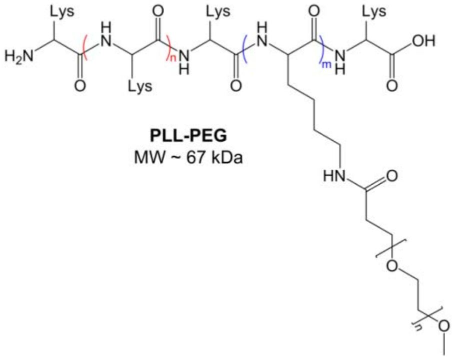

Figure 2. 16 Structure of PLL-PEG molecule.

Considering the recently grow interest of using miRNAs as promising circulating biomarkers, we studied the effect of serum matrix, one of the most complex biofluids, by employing synthetic miRNA capturing probes and target sequences (t-miRNA).

We tested the fouling properties of the conventional thiol-chemistry based approaches studied so far: the SH-DNA probe/MCH and the MHDA/MUOH SAMs. Two different gold sensor chips were functionalized with the two different methodologies applying the previously optimized conditions. Their fouling properties were assessed by the biosensor responses to undiluted commercial serum samples. We also tested the fouling properties of the generated monolayers after a subsequent passivation of the surface with a solution of 1 mg/mL of PLL-PEG compound. The copolymer PLL-PEG creates a brushed coating on the surface, which has proven to successfully prevent and reduce nonspecific adsorption of proteins due to its hydrophilic properties.[141, 143] We compared the fouling effect of the SAM before and after blocking with the PLL-PEG by flowing undiluted serum and comparing the background signal obtained. As can be observed in **Figure 2.17**, both SAMs presented a significant increase of the SPR signal produced by nonspecific bindings with similar sensor responses (ΔRs (%) ~ 6), corresponding to the non-specific adsorption of matrix components from serum. In contrast, the presence of PLL-PEG helped reduce the non-specific adsorption in 70% (ΔRs (%) ~ 2.00) for both SAMs, compared with the surface without this polymer, corroborating its blocking effect. Since both SAMs showed the same anti-fouling properties and due to the easiness in the formation of SH-DNA SAMs and the greater bio-stability of the monolayer throughout several hybridization/regeneration cycles, we chose this approach to continue with the biofunctionalization optimization process.

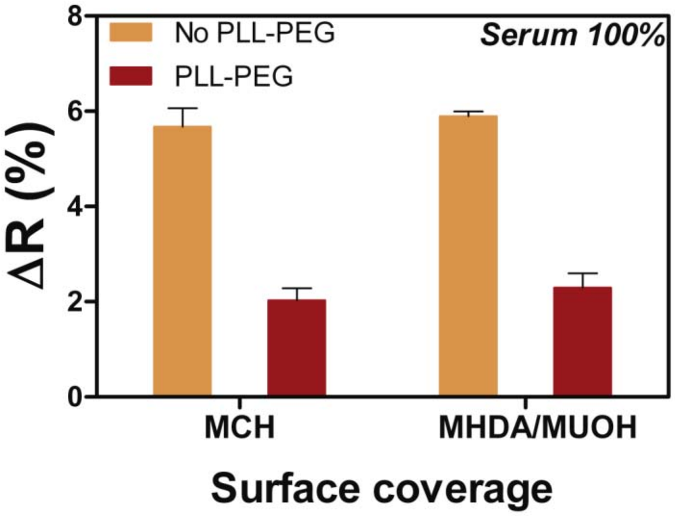

Figure 2. 17 Non-specific adsorption of commercial serum 100% over the two different thiol-chemistry based approaches with and without PLL-PEG passivation.

Next we explored the addition of different surfactants to further reduce the background signal. For that purpose, we evaluated the non-specific adsorption of 1:1 diluted serum in 5x SSC hybridization buffer containing different concentrations (% w/v) of Tween 20. As can be appreciated in **Figure 2.18A**, increasing concentrations of Tween 20 up to 5% greatly improved the reduction of the background signal in 70%. Percentages higher than 5% produced an increment of the non-specific adsorption than free-Tween samples, indicating the presence of residual background signal generated by the addition of such amount of surfactant. Additionally, we tested the influence of 3-[(3-cholamidopropyl)dimethylammonio]-1-propanesulfonate (CHAPS). CHAPS is a zwitterionic detergent used to solubilize biological macromolecules preventing from undesirable hydrophobic interactions. It, therefore, may help to improve non-specific adsorption on the sensor surface. **Figure 2.18B** shows the anti-fouling effect produced by the combination of the PLL-PEG blocking agent and a 5% of Tween 20 with different concentrations of CHAPS (from zero to 8 mM). An almost complete reduction of the non-specific adsorption to background noise was achieved with a 2 mM concentration of this detergent (ΔR (%) = 0.07), corroborating its positive effect in reducing the background signal for serum samples.

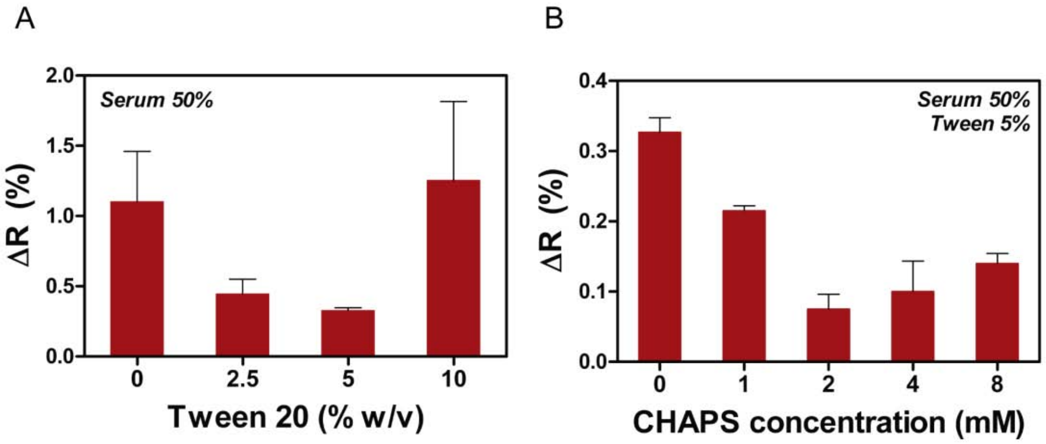

Figure 2. 18 Antifouling effect by the employment of different additives to the hybridization buffer: (**A**) Tween 20 and (**B**) CHAPS.

The combination of Tween 20 and CHAPS with PLL-PEG for surface blocking produced a reduction of the nonspecific binding of two-time diluted serum of 94% compared to standard conditions (5x SSC buffer with PLL-PEG). However, these changes in the hybridization buffer can also affect to the hybridization process itself. Thus, the hybridization efficiency was evaluated with these new conditions. In addition, for a total reduction of the background signal, a 2% of serum in the running buffer was introduced. This small quantity of commercial serum may help to overcome the elimination of the remaining background signal. We evaluated the sensor response by spike-in a quantity of 50 nM of t-miRNA$_1$ in a sample containing a 50% of serum and the combination of the tested surfactants. As can be observed in the sensogram (**Figure 2.19)**, the signal from the control sample (Serum 50%) returned to the baseline after washing with the continuous running buffer, which meant a reduction of the non-specific adsorption to the background noise after adding a 2% of commercial serum in the running buffer. In addition, despite the addition of the different surfactants to the hybridization buffer and the presence of 50% serum, the hybridization of the target was comparable to the one obtained using only 5x SSC buffer, showing equal ΔR (%) shifts at this target concentration (~ 0.56).

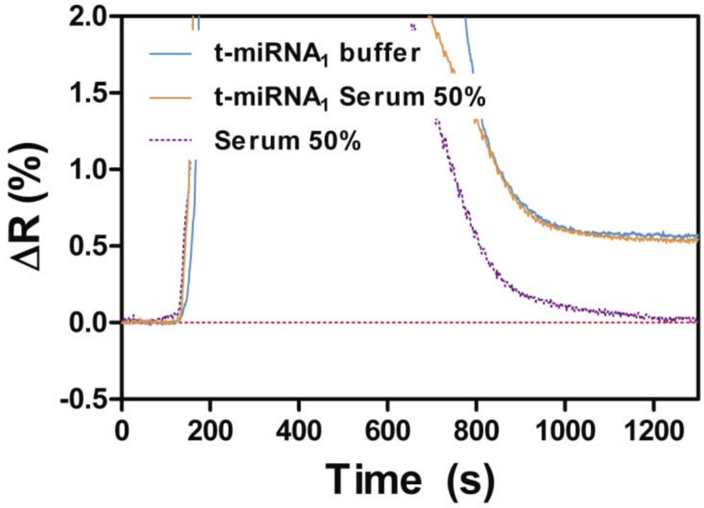

Figure 2. 19 Study of the hybridization efficiency of the target after applying the antifouling buffer.

Despite such encouraging results, we found a low reproducibility of the antifouling effect when trying to repeat the experiments in newly formed SAMs (CV = 107%), needing to readjust the surfactants concentration to achieve similar results. This low reproducibility can be explained since the blocking process of the PLL-PEG is performed after the SAM formation, leading to a random coverage of the sensor surface by these polymers. Moreover, the elaboration of a non-fouling surface based on physical adsorption of these macromolecules presents a deficiency since they are bonded through relatively weak forces, like electrostatic, hydrogen and Van der Walls interactions. For the development of a reliable biosensor, stable coating with no depletion is necessary.

SH-PEG modified layer

Due to the low reproducibility provided by the PLL-PEG adsorption, we decided to elaborate monolayers incorporating the PEG polymer through covalent grafting. For that purpose, we employed several thiolated PEGs (SH-PEGs) carrying different functional groups (-CH_3, NH_2 and CO_2H) mixed with the SH-DNA probe in a 1:1 molar ratio (2 µM). Additionally, the fouling effect was evaluated combining the different PEGs at a 1:1 molar ratio. PEG molecules will serve in this case as both, a surface backfiller, preventing from non-specific adsorptions, and as a horizontal spacer for the SH-DNA probes, aiding the control of the probe density. Therefore, we did not seize the employment of MCH as a lateral spacer this time. We tested the antifouling properties of the generated SAMs by flowing two-times diluted serum in buffer containing a 5% of Tween 20 and evaluated the shift of the SPR sensor baseline. As can be appreciated in **Figure 2.19**, adsorption from undesired molecules gave shifts in the ΔR (%) between 0.14 and 1.23.

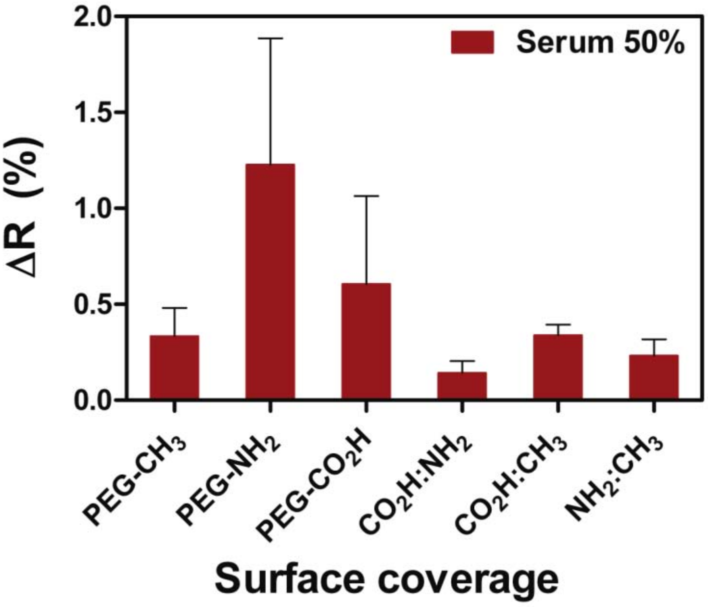

Figure 2. 20 Antifouling effects produced by different gold surface coatings.

PEG-NH_2 and PEG-CO_2H showed lower fouling properties (ΔRs of 1.23% and 0.60% respectively) than the ones obtained for the adsorbed PLL-PEG molecules in the same conditions (ΔR (%) = 0.32). This effect was probably due to the formation of polar surfaces either by the contribution of positive charges by the amine terminal groups, or negative charges because of the carboxyl groups of the grafted PEGs. In contrast, the fouling effect was extremely high in SAMs containing a mix of these PEG molecules, i.e. carrying either CO_2H or NH_2 groups, reaching the best antifouling response (ΔR (%) = 0.14). Such mixed SAM may form a zwitterionic surface which improves the anti-fouling properties of the monolayer by preventing hydrophobic interactions from the complex biofluid with the sensor surface. In fact, such effect was remarkably high after the addition of a 2% of commercial serum in the running buffer (**Figure 2.20**).

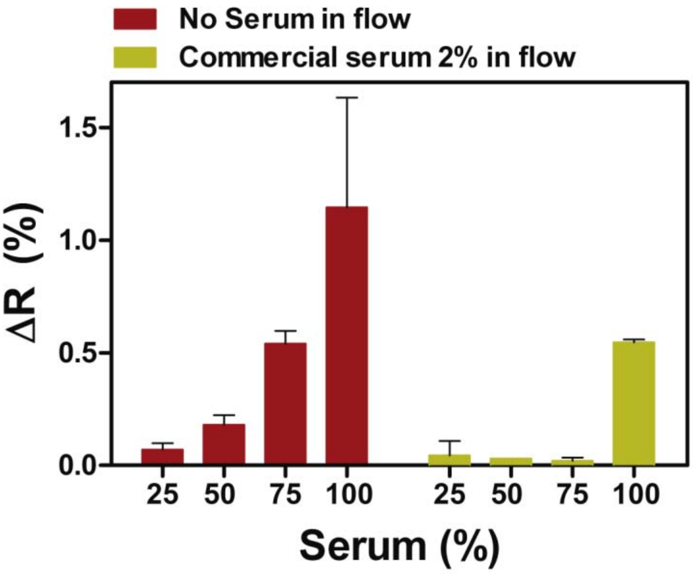

Figure 2. 21 Antifouling effect of the SH-PEG CO_2H/NH_2 monolayer before and after adding 2% commercial serum in the continuous buffer.

Undiluted serum samples produced a positive and stable background signal of ΔR (%) = 0.5 since they did not have the influence of the Tween 20 surfactant. However, in samples with up to 75% serum, non-specific adsorptions were reduced to the background noise level.

We studied the hybridization efficiency at different serum dilutions. All the serum dilutions showed similar and non-variable hybridization efficiencies, with low coefficient of variability (CV = 2%) compared with the signal obtained in buffer solution (**Figure 2.21A**). However, when analyzing the target in non-diluted serum the hybridization efficiency decreased in 45%. This result, together with the background noise produced in such samples that may obscure the detection at lower sample concentrations, made difficult the detection in undiluted serum samples. Nevertheless, 75% serum samples showed extremely high hybridization efficiency while maintaining a close-to-zero background noise (**Figure 2.22B**), making possible the detection of minimally diluted serum samples without compromising the limit of detection of the methodology.

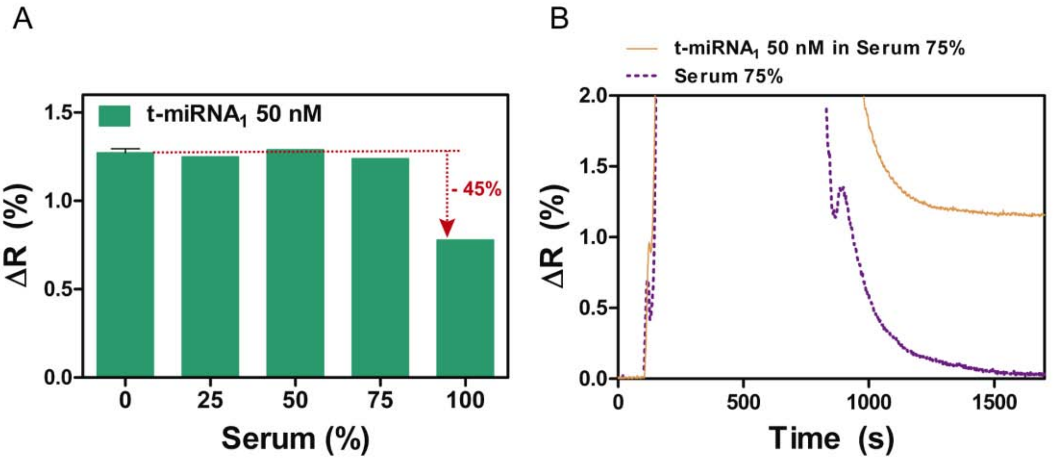

Figure 2. 22 Hybridization efficiency study of t-miRNA$_1$ hybridization in diluted serum samples. (**A**) Hybridization efficiency in different dilutions of serum samples. (**B**) Sensogram monitoring the specific hybridization of t-miRNA$_1$ in serum 75%.

Despite the harsh conditions employed for the optimization of the antifouling strategy (sample with high serum content and surfactant concentrations) the generated monolayer was capable of withstanding up to 40 hybridization/regeneration cycles with no apparent variation in its fouling capabilities or signal loss in target recognition (CV = 4%). In addition, the same antifouling properties were conserved after the generation of different monolayers with the same characteristics, suggesting this strategy as a reliable and robust approach for label-free detection of circulating nucleic acids in complex real-world samples.

Antifouling effect in urine samples

Another important biofluid for the exploration of circulating biomarkers is urine. Although biomarkers are present in much less quantities, urine represents an ideal biofluid for disease biomarker determination as it can be obtained in large amounts by non-invasive methods. Human urine consists primarily of water with organic solutes, such as urea or creatinine, inorganic ions to a much less extent, also small organic substances and metabolites, enzymes and proteins (**Figure 2.23**). The matrix effect of urine in direct analysis might be less severe than serum or plasma. However, the different salt content and the presence of other chemical components in the urine samples may interfere during the hybridization and can affect the assay behavior. Also we cannot discard potential nonspecific adsorptions of proteins on the sensor surface.

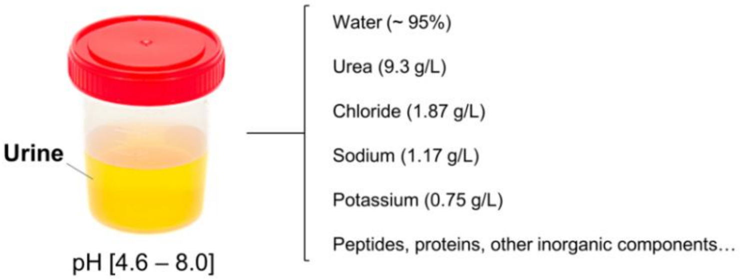

Figure 2. 23 General composition of human urine samples.

The antifouling properties of the proposed monolayer were also tested for the analysis of urine samples. A mixed monolayer of SH-PEGs CO_2H/NH_2 with SH-DNA probes was generated and the adsorption of undiluted urine samples was analyzed. We also evaluated different spike-in t-miRNA$_1$ concentrations in pure urine. As can be observed in **Figure 2.24A**, bulk change induced by the presence of the pure urine at the sensor surface produced a negative shift in the reflectivity. Such negative change is due to a lower ionic strength of the undiluted urine samples compared to the employed running buffer. Surprisingly, pure urine with a non-complementary spiked mRNA leads to background signal close to background noise without the need for any additional surfactant (Figure 2.24A *purple dashed line*). Moreover, hybridization efficiency of the target did not show any alteration when spike-in the target in undiluted urine, allowing for the direct detection of the target directly from urine samples with no change in the target signal (CV = 1%) (**Figure 2.24B**).

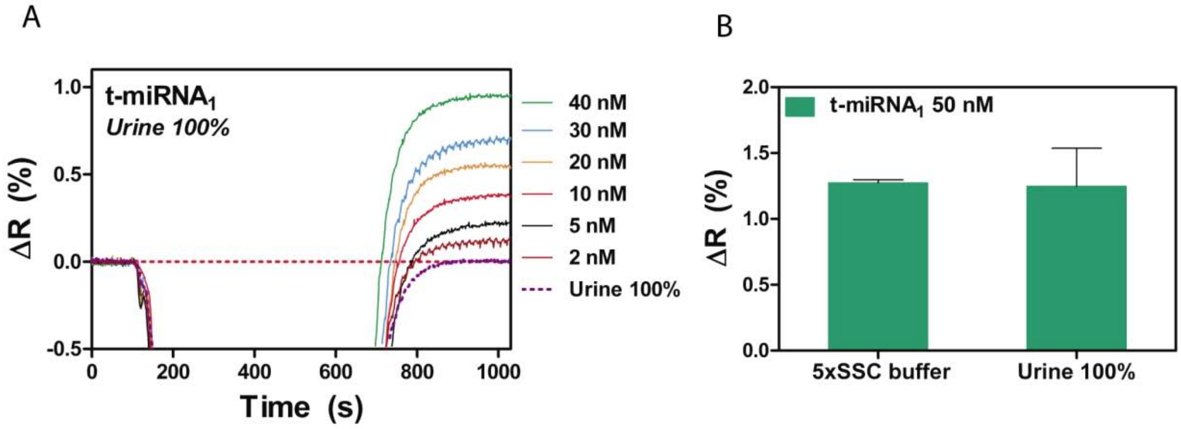

Figure 2. 24 Hybridization efficiency study of t-miRNA$_1$ in undiluted urine samples. (**A**) Sensogram monitoring the specific hybridization of different concentrations of t-miRNA$_1$ spiked in undiluted urine samples. (**B**) Comparison of the hybridization efficiency between buffer and undiluted urine conditions.

In the same way as in the serum sample analyses, the monolayer had the capability of obtaining reproducible signals (CV = 10%) throughout at least 55 hybridization/regeneration cycles, despite of the harsh conditions in terms of pH and concentration of organic solutes encountered in the pure urine samples. These results corroborate the ones obtained for the serum sample analyses and are the proof that the proposed antifouling strategy is a promising approach for the analysis of nucleic acids in highly concentrated serum samples or pure urine samples avoiding previous purification processes neither risking the sample input nor compromising the detection limit of the methodology.

2.2.3. PolyA based strategy

Recently, another direct graft of DNA probes on gold surfaces has been proposed. This approach relies on the unusually strong interaction between adenine nucleotides (A) and gold.[117, 144] The adsorption of adenine on gold surfaces has been a subject of interest in recent years due to its biological relevance and also to its potential application in biosensors and in the development of biocompatible materials. Nucleotide affinities for gold follow the order A > G ≈ C >> T, as previously demonstrated.[145] Although the interaction mechanism between adenine and gold still remains unclear, an adsorption model has been proposed consisting of the adenine coordination to the metal surface by the NH_2 group and most likely with the contribution of the N_7 ring atom[146, 147] (**Figure 2.25**).

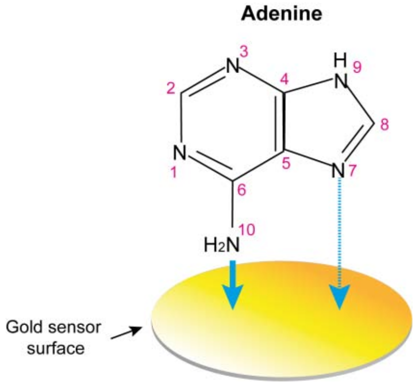

Figure 2. 25 Proposed mechanism for adenine adsorption on gold surfaces. Major interaction is attributed to coordination to the metal by the N atoms of the amine group and by the N_7 atom.

This mechanism attributes major coupling forces to electrostatic interactions with the surface, stacking interaction between adenine molecules and hydrogen bonding, leading to nearly flat and relatively strong interaction with gold. Therefore, when a block of adenines is incorporated into a DNA strand at one end it can be grafted by adsorption of such blocks on the gold surface. Such adsorption results in the saturation of the gold surface by the adenine blocks, forcing the rest of the strand containing the probe sequence into an upright conformation. With an additional block of thymine nucleotides between the probe sequence and the adenine block this upright conformation gets even more favored, adopting an L-shape conformation, where the polyA tail binds completely flat to the surface while the polyT chain extends away from the surface, vertically oriented (**Figure 2.26**). Contrary to what might be expected, the hairpin conformation of self-complementary polyT$_n$-polyA$_m$ oligonucleotides in solution is disrupted in presence of gold, resulting in close–saturation coverage of the metal sensor surface by the polyA blocks. Adjusting the length of adenine blocks there is a control of the footprint of each probe on the surface, thereby controlling the surface density. This approach has been proposed as an alternative to SH-DNA probes for achieving a more controlled grafting process, avoiding the use of backfillers (such as MCH) with different immobilization kinetics, and thus improving the reproducibility of the assay.

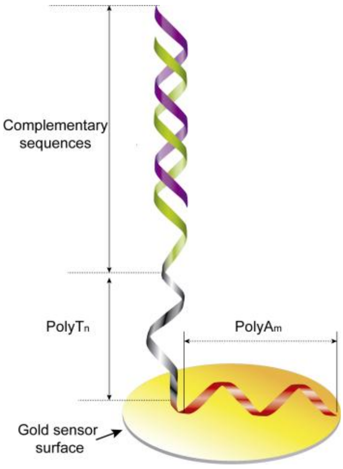

Figure 2. 26 DNA probes immobilized on gold sensor surface in L-shaped conformation.

Optimization and assessment of the polyA based strategy

To test the immobilization based on polyA tails, we compared its immobilization performance with the conventional thiol-chemistry based methodologies explored previously in this chapter. A $CaCl_2$-TE buffer was employed for polyA grafting on the gold sensor chip.[111] As can be appreciated in **Figure 2.27** immobilization in $CaCl_2$-TE buffer provided a high sensor response comparable to those obtained with SH-DNA probes, procuring a good probe density.

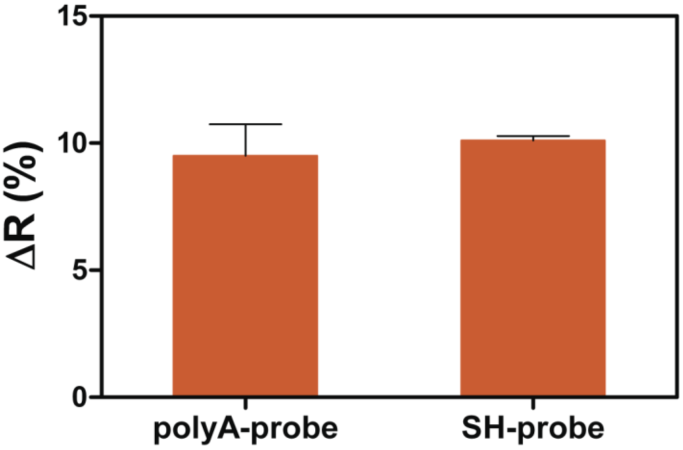

Figure 2. 27 Immobilization signals for both polyA-DNA and SH-DNA probes.

We evaluated the hybridization performances with two different polyA$_m$ block lengths, where m is the number of adenine nucleotides employed (m = 7, 15), i.e. PolyA$_7$ and PolyA$_{15}$. Likewise, we tested combination of the probes with the two block lengths at different polyA$_7$/polyA$_{15}$ molar ratios (1:1, 1:2 and 2:1). As shown in **Figure 2.28**, longer polyA$_m$ blocks (m = 15) allowed a better accessibility of the targets, leading to higher SPR responses. However the intensity of the signal was largely improved by using a mix of the two polyA lengths, achieving the most suitable conditions at a molar proportion of 2:1 of polyA$_7$/polyA$_{15}$. This combination of polyA blocks further improved the target accessibility (ΔR (%) = 0.88), achieving values close to those obtained with the optimized SH-DNA probe immobilization (SH-DNA/MCH 20:1) at the 50 nM target concentration (ΔR (%) = 0.92). In addition, these values were maintained until 25 hybridization/regeneration cycles with a variation of 3%. Direct grafting of DNA probes produces more stable monolayers allowing a higher number of evaluating cycles of the target DNA.

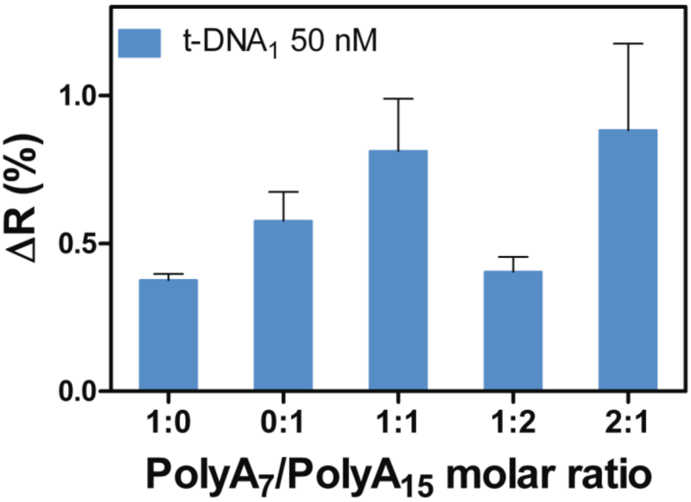

Figure 2. 28 Hybridization signals of t-DNA$_1$ at different polyA$_7$/polyA$_{15}$ DNA-probe molar ratio monolayers.

Antifouling test of polyA based strategy

The fouling properties of this new immobilization approach were assessed. Gold sensor surfaces coated with adenine oligos are resistant to nonspecific adsorption of unwanted nucleic acid adsorption[117] even at low probe densities due to the greater coverage area on behalf of the grafted polyA blocks. This characteristic could provide an advantage in obtaining a suitable low-fouling monolayer for non-purified real sample analysis.

A gold sensor chip was functionalized employing the optimized conditions described above for the polyA strategy. As can be observed in **Figure 2.29**, the monolayer coated with polyA blocks presented a high resistance to unwanted non-specific adsorptions from the matrix components of a serum sample (ΔR (%) = 2.4), showing a decrease in the background signal of 41% with regard to the previously studied surface coatings based on thiol-chemistry (ΔR (%) ~ 6).

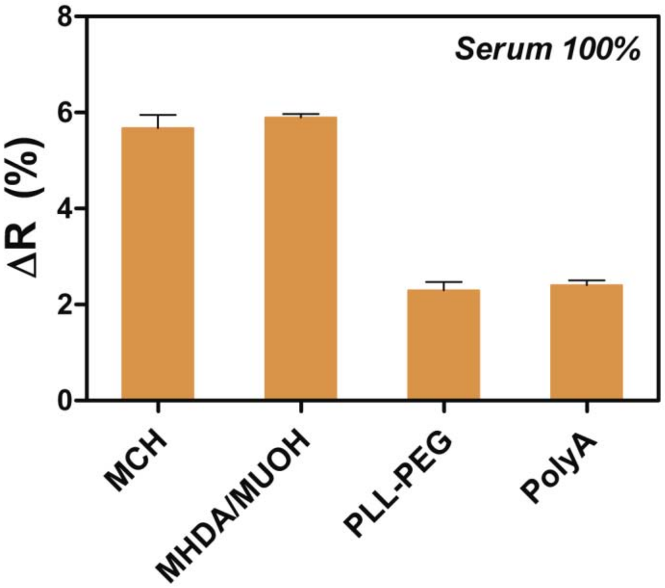

Figure 2. 29 Comparison of the non-specific adsorption of serum 100% over polyA-based monolayers with different surface coatings.

These results are quite comparable with the one obtained when coating the surface with PLL-PEG molecules (ΔR (%) = 2.03) without using of any additive, evidencing the great fouling properties provided by this approach. Further optimization of the methodology by surfactant addition may lead to background signals close to the background noise, rendering this approach as a good candidate for the analysis of nucleic acids contained in complex matrices such as serum.

PolyA surface recycling

Another advantage of the polyA-based immobilization strategy is the weaker interaction of the polyA blocks compared to the strong chemisorption provided by the thiol group. It offers the possibility of recycle the biosensor surface by breaking the interaction of the immobilized poly-adenilated DNA probes and, subsequently, generating a new SAM of polyA-DNA probes. Therefore, we can perform different assays on the same sensor surface without replacement of the gold sensor chip, saving time and resources. Acidic medium may interfere on the adenine interaction with the gold by breaking the hydrogen bonds as well as interrupting the electrostatic interactions and the electron exchange established with the adenine ring. This may allow the complete removal of the polyadenilated probes from the sensor surface, remaining free of molecules for a new immobilization process.

We studied the effect of an HCl solution on a previously generated SAM of polyA-DNA probes (immobilization 1) and we tested the surface reusability by carrying out a second immobilization (immobilization 2). **Figure 2.30** shows a sensogram with the sequence of the experiments carried out. First, a solution containing the polyadenilated probes was flowed. As a consequence of the attachment of the polyA blocks onto the gold surface, a positive shift of the baseline (ΔR (%) = 5.44) was observed. Subsequently, a t-DNA$_1$ concentration of 10 nM was injected, producing an increment in the sensor response of 0.39%, which was efficiently regenerated by exposure to 35% FA. Next, we employed a strong HCl solution (3M) to remove the attached polyA-DNA probes from the gold sensor surface. The signal returned to a level close to the baseline prior to probe immobilization, indicating that most of the probes attached to the gold surface were removed. A second immobilization procedure produced an increment in the reflectivity of 3.7%, indicating the attachment of the probes to the freshly recycled gold sensor surface. This increment was not as high as in the first immobilization, suggesting that more strict conditions should be applied to the surface for a complete removal of the grafted molecules. However, we were able to hybridize the t-DNA$_1$ with essentially the same efficiency as in the immobilization 1.

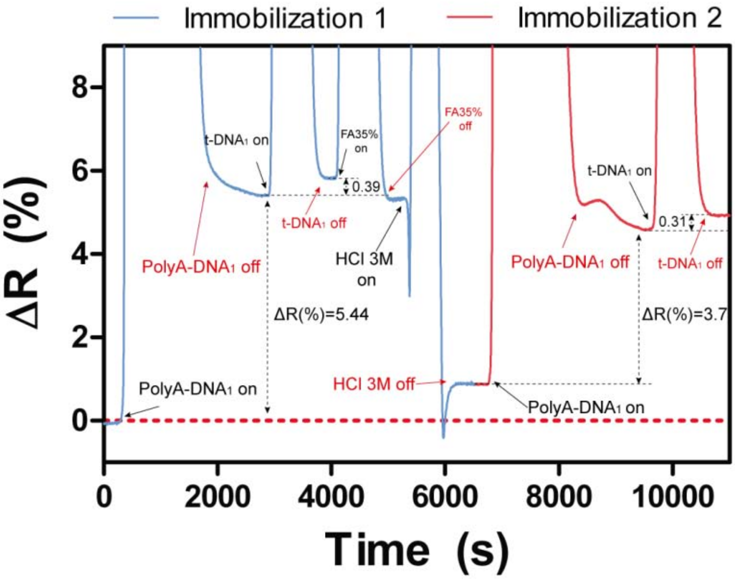

Figure 2. 30 Poly-A monolayer recycling assay monitored by the SPR biosensor.

Although further improvement of the surface recycling should be done, these promising results provide the generation of many bioreceptor layers on the same gold sensor chip. It opens the opportunity for a faster and cost-effective operation, greatly reducing the number of sensor chips employed as well as the time of the analyses.

2.2.4. Conclusions

We have optimized two of the most widely used strategies for DNA-probe grafting on gold surfaces for nucleic-acid biosensor development: the direct grafting of thiol-modified DNA molecules and the covalent linkage to functional surfaces generated by organosulfur molecules. Both rely on the well-known thiol-gold chemistry. We have evaluated their grafting efficiency under *in-situ* conditions and optimized the procedure to achieve the most suitable conditions. We have demonstrated that the direct immobilization SH-DNA probes renders in monolayers with a greater stability and with improved capture efficiencies than the covalent bonding of NH$_2$-DNA probes to functional surfaces. We also assessed the fouling properties of the two different monolayers and confirmed that both approach shows very low-fouling properties with similar non-specific adsorption from undesired molecules contained in a complex biofluid such as serum.

An ultralow-fouling monolayer was optimized by covalently grafting PEG molecules on the gold sensor surface. The developed methodology prevented completely from non-specific interactions in undiluted urine samples and 75% serum samples, producing stable and highly robust monolayers for the analysis of minimally-processed real samples.

Lastly, a new immobilization protocol on gold surfaces has been studied based on the grafting of poly-A blocks. The strategy showed great grafting density and low fouling properties compared to the conventional thiol-gold chemistries. Additionally, a surface recycling protocol has been proposed, allowing the generation of a new bioreceptor monolayer without the need of the gold sensor chip replacement. This advantage places this strategy as a time and cost-effective methodology for the generation of multiple bioreceptor monolayers on the same gold sensor chip.

2.3. Biofunctionalization of the Si_3N_4 sensor area

Silicon-based materials are commonly used for the development of integrated optical waveguide biosensors due to their robustness and their easy fabrication using conventional silicon microfabrication techniques. They have good optical properties, high stability at different temperatures, inertness to many chemicals and solvents, low surface roughness and a versatile chemical functionalization.

As mention in **Chapter 1**, the sensor area of the BiMW interferometer is located along the bimodal section where an opened window at the SiO_2 upper-cladding layer puts in contact the Si_3N_4 sensor surface with the external medium. The probe-anchoring on the Si_3N_4 core waveguide surface is one of the most critical steps in the BiMW biosensor development. This step requires a well-controlled and stable chemical surface functionalization, providing active functional groups on the surface. Most DNA functionalizations on silicon surfaces have been almost exclusively done with *organosilanes*. Surface modification with organosilanes has received widespread application due to their considerable stability and rapid covalent linkage.[148] Alkylsilane monolayers can be formed by the reaction of a silane with the surface hydroxyl groups of oxidized Si_3N_4 surfaces in a process called *silanization*.

The general formula of alkylsilane $R_nSiX_{(4-n)}$ shows a dual behavior, organic and inorganic. The core consists of a silicon atom (Si) bonded to an organic functional group (R_n-) (NH_2-, SH-, Cl-, C_2H_3O- (Epoxy)) and a hydroxyl or a reactive hydrolysable group (-X) (-Cl, -OMe, -OEt, etc.). While the inorganic part reacts onto hydroxyl-terminated silicon-based surfaces, the organic moiety provides the anchorage points for the attachment of biomolecules. Reaction of silane molecules to surface silanol groups of silica leads to the formation of quite stable siloxane bonds (Si-O-Si). The siloxane bond is thermally stable and is relatively chemically stable.

The reaction of organosilanes involves two steps (**Figure 2.31**). In the first step, substituents of the silicon atom are hydrolyzed to form silanols. The alkylsilanols stablish hydrogen bonds with the free hydroxyl groups on the surface or with adsorbed water molecules on the surface. In the second step, the covalent bonding is carried out by condensation and release of water molecules. Water has a catalytic effect; its presence and concentration should be carefully controlled in order to ensure reproducibility.

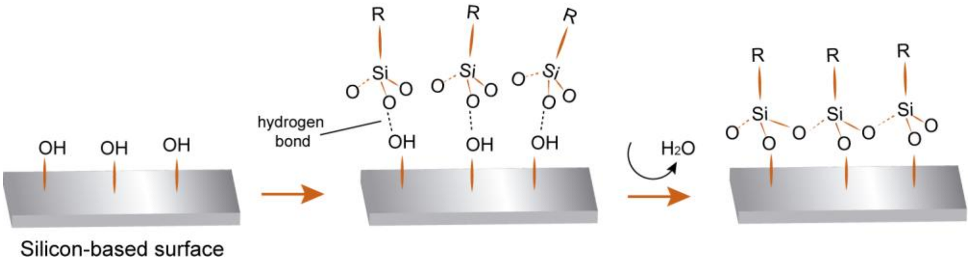

Figure 2. 31 Scheme of the formation of an organosilane monolayer onto silicon-based surfaces.

The choice of the type of silane is of importance. An appropriate choice of the functional “tail group” (R) introduces the specific surface functionalization for the subsequent immobilization of the biorecognition elements. The silanization reaction is largely related to the experimental conditions, where the most relevant parameters are the nature of the silane and its concentration, the nature of the solvent and its water content, temperature and time.[149]

2.3.1. Surface modification using an amino-terminated silane (APTES)

One of the most widespread used silanes for functionalization of Si_3N_4 surfaces is the 3-aminopropyltriethoxy silane (APTES) due to its feasibility for the formation of SAMs under controlled conditions. Silanized surfaces with APTES offer biomolecule stability, high immobilization density, reduced biofouling, leach-proof biomolecule binding, and enhanced analytical performance. APTES not only serves as a mean to anchor the target biomolecule on a solid surface, but also acts as a spacer due to the three siloxanes bond stablished (one with the surface and two with the neighbor APTES silanes), allowing more steric freedom to the biomolecule during the immobilization step. Several studies of APTES grafting onto silicon-based surfaces has been reported.[150] This silane provides silicon surfaces with amino groups[151, 152] that can incorporate different *crosslinkers* for the biofunctionalization of biomolecules carrying specific liker groups (**Figure 2.32**). Crosslinkers are a class of molecules capable of linking two functional groups together, e.g. surface groups and biorecognition elements in solution. They are attributed with two functional end groups and can be classified in *homobifunctional* and *heterobifunctional* crosslinkers. Homobifunctional crosslinkers carry two identical chemical groups that can cause undesired side effects such crosslinking between surface groups or biorecognition elements, which can actually inhibit the functionalization process. On the other hand, heterobifunctional crosslinkers are more specific, overcoming those side-effects due to the different nature of their reactive groups.

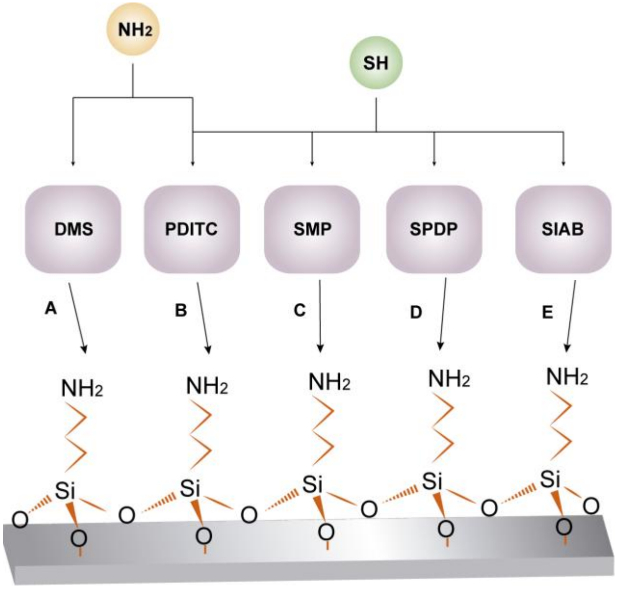

Figure 2. 32 Schematic representation of the versatile derivatization of APTES monolayers. (**A**) Dimethylsuberimidiate (DMS). (**B**) 1,4-phenylene diisothiocyanate (PDITC). (**C**) N-succinimidyl-3-maleimidopropionate (SMP). (**D**) N-succinimidyl-3-(2-pyridyldithio) propionate. (**E**) N-succinimidyl (4-iodoacetyl) aminobenzoate (SIAB).

Such versatility in tailoring the surface on demand provides the APTES modified Si_3N_4 surfaces the capability of performing multiplexed biosensing by the attachment of different biomolecules through different reactive groups. Due to the multiplexing capability of the BiMW biosensor, which can detect simultaneously different biomarkers such as proteins, lipids, or nucleic acid molecules (DNA, mRNA, snc-RNAs…), we optimized a protocol for the assembly of APTES monolayers onto the BiMW surface. Concretely, we focused on the development of an efficient protocol for DNA-probe coupling for the detection of nucleic acid-based biomarkers.

APTES silanization of Si_3N_4 surfaces

The first step in the optimization of the protocol was the APTES grafting onto the Si_3N_4 surface. The APTES grafting reaction is a condensation of its ethyl-groups to the free hydroxyl groups of the Si_3N_4 surface and neighbor silanes, generating a well-packed monolayer. The solid surface must be adequately prepared prior to the silanization reaction in order to create a constant density of hydroxyl groups (silanols) and to improve the density of silane grafting and the repeatability of the reaction. The optimization study was carried out employing bare silicon nitride chips. To remove contamination that may hamper the reaction to the surface hydroxyls, a prior surface cleaning was carried out. We employed a sequence of different solvents with increasing polarity (Acetone, EtOH and milli-Q H_2O) to remove organic and inorganic contamination on the substrate. The cleaning process was finished by ultrasonication of the Si_3N_4 surfaces in a 1:1 Metanol/Hydrochloric acid (MetOH/HCl) solution to remove other inorganic contamination. After that, a layer of active hydroxyl group was generated on the sensor surface by UV-ozone activation and exposition to 15% nitric acid, revealing the oxide groups on the silicon surface.

APTES can precipitate in the presence of water.[150] Therefore, in order to exclude any traces of water over the course of the reaction between the silicon surfaces and APTES, we employed water-free toluene as the reaction solvent and performed the silanization process under an argon atmosphere, for a better control of the humidity, O_2 content and pressure. The cleaned and hydroxyl-activated chips were immediately transferred in a 1% v/v APTES solution prepared in water-free toluene. In addition, we employed *N*,*N*-Diisopropylethylamine (DIPEA) which helps to catalyze the hydrolysis reaction in the absence of water molecules, generating residual EtOH molecules. To limit the possibility of the formation of multilayers of APTES, the samples were incubated in the silane solution for 1 hour. Finally, a curing step was performed at 110ºC to ensure the total condensation of the triethoxy-sylane onto the surface. After this procedure, the formation of APTES layers was assessed by contact angle and X-ray photoelectron spectroscopy (XPS) techniques. The results of the wettability of the Si_3N_4 chips are summarized in **Table 2.1**.

Table 2. 1 Contact angle values of the different steps during APTES-modification of Si_3N_4 surfaces.

Sample	**Contact Angle (º)**
Untreated Si_3N_4 chip	35.1 ± 1.19
Clean Si_3N_4 chip	22 ± 1
APTES-modification	67.1 ± 0.11

The values of contact angles in untreated and APTES-modified surfaces are in good correlation with other published results.[153] The clean and untreated Si_3N_4 chips presented a lower contact angle value compared to the ones derivatized with APTES. The presence of the silane made the surface more hydrophobic, which is due to the contribution of the organic layer formed by the functional amine group of APTES molecules.

XPS was used to evaluate the chemical composition of the silicon surface after each treatment and the nature of the chemical bonding associated with transformations that occurred on the surface. XPS technique can measure the binding energy (eV) of a given substrate, which can be related to its composition. We compared the untreated and the APTES modified surfaces compositions. Untreated silicon surfaces gave rise to a strong Si (2p) peak, indicating the presence of nitride in the surface (**Figure 2.33**). However, this peak is reduced after the APTES modification, indicating that the silane is concealing the measurement of the nitrogen content from the surface.

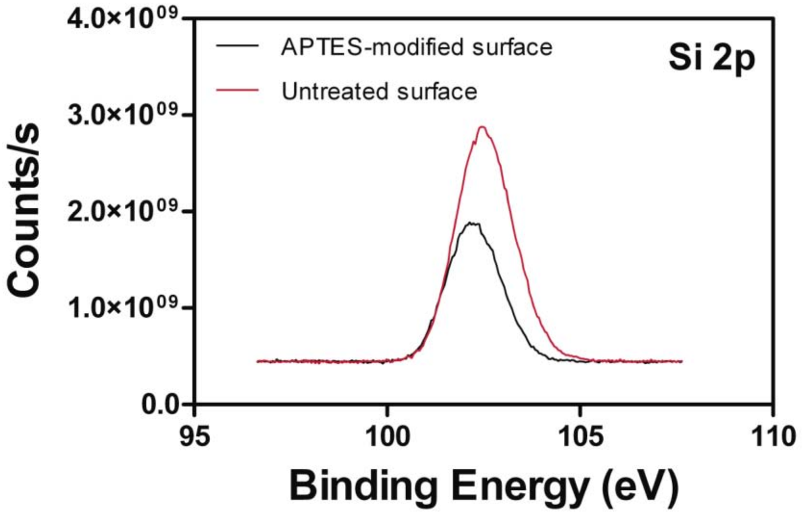

Figure 2. 33 XPS analysis of the Binding energy for Si 2p bonds in untreated (*red line*) and APTES-modified Si_3N_4 surfaces (*black line*).

The narrow scan of the C 1s signal was used to probe the chemical states of carbon on the surface. Organosilane attachment to the Si_3N_4 surface resulted in an increase in the C 1s signal compared to the untreated surface (**Figure 2.34**). The deconvolution of the C 1s peak for the modified surface with APTES showed a main band at 284.7 eV, due to the elongation of the hydrocarbon chain in contrast with the soft peak from the untreated surface, probably due to organic contamination (**Figure 2.34A**). More importantly, a new peak contribution was detected at 285.7 eV, attributable to C-N bonds (**Figure 2.34B**). All electron binding energies of the different types of carbon peak positions were derived from the literature for other similar systems.[154, 155] These results corroborated the successful grafting of the silane onto the surface and evidenced the formation of a silane layer onto the Si_3N_4 with terminal amine functional groups for further attachment of biomolecules.

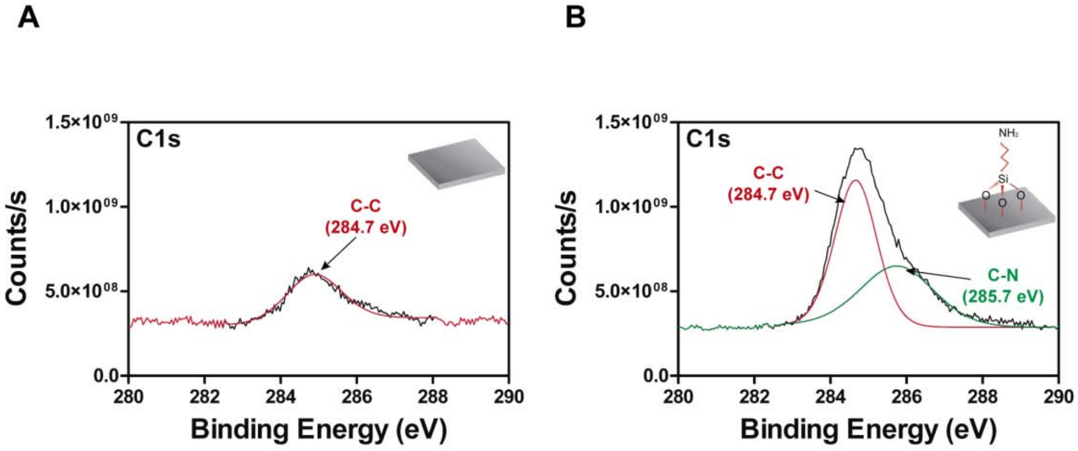

Figure 2. 34 XPS analysis of the Binding energy for C1s bonds in untreated (**A**) and APTES-modified Si_3N_4 surfaces (**B**).

DNA probe coupling by an heterobifunctional crosslinker

Next, we studied the covalent bonding of DNA probes to the APTES monolayer through the heterobifunctional crosslinker N-(γ-Maleimidobutyryloxy) sulfosuccinimide ester (sulfo-GMBS). Sulfo-GMBS is a water-soluble amine-to-sulfhydryl crosslinker that contains NHS-ester and maleimide reactive groups at opposite ends of a medium-length spacer arm (7.3 angstroms) (**Figure 2.35**). Sulfo-NHS ester end couples with primary amines to form stable amide bonds while the maleimide end reacts with –SH groups forming stable thioether linkages.

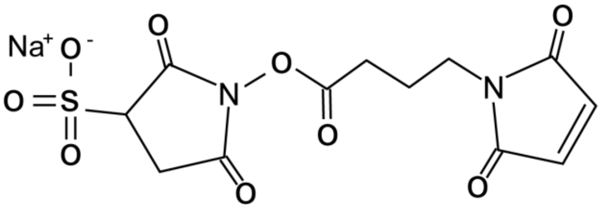

Figure 2. 35 Scheme of the heterobifunctional crosslinker sulfo-GMBS.

APTES-modified Si_3N_4 surfaces were incubated with Sulfo-GMBS crosslinker for the coupling to reactive amine groups. Then, the crosslinker-modified surfaces were incubated with a solution of 1 µM SH-DNA probes for the binding between the thiol-group with the maleimide end of the Sulfo-GMBS. Prior to the surface DNA functionalization, SH-DNA probes were incubated with a two-fold molar excess of tris(2-carboxyethyl)phosphine (TCEP). TCEP is a reducing agent commonly employed to break possible probe crosslinking through disulfide bonds (S-S bonds) and to maintain the thiol groups in their reactive, reduced state. It contributes to a better interaction with the maleimide group during the biofunctionalization process.

To assess not only the proper bioconjugation but also the applicability of the biofunctionalization for target capture, hybridization of the SH-DNA probe was evaluated through fluorescence assays. Biofunctionalized surfaces were incubated with a solution containing 1 µM of 3'-Cyanine 3 (Cy3) modified DNA sequences complementary to the immobilized probe for 1 hour in 5x SSC buffer (pH 7). Cyanine dyes are used widely as labels for nucleic acids. Concretely, Cy3 is excited maximally at 550 nm and emits in the red end of the spectrum at 570 nm, giving rise to bright orange-fluorescent colored surfaces. Additionally, treated Si_3N_4 chips interrupted at different steps along the biofunctionalization process were also incubated with the fluorescent target as control samples. Fluorescence was evaluated through optical microscopy. **Figure 2.36A** represents a scheme of the sequence employed during the surface biofunctionalization.

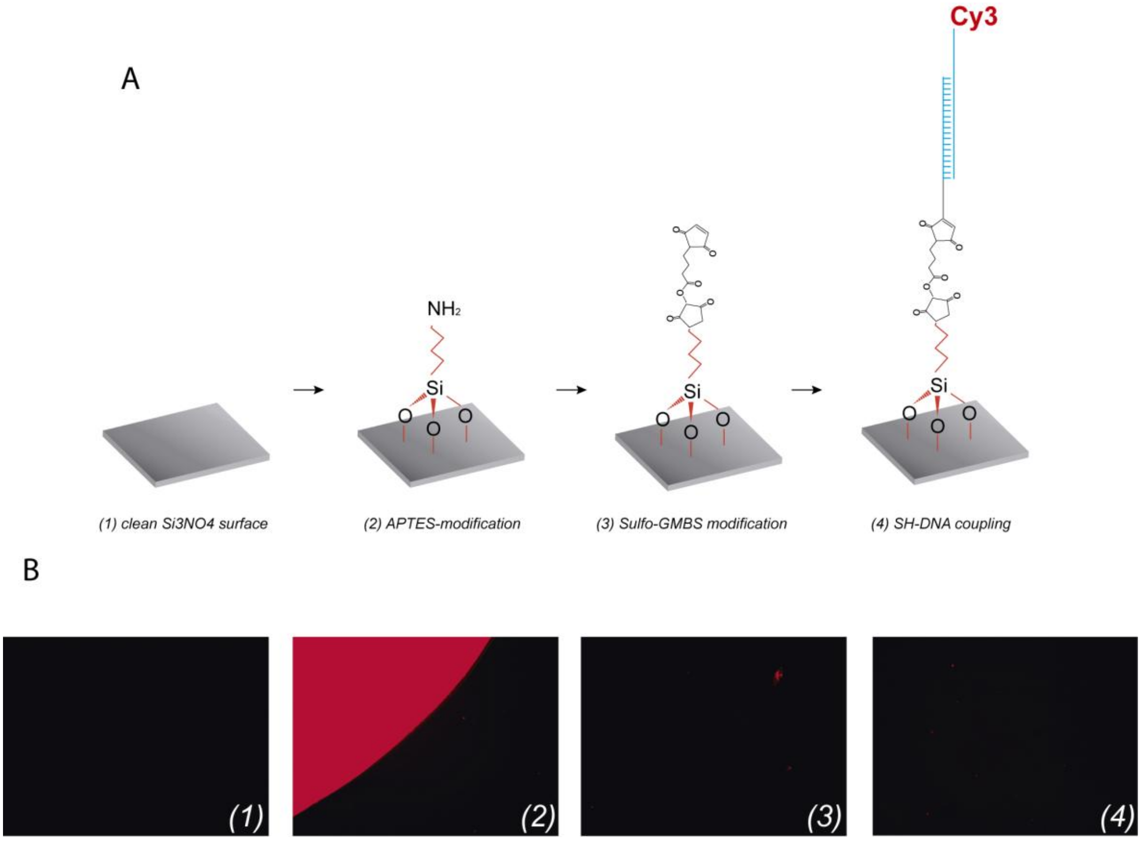

Figure 2. 36 Surface characterization of the biofunctionalization process by fluorescence. (**A**) Scheme of the protocol. (**B**) Fluorescent signals for each biofunctionalization step.

Figure 2.36B shows the microscope images after incubation with the Cy3-DNA target. Untreated surfaces did not show any fluorescence from the target, indicating that none unspecific physical adsorption took place onto the Si_3N_4 surface (**Figure 2.36B** *(1)*). Therefore, we used it as a negative control. Surprisingly, as can be appreciated in (**Figure 2.36B** *(2)*), a strong fluorescent signal from the APTES-modified surfaces was observed. This effect can be attributed to electrostatic interactions between the fluorescent DNA target (negatively charged) and the primary amine functional groups of the APTES (positively charged). After the crosslinker modification, amine groups were replaced by the maleimide end of the sulfo-GMBS, which prevents better for nonspecific adsorption of the target and, therefore, no fluorescence was observed in the surface (**Figure 2.36B** *(3)*). This also indicates a proper linkage of this crosslinker to the APTES. However, samples incorporating the specific DNA probes did not show any fluorescence after incubation with the complementary fluorescent target (**Figure 2.36B** *(4)*), which suggests that hybridization was hindered either due to non-efficient linkage of the SH-DNA probes or to steric or electrostatic effects reducing the target accessibility.

To check the covalent attachment of the DNA probes onto the Sulfo-GMBS modified surface, we employed 3’ Cy3-labeled, 5’ thiol-modified DNA probes applying the same conditions described above and evaluating the fluorescent signals. Surprisingly, no fluorescent signal was appreciated, indicating that the DNA probes did not react with the crosslinker and, therefore, no immobilization took place.

In order to improve the efficiency of the crosslinking, fluorescent SH-DNA probes were incubated with Sulfo-GMBS crosslinker before anchorage to the silane layer. The probes previously treated with TCEP were incubated with increasing concentrations of Sulfo-GMBS crosslinker (5, 10 and 20 µM). An excess of 5’-Cy3, SH-DNA probe (20 µM) was employed to guarantee that most of the crosslinker reacted with the thiolated probes and little quantity of crosslinker remained free for possible competition during the linkage to the amine group of the silanized surface. Fluorescence results (**Figure 2.37**) showed an enhancement in the fluorescent emission with increasing concentrations of crosslinker, indicating more quantity of probes attached to the surface at a higher crosslinker concentration. No fluorescent emission at the lowest concentration of crosslinker (5 µM, **Figure 2.37** *(a)*) confirmed the need for higher concentration of crosslinker for the DNA-probe immobilization.

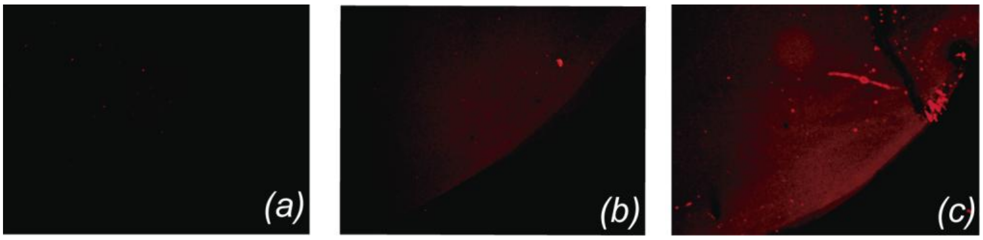

Figure 2. 37 Fluorescent signals after the incubation of the SH-DNA probe with different sulfo-GMBS crosslinker concentrations: *(a)* 5, *(b)* 10 and *(c)* 20 µM previously to surface biofunctionalization.

Although the above results evidenced a good functionalization of the APTES modified surface through the heterobifunctional Sulfo-GMBS crosslinker, the high quantity of DNA probe and crosslinker needed for the process made the proposed methodology unsuitable for the development of a DNA-based biosensor. For that reason, a new strategy was proposed by employing another crosslinker molecule, i. e. p-Phenylene diisothiocyanate (PDITC) crosslinker.

DNA probe coupling by an homobifunctional crosslinker

PDITC (**Figure 2.38**) is a small homobifunctional crosslinker which is commonly used in bioconjugation chemistry.[156] Isothiocyanate (R-NCS) group is quite stable in solution and it is known to be reactive either to primary amine groups, yielding thiourea bonds, or to thiol groups, forming thiocarbamate bonds. Indeed, conjugation of biomolecules to isothiocyanate functional groups proceeds mostly through reaction with thiol groups in a fast reaction.[157]

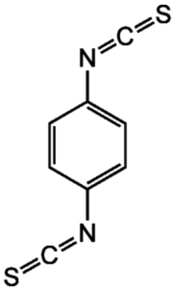

Figure 2. 38 Scheme of the homobifunctional crosslinker PDITC.

Taking advantage of this dual reactivity, we established a protocol for the modification of aminated surfaces with PDITC and subsequent coupling to the thiol-modified DNA probes through thiocarbamate bonds. Thus, the APTES-modified surfaces were reacted with 20 mM PDITC in a solution of 10% anhydrous pyridine in N,N-dimethylformamide (DMF). Activated surfaces where incubated with 1 µM of SH-DNA probe in 0.1M Na_2CO_3 buffer at pH 9.5. Basic pH leads to the reactive state of the APTES primary amine, promoting the reaction with the NCS group. Furthermore, the reaction was amine catalyzed by addition of 1 equivalent (eq) of triethylamine (NEt_3) to accelerate the reaction.[157] After the incubation time, surfaces were carefully rinsed with water and dried under gentle nitrogen flux. Hybridization of fluorescent target was performed as previously described.

Fluorescent signals showed a clear specific signal for the surface functionalized with the DNA probe (**Figure 2.39B**). This fluorescent signal showed a homogeneous distribution along the Si_3N_4 surface, which is an indication of a good assembly of the silane monolayer with no precipitation or multilayer formation. However, a slight fluorescent signal was noticed with the PDITC activated monolayers, probably due to some non-specific adsorption of the labeled-DNA (**Figure 2.39A**). To corroborate that the fluorescence signal from the DNA functionalized surfaces were due to specific hybridization of the complementary Cy3-DNA, we functionalized a second surface with a non-complementary probe and incubate with the fluorescent target. As can be appreciated from **Figure 2.39C**, no fluorescent emission was detected in this chip, indicating that the biofunctionalization was performed properly at the established conditions.

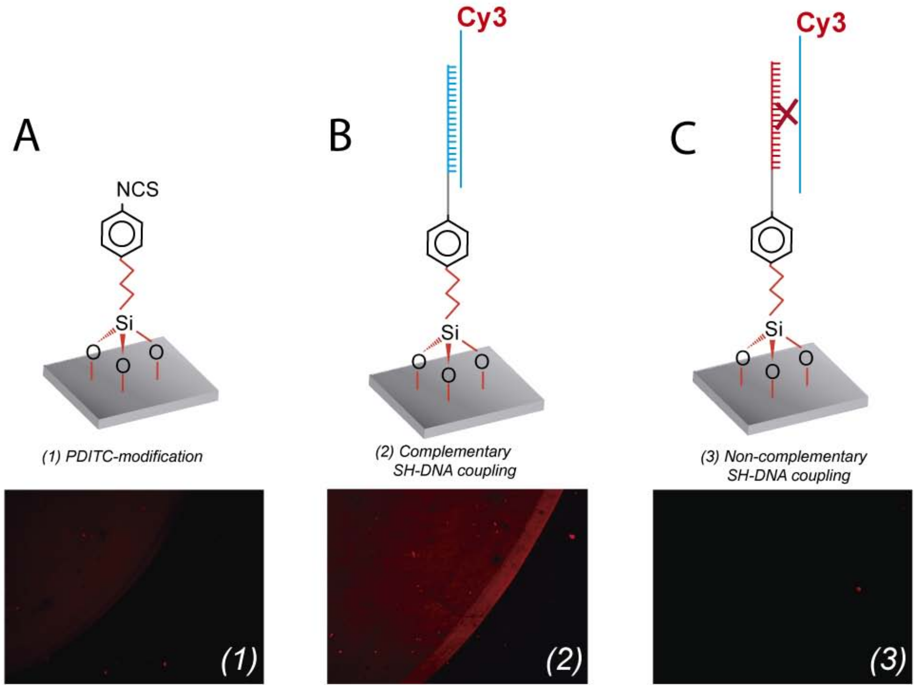
A
B
C
NCS
Cy3
Cy3
Si
Si
Si
O O O
(1) PDITC-modification
(2) Complementary SH-DNA coupling
(3) Non-complementary SH-DNA coupling
(1)
(2)
(3)

Figure 2. 39 Fluorescent signals of the PDITC biofunctionalization approach for (**A**) PDITC-activated surface; (**B**) Complementary DNA-probe functionalized surface; and (**C**) Non-complementary DNA-probe functionalized surface.

Such results also agreed with the evaluation of static contact angle (**Table 2.2**), which showed increasing hydrophilicity after PDITC activation and DNA functionalization, 59.6º and 51.7º respectively, in contrast with the APTES modified surfaces (67.1º).

Table 2. 2 Contact angle values for PDITC-modified and DNA functionalized Si_3N_4 surfaces.

Sample	Contact Angle (º)
APTES-modification	67.1 ± 0.11
PDITC-modification	59.6 ± 0.12
DNA functionalization	51.7 ± 0.82

The effectiveness of the functionalization was further assessed through the immobilization of the DNA probes and hybridization assays in the SPR biosensor. For that purpose, we generated an aminated monolayer onto the gold sensor surface by *ex-situ* immobilization of amino-modified SH-PEG molecules. Primary amines on the surface were activated with PDITC crosslinker as previously described. Then, activated gold sensor chip was placed in the device and *in-situ* functionalized with SH-DNA_1 probes. Immobilization was monitored in real-time course. Different conditions were employed as controls of the process (Bare gold, SH-PEG-CO_2H, and non-PDITC-activated SH-PEG-NH_2 surfaces). In addition, the same conditions were applied for NH_2-DNA probes.

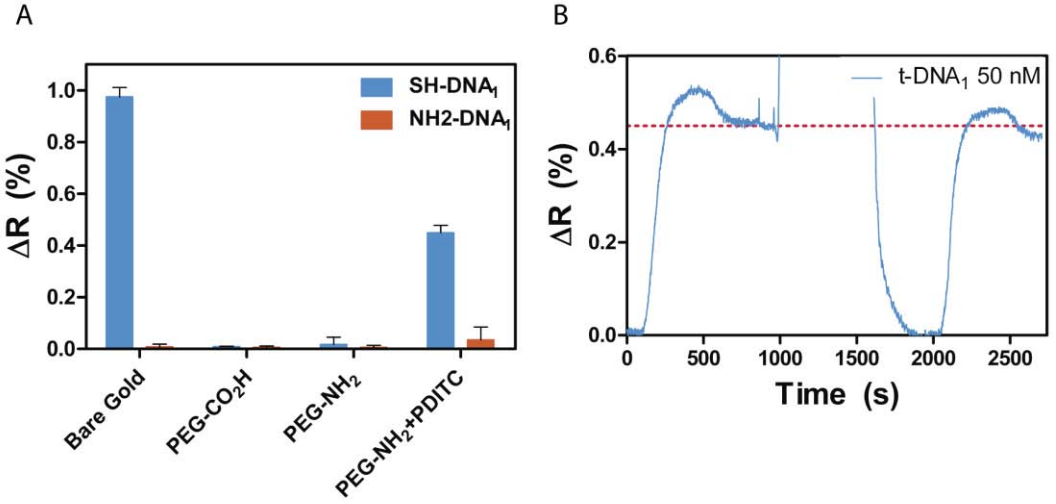

Figure 2. 40 SPR evaluation of the optimized PDITC biofunctionalization. (**A**) Immobilization on different surface coverages. (**B**) Sensogram of hybridization/regeneration cycle of t-DNA_1 in PDITC activated PEG-NH_2 surface.

As can be appreciated in **Figure 2.40A**, bare gold surfaces showed a high chemisorption of thiolated molecules (ΔR (%) = 0.97) in contrast with the negligible grafting of NH_2-DNA probes. However, this chemisorption was prevented after the gold surface coverage with both non-activated SH-PEG-CO_2H and SH-PEG-NH_2 surfaces. No immobilization of DNA molecules was noticed in the non-activated surfaces. By contrast, after PDITC activation, SH-DNA probes produced an increase in the reflectivity (ΔR (%) = 0.45), indicating that a covalent coupling was taken place. Amine-modified probes did not achieved the same level of immobilization, which suggests that thiourea bonds may require longer incubation times for the covalent attachment of biomolecules as described elsewhere.[157] Subsequent hybridization/regeneration cycles of the complementary target confirmed the site-specific immobilization of the DNA probes (**Figure 2.40B**).

2.3.2. Application of the biofunctionalization protocol using APTES to the BiMW device

The final goal of the development of this biofunctionalization protocol was its application for the attachment of DNA probes onto the Si_3N_4 sensor area of the BiMW biosensor. The biofunctionalization was performed following the optimized protocol described above. After silanization with APTES and PDITC-activation, the BiMW chip was placed in the experimental set-up and encapsulated with the fluidic cell. The covalent binding of the SH-DNA probe to the PDITC-activated surface was then monitored in real-time by the analysis of the modulated interferometric signals of the BiMW sensor (**Figure 2.41**). As can be appreciated, the anchorage of biomolecules onto the surface gave rise to a positive shift in the phase change ($\Delta\Phi$ (rad) = 62), indicating that the DNA-probe coupling through thiocarbamate bonds was taken place at the sensor surface.

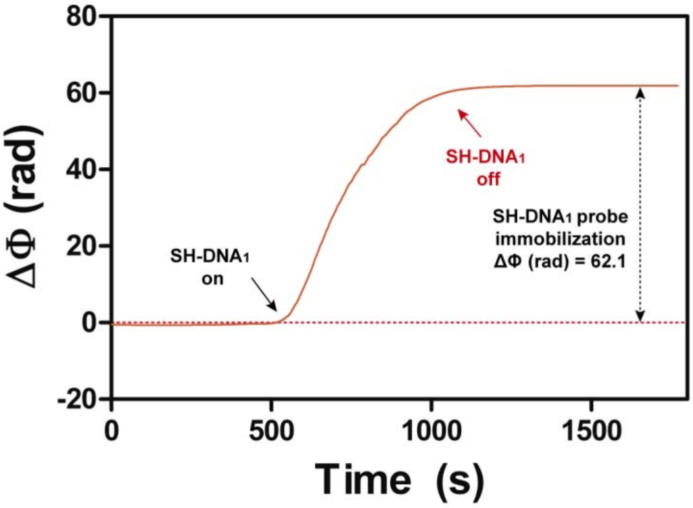

Figure 2. 41 BiMW biosensor response for the immobilization of SH-DNA_1 over a PDITC-activated APTES monolayer.

The efficiency of the immobilization process was also assessed by hybridization/regeneration assays, and the selectivity of the generated monolayer was tested. First, a concentration of 10 nM of the complementary target (t-DNA_1) was flowed in the sensor microfluidic. Likewise, the same concentration of a non-complementary target (t-DNA_4) was evaluated with the same monolayer after regeneration of the biosensor surface with FA 35%. **Figure 2.42** represents the sensograms obtained during the interaction of the two different DNA sequences with the monolayer. As can be observed, specific target t-DNA_1 produced a positive shift in the phase change ($\Delta\Phi$ (rad) = 0.31) while the non-specific target signal returned to the baseline level after it interaction with the biosensor surface. Such results reflected the specificity of the generated monolayer.

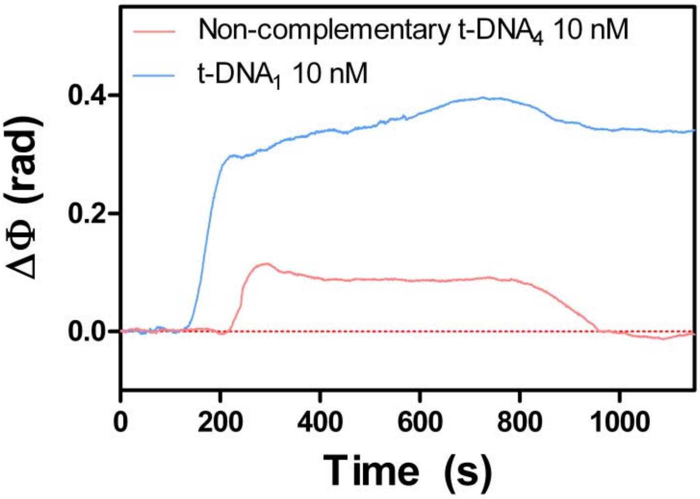

Figure 2. 42 Real-time sensogram of the specific hybridization of t-DNA1 with the immobilized probe in the BiMW biosensor.

The reproducibility of the signals and the bio-stability of the generated monolayer were also assessed. The monolayer was able to generate reproducible signal throughout 20 hybridization/regeneration cycles, showing a coefficient of variation of 7%. Regarding the monolayer accessibility, the addition of lateral spacers such as MCH or SH-PEG molecules as described for the SPR biosensor can further improve the biosensor performance. Therefore, a proper optimization can greatly enhance the target capture efficiency as well as elongate the half-life of the biosensor.

2.3.3. Si_3N_4 surface recycling

Due to the potential commercial applications in medical diagnosis, the BiMW biosensor reuse is desirable to reduce costs. Normally, surface recycling involves harsh, wet chemistry treatments to remove surface chemistry from the sensor. Strong acid or base treatments can be employed but usually result in a damage of the transducer element which reduce the sensor performance and increase the noise due to the optical transducer degradation, diminishing the biosensor sensitivity and specificity.[158] An alternative approach is a dry-chemistry method based on O_2 plasma treatment.[159] This treatment completely removes the recognition moiety, allowing the transducer surface to be refreshed with new recognition elements and thus enabling the sensor to be recycled. O_2 plasma has been employed for the removal of organic layer onto surfaces.[159] The various oxygen species in the plasma can react with the organic fragments, converting them to combustion-like products (H_2O, CO, and CO_2) or low-molecular-weight hydrocarbons, all of which have high vapor pressures and are easily removed from the surface during evacuation of the plasma chamber.[160] Then, exposition of the surface to a concrete oxygen flow and power can eliminate the organic compounds attached to the surface without negatively impacting the device structure, and leave a fresh surface that can be recycled.[159]

Great care should be taken in order to not to damage the biosensor surface, which may imply a reduction of the thickness of the Si_3N_4 core layer, an important value for BiMW interferometers. The time of exposure is an important parameter in the recycling process since it will provide the time necessary to remove the whole organic layer leaving the surface in perfect conditions without compromising the performance of the following biofunctionalization process. Four different Si_3N_4 chips were functionalized with APTES as previously described. The silanization process was checked by the non-specific fluorescent signal provided by the fluorescent t-Cy3-DNA. The fluorescence data of this initial silanization confirmed that the surfaces were uniformly covered with APTES (**Figure 2.43**).

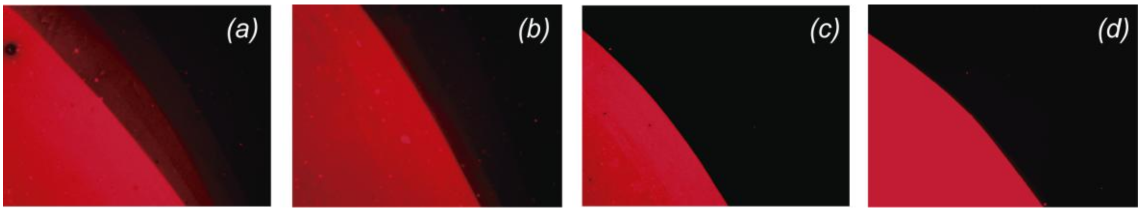

Figure 2. 43 Fluorescent signals given by the non-specific adsorption of the t-Cy3-DNA onto APTES monolayers.

To study the feasibility of using O_2 plasma treatment to recycle Si_3N_4 surfaces, we exposed the silanized chips over a series of time intervals (1, 2, 3 and 4 min). To verify that organic compounds were removed from the surfaces, we checked their fluorescence after O_2 plasma treatment. No fluorescence was perceived after each exposition time. After the O_2 plasma treatment, the surface was again incubated with the fluorescent target to further verify that the silane had been completely removed. Fluorescence microscopy on these samples did not yield any intensity compared to substrate background, indicating that no fluorescent labeling occurred (**Figure 2.44**). These results confirmed that the APTES was completely removed from the surface at any of the interval tested.

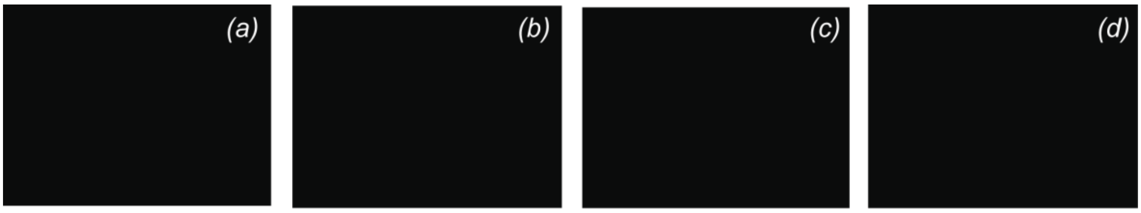

Figure 2. 44 Fluorescent emissions after incubation with fluorescent target in recycled Si_3N_4 surfaces at different intervals*: (a)* 1, *(b)* 2, *(c)* 3 and *(d)* 4 min.

To verify if the O_2 plasma treatment enables the surface recycling, the different chips were cleaned and resilanized with the same protocol. After the second silanization, the chips were again fluorescently labeled. As with the first silanization, the chips showed fluorescent after the labeling (**Figure 2.45**). However, only the chip with an exposition time of 3 minutes showed a uniform coverage (panel *(c)*), suggesting such time of exposure as the most suitable for APTES-modified surfaces recycling. Times below 3 minutes showed a poor and non-uniform coverage (panels *(a)* and *(b)*), probably due to an insufficient removal of the organic compounds at the surface. On the other hand, an exposition time of 4 minutes (panel *(d)*) also showed a poor surface coverage, suggesting that such conditions could probably be damaging the surface, impeding further biofunctionalization processes after recycling.

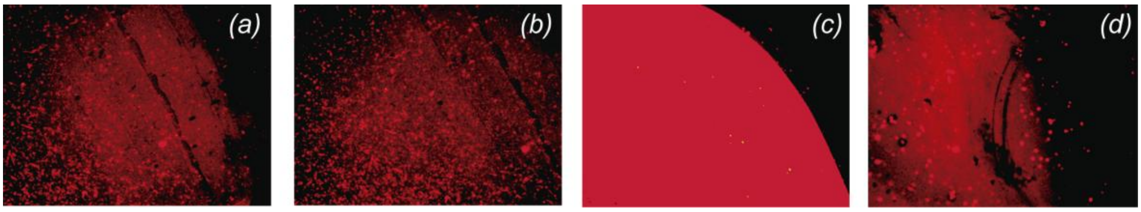

Figure 2. 45 Fluorescent emission after a second silanization process in recycled Si_3N_4 surfaces at different intervals*:* *(a)* 1, *(b)* 2, *(c)* 3 and *(d)* 4 min.

In order to determine the effect of surface recycling in the BiMW biosensor performance, we recycled the BiMW chip employed in **section 2.3.2** with O_2 plasma during 3 min. Then, the sensor chip was again biofunctionalized with the same SH-DNA probe and the biosensor performance was assessed. **Figure 2.46** shows the sensograms for the two different biofunctionalizations (**A**) and subsequent target hybridizations (**B**). As can be observed, second biofunctionalization gave the similar responses ($\Delta\Phi$ (rad) = 71.8) compared to the first biofunctionalization ($\Delta\Phi$ (rad) = 62) (%CV = 10). The disparity between biofunctionalization signals came probably from the presence of a small bubble in the fluidic cell in the moment the sample reached the biosensor surface, as indicated in the sensogram. This confirmed the formation of a proper APTES-monolayer after recycling the chip. In addition, hybridization efficiencies showed similar values in both assays with a CV of 13%, suggesting that after the O_2 plasma treatment of the surface, we could generate monolayers with the same characteristics in terms of surface distribution and target capture efficiency.

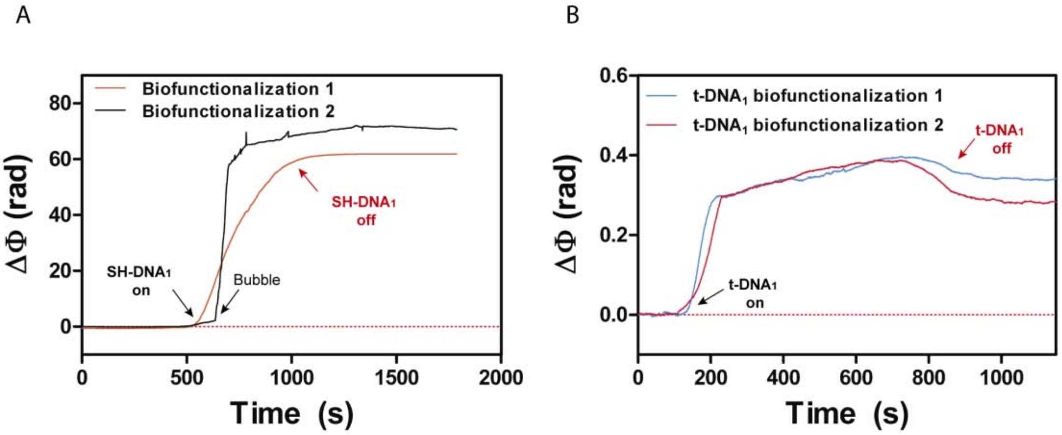

Figure 2. 46 BiMW sensograms for two different biofunctionalization processes performed on the same chip: (**A**) SH-DNA probe immobilization signals (**B**) DNA target hybridization signals.

Further studies should be performed in order to confirm the stability of the monolayer generated in the second biofunctionalization process after recycling. Also, it could be of interest to determine the maximum number of recycling cycles that could be performed on the same BiMW sensor chip that guarantee a proper performance of the biosensor regarding stability, reproducibility and sensitivity of the different monolayers.

2.3.4. Conclusions and future perspectives

We established a biofunctionalization protocol for SH-DNA probes on Si_3N_4 surfaces. The protocol involved the generation of APTES monolayers and the covalent bonding of the probes through the PDITC crosslinker under controlled conditions. The excellent performance of the different biofunctionalization steps was demonstrated through different characterization techniques (static contact angle, XPS and fluorescence) and its functionality and accessibility was assessed by SPR biosensor assays, which corroborated its effectiveness for SH-DNA probe anchorage to amine-functionalized surfaces. We finally validated the optimized methodology by its application to the BiMW biosensor, demonstrating its high sensitivity and selectivity and the robustness of the generated monolayer during target analyses.

The presented methodology constitutes a suitable approach for the generation of nucleic-acid based biosensors on Si_3N_4 surfaces through thiocarbamate bonds. This kind of chemistry is very convenient for the transference of methodologies generated on gold surfaces to the BiMW interferometer for achieving better sensitivities and lower limit of detections. Due to the wide range of possibilities of this silane to incorporate different crosslinkers and, therefore, functional groups, the developed methodology is presented as a suitable strategy for multiplexed BiMW interferometers biofunctionalization. It can incorporate biomarkers of different nature that requires another covalent bonding to the sensor surface, permitting a simultaneous analysis of multiple different-nature analytes.

Finally, we demonstrated the reusability of the same BiMW chip by recycling through O_2 plasma treatment. We established the proper conditions for surface recycling and demonstrated its capability for the generation of a new functional monolayer after a second biofunctionalization process. Although further characterization assays such as XPS should be done to fine-tune the proper conditions to completely remove the organic monolayer from the Si_3N_4 surface, the proposed approach constitutes a facile dry-chemistry route for the complete regeneration of functionalized surface without negatively impacting the device performance. Thus, it will be possible to perform multiple biofunctionalization processes onto the same BiMW sensor chip, greatly reducing costs.

2.4. Materials & Methods

2.4.1. Chemical Reagents and Buffers Composition

Solvents used for the cleaning of the sensor chips were purchased to Panreac Applichem (Spain): Acetone 99.5%, Ethanol 99% and Methanol 99%. Main salts and chemical reagents for sensor cleaning, buffer preparation and biofunctionalization were acquired from Sigma-Aldrich (Germany): Sodium Dodecyl Sulfate (SDS), Hydrochloric Acid (HCl), anhydrous Toluene 99.8%, Sodium Phosphate monobasic (NaH_2PO_4) 99%, Sodium Phosphate dibasic (Na_2HPO_4) ≥99%, Sodium Chloride (NaCl) ≥99.5%, Sodium Citrate dihydrate ≥99%, TRIS Hydrochloride (Tris-HCl), Magnesium Chloride ($MgCl_2$), Potassium Chloride (KCl) ≥99.5%, 2-(N-Morpholino)ethanesulfonic acid (MES), Sodium carbonate (Na_2CO_3) ≥99, bovine serum albumin (BSA), N,N-dimethylformamide anhydrous ≥99.8%, (DMF), triethylamine ≥99% (NEt_3), Pyridine anhydrous 99.8%, Tween 20, CHAPS ≥98%, Comercial Human Serum, 6-Mercapto-1-hexanol (MCH) 97%, 6-amino-1-hexanol (AH), alkanethiols for SAM formation (16-mercaptohexadecanoic acid (MHDA) and 11-mercaptoundecanol (MUOH)), reagents for carboxylic group activation (1-ethyl-3(3-dimethylaminopropyl)carbodiimide hydrochloride (EDC) and N-hydroxysulfosuccinimide (sulfo-NHS)), ethanolamine, crosslinking molecule p-Phenylene diisothiocyanate 98% (PDITC), 3-Aminopropyltriethoxy silane ≥98%, (APTES), *N,N*-Diisopropylethylamine (DIPEA), Urea and Formamide ≥99.5% (FA). The copolymer poly-(L-lysine)-graft-PEG (PLL-PEG, MW~67.000 g/mol) was purchased to SuSoS (Switzerland) and metil-, amine- and carboxyl- SH-PEGs (SH-PEG-CH_3, MW 2000 g/mol; SH-PEG-NH_2, MW 3400 g/mol; SH-PEG-CO_2H, MW 2000 g/mol) to Laysan Bio. Crosslinking molecule N-(γ-Maleimidobutyryloxy) sulfosuccinimide ester (sulfo-GMBS) was purchased from Thermofisher Scientific (Spain).

Several buffers and solvents have been prepared either for functionalization or target analysis: PBS 50 mM (50 mM Phosphate buffer, 0.75 mM NaCl –pH 7-), $CaCl_2$-TE buffer (1 M $CaCl_2$, 1x TE (10 mM Tris-HCl, 1 mM EDTA) –pH 7-), 20xSSC (3 M NaCl, 0.3 M sodium citrate –pH 7-), $Tris_{Mg}$ buffer (10mM Tris-HCl, 15 mM $MgCl_2$ –pH 7.4-), HEPES buffer (10 mM, pH 7.0), MES ((2-N-morpholino ethanesulfonic acid) 0.1M MES + 0.5M NaCl pH 5.5-6), Ethanolamina 1M pH 8.5, Na_2CO_3 buffer ($NaHCO_3$ 0.1 M**,** Na_2CO_3 0.1 M**,** EDTA 1mM, pH 9.2). Buffer solutions were prepared by using H_2O milliQ incubated O/N with 2% DEPC and autoclaved at 121ºC during 1 hour. All solid materials were autoclaved at 121ºC/20 min for plastic and 134ºC/10 min for glass.

2.4.2. DNA/RNA sequences

DNA and mRNA isoform sequences were obtained from Esmbl gene browser (http://www.ensembl.org/index.html). MiRNA sequences for probes and target design were obtained from the miRNA data base miRBase, (http://www.mirbase.org). To study the likelihood of the probe secondary structures formation by self-complementarity we took advantage of *Oligo Analizer* software, a freeware application for the generation of DNA-based probes.

All DNA probes and DNA/RNA synthetic targets were purchased from IBA GmbH (Goettingen, Germany) and are summarized in **Table 2.3.** DNA probe sequences incorporate a functional group at the 5'-end, i.e. SH- or NH_2-, or a $polyA_m$ sequence (m being 7 or 15) to enable coupling with either directly to the gold sensor surface or a CO_2H-functional monolayer, previously generated at the surface. In addition, a spacing region which consists of a 15 thymines ($polyT_{15}$) sequence is placed between the functional group and the matching region for enhancement of target accessibility.[111] Oligo Analyzer software and RNA fold webserver have been employed for secondary structure and self-annealing prediction of the probes and targets.

Table 2. 3 Sequences for probes and DNA/RNA synthetic targets employed in this thesis.

Name	Sequence
DNA$_1$ probe	5'- (SH/NH$_2$)- PolyT$_{15}$ -CTTTCTCTTCACTTCCTCTTTG-3'
DNA$_2$ probe	5'- (SH)- PolyT$_{15}$ -AGATCTGGATCCTTCCTCTTTG-3'
DNA$_3$ probe	5'- (SH)- PolyT$_{15}$ - CACCCCAAGTTAGAT-3'
DNA$_4$ probe	5'-(SH)- PolyT$_{15}$-AGTATCCCAGCCGCCGTTC 3'
miRNA$_1$ probe	5'-PolyT$_{15}$-ACTCACCGACAGCGT 3'
t-DNA$_1$	5'ATGTGAACATGGAATCATCAAGGAATGCACACTCACCAGCAACACCAAGTGCAAAGAGGAAGTGAAGAGAAAGGAAGTACAGAAAACATGCAGAAAGCACAGAAAGGAAAACCAAGGTTCTCATGAATCTCCAACTTTAAATCCT 3'
t-DNA$_2$	5'ATGTGAACATGGAATCATCAAGGAATGCACACTCACCAGCAACACCAAGTGCAAAGAGGAAGGATCCAGATCTAACTTGGGGTGGCTTTGTCTTCTTCTTTTGCCAATTCCACTAATTGTTTGGGTGAAGAGAAAGGAAGTACAGAAAACATGCAGAAAGCACAGAAAGGAAAACCAAGGTTCTCATGAATCTCCAACTTTAAATCCT 3'
t-DNA$_3$	5'GTAGACAAGGAGATGCAGGTATTGGTGAGTCGGATCGCAGCTTGGATGGCCACTTACCTGAATGACCACCTAGAGCCTTGGATCCAGGAGAACGGCGGCTGGGATACTTTTGTGGAACTCTATGGGAACAATGCAGCAGCCGAGAGCCGAAAGGGCCAGGAACGCTTCAACCGCTGGTTCCTGACGGGCATGACTGTGGC 3'
t-DNA$_4$	5'GAGGCAGGCGACGAGTTTGAACTGCGGTACCGGCGGGCATTCAGTGACCTGACATCCCAGCTCCACATCACCCCAGGGACAGCATATCAGAGCTTTGAACAGGATACTTTTGTGGAACTCTATGGGAACAATGCAGCAGCCGAGAGCCGAAAGGGCCAGGAACGCTTCAACCGCTGGTTCCTGACGGGCATGACTGTGGC 3'
t-miRNA$_1$	5'AACAUUCAACGCUGUCGGUGAGU 3'
t-miRNA$_2$	5'UGUAACAGCAACUCCAUGUGGA 3'

2.4.3. Gold surface biofunctionalization

Gold sensor chip cleaning.

The sensor chips consist of a glass surface (10 × 10 × 0.3 mm) coated with 2 nm of chromium and 45 nm of gold (SSens, Enschede –The Netherlands). Prior to DNA-probe immobilization, gold sensor chips were cleaned by consecutive sonication cycles (1 min) with solvents of decreasing polarity (i.e. acetone, ethanol and MilliQ H_2O) previously heated up to their boiling point. Then, substrates are dried under nitrogen flux and placed in an UV/O_3 generator (BioForce Nanosciences, USA) for 20 min. After that, gold sensor chips are subsequently rinsed with ethanol and water and dried under nitrogen flux.

Thiol-DNA probes immobilization

Formation of self-assembled monolayers (SAMs) of SH-DNA probes was carried to study the gold sensor surface coverage. Different probe concentrations (0.15, 0.25, 0.5, 1 and 2 µM) diluted in 250 µL PBS 50 mM (pH 7) were tested. H_2O-DEPC was selected as running buffer for the immobilization procedure at a constant rate of 12 µL/min, approximately.

Formation of mixed self-assembled monolayers (SAMs) of DNA-probe/MCH (1 µM) was carried out *in-situ* on the gold sensor chip by flowing 250 µL of the mix in PBS 50 mM (pH 7) at 12 µL/min rate. Different DNA-probe/MCH molar ratios (1:0, 10:1 and 20:1) were employed depending on the experiment carried out.

DNA-probe/SH-PEGs mixed monolayers at different molar ratios (0:1 and 1:1) (2 µM) in PBS 50 mM (pH 7) were *in-situ* immobilized on the gold sensor chip at 12 µL/min rate.

To test the PDITC crosslinker approach, SH-PEG-NH_2 (2 µM) and SH-PEG-CO_2H (2 µM) in PBS 50 mM (pH 7) were incubated *ex-situ* for 3 h at room temperature (RT). Chips were rinsed with MilliQ water and dried gently with N_2 stream. Then, they were either placed directly in the SPR biosensor or incubated for 2 h in a DMF/Pyridine/EtN_3 for PDITC-crosslinker activation. Activated monolayers were placed in the SPR biosensor. 1 µM of SH-DNA probes in PBS 50 mM (pH 7) at 12 µL/min constant rate were flowed over the monolayer to test the biofunctionalization performance.

Amine-DNA probes immobilization

Formation of self-assembled monolayers (SAM) of carboxylic/alcohol-ended alkanethiols was carried out by coating the sensor chip overnight at room temperature (RT) with 250 µM of different MHDA/MUOH molar ratios (1:0, 1:5, 1:10 and 1:20) in ethanol. Once the SAM is formed, the chip was rinsed with ethanol and MilliQ water, dried with N_2 stream and mounted on the sensor platform. H_2O-DEPC was selected as running buffer for the immobilization procedure at a constant rate of 12 µL/min. Activation of carboxylic groups was performed by flowing a 0.2M EDC/0.05 M sulfo-NHS solution in MES buffer for 20 min, followed by the NH_2-DNA probe solution in 1x PBS buffer. Finally, 1M ethanolamine solution (pH 8.5) was used to deactivate the unreacted carboxylic groups.

PolyA-DNA probes immobilization

Formation of monolayers of polyA-DNA probes was carried *in-situ* at 1 µM concentration in $CaCl_2$-TE buffer. Different polyAm block lengths were employed, where m is the number of adenine nucleotides employed (m = 7, 15), i.e. PolyA7 and PolyA15. The combination of the probes presenting the two different block lengths at different polyA7/polyA15 molar ratios (1:0, 0:1, 1:1, 1:2 and 2:1) was tested. H_2O-DEPC was selected as running buffer for the immobilization procedure at a constant rate of 12 µL/min, approximately. For polyA-DNA monolayer recycling we employed 250 µL of a 3M HCl solution at 12 µL/min to remove the attached polyA-DNA probes from the gold sensor surface.

2.4.4. BiMW sensor chip and Si_3N_4 surface biofunctionalization

We employed 1x1 cm^2 chips for surface characterization during the optimization of the Si_3N_4 surface biofunctionalization and, eventually, the BiMW chip for validation of the optimized protocol. The BiMW sensors are fabricated at wafer level using standard microelectronic technology in the CSIC Clean Room facilities (Centro Nacional de Microelectronica, CNM-IMB-CSIC, Barcelona (Spain)).

End-facets polishing.

A polishing step is required prior to the BiMW sensor chip optical characterization to achieve an optical quality facet and minimize scattering (insertion) losses during light end-fire coupling. Chips are manually polished employing a lapping machine Logitech CL50. A micrometric positioner is necessary to guarantee a correct positioning of the chip, perfectly vertical, over the rotating platform. Adhesive abrasive papers with decreasing grain size are used, starting from a roughness of 9 µm till 0.3 µm. A water flow is used to wash out particles and debris which could compromise the surface quality. After this step the chip is considered optically flat.

Polymeric flow channels fabrication.

The flow cell is based on Polydimethylsiloxane (PDMS) channels and are fabricated by polymer casting using a methacrylate mold. Elastomer and curing agent are mixed in a ratio 10:1 and air bubbles originating from their mixing are removed by a vacuum degas process. The mixture is then cured for 1 hour at 75°C to ensure cross-linking of the polymer. After this thermal process the channels can be released from the methacrylate mold.

The high hydrophobicity of the resulting PDMS channels is reduced by application of a Polyethylene glycol coating (PEG200, Sigma-Aldrich) after an ozone plasma treatment to expose functional groups on the polymer surface. Finally, PolyTetraFluoroEthylene (PTFE) tubes are inserted at each channel extremities and fixed with PDMS to avoid leakages or air insertion. The final fluidic cell has four independent channels, with a volume of 15 µl. Each fluidic channel addresses a group of four BiMW sensors on the fabricated chips.

Si_3N_4 surface cleaning

In order to remove the protective photoresist added after the Clean Room fabrication process and eventual residues from the polishing process, the Si_3N_4 surfaces undergo an accurate cleaning prior to the optical characterization process. First the chips are sonicated sequentially in acetone, ethanol and water, 2 min each. The cleaning process was finished by sonication of the Si_3N_4 surfaces in a 1:1 Metanol/Hydrochloric acid (MetOH/HCl) solution to remove other inorganic contamination. The chips are rinsed with milli-Q H_2O and dried under a N_2 stream.

APTES silanization

After chip cleaning, a layer of active hydroxyl group was generated on the surface by UV/O3 activation (BioForce Nanosciences, USA) and exposition to 15% nitric acid at 75ºC for 25 min, revealing the oxide groups on the silicon surface. Clean and hydroxyl-activated chips were immediately transferred in a 1% v/v APTES solution prepared in water-free toluene under an argon atmosphere for 1 hour. 0.3 % v/v of *N*,*N*-Diisopropylethylamine (DIPEA) was employed to catalyze the hydrolysis reaction in the absence of water molecules. Finally, a curing step was performed at 110ºC for 1 hour.

Sulfo-GMBS-modified surfaces. APTES-modified Si_3N_4 surfaces were incubated with 2 mM of Sulfo-GMBS crosslinker in 1x PBS for 2 hours. After that time, crosslinker-modified surfaces were rinsed carefully with Milli-Q water to remove non-convalently bond molecules and dried with N_2 flux. Then, chips were incubated for 1 hour with a solution of 1 µM SH-DNA probes for the binding between the thiol-group with the maleimide end of the Sulfo-GMBS. Prior to the surface DNA funtionalization, SH-DNA probes were incubated with a two-fold molar excess of tris(2-carboxyethyl)phosphine (TCEP). Functionalized chips were cleaned thoroughly with milliQ water and dried under N_2 flux and kept at 4ºC until use.

In order to improve the efficiency of the crosslinking, fluorescent SH-DNA probes were incubated with Sulfo-GMBS crosslinker before anchorage to the silane layer. The probes previously treated with TCEP were incubated with increasing concentrations of Sulfo-GMBS crosslinker (5, 10 and 20 µM). An excess of 5'-Cy3, SH-DNA probe (20 µM) was employed to guarantee that most of the crosslinker reacted with the thiolated probes and little quantity of crosslinker remained free for possible competition during the linkage to the amine group of the silanized surface.

PDITC-modified surfaces. APTES-modified surfaces were reacted with 20 mM PDITC in a solution of 10% anhydrous pyridine in N,N-dimethylformamide (DMF) for 1 hour in darkness. Activated surfaces where incubated with 1 µM of SH-DNA probe in 0.1M Na_2CO_3 buffer at pH 9.5 for 1 hour. The reaction was amine catalyzed by addition of 1 eq of triethylamine (NEt_3) to accelerate the reaction. After the incubation time, surfaces were carefully rinsed with water and dried under gentle nitrogen flux.

Surface recycling. Si_3N_4 surface recycling was performed with an O_2 plasma generator (Diener electronic GmbH, Germany) at different time intervals (1, 2, 3 and 4 minutes).

2.4.5. Surface characterization

Contact angle

The contact angle measurements were performed using an Easy drop standard apparatus (Krüss GmbH, Hamburg –Germany-). Drops of Milli-Q water were placed on the Si_3N_4 surface with a volume of 5 µl. Each result corresponds to the average of 3 different measurements done along the Si_3N_4 surface.

XPS

XPS measurements were carried out with a Phoibos 150 analyzer (SPECS GmbH, Berlin, (Germany)) in ultra-high vacuum conditions (base pressure $1x10^{-10}$ mbar) and a monochromatic Kalpha x-ray source (81486.7 eV at a take-off angle of 0 and 54º). Data generated was analyzed by CasaXPS software.

Fluorescence

Biofunctionalized-Si_3O_4 surfaces were incubated with a solution containing 1 µM of 3'-Cyanine 3 (Cy3) modified DNA sequences complementary to the immobilized probe for 1 hour in 5x SSC buffer (pH 7). Additionally, treated Si_3N_4 chips interrupted at different steps along the biofunctionalization process were also incubated with the fluorescent target as control samples. Fluorescence was evaluated with a Zeiss Axio Observer Z1m optical microscope. Images of the same experiment were taken with the same parameters of camera exposition for a reliable comparison.

2.4.6. DNA/RNA Hybridization

DNA/RNA target detection was performed by injection of 250µL of the samples into the SPR or BiMW biosensors at a 15 µL/min rate and subsequent hybridization with their complementary DNA probes immobilized on the sensor surface. These samples were dissolved in 5xSSC. For antifouling effect, 5xSSC hybridization buffer was mixed with some additives at different concentrations such as Tween 20, CHAPS or commercial serum. To prevent from RNAse activity during measurements, the microfluidic was cleaned by sequentially flowing SDS 0.5%, HCl 0.1 M, EtOH 100%, 0.5 M NaOH, and sterile H_2O

.

Chapter 3·Quantitative evaluation of alternatively spliced mRNA isoforms by label-free real-time biosensing

Aberrant regulation of the alternative splicing process leads to human diseases, including cancer, emphasizing its importance as a biomarker. Here we propose the use of optical biosensors for the quantification of alternatively spliced mRNA isoforms and the analysis of their expression in cancerous cells. Different methodologies are assessed in the SPR biosensor focusing mainly in their selectivity and the avoidance of cross-hybridization. Their sensitivity and reproducibility are also evaluated. Analysis of HeLa cell samples is attempted to test the feasibility of the methodology. Finally, the BiMW biosensor is employed for the evaluation of alternative splicing events as a first approach towards the implementation of highly sensitive and multiplex detection of circulating mRNA isoforms.

3. Quantitative evaluation of alternatively spliced mRNA isoforms by label-free real-time biosensing

3.1. Introduction

In eukaryotic cells, genes consist of sequences formed by codifying DNA called exons which are alternated with intervening sequences (introns). Once a gene is transcribed into a pre-mRNA by the nuclear RNA polymerase II (RNAPII), these introns are accurately removed by pre-mRNA splicing (**Figura 3.1**). During this process, exons are joined together yielding a mature, functional mRNA ready to be translated in the cytosol. In addition, these primary transcripts contain several alternative exons whose usage can be combined, largely increasing the diversity of the mRNA expressed from the genome, and giving this alternative splicing a central role in the formation of complex organisms. In this way, this process allows for the generation of complex proteomes from a limited number of genes. Alternative splicing patterns constantly change under physiological conditions, equipping cells with a powerful tool to regulate gene expression and allowing the organism to respond to changes in the environment by triggering the most convenient genome expression profile.

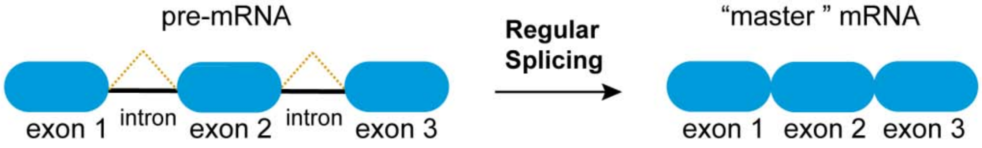

Figure 3. 1 Regular splicing process.

The generation of new alternative exons could be a driving force in evolution, since the amount of alternative splicing increases from invertebrates to vertebrates. Alternative splicing contributes to species-specific differences and correlates with the organizational complexity of a given organism. This post-transcriptional process occurs very frequently and it is estimated to take place in 95-100% of multiexon human pre-mRNAs,[161, 162] suggesting that alternative splicing of human genes is the rule and not the exception. Most human genes are alternatively spliced to generate an average of 5-7 isoforms, with examples in which up to tens of thousands of variants can be produced from a single gene.[163, 164] Displays of distinct alternative splicing patterns contribute to differences in gene expression and phenotypes among individuals from the same species. Moreover, distinct splicing patterns are observed in different cellular environment. Such regulation can be tissue specific[165-167] or dictated by developmental[168] or differentiation[6, 169] specific signals. Likewise, some alternative splicing patterns have been shown to be modulated in response to external stimuli.[163]

3.1.1. Mechanism and regulation of alternative splicing

Alternative splicing involves the use of different splice sites within the same mRNA to create protein diversity. Most alternative splicing events can be classified into four basic splicing patterns: alternative 5’ splice-site choice, alternative 3’ splice-site choice, cassette-exon inclusion or skipping, and intron retention (**Figure 3.2**). Splicing is a complex two-step *trans*-esterification reaction[170] that is arranged in a step-wise manner by the spliceosome, a macromolecular ribonucleoprotein complex that assembles on the pre-mRNA,[171-173] while the pre-mRNA is synthesized by RNA polymerase II in the nucleus.

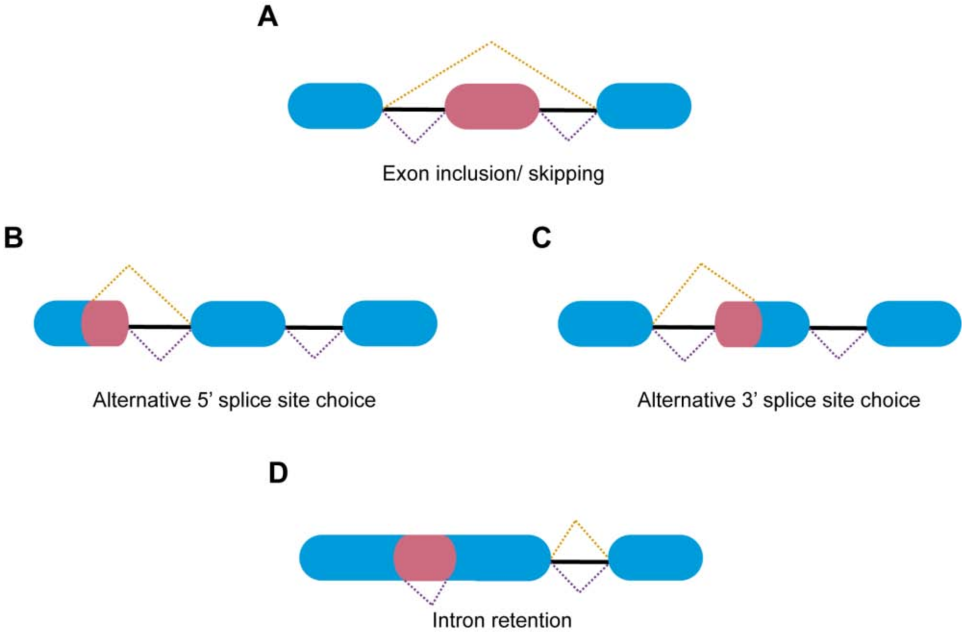
A
Exon inclusion/ skipping
B
Alternative 5’ splice site choice
C
Alternative 3’ splice site choice
D
Intron retention

Figure 3. 2 Types of alternative splicing: (**A**) Cassette-exon inclusion or skipping. (**B**) Alternative 3′ splice-site selection. (**C**) Alternative 5′ splice-site selection and (**D**) Intron retention.

Exons are defined by three major sequence elements: the 5’ splice site, the 3’ splice site and the branch point.[173] Alternatively spliced exons have these sequences degenerated, which implies a lowered affinity to the spliceosome, resulting in reduced recognition and rendering the sequences sensitive to a combinatorial regulation that will produce different alternative splicing arrangements. Additional sequence elements located in the exon or in adjacent intronic elements aid their recognition by binding to regulatory proteins. Hence, the regulation of alternative splicing involves both *cis*-sequences (known as exonic and intronic splicing silencers or enhancers –ISS, ISE, ESS, and ESE) and *trans*-components, which are composed of sequences in the pre-mRNA and cellular factors (RNA or protein) respectively. The most studied splicing regulators so far are members of the serine/arginine-rich (SR) protein and heterogeneous nuclear ribonucleoprotein (hnRnp) families. SR proteins are RNA-binding proteins that generally enhance splicing by binding to the sequences corresponding to exons and recruiting components of the spliceosome. By contrast, hnRnPs repress splicing by binding to sequences corresponding to exons or introns and the ability of interfering with the core splicing machinery to engage splicing sites. In general, these proteins bind weakly to RNA and work in concert with an ever-increasing number of additional auxiliary regulators. They respond to a ‘yin-yang’ model[163] in which the decisions to activate or repress the alternative splicing of a concrete exon resides on the number of positively acting sites (splicing enhancers that are bound by SR proteins) and negatively acting sites (splicing silencers bound by hnRNPs), defined by the "splicing code". This code is highly contextual in nature, varying among different tissues and distinct homeostatic environments, and is difficult to characterize. Furthermore, the splicing machinery is typically recruited to pre-mRNA (recruitment model) in a co-transcriptional manner (called "functional coupling") suggesting an epigenetic control for alternative splicing regulation.[172] It appears that epigenetic regulation is not limited to controlling what regions of the genome are expressed, but also to how they are spliced. Epigenetic modifications correlate with alternative splicing and influence the process mechanistically. Histone modifications[174-176] and DNA methylation patterns[177] contribute to chromatin structure and mRNA transcription, influencing the transcription rate and generating different patterns of alternative splicing in a so called kinetic model. There is also an emerging evidence of a role of non-coding RNA in exon selection such us micro-RNAs,[178-180] long non-coding RNAs[181] and snoRNAs.[182]

3.1.2. Alternative Splicing as a biomarker

The overall function of alternative splicing is to increase the diversity of the mRNA expressed from the genome. Alternative splicing modulates transcript expression by inserting or deleting sections as well as possibly altering the reading frame and subsequently the protein amino acid sequence. About a third of alternative splicing events result in splice variants containing premature termination codon, either leading to non-sense-mediated decay of the RNA product[183] or resulting in short polypeptide products.[184] The magnitude of alternative splicing regulation ranges from subtle modifications of protein functions to making binary on/off switches, as observed in apoptosis. Given the widespread functions of alternative splicing, it is not surprising that aberrant regulation of alternative splicing leads to human diseases. Alterations in alternative splicing decisions can trigger the onset or influence the progression of multiple pathologies, including cancer,[185-187] underscoring the fundamental importance of this regulatory process. Cancer cells can remodel their proteome producing those proteins that best fuel growth and spreading of tumors by inducing alternative splicing changes, e.g. in genes that are involved in metabolism, apoptosis, cell cycle control, invasion, metastasis, or angiogenesis.[188] Therefore, deregulated alternative splicing patterns could be considered as a hallmark of cancer and the identification of alternatively spliced variants as biomarkers could cast light on cancer development.[9] Moreover, modulation of splicing isoforms can be considered as a potential therapeutic approach. Consequently, monitoring of alternative splicing can offer cues for cancer diagnosis and medical care by developing approaches aimed at detecting and eventually reverting and following up the deregulated patterns of alternative splicing.[14]

Current methodologies, such as exon microarrays or RNA-Seq, can be used to analyse differences at the exon and/or at transcript variant level, enabling the identification of splicing differences between various types of cancer samples. This isoform-level profiling is yielding more precise cancer signatures than gene-level expression profiles.[189] However, microarray-based or RNA-Seq methods are time consuming, expensive and complex for clinical purposes. So far, methods based on quantitative reverse-transcriptase PCR (RT-qPCR) using exon-specific or splice-junction specific primers[190] remain the most suitable approaches. Nevertheless, despite their widespread use, RT-qPCR-based methods are far from fulfilling the needs of routine clinical analysis because of the requirement for amplification steps and the use of expensive reagents. Moreover, they often exhibit complications in discerning between closely related isoforms (i.e. isoforms sharing exons or resulting from insertions of a few nucleotides) due to cross-hybridization. Alternative splicing isoforms are intrinsically prone to cross-hybridization (i.e. a not intended binding between a probe and an off-target transcript) which constitutes one of the main sources of systematic error in the study of alternative splicing. The correction of probe-level noise due to cross-hybridization is an indispensable requisite for alternative splicing monitoring.[191] Therefore, the avoidance of cross-hybridization significantly increases the reliability of experimental data.

Regarding the analysis of alternative splicing in routine clinical practice, it is necessary to develop a robust methodology to accurately evaluate the expression of the isoforms with minimal operator training and in an easy-to-perform procedure. Currently, single mRNA spliced variants from *BRCA1* gene have been identified and quantified in living cells using a biosensor approach.[192] However, one major drawback of this approach is the requirement of complex and highly specialized optical set-ups and processes that hamper its routine use for diagnosis.

Our research aims at the development of a general and direct methodology for monitoring alternative splicing events in real-time and in a label-free scheme using minimally processed samples. We will focus on the analysis of the well-studied *Fas* gen splicing variants by the SPR biosensor. The methodology will be evaluated in terms of selectivity and sensitivity, paying special attention to the prevention of undesired cross-hybridization signals. Also, its reproducibility and robustness will be evaluated. To study the versatility of the methodology we will assess the analysis of the splicing variants generated from *BCL-X* gene alternative splicing. The methodology will be validated with the analysis of different HeLa cell samples. Finally, the transference of the developed methodology to the BiMW biosensor will be addressed in order to demonstrate its capability for achieving much better limit of detections.

3.2. *Fas* gene alternative splicing and strategy design

The well-characterized alternative splicing of *Fas* gene has been chosen as a model system for the methodology development. Alternative splicing of *Fas* exon 6 generates two isoforms corresponding to the inclusion (*567* isoform) or skipping (*57* isoform) of this exon (**Figure 3.3**). The pro-apoptotic *567* isoform encodes for a full-length transmembrane protein receptor known as APO-1 (or CD95) that binds to Fas ligand (FasL), therefore activating the characteristic signaling cascade of the extrinsic apoptotic pathway.[193] Exon 6 skipping generates an anti-apoptotic isoform that lacks the trans-membrane domain, producing a soluble protein known as sFas that acts as a decoy in the extra-cellular environment by binding to FasL. This version of *Fas*, which is overexpressed in cancer cells,[194, 195] contributes to cancer aggressiveness[196, 197] and its detection has been proposed as a potential biomarker for the early diagnosis of cancer.[198]

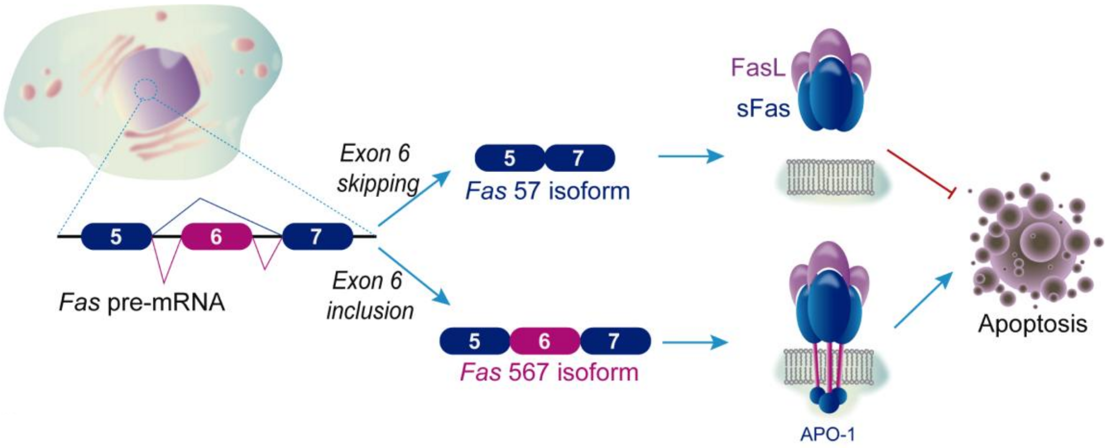

Figure 3. 3 Schematic representation of the different RNA and protein isoforms generated by alternative splicing of *Fas* gene/*CD95*.

However, detection of splicing isoforms entails several difficulties due mainly to the similarities in their sequences as isoforms share many exonic sequences. Particularly, *Fas* gene isoforms have in common all their exonic sequences except for the one defining exon 6. Cross-hybridization signals of the non-complementary isoforms are very likely to occur during their analysis. Thus, the development of a suitable biosensor for the detection of splicing variants requires an exhaustive adjustment of the detection conditions to avoid or to correct these cross-hybridizations as well as the optimization of the biofunctionalization procedures that ensure high analytical sensitivity and selectivity. For this reason, we have proposed several strategies for the detection of splicing variants. We carefully optimized each biofunctionalization and detection conditions using ~140-200 nucleotide-length DNA versions of both isoforms, i.e. *Fas567* and *Fas57*, containing the exons of interest (exons 5, 6 and 7 in one case, exons 5 and 7 in the other) (see **Table 3.1**).

3.2.1. Strategy 1: Two-step selective recognition of alternative splicing isoforms

This strategy focused on the correction of the off-target cross-hybridization by employing a two-step based detection. In a first step, both isoforms were simultaneously captured with the same biosensor surface composed by two different SH-DNA probes matching the splicing junction of the two isoforms (**Table 3.7**). Splice-junctions (i.e. complementary to exon sequences flanking the splice junction) represent a unique sequence feature of each transcript. These DNA probes permit the capture of both isoforms more effectively, reducing the probability of competition between the isoforms during hybridization. Once the isoforms were hybridized, *Fas567* isoform was identified in a second recognition step through a complementary sequence (T-*Exon6*) matching with a concrete region of exon 6 (**Figure 3.4**). Since exon 6 is the only different sequence between the isoforms, present only in *Fas567* isoform, this second capture allowed us to quantify the *Fas567* isoform concentration hybridized in the first step. Determination of the *Fas57* isoform concentration could be done by simple mathematical calculation.

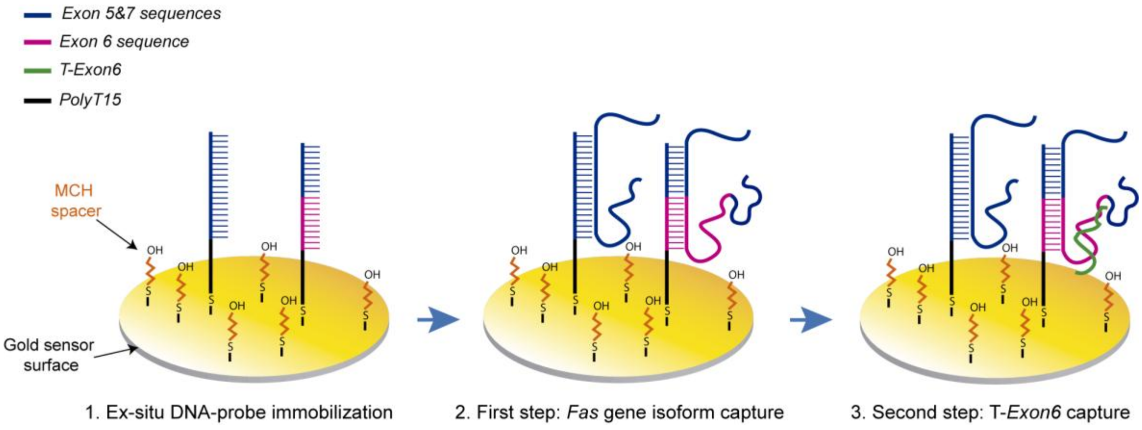
Exon 5&7 sequences
Exon 6 sequence
T-Exon6
PolyT15
MCH spacer
Gold sensor surface
OH
S
1. Ex-situ DNA-probe immobilization
2. First step: Fas gene isoform capture
3. Second step: T-Exon6 capture

Figure 3. 4 Strategy 1 design.

For the optimization of the strategy, we focused on: (i) obtaining the largest signal for both isoforms in the first hybridization step and (ii) assuring a maximal signal for the T-*Exon6 probe* in the second capture step. Different molar ratios of the thiol-modified DNA probes (*Fas*57/*Fas*567) at a 1 µM concentration were generated by *ex-situ* immobilization in PBS (1:1, 1:2 and 2:1). Each proportion was analyzed by serial injections of 50 nM of both targets in 5xSSC hybridization buffer.[39, 64] Second-step recognition was performed by injection of 1 µM of T-*Exon6* probe in the same hybridization conditions.

Hybridization signals of both isoforms (*Fas567* and *Fas57*) for the different DNA probe molar ratios are shown in **Figure 3.5A**. As can be seen, the 1:1 ratio was the one rendering the largest target signals. With regard to the recognition of the *Fas567* isoform in the second step detection, we evaluated T-*Exon6* capture by the hybridized *Fas567* isoform (50 nM). Among the three molar ratios tested, only 1:1 ratio showed a specific signal from T-*Exon6*, while the others (1:2 and 2:1) presented signals close to the background levels. However, the signal obtained for *Fas567* 50 nM at a 1:1 ratio was very poor (ΔR(%)= 0.12), suggesting that some steric hindrance effect was preventing to T-*Exon6* reaching its target sequence (**Fig. 3.5B**).

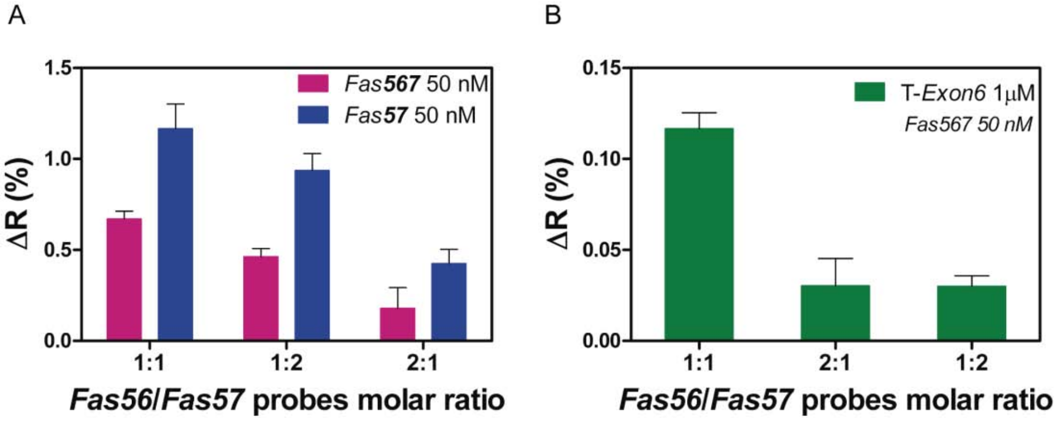

Figure 3. 5 Strategy 1 optimization: (**A**) *Fas57* and *Fas567* isoforms signals. (**B**) T-*Exon6* signal.

For further improvement of the T-*Exon6* probe capture efficiency, DNA probes at 1:1 (1µM) molar ratio were also mixed with a lateral spacer (mercaptohexanol, MCH) to improve the accessibility and minimize steric hindrance. We tested different MCH concentration (50, 100, 150 and 200 nM) and evaluated the spacing effect in the detection of both *Fas* isoforms at a target concentration of 50 nM. Subsequently, we carried out the recognition of *Fas567* isoform with the second step for all the conditions. As can be seen in **Figure 3.6A**, MCH concentrations above 50 nM exhibited an enhancing effect in isoform detection, improving target recognition. This effect was particularly beneficial when the MCH concentration was 100 nM, greatly increasing detection of both isoforms and equalizing their signals, an important feature in the simultaneous detection of both isoforms. Furthermore, LODs independently obtained at this ratio for both isoforms were **458** and **514 pM** for *Fas567* and *Fas57* isoforms, respectively (**Figure 3.6B**). The achieved LODs are within the appropriate range for ~200 nt-length nucleic acids according to literature.[60]

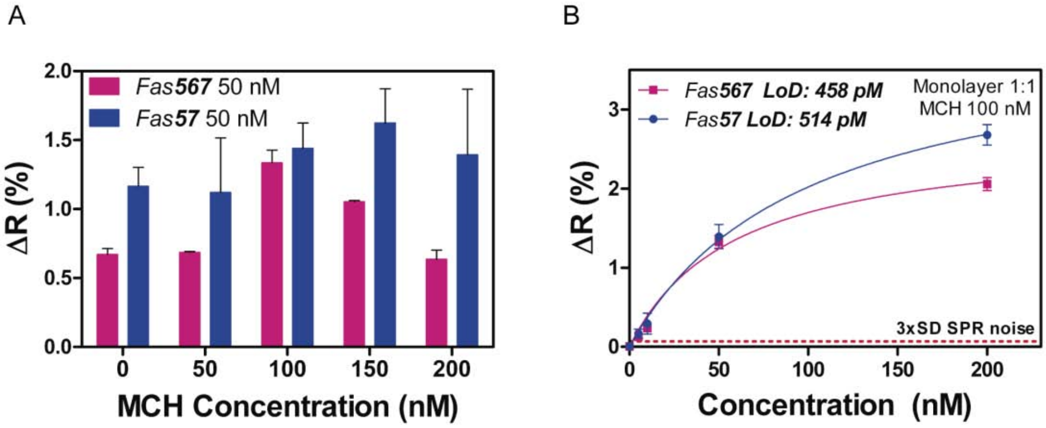

Figure 3. 6 (**A**) MCH spacing effect in the 1:1 monolayer. (**B**) Calibration curves for independently analyzed isoforms.

The effect of the incorporation of 100 nM of MCH was also reflected in the second-step detection, where the detection efficiency of the T-*Exon6* probe was improved by 200 % (**Figure 3.7A**). **Figure 3.7B** represents a real-time sensogram of the selective recognition of T-*Exon6* at a concentration of 100 nM of MCH in the 1:1 monolayer. A variation in the reflectivity of 0.33% in the second step signal corresponded to a concentration of 50 nM of the *Fas567* isoform in the first step. However, despite such an improvement, these values were not large enough to assure a significant detection for real diagnosis if for example the target concentrations are below 50 nM.

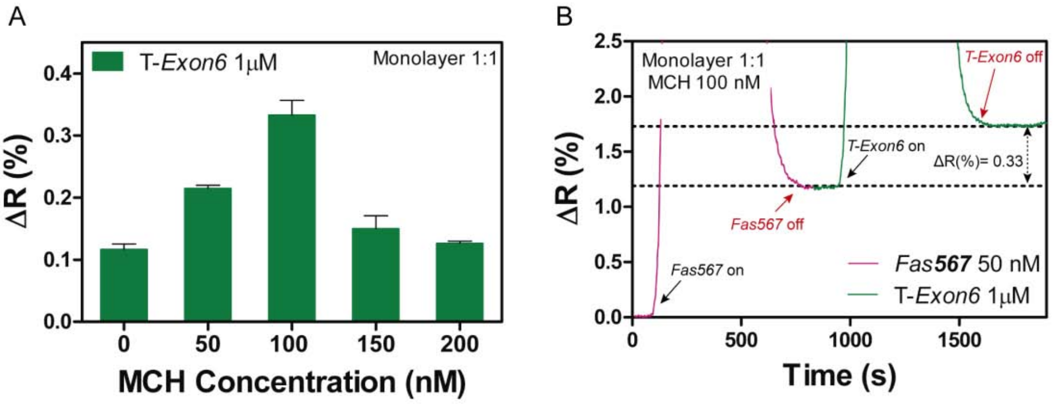

Figure 3. 7 (**A**) T-*Exon6* capture at different concentrations of MCH. (**B**) Sensogram of the *Fas567* isoform and subsequent capture of the T-*Exon6* probe.

In conclusion, although we were able to specifically identify both isoforms by the second-step capture of exon 6 and avoided possible signal bias produced by cross-hybridization, the strong steric hindrance presented during this second capture led to very low sensor responses for all configurations, making it difficult to overcome by using lateral spacers. Furthermore, the use of a single monolayer for simultaneously capturing both isoforms may complicate the isoform hybridization due to DNA probe competition and steric hindrance forces in a RNA pool where both isoforms will be present.

3.2.2. Strategy 2: One-step selective detection of alternative splicing isoforms

We next proposed an *in-situ* strategy aimed at independently detecting the isoforms. For this strategy we took advantage of the 2 parallel sensing areas of the SPR biosensor that can be used individually. *In-situ* immobilization involves shorter times for the generation of SAMs which can compromise the reproducibility of the assay. However, this approach can produce SAMs of different DNA probes separately for the independent detection of the alternative splicing variants in the same sample in a one-step assay. Concretely, this strategy involved the immobilization of a specific SH-DNA probe for *Exon6*, for specific hybridization of *Fas567* isoform in one channel (**Table 3.7**). The other channel was biofunctionalized with the *Fas57* probe used in *strategy 1*, for the quantification of this isoform (**Figure 3.8**). Although this DNA probe could bind to any of the isoforms, we determined the quantity of the *Fas57* isoform once quantified the *Fas567* isoform with the *FasExon6* probe.

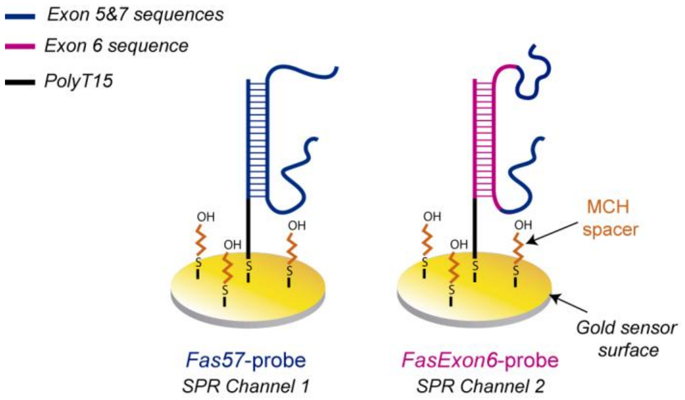

Figure 3. 8 Design of Strategy 2.

In order to optimize the efficiency of isoform capture, we compared the performance of using mixed solutions of the thiol-modified DNA probes and MCH. We chose three different DNA-probe/MCH ratios (1:0, 20:1 and 10:1), and biofunctionalized the sensor surface *in-situ*. Each condition was analyzed by serial injections of 50 nM of the two isoforms separately.

As shown in **Figure 3.9A** and **B**, both receptors achieved their highest response at a ratio of 20:1. *Fas57* receptor showed a 44% of cross-hybridization from the off-target sequence, as expected. On the other hand, *FasExon6* receptor exhibited a cross-hybridization close to background levels, making possible the specific quantification of *Fas567* isoform and the subsequent calculation of *Fas57* levels through the signal quantified with *Fas57* probe.

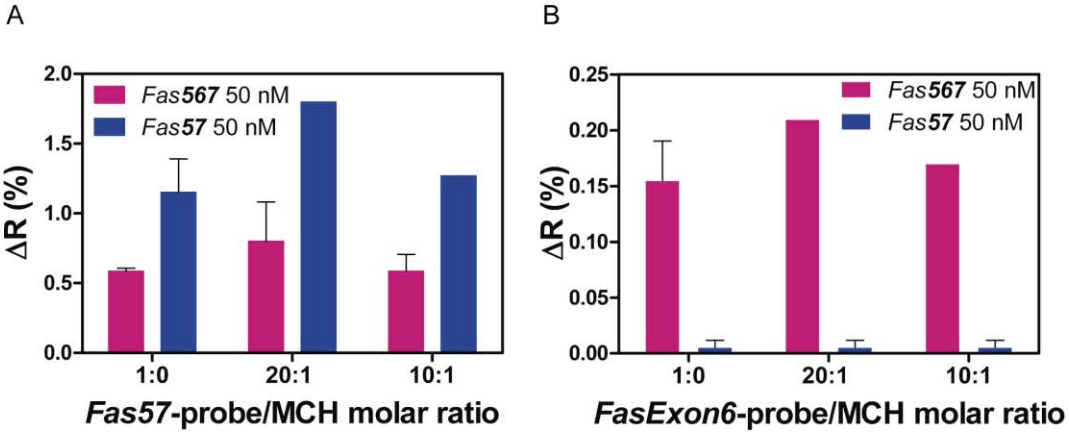

Figure 3. 9 (**A**) *Fas57*-probe/MCH ratio study. (**B**) *FasExon6*-probe/MCH ratio study.

However, proper values for the *Fas567* isoform were not obtained at any of the tested configurations. To improve the *Fas567* isoform detection, several concentrations of formamide (FA), ranging from 10% to 35%, were added to the hybridization buffer. Solutions containing an adequate percentage of FA reduce the presence of secondary structures and increases specificity by lowering the melting temperature of oligonucleotides.[127] As can be observed in **Figure 3.10,** the addition of 20% FA to the hybridization buffer helped to increase the *Fas567* isoform signal by 120%. However, in spite of this achievement, such signal intensity was still very poor, yielding a very low sensitivity level. Consequently, we could not consider this strategy as a suitable tool for quantification of *Fas* gene isoforms in clinical analyses.

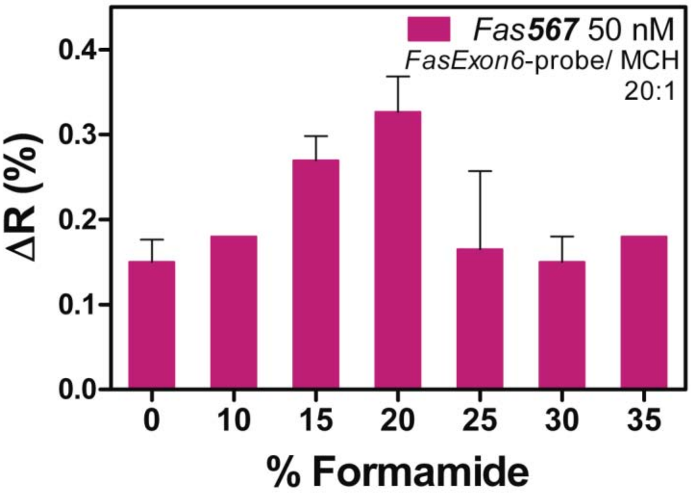

Figure 3. 10 Formamide effect on the *Fas567* isoform hybridization with *FasExon6* probe.

The difficulties found in strategy 1 for the second-step detection of *Fas567* by T-*Exon6* target, together with the difficulties found with the *in-situ* strategy for the direct capture of this isoform through pairing with *FasExon6* receptor, strongly suggested that steric factors in the exon 6 region were taking place. In addition, the improvement obtained with the addition of formamide confirmed that secondary structures could possibly hinder the efficient hybridization of the isoform. Therefore, this strategy was considered unsuitable for alternative splicing detection and a different strategy based on *in-situ* biofunctionalization was explored.

3.2.3. Strategy 3: Direct and specific quantification of alternative splicing isoforms

The new strategy was designed employing the same DNA probes as in strategy 1 to capture the splice-junctions of the two isoforms. However, they were *in-situ* immobilized separately in the two sensor channels for independent detection of the isoforms. Since both isoforms could bind both receptors but with different affinities due to the similarity of their sequences, the optimization was focused on the minimization of cross-hybridization signals from the off-targets in order to obtain a direct and specific signal from both *Fas* gene isoforms (**Figure 3.11**).

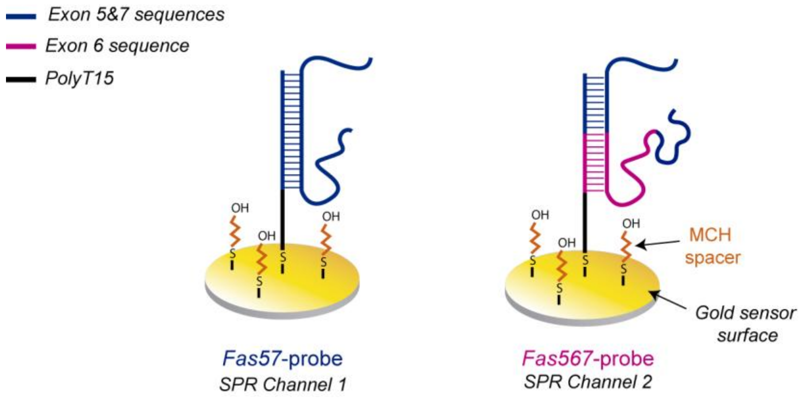

Figure 3. 11 SPR Strategy 3 for the quantitative evaluation of *Fas* gene alternatively spliced mRNA isoforms.

Mixed solutions of the DNA probes and MCH were compared and three different DNA-probe/MCH ratios were chosen (1:0, 20:1 and 10:1). Each condition was analyzed by serial injections of 50 nM of specific target in 5x SSC hybridization buffer.[64] As shown in **Figure 3.12A** and **B**, the 20:1 ratio remarkably improved the accessibility of the targets to their probes, increasing capture efficiency by 70% for *Fas567* and 50% for *Fas57*, respectively. However, a notably high cross-hybridization was produced by the non-specific isoforms, showing percentages of cross-hybridization from the off-target transcripts of 169% for *Fas567* probe and 47% for *Fas57* probe, respectively. The evident preference of *Fas567* probe for *Fas57* isoform over *Fas567* isoform at all of the ratios tested made indispensable the avoidance of such cross-hybridization in order to achieve a specific recognition.

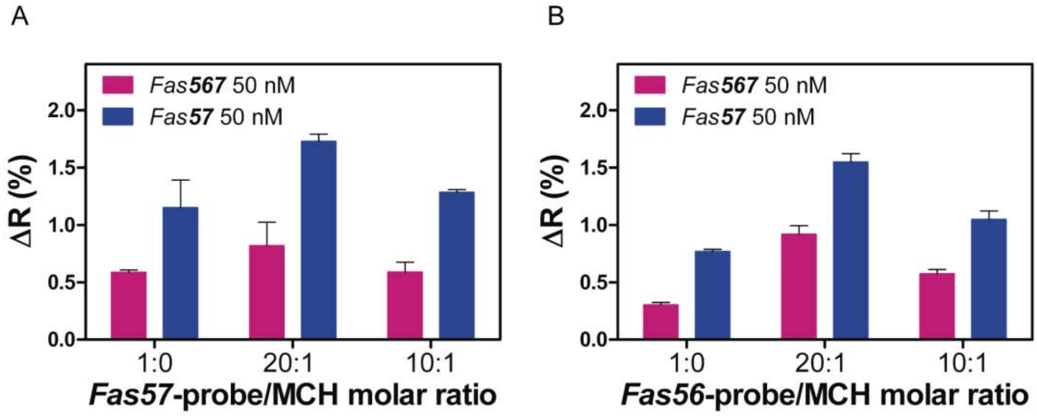

Figure 3. 12 Detection signals obtained by employing different concentration of MCH in the immobilization of *Fas57* (**A**) and *Fas56* (**B**) probes, respectively.

Taking advantage of the capacity of FA for destabilizing nucleic acid duplexes and increasing hybridization stringency[127] we studied its effect in the off-target-receptor interaction at different concentrations (from 25% to 65%). The addition of FA had a drastic effect on specificity, leveraging the sensitivity of the specific targets compared to the alternative ones in more than 75% (**Figure 3.13A** and **B**). It was particularly evident with the *Fas56* probe, which presented an extensive cross-hybridization of *Fas57* isoform in the absence of FA. Furthermore, there was an increment in the target signal, corroborating the enhancing effect of this compound for the attachment of oligonucleotides to their specific receptors in saline solutions.[127]

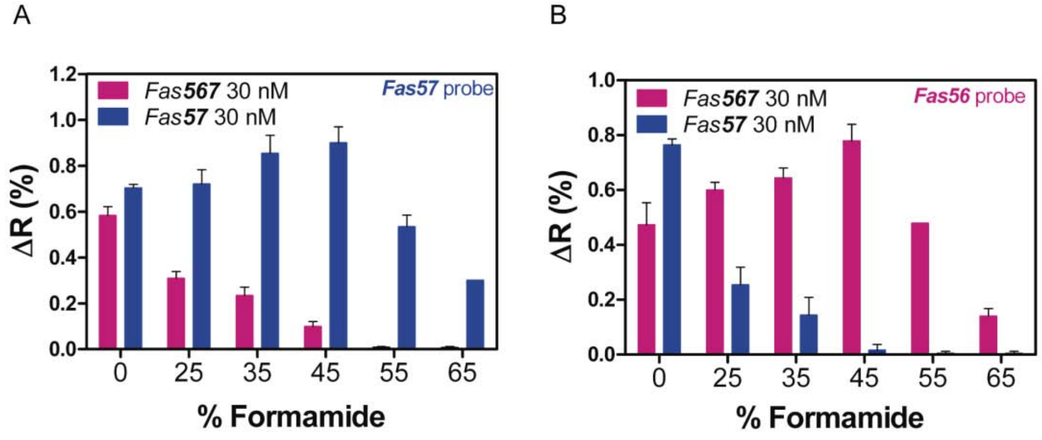

Figure 3. 13 Formamide effect in the cross-hybridization response of *Fas57* (**A**) and *Fas56* (**B**) probes.

To further improve the specific detection, we carried out a slight adjustment in the saline concentration of the hybridization buffer. We decreased to 3x and 4x the saline concentration of the hybridization buffer while maintaining a 45% FA and compared the signals from both isoforms. Reduction of the cross-hybridization to background levels was achieved at a 3x concentration of the hybridization buffer (**Figure 3.14A** and **B**). Changes in the ionic strength of the hybridization buffer led to an increase in stringency, decreasing the likelihood of hybridization and thus favoring binding of the fully complementary isoforms over non-fully complementary ones.[199, 200]

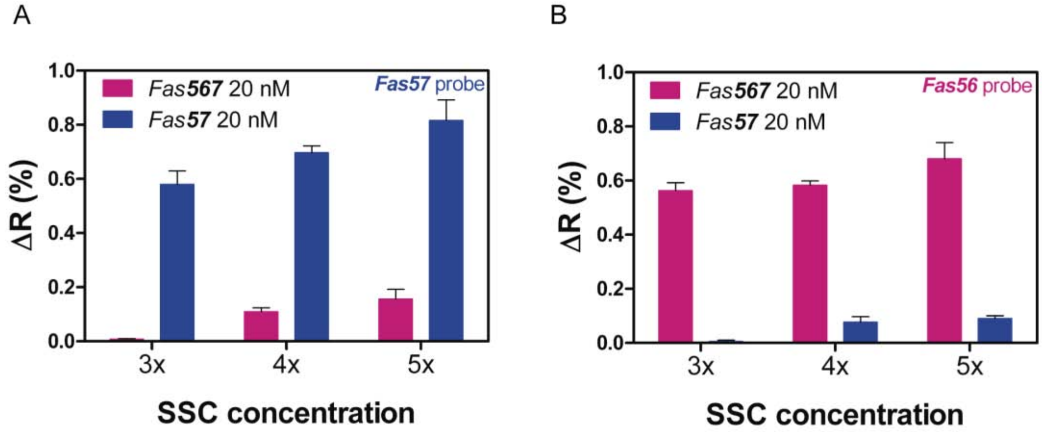

Figure 3. 14 Effect of the change in the ionic strength of the hybridization buffer on isoform specificity for (**A**) *Fas57* probe and (**B**) *Fas56* probe.

After applying the optimized conditions, we were able to accurately discriminate between the different splicing isoforms while retaining high sensitivity. We achieved sensitivity levels at the pM-nM range as depicted in the calibration curves (**Figure 3.15**). Cross-hybridization was negligible even at the highest concentration evaluated of non-cognate transcripts (50 nM). We obtained LODs of **387 pM** (R^2 = 0.99) for isoform *Fas57* and **438 pM** (R^2 = 0.99) for *Fas567* and limits of quantification (LOQ), of 1.3 nM and 1.5 nM, respectively. A control DNA sequence was also evaluated at a concentration of 50 nM which produced a zero shift of the reflectivity, clearly showing the sensitivity of the DNA probes for their specific target sequences.

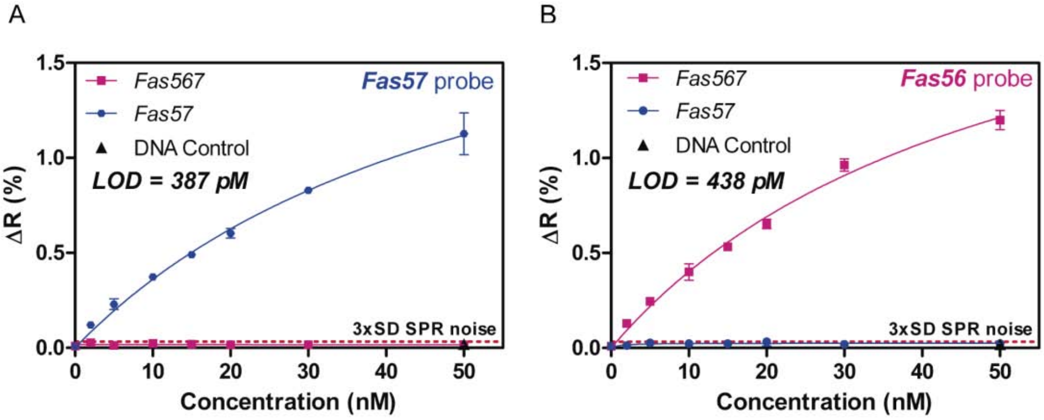

Figure 3. 15 SPR calibration plots for *Fas57* (**A**) (R^2= 0.99) and *Fas56* (**B**) (R^2=0.99) probes using the optimized hybridization and detection conditions. Solid lines (blue and pink) correspond to the non-linear fit of the calibration curves. Red dashed line corresponds to 3xSD SPR noise, which is the limit for the minimum signal detectable. All data show mean ± SD of triplicate measurements.

The direct quantification of *Fas* gene alternative spliced isoforms together with the good levels of specificity and negligible cross-hybridization, showed the strong capability of this strategy for discerning and determining alternative splicing isoform levels. This quantification would permit to obtain the isoform expression ratio, which can be employed as a diagnostic tool to establish the onset and/or stage of a certain cancer. Thus, the optimized methodology was chosen for further assessment in order to demonstrate its advantages against the conventional methodologies currently used for alternative spliced isoform ratios determination.

Repeatability and reproducibility

To demonstrate the robustness of the biosensor methodology, we assessed its repeatability and reproducibility, key parameters in the development of a reliable tool for analytical purposes. We determined the Coefficient of Variability (CV) of the signal for different target concentrations both within the same sensor chip (intra-assay) and among different biofunctionalization processes (inter-assay). In addition, we studied the variability between two different operators. **Table 3.1** shows the CVs calculated for four concentrations (2, 5, 10 and 30 nM) of the isoforms located in the linear range of the calibration curves. The intra-assays showed a signal variation well-below the maximum variability recommended for analytical methods (~15%),[131] with CVs between 2-11 %. Target detection maintained a stable response through at least 80 regeneration cycles with no notable signal loss compared to initial values (3% CV). Furthermore, the reproducibility was markedly accurate even when measurements were carried out by different operators, obtaining CVs between 5-9 % and LODs with a variability of 1-11%

in the inter-assay analysis. This statistical analysis proves the robustness of the methodology and its potential use in environments such as clinical settings, where simple, highly accurate and reproducible approaches are the main requirements. In addition, the consistency of these results is a unique advantage of this methodology, making it possible to analyze a set of samples with the same sensor chip, thereby saving time and resources and minimizing the experimental errors that could arise from different assays.

Table 3. 1 Variability of the SPR sensor response for *Fas* isoforms in intra- and inter-assays performed by different operators. All Pvalues indicated not significant variation between the measurements ($P>0.05$, one-way ANOVA test).

Concentration (nM)	**ΔR(%)**							
	Intra-assay 1[a]		***Intra-assay 2***[a]		***Intra-assay 3***[b]		***Inter-assay***[ab]	
***Fas567* isoform**	**Mean±SD**[1]	**CV(%)**	**Mean±SD**[1]	**CV(%)**	**Mean±SD**[1]	**CV(%)**	**Mean±SD**[2]	**CV(%)**
2	0.13±0.01	8	0.13±0.01	9	0.14±0.01	4	0.13±0.01	9
5	0.24±0.01	4	0.20±0.01	6	0.25±0.01	2	0.23±0.02	9
10	0.38±0.02	4	0.35±0.01	3	0.39±0.02	6	0.38±0.02	6
30	0.96±0.03	3	0.98±0.05	5	0.99±0.08	8	0.98±0.05	5
LOD (pM)	438	-	516	-	423	-	459±50	11
***Fas57* isoform**	**Mean±SD**[1]	**CV(%)**	**Mean±SD**[1]	**CV(%)**	**Mean±SD**[1]	**CV(%)**	**Mean±SD**[2]	**CV(%)**
2	0.12±0.01	8	0.12±0.02	13	0.15±0.01	8	0.13±0.02	14
5	0.23±0.02	9	0.19±0.01	5	0.24±0.01	5	0.22±0.03	12
10	0.37±0.01	2	0.33±0.02	5	0.39±0.03	6	0.36±0.03	9
30	0.83±0.02	2	0.86±0.05	6	0.85±0.04	4	0.85±0.04	4
LOD (pM)	387	-	373	-	380	-	380±7	2

[a] Measurements performed by operator 1.
[b] Measurements performed by operator 2.
[1] Mean ± SD of 3 replicates performed in the same biofunctionalized sensor chip.
[2] Mean ± SD of 9 replicates performed in 3 different biofunctionalized sensor chips.

BCL-X alternative splicing detection

The development of a robust methodology that ensures the fidelity of specific splicing isoform detection with a minimized optimization is challenging. Thereby, we tested the versatility of our methodology in the detection of alternatively spliced isoforms from another clinically relevant gene, i.e. the *BCL-X* gene. Deregulation of *BCL-X* gene[201] alternative splicing is involved in cancer development and can have an important impact in therapeutic decisions.[202] This gene has a three-exon structure and two 5'-alternative spliced sites in the first coding exon, generating the *BCL-X*$_L$ and *BCL-X*$_S$ mRNA isoforms.[201] When the upstream 5'-splice site is used, it generates the *BCLX*$_S$ mRNA isoform, leading to a pro-apoptotic transmembrane protein. The use of the downstream 5' splice site leads to production of the anti-apoptotic *BCLX*$_L$ mRNA isoform that encodes a large transmembrane protein (BCL-X$_L$) expressed in the mitochondrial membrane (**Figure 3.16**).

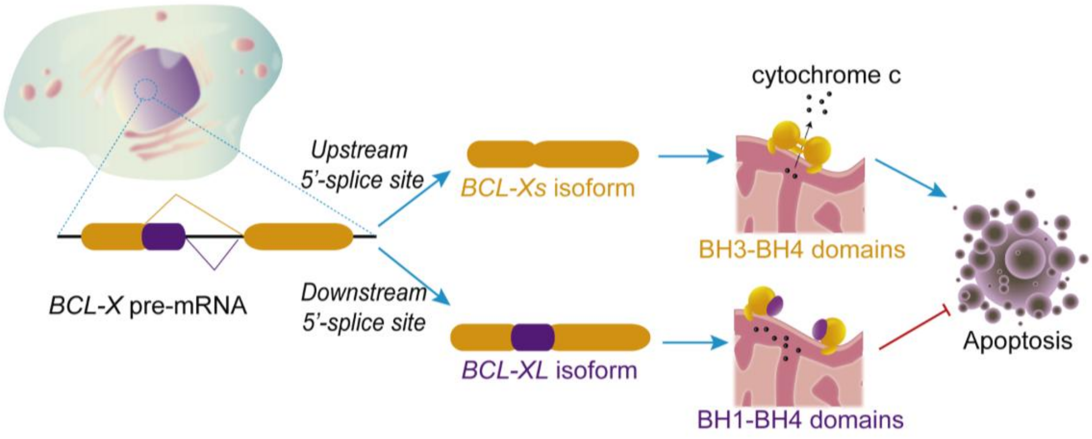

Figure 3. 16 Schematic representation of the different RNA and protein isoforms generated by alternative splicing of *BCL-X gene*.

To analyze the mRNA expression levels of $BCL\text{-}X_L$ and $BCL\text{-}X_S$ isoforms, we followed the same SPR methodological approach using specific DNA probes matching the splice-junctions (**Table 3.7**) and employed the optimized conditions developed for *Fas* gene detection described above.

We obtained similar results to *Fas* gene, achieving the same degree of specificity with near background levels of cross-hybridization (**Figure 3.17**). The LODs were **356 pM** (R^2 = 0.99) for $BCLX_L$ and **155 pM** (R^2 = 0.99) for $BCL\text{-}X_S$, with LOQs of 1.2 nM and 0.5 nM respectively. Variability of the signals was below 15% for all the concentrations evaluated (**Table 3.2**), supporting the robustness of our methodology as an analytical tool for monitoring splicing events.

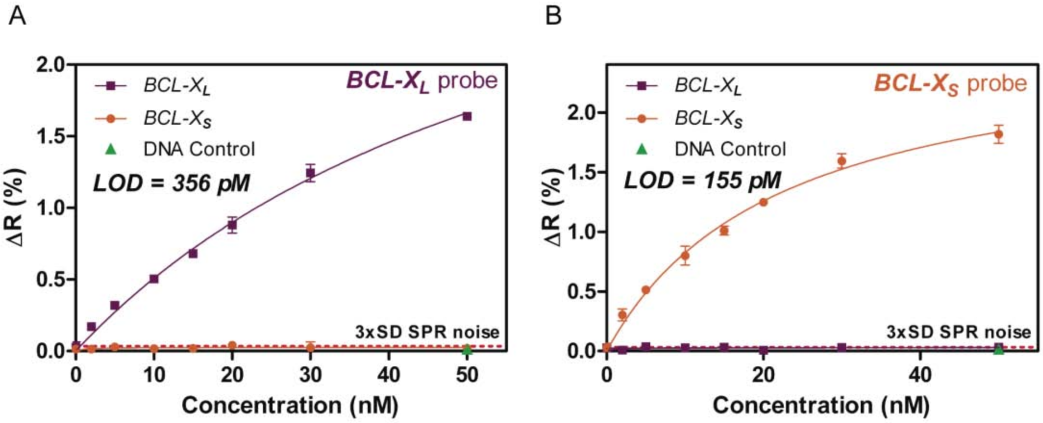

Figure 3. 17 SPR calibration plots for the detection of $BCL\text{-}X_L$ (**A**) (R^2= 0.99) and $BCL\text{-}X_S$ (**B**) (R^2= 0.99) synthetic isoforms based on the previously optimized detection conditions of *Fas* gene isoforms. Solid lines (purple and orange) correspond to the non-linear fit of the calibration curves. Red dashed line corresponds to 3xSD SPR noise, which is the limit for the minimum signal detectable. All data show mean ± SD of triplicate measurements.

Table 3. 2 Variability of the SPR sensor signal for *BCL-X* isoforms intra-assays performed by different operators. The Mean ± SD are from 3 replicates performed in the same biofunctionalized sensor chip. All Pvalues indicated not significant variation between the data ($P>0.05$, one-way ANOVA test).

	ΔR(%)			
	***BCL-X_L* isoform**		***BCL-Xs* isoform**	
Concentration (nM)	**Mean±SD**	**CV(%)**	**Mean±SD**	**CV(%)**
2	0.17±0.01	3	0.27±0.04	14
5	0.32±0.02	6	0.51±0.02	4
10	0.5±0.01	4	0.8±0.08	10
30	1.24±0.06	5	1.51±0.10	6
LOD (pM)	356	-	155	-

Hence, the methodology was easily reproduced with the same efficiency, highlighting its potential as a tool for the monitoring of alternative splicing events of different genes and within different biological and pathological contexts.

3.3. Experimental validation of *Fas* alternative splicing with HeLa cells

To study the feasibility of the methodology in biological samples, we first tested it in ideal conditions. Total RNA from HeLa cells transfected with a minigene expressing *Fas* genomic sequences between exons 5 and 7 (~2000 nucleotide primary trancripts), was purified either alone or co-transfected with a vector expressing the Polypyrimidine-Tract-Binding protein (PTB). PTB induces skipping of *Fas* exon 6 acting through an exonic silencer sequence.[203] While expression of the minigene alone leads to preferential accumulation of exon 6-including transcripts, co-expression of *Fas* 567 minigene with PTB leads to higher accumulation of transcripts that skip exon 6.[204] In this study, mature transcripts from the transfected minigene generated *Fas* isoforms with approximately similar lengths to those employed during the optimization. Thus, the minigene expression in both cell lines was quantified by applying the conditions and calibration curves generated during the optimization process.

Samples were diluted in 3xSSC (45% FA) to a final concentration of 20 ng/µL of purified total RNA. Purified total RNA from bacteria (XLI Blue) was used as a negative control and the response of HeLa cells expressing only endogenous levels of *Fas* transcripts was also evaluated. Shifts in isoform ratios were independently evaluated for each HeLa cell line by RT-PCR using primers corresponding to the flanking constitutive exons after fractionation by polyacrylamide gel electrophoresis or by RT-qPCR using isoform-specific primers.

As can be observed in both sensograms (**Figure 3.18A** and **B**), mRNAs generated by the expression of the transfected minigenes were clearly detected by the SPR biosensor. Bacteria RNA control samples showed zero ΔR (%) while samples from minigene-tranfected HeLa-cells presented a ΔR (%) higher than zero for both isoforms, indicating specific detection of the *Fas* isoforms. Isoforms from HeLa cells expressing only endogenous levels of *Fas* transcripts were not detected under these conditions. Expression of the 567 minigene led to higher detection levels of *Fas567* isoform compared to *Fas57* isoform, while co-expression of the 567 minigene and PTB expression vector led to higher detection of the *Fas57* isoform compared to the *Fas567* isoform, as previously reported[203] and independently validated in these experiments (**Figure 3.19**).

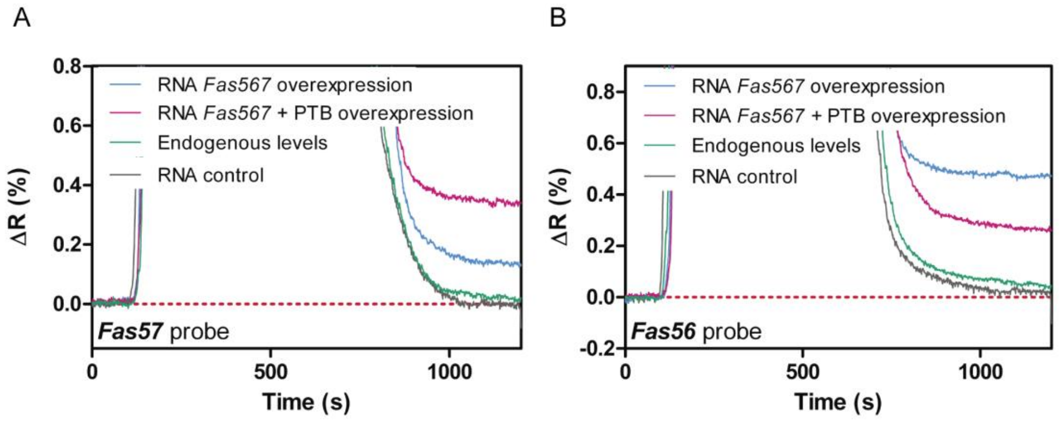

Figure 3. 18 SPR sensograms of the detection of 20 ng/ µL of total HeLa cell RNA for the minigene-expression in both *Fas567* probe (**A**) and *Fas57* probe (**B**).

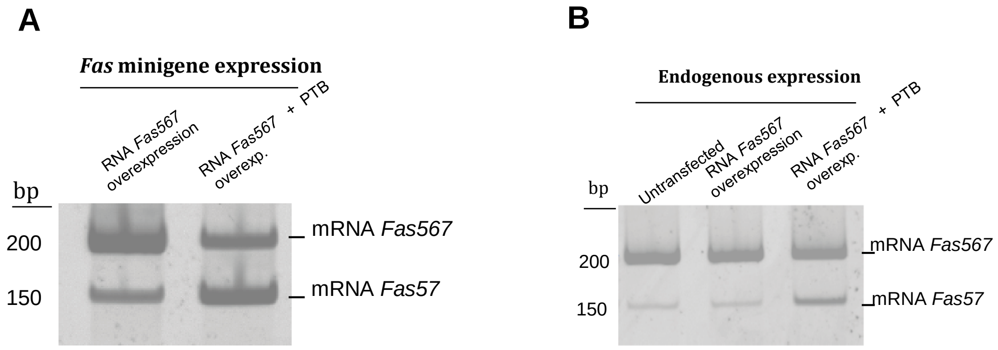
A
Fas minigene expression
RNA Fas567 overexpression
RNA Fas567 overexp. + PTB
bp
200
150
mRNA Fas567
mRNA Fas57
B
Endogenous expression
Untransfected
RNA Fas567 overexpression
RNA Fas567 overexp. + PTB
bp
200
150
mRNA Fas567
mRNA Fas57

Figure 3. 19 Acrylamide gel electrophoresis fractionation of RT-PCR products obtained from RNA isolated from HeLa cells transfected with a *Fas* minigene expressing genomic sequences from exons 5 to 7, with or without overexpression of PTB. Vector-specific PCR primers were used for detecting specifically minigene-derived transcripts (**A**), while primers outside of the *Fas* genomic sequences included in the vector were used for detecting endogenous *Fas* expression (**B**).

SPR responses were converted to quantitative data by their direct interpolation in the calibration curves (**Figure 3.15**). These values were also corrected with their respective dilution factors with respect to the particular total RNA concentration of each sample. SPR quantitative data correlated very closely with the quantitative data obtained with RT-qPCR for the minigene products (**Table 3.3**). Both, RT-qPCR and SPR techniques showed an exon-skipping shift of 37% and 38% respectively after co-expression with PTB. 567/57 ratios were fairly comparable between both techniques with values of 2.2 (RT-qPCR) and 2.5 (SPR) for *Fas567* overexpression and 0.38 (RT-qPCR) and 0.45 (SPR) with PTB co-expression. Both techniques showed a high correlation ($R^2 = 0.97$, **Figure 3.20A**) and all data were found within the limits of agreement (**Figure 3.20B**). We concluded that the SPR biosensor data were fully validated by independent quantitative measurements under these ideal conditions.

Table 3. 3 RT-qPCR and SPR comparison of the isoform content analysis from HeLa cells endogenous expression and minigene-induced overexpression. Isoform concentration in nM for SPR was calculated through the calibration curves obtained for each receptor according to their ΔR(%).

Sample type	*Fas* isoform	Concentration (nM)		567/ 57ratio	
		RT-qPCR	SPR	RT-qPCR	SPR
RNA *Fas567* overexpression	567	204.6	240 ± 23[a]	2.2	2.5 ± 0.3
	57	93.2	97 ± 23[a]		
RNA *Fas567* overexp. + PTB	567	74.9	92 ± 14[a]	0.38	0.45 ± 0.06
	57	198.8	204 ± 22[a]		

[a] Mean ± SD of three independent SPR measurements.

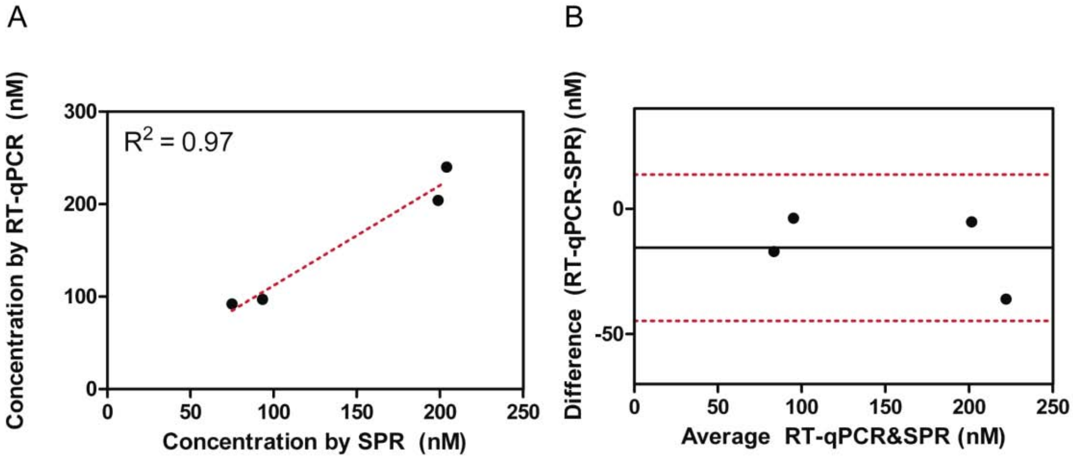

Figure 3. 20 Demonstration of agreement between SPR biosensor and RT-qPCR technique for minigene expressed isoforms. (**A**) Line of equality plots and (**B**) difference against mean plots (Almant-Bland model for replicated measurements)

The deficient detection of endogenous HeLa cell *Fas* RNAs can be attributed to the much longer length of the *Fas* transcripts endogenous isoforms. Target size is an important factor because of the generation of complex secondary structures that can hinder their accessibility to the monolayer.[60] To overcome this potential problem, we introduced a step of RNA fragmentation before the detection of endogenous isoforms. RNA molecules can be easily hydrolyzed. The phosphodiester bond in the ribose sugar-phosphate backbone of RNA can be efficiently broken by a base-catalyzed hydrolysis, cleaving the RNA molecule.[205] In our study, we implemented two RNA fragmentation strategies to get ~200 nt mRNA fragments (isoforms length used during the methodology optimization): (i) an *alkaline hydrolysis*,[206] in which our single-stranded mRNA could be spontaneously auto-cleaved in a basic medium in a random manner and (ii) a *RNase H cleavage*,[207] that allowed us to cleave the RNA at specific sites. Both reactions can be used to produce RNA fragments with a desired length, presenting different advantages and disadvantages to the process.

Alkaline hydrolysis

Because alkaline hydrolysis has been used for different purposes such as the detection of cell-extracted 16S rRNAs using SPR imaging[69] or as a tool for genome-wide mapping of RNA,[208] we attempted RNA fragmentation using this method. The time of hydrolysis was optimized as previously described[208] to achieve RNA fragments of the desired length (~200 nt). We exposed total RNA samples to different incubation times (zero, 1, 2, 3, 4, 5 and 7 minutes) in an alkaline buffer (pH 9.2). Samples were preheated at 95ºC for 15 s and mixed with preheated 1x alkaline hydrolysis buffer to start the hydrolysis reaction. After each incubation time, samples were placed on ice and mixed with sodium acetate (pH 5.2) to stop the reaction. The fragmented RNA was isolated and resuspended in nuclease-free water. The fragmentation was evaluated by agarose gel electrophoresis. As can be seen in **Figure 3.21**, bands of 200-nt RNA length were found after 3 and 4 min in alkaline medium, indicating that most of the RNA present in those samples had an average of 200 nt between those exposition times. Therefore, we established 3.5 min of alkaline RNA treatment for our mRNA digestion.

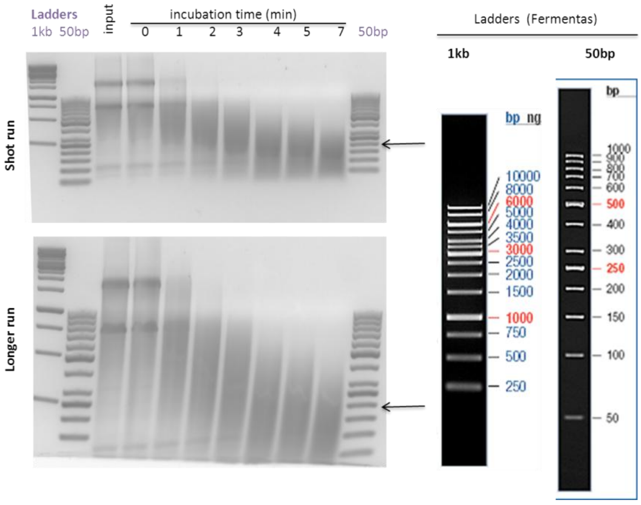

Figure 3. 21 Ag**a**rose electrophoresis analysis of HeLa cells total RNA fragmentation after different incubation times in alkaline buffer.

RNase H cleavage

The RNase H approach can be used to perform a sequence-specific cleavage, offering a more controlled cleavage reaction. This enzyme is known to specifically degrade the RNA strand of RNA-DNA hybrid duplexes.[207] This cleavage has been applied as a tool for the detection and quantification of a particular group of microbes based on the specific cleavage of rRNAs[209] and fusion enzymes have been developed by providing the RNase H with a zinc finger that recognizes a concrete sequence in DNA-RNA hybrids for an even more controlled fragmentation.[210]

In order to test the RNase H cleavage, we carried out a protocol previously described. We employed two internal DNA probes, 428 and 429 matching the + strand (sense strand) and the – strand (antisense strand) of exon 6 respectively (**Figure 3.22**).

428	GATCCAGATCTAACTTGGGGTG
429	CCCAAACAATTAGTGGAATTGGC
FasExon 5 sense	GAACATGGAATCATCAAGGAATGCAC
FasExon7 antisense	GGTTGGAGATTCATGAGAACCTTGG

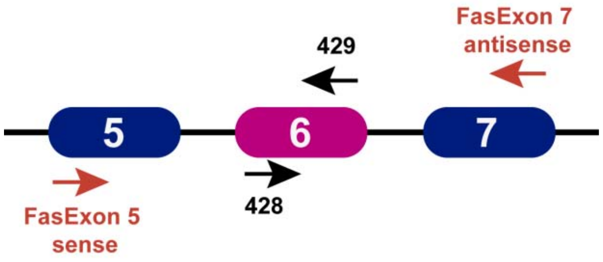

Figure 3. 22 Scheme of the RNase H test. Binding sites of DNA probes 428 and 429 for RNA cleavage and of *Fas* exon 5 sense primer and *Fas* exon 7 antisense primer for PCR amplification are indicated.

We applied different conditions (**Table 3.4**) to HeLa cell samples expressing endogenous levels of *Fas* isoforms and checked the results in electrophoresis gels using primers for exon 5 (forward) and exon 7 (reverse). Likewise, we employed the same conditions in control samples containing cells not expressing the *Fas* gene isoforms. Fragmentation should only take place in the sample incubated with the 428 DNA probe, which is complementary to the + strand of exon 6, cleaving the isoform and not allowing the fragment to be amplified by PCR. We incubated our total RNA with 10 µM concentration of each DNA probe at 95 ºC for 2 min for the probe-annealing and cooled it on ice for 5 min. After the annealing, enzyme cleavage was carried out at 37 ºC for 60 min with an enzyme concentration of 250 U/mL in 1xRNase H enzyme buffer. RNase H catalysis was inactivated by incubating at 65ºC for 15 min.

Table 3. 4 Conditions employed for the RNase cleavage test.

Lane	428	429 probe	RNase H
1, 5	-	-	-
2,6	-	-	+
3, 7	+	-	+
4, 8	-	+	+
9 (control)		Non-treated	

As can be seen in **Figure 3.23**, fragmentation worked well in lane 7, the only sample incubated with the 428 probe. A decrease in the band intensity was observed in this lane, suggesting that the fragmentation had taken place. The lanes incubated with the 429 probe (lanes 4 and 8) showed an unusual band pattern possibly because of a non-specific amplification due to the presence of the 429 probe acting as an extra primer. As we did not employed an amplification step for SPR detection, we did not considered this issue as a major problem.

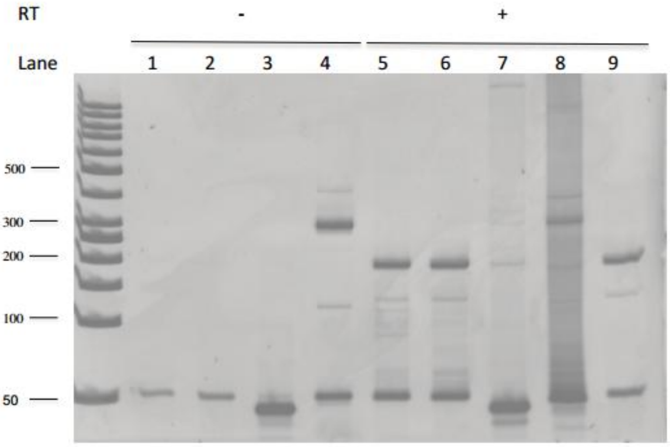

Figure 3. 23 Agarose electrophoresis analysis of HeLa cells total RNA fragmentation after different RNase H cleavage conditions. Lanes and conditions employed are indicated for each of the lanes.

Therefore, we decided to apply both cleavage conditions to the RNA samples and test the cleavage in the SPR biosensor. We designed 25 nt DNA probes complementary to the sequences flanking exon 5 (3' end of exon 4) and exon 7 (5' end of exon 8) to cleave the isoforms and to produce fragments of 200 nts (**Table 3.8**).

We applied the RNase H cleavage protocol by hybridizing these probes to the endogenously expressed *Fas* isoforms in HeLa cell samples and evaluated them before and after the fragmentation by SPR. Parallel quantification of the same samples was carried out by RT-qPCR in order to corroborate the good performance of the cleavage. As can be seen in **Figure 3.24**, the fragmentation was only noticeable for the *Fas567* isoform. The *Fas57* isoform showed the same levels in all of the cases studied. In addition, although the isoform ratio increased three-folds in the fragmented samples (3.5) compared with the not fragmented ones (1.2), it was still far from reaching the values obtained with RT-qPCR (17.9) (**Table 3.5**), suggesting that the fragmentation was not fully completed.

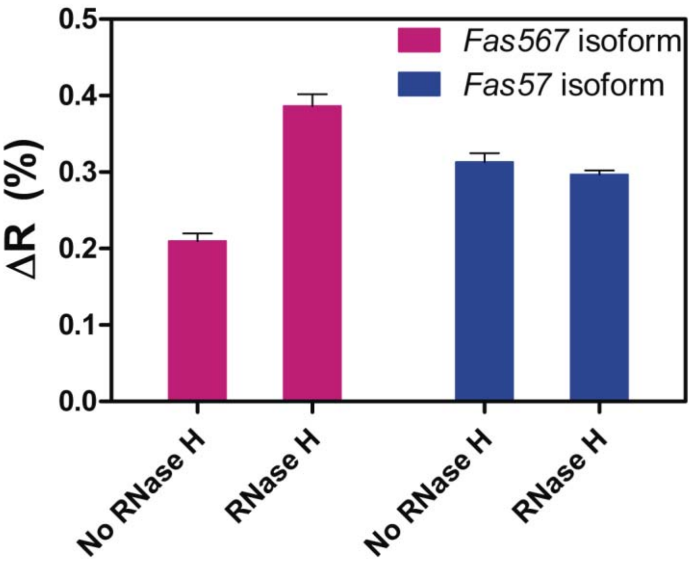

Figure 3. 24 SPR signal for each of the conditions tested.

Table 3. 5 SPR results after application of RNase H cleavage to HeLa cell endogenous level samples.

Sample type	**567/ 57ratio**	
	qRT-PCR	**SPR**
RNase H	17.9	**3.5**
No RNase H	-	1.2

Therefore, we decided to further optimize the RNase cleavage by studying the activity of the enzyme with the SPR biosensor. RNase H enzyme has been previously employed for RNA-based biosensor due to its capability for cleaving RNA molecules hybridized to DNA-probes, rendering the biosensor surface ready for further analyses.[211] We tested three parameters of the reaction: (i) the reaction buffer concentration, (ii) the enzyme concentration, and (iii) the reaction temperature. We employed a short RNA sequence (RNA_1) (**Table 2.3**) for the evaluation of the enzyme activity. We immobilized a specific DNA probe (RNA_1 probe) for the RNA sequence on the gold sensor surface and, subsequently, monitored the RNA hybridization and RNase H activity in real time (**Figure 3.25**).

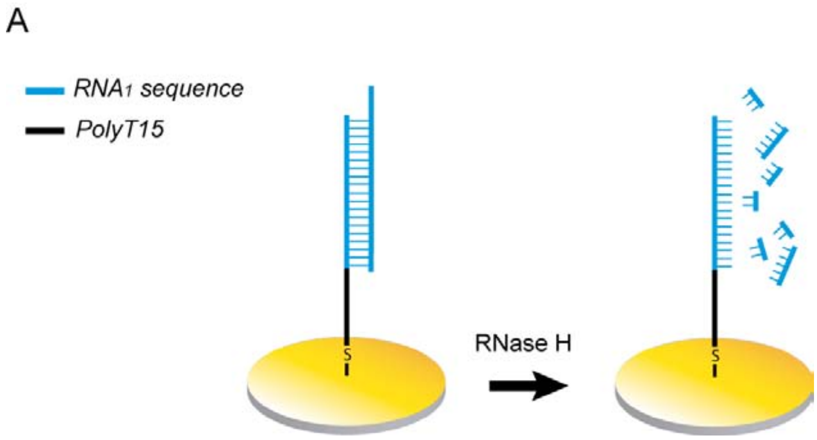

Figure 3. 25 Scheme of the strategy followed for the optimization of the RNase H activity.

To determine the most suitable buffer concentration for the reaction, we explored the RNase H buffer at three different concentrations: 1x, 2x and 3x. First, the miRNA was hybridized at a 50 nM concentration with its receptor in the biosensor surface and, subsequently, 250 U/mL of the enzyme was flowed in the different buffer concentrations at room temperature (RT). The capability of the enzyme at each buffer concentration to return the sensor signal to the initial levels as a consequence of the cleavage was evaluated. As can be appreciated in **Figure 3.26**, at a 1x buffer concentration, which was the concentration previously employed for RNA cleavage, the baseline did not return to the initial level but it only removed a 48% of the hybridized RNA. This data supports the results obtained in the first attempt with the RNase H, where the reaction resulted in an incomplete cleavage. On the contrary, the baseline completely returns to the initial level at a 2x buffer concentration, meaning that the RNase H was fully active at this buffer concentration.

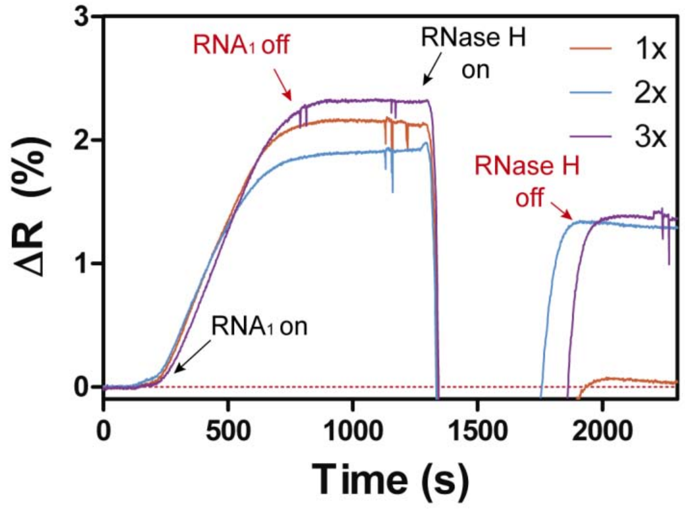

Figure 3. 26 RNase H buffer concentration test.

Once we had established 2x as the proper buffer concentration, we tested the enzyme concentration needed for the reaction. We injected four different concentrations of RNase H enzyme: none, 1, 10, 50 and 100 U/mL. As depicted in **Figure 3.27**, the latter one cleaved the hybridized RNA almost completely and achieved the same results as when using 250 U/mL, suggesting that a concentration of 100 U/mL of RNase H was sufficient to carry out a complete cleavage.

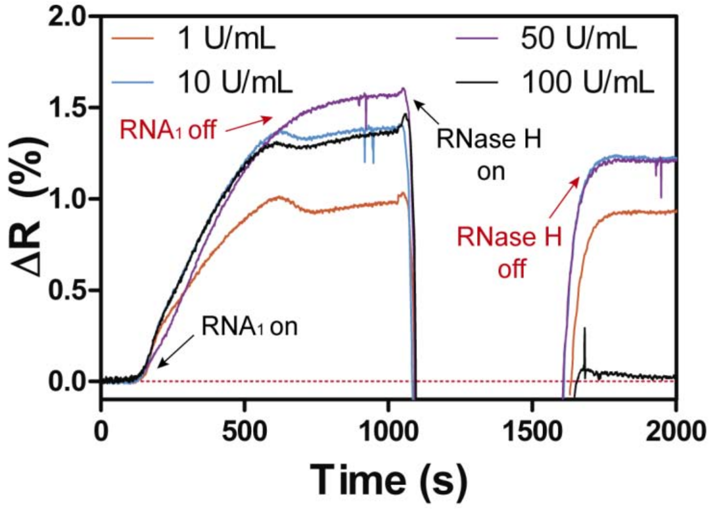

Figure 3. 27 RNase H concentration test.

Finally, after achieving such good results using RT conditions, we explored the enzyme activity at different reaction temperatures. We tested RT, 37 ºC and 50 ºC by preheating the RNase H solution before flowing it in the SPR biosensor. Surprisingly, at the recommended temperature (37ºC), the enzyme was not fully active, cleaving less than half of the hybridized RNA (**Figure 3.28**). On the contrary, RT conditions achieved the best results, returning the sensor signal to the initial levels.

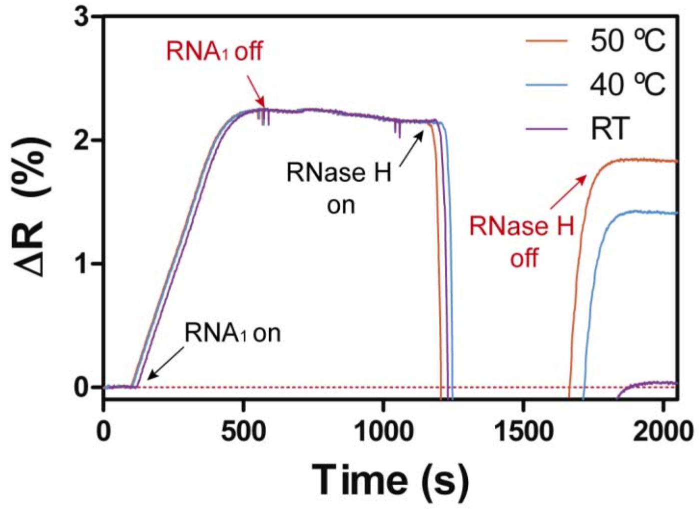

Figure 3. 28 Temperature test for RNase H reaction.

In conclusion, the parameters used in the first cleavage conditions did not allowed a proper cleavage as corroborated by the RNase H activity study by the SPR biosensor, giving rise to misleading results in the SPR measurements compared to the RT-qPCR quantification. Therefore, we employed the optimized conditions to cleave *Fas* gene isoforms present in the HeLa cell samples previous to the analysis in the SPR biosensor.

Due to the encouraging results with the optimized fragmentation procedures, we applied both protocols to the HeLa cell samples. Samples were diluted in 3xSSC (45% FA) to 20 ng/µL of purified total RNA. To monitor the isoform levels, duplicate measurements were carried out in the SPR sensor for each fragmentation protocol. Isoform concentrations were calculated by interpolation of the sensor signal to the calibration curves obtained for each receptor. In parallel, RT-PCR assays and agarose electrophoresis gel or RT-qPCR were carried out using the same samples for validation of the biosensor data. **Figure 3.29** shows the SPR sensograms obtained after injection of HeLa RNA samples for each receptor. As can be seen, endogenous RNAs generated readily detectable signals above background after the application of both fragmentation protocols, confirming our hypothesis that RNA fragmentation could increase the detection response by SPR.

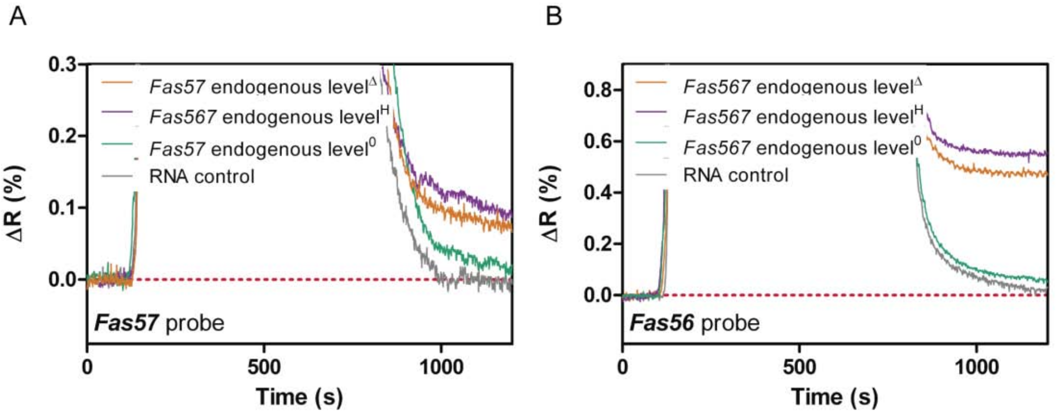

Figure 3. 29 SPR sensograms of the detection of 20 ng/ µL of total HeLa cell RNA for the endogenous expression of the two isoforms in both *Fas567* probe (**A**) and *Fas57* probe (**B**) after applying RNA hydrolysis (Δ), RNase H cleavage and without any treatment (0).

The results of **Table 3.6** show that SPR data generated a slight underestimation of isoform concentrations in the two fragmentations with respect to RT-qPCR quantification. This different quantification may be due to incomplete (or excessive) cleavage by the fragmentation protocols applied, suggesting that a further optimization of the fragmentation step could generate better matches between SPR and RT-qPCR values. Due to this underestimation, the correlation between both techniques was lower in comparison to ideal conditions for both, the alkaline hydrolysis (R^2 = 0.86, **Figure 3.30A**) and the RNase H cleavage (R^2 = 0.92, **Figure 3.30C**). However, among the samples tested, 83% (5/6) for alkaline hydrolysis and 100% (6/6) for RNase H cleavage were found within the limits of agreement (**Figures 3.30B** and **D**).

Table 3. 6 RT-PCR and SPR comparison of the isoform content analysis from HeLa cells endogenous expression. Isoform concentration in nM for SPR was calculated through the calibration curves obtained for each receptor according to their ΔR(%). Data used for ratio determination in SPR was calculated from 2 independent measurements of each sample type with each receptor.

Sample type	*Fas* isoform	Concentration (nM)		567/ 57ratio	
		qRT-PCR	SPR	qRT-PCR	SPR
Fas endogenous levels	567	365 ± 17[a]	262 ± 27[Δ] 295 ± 14[H]	17.9 ± 0.4[a]	22.9 ± 1.4[Δ]
	57	20.3 ± 0.4[a]	12.0 ± 0.8[Δ] 13.1 ± 0.3[H]		22.0 ± 0.7[H]

[a] Mean ± SD of endogenous concentration of HeLa cell's total RNA calculated from 2 differents qRT-PCR experiments.

[Δ] Mean ± SD of the concentration obtained in SPR from 2 different measurements from purified samples of HeLa cell's total RNA after alkaline hydrolysis.

[H] Mean ± SD of the concentration obtained in SPR from 2 different measurements from purified samples of HeLa cell's total RNA after RNase H cleavage.

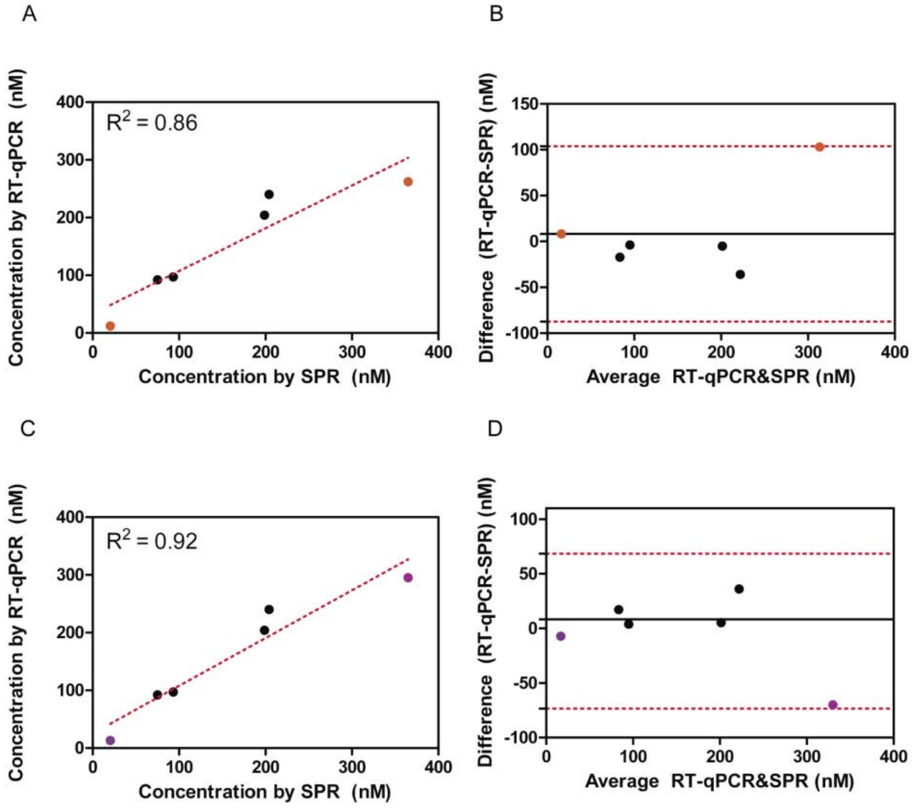

Figure 3. 30 Demonstration of the agreement between the SPR biosensor and the RT-qPCR technique for all HeLa cell lines in both fragmentation procedures. (**A**) Line of equality plot for alkaline hydrolysis. (**B**) Difference against mean plots (Almant-Bland model for replicated measurements) for alkaline hydrolysis. (**C**) Line of equality plot for RNase H cleavage. (**D**) Difference against mean plots (Bland-Altman model for replicated measurements) for RNase H cleavage.

Importantly, a comparison of the ratios between isoforms revealed comparable values for the two techniques, 17.9 for RT-qPCR and 22.9 (alkaline hydrolysis) and 22 (RNase H cleavage) for SPR. Indeed, isoform ratios showed a very significant correlation (R^2 = 1, **Figure 3.31A** in alkaline hydrolysis; R^2 = 1, **Figure 3.31C** in RNase H cleaved samples) and presented a 100% validation ratio (3/3) between both techniques regardless of the fragmentation protocol employed (**Figures 3.31B** and **D**). The higher correlation obtained with the RNase H cleavage suggest that a site specific RNA fragmentation induces to lower errors in the isoform quantification probably due to a lesser loss of sample input than when applying a random fragmentation.

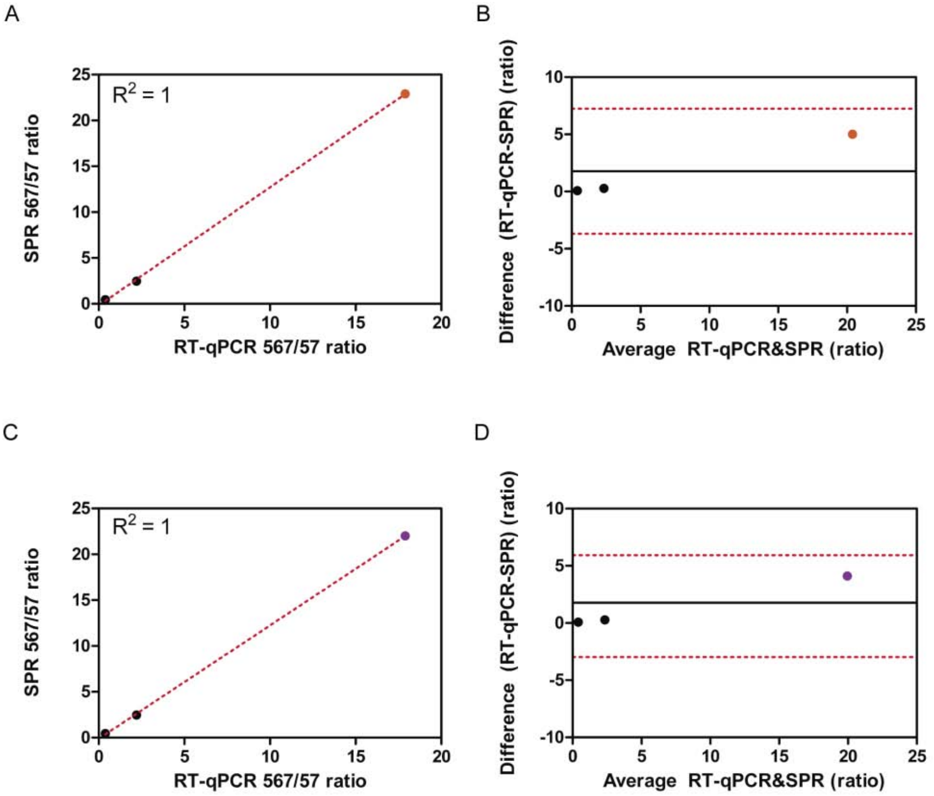

Figure 3. 31 Demonstration of the agreement between the SPR biosensor and the RT-qPCR technique for isoform ratios in both fragmentation procedures. (**A**) Line of equality plot for alkaline hydrolysis. (**B**) Difference against mean plots (Almant-Bland model for replicated measurements) for alkaline hydrolysis. (**C**) Line of equality plot for RNase H cleavage. (**D**) Difference against mean plots (Bland-Altman model for replicated measurements) for RNase H cleavage.

These results suggest that, in spite of the underestimation of the signals by SPR, they can be possibly improved by further optimization of RNA hydrolysis, a precise determination of isoform ratios (a key feature for diagnostic/prognostic purposes) were achieved by our technology. Therefore, this validates its use for profiling of alternative splicing events

3.4. Conclusions

Deregulation of alternative pre-mRNA splicing is known to contribute to the development and progression of an increasing number of human malignancies, possibly representing a hallmark of cancer. A growing interest in splicing profiling has emerged for diagnostic and prognostic purposes in cancer and the use of alternatively spliced isoforms as biomarkers is likely to expand in the near future. In addition, modulation of isoform ratios can be of potential use in therapeutic approaches for cancer treatment. Despite the significant advances in recent years, technologies for analyzing splicing variants with high sensitivity and specificity for routine clinical use have not yet been developed.

We have presented a methodology for monitoring alternative splicing events in real-time employing a portable SPR biosensor. It involves minimal sample manipulation and avoids the use of labels or pre-amplification in contrast with the current gold standard RT-qPCR technique which is prone to introduce bias due to the cDNA conversion and amplification processes. Furthermore, our methodology strictly discriminates against the non-complementary isoforms in the pM-nM range. It has been easily reproduced with the same efficiency when it is applied to a different gene. These results highlight its feasibility as a tool for the monitoring of alternative splicing events of different genes and within different biological and pathological contexts. This advantage reduces greatly the time and material employed during the experimental setup of the methodology prior evaluation and, therefore, minimizes the cost. Moreover, it reduces the systematic errors arisen from different probe affinities in the amplification process, leading to a more reliable analysis.

The feasibility of the methodology was tested in complex RNA mixture purified from HeLa cells transfected and not transfected with various DNA expression constructs. Results strongly correlated with RT-qPCR data. Additionally, the biosensor can be reused up to 80 hybridization/regeneration cycles with no apparent signal loss, which demonstrates its robustness and reproducibility for long-term use.

The simplicity of our SPR methodology, along with the label-free detection and the minimized sample manipulation, makes it really useful for the real-time monitoring of splicing events. In our view, these results represent a landmark in mRNA analysis and open the door for this tool to be routinely employed for the analysis of alternatively spliced isoforms as biomarkers for diagnosis and patient follow-ups during therapy, providing a more informative, specific and accurate analysis.

3.5. BiMW biosensing of mRNA splicing isoforms

So far we have developed a methodology for the specific detection of mRNA isoforms generated by alternative splicing and demonstrated its feasibility by the direct detection of *Fas* gene isoforms in model HeLa cell lineages. However, although the results suggest a very promising diagnostic tool in good agreement with the gold-standard technology, the SPR sensitivity may compromise its further use in clinical diagnosis. Levels of mRNA isoforms in normal and cancer tissues could be greatly reduced in contrast with the once yielded by HeLa cell cultures. Moreover, it has been demonstrated that the presence of circulating mRNA in blood stream from cancer patients can be associated with the tumor progression[212] which could be a promising approach for detecting deregulation of alternative splicing events in a less-invasive way. However, higher sensitivity levels are a main requirement in such cases.

Due to the improved sensitivity levels provided *a priori* by the BiMW interferometer, we decided to transfer to this biosensor platform the methodology previously developed in the SPR biosensor. An evaluation of the analytical performance for the direct detection of *Fas* gene isoforms was carried out. We functionalized the BiMW biosensor surface following the described silanization protocol optimized in **Chapter 2**. The BiMW sensor chip was placed into the microfluidic cell and two different microfluidic channels were supplied with a solution containing either SH-*Fas57* or SH-*Fas56* probes with MCH at a 20:1 molar ratio for the parallel detection of each isoform. The sensor gave an increment in the response ($\Delta\Phi$ (rad)) of 55 and 49 for SH-*Fas57* and 67 for SH-*Fas56*, respectively. For detection assays, we employed the previously optimized hybridization conditions with the SPR biosensor (i.e. hybridization buffer: 3x SSC/FA45%). We also employed the hybridization buffer as running buffer to avoid excessive bulk change sensing due to the high sensitivity of the BiMW biosensor.

To assess the selectivity and sensitivity of each biofunctionalized monolayer on the BiMW biosensor, we monitored the biosensor response to a concentration of 50 pM of each isoform in both monolayers. As can be appreciated in **Figure 3.32**, each isoform led to an increase in the phase shift after the sensograms stabilization in the monolayer containing their specific probes. The signal corresponding to the off-targets returned to the former baseline levels, which indicated that no binding took place. These results demonstrated the specificity of the methodology and the success in isoform discrimination by the BiMW biosensor.

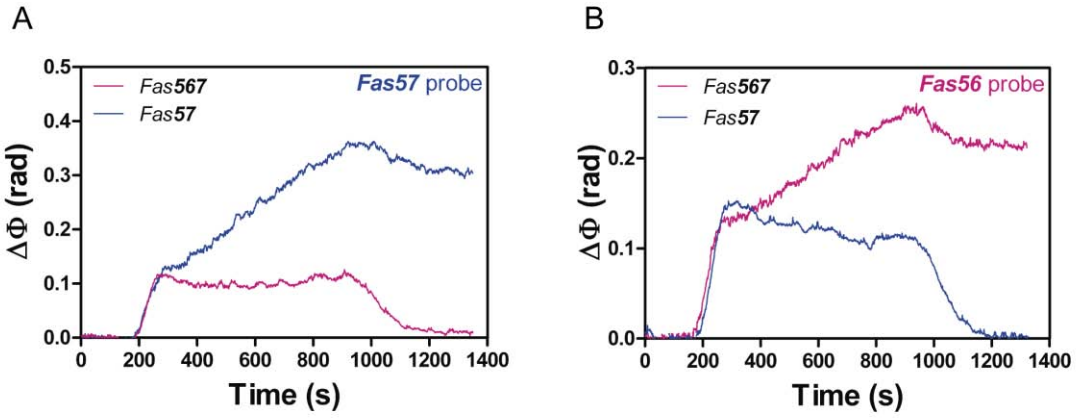

Figure 3. 32 BiMW real-time sensograms of *Fas* isoforms for (**A**) *Fas57* probe and (**B**) *Fas56* probe.

Having demonstrated the specificity of the BiMW biosensor, we performed a calibration curve for each isoform. We employed different concentrations of *Fas57* and *Fas567* from standard solutions concentrations, ranging from 50 pM to 1 pM and fitted the signals to a non-linear curve. As can be observed in **Figure 3.33**, the BiMW device was able to precisely discriminate the non-complementary isoforms and clearly detect the specific ones achieving **LODs** of **580** and **735 fM** for *Fas57* (R^2 = 0.98) and *Fas567* (R^2 = 0.98) probes, respectively. The obtained LOD were three orders of magnitude better than the one achieved with the SPR sensor. The monolayers showed a great reproducibility, with %CV below the minimum value acceptable (≤ 14%). Both monolayers showed stable detection signal at least up to 61 hybridization/regeneration cycles.

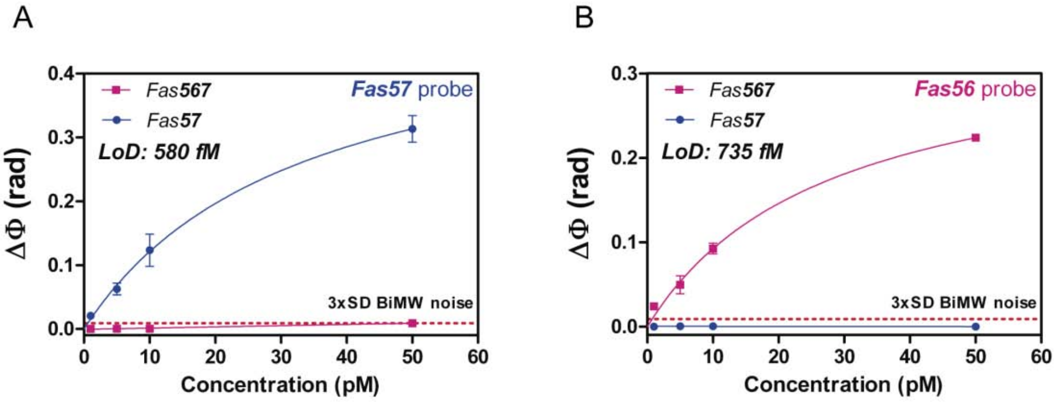

Figure 3. 33 BiMW calibration curves for (**A**) *Fas57* probe and (**B**) *Fas56* probe. Solid lines (blue and pink) correspond to the non-linear fit of the calibration curves. Red dashed line corresponds to 3xSD SPR noise, which is the limit for the minimum signal detectable. All data show mean ± SD of triplicate measurements.

3.6. Conclusions and future perspectives

Due to the strong demand for highly sensitive analysis to ensure the detection of mRNA isoforms at very low concentrations in different human tissues and in blood stream circulation, we applied the developed methodology for monitoring alternative splicing events in the SPR biosensor to the highly sensitive BiMW device. This biosensor allowed for the parallel detection of both isoforms at concentrations as low as 1 pM, achieving LODs in the fM range, improving in 3 orders of magnitude the one achieved by the SPR biosensor. The methodology showed the same degree of discrimination as previously reported for the SPR biosensor, constituting an excellent approach for alternative splicing event monitoring in any tissue or biofluid.

Further studies should be done related to the monolayer optimization to find the best conditions for isoform detection. Also, HeLa cell samples should be tested after the application of the different proposed fragmentation protocols to test its feasibility in real samples analysis. Finally, a validation study in mRNA isoform detection in tissues or circulating blood must be done in order to confirm its utility in isoform rate prediction.

3.7. Materials and Methods

3.7.1. DNA sequences

mRNA isoform sequences were obtained from Esmbl gene browser (http://www.ensembl.org/index.html). DNA/RNA sequences employed are summarized in **Table 3.7**.

Table 3. 7 Sequences for probes and DNA/RNA synthetic targets employed in this thesis.

Name	Sequence
***Fas57* probe**	5’- (SH)- PolyT$_{15}$ -CTTTCTCTTCACTTCCTCTTTG-3‘
***Fas56* probe**	5’- (SH)- PolyT$_{15}$ -AGATCTGGATCCTTCCTCTTTG-3’
***FasExon6* probe**	5’- (SH)- PolyT$_{15}$ - CACCCCAAGTTAGAT-3‘
***BCL-*X_L probe**	5’- (SH)- PolyT$_{15}$-AGTATCCCAGCCGCCGTTC 3’
***BCL-*X_S probe**	5’- (SH)- PolyT$_{15}$-AGTATCCTGTTCAAAGCTCTGAT 3’
***Fas57* isoform**	5’ATGTGAACATGGAATCATCAAGGAATGCACACTCACCAG CAACACCAAGTGCAAAGAGGAAGTGAAGAGAAAGGAAGT ACAGAAAACATGCAGAAAGCACAGAAAGGAAAACCAAGG TTCTCATGAATCTCCAACTTTAAATCCT 3’
***Fas567* isoform**	5’ATGTGAACATGGAATCATCAAGGAATGCACACTCACCAG CAACACCAAGTGCAAAGAGGAAGGATCCAGATCTAACTTG GGGTGGCTTTGTCTTCTTCTTTTGCCAATTCCACTAATTGTT TGGGTGAAGAGAAAGGAAGTACAGAAAACATGCAGAAAG CACAGAAAGGAAAACCAAGGTTCTCATGAATCTCCAACTTT AAATCCT 3’
***BCL-*X_L isoform**	5’GTAGACAAGGAGATGCAGGTATTGGTGAGTCGGATCGCA GCTTGGATGGCCACTTACCTGAATGACCACCTAGAGCCTTG GATCCAGGAGAACGGCGGCTGGGATACTTTTGTGGAACTCT ATGGGAACAATGCAGCAGCCGAGAGCCGAAAGGGCCAGG AACGCTTCAACCGCTGGTTCCTGACGGGCATGACTGTGGC 3’
***BCL-*X_S isoform**	5’GAGGCAGGCGACGAGTTTGAACTGCGGTACCGGCGGGCA TTCAGTGACCTGACATCCCAGCTCCACATCACCCCAGGGAC AGCATATCAGAGCTTTGAACAGGATACTTTTGTGGAACTCT ATGGGAACAATGCAGCAGCCGAGAGCCGAAAGGGCCAGG AACGCTTCAACCGCTGGTTCCTGACGGGCATGACTGTGGC 3’

3.7.2. HeLa cell mRNA samples.

Expression analyses of HeLa cells were performed in collaboration with the Group of Prof. J. Valcárcel from the Regulation of Alternative pre-mRNA Splicing during Cell Differentiation, Development and Disease group at the Center for Genomic Regulation (CRG), Barcelona (Spain).

Exponentially grown human cervical carcinoma HeLa cells (aprox. 1.5 million cells) were transfected at 50% confluency with 0.4 micrograms of *Fas* minigenes and 10 micrograms of plasmid DNA expressing either beta galactosidase or PTB, per culture plate of 10 cm. When 6-wells plates were used, per well 50 ng minigene and 3 micrograms of expression plasmid DNA were transfected per well. When minigene and protein expression vector were used, cells were collected 48 hours post-transfection. Total RNA was isolated using the RNeasy kit (Qiagen) and the pattern of alternative splicing was analyzed by RT-PCR. Reverse transcription was carried out using AMV-Reverse Transcriptase (Promega) and specific reverse primers .

Polymerase chain reaction was carried out using GoTaq (Promega) and forward and reverse primers corresponding to the exonic regions flanking the alternatively spliced sequences. The products were analyzed on a 6% acrylamide gel and the pattern of alternative splicing was quantified with ImageQuant.

mRNA fragmentation

Alkaline hydrolisis

To achieve an average length of ~200 nt from the isoforms and to establish a more general methodology, total RNA from HeLa cells was cleaved prior to analysis. Samples were preheated at 95ºC for 15 s and mixed with preheated 1xAlkaline hydrolysis buffer (Carbonate/Bicarbonate 50mM, EDTA 1mM, pH 9.2) to start the hydrolysis reaction. Total RNA samples were exposed to different incubation times (zero, 1, 2, 3, 4, 5 and 7 minutes). After each incubation time, samples were placed on ice and reaction was stopped with RNA fragmentation stop solution (3M Sodium Acetate, pH 5.2). The fragmented RNA was isolated and resuspended in nuclease-free water. The products were analyzed on a 6% agarose gel.

RNase H cleavage

In order to perform RNase H cleavage, we carried out a protocol previously described. We employed two internal DNA-probes, 428 and 429 matching the + strand (sense strand) and the – strand (antisense strand) of exon 6 respectively (**Table 2.2**). After applying the fragmentation protocol, endogenous levels of *Fas* isoforms were checked in different cell lineages in electrophoresis gels using primers for exon 5 (forward) and exon 7 (reverse). We incubated our total RNA with 10 µM concentration of each DNA-probe at 95ºC for 2 min for the probe-annealing and cooled it on ice for 5 min. After the annealing, enzyme cleavage was carried out at 37ºC for 60 min with an enzyme concentration of 250 U/mL in 1xRNase H enzyme buffer (50 mM Tris-HCl, 75 mM KCl, 3 mM $MgCl_2$, 10 mM DTT –pH 8.3-). RNase H catalysis was inactivated by incubating at 65ºC for 15 min.

Table 3. 8 DNA probes for RNase H cleavage and *Fas* mRNA fragments generated.

Name	Length (nt)	Sequence
***Fas* 567 isoform fragment after RNase H**	214	5'CCAAAUGUGAACAUGGAAUCAUCAAGGAAUGCACACUCACCAGCAACACCAAGUGCAAAGAGGAAGGAUCCAGAUCUAACUUGGGGUGGCUUUGUCUUCUUCUUUUGCCAAUUCCACUAAUUGUUUGGGUGAAGAGAAAGGAAGUACAGAAAACAUGCAGAAAGCACAGAAAGGAAAACCAAGGUUCUCAUGAAUCUCCAACUUUAAAUCCU3'
***Fas* 57 isoform fragment after RNase H**	149	5'CCAAATGTGAACATGGAATCATCAAGGAATGCACACTCACCAGCAACACCAAGTGCAAAGAGGAAGTGAAGAGAAAGGAAGTACAGAAAACATGCAGAAAGCACAGAAAGGAAAACCAAGGTTCTCATGAATCTCCAACTTTAAATCCT3'
***Fas* exon 4 probe**	25	5' TGCAAGGGTCACAGTGTTCACATAC 3'
***Fas* exon 8 probe**	25	5' CAGATAAATTTATTGCCACTGTTTC 3'

3.7.3. DNA-probes immobilization.

Formation of mixed SAMs of SH-DNA probe/MCH (1 µM) was carried out *in-situ* on the bare gold sensor chip and the PDITC-activated BiMW surface (silanization process described in **Chapter 2**) by flowing 250 µL of the mix in PB buffer solution at a 12 µL/min rate. Different SH-DNA probe/MCH molar ratios (no MCH, 10:1 and 20:1) were employed depending on the experiment carried out.

3.7.4. Isoforms hybridization and biosensor regeneration.

Splicing variants detection was performed by injection of the target splicing variant samples into the biosensors at a 15 µL/min rate and subsequent hybridization with their complementary DNA-probes immobilized on the sensor surface. These samples were dissolved in either 5xSSC (0.75 M in NaCl, 0.075 M in sodium citrate) or 3xSSC (0.45 M in NaCl, 0.045 M in sodium citrate). Different concentrations of Formamide ≥99.5% (Sigma Aldrich, Steinhem – Germany-) were used for improving specificity. Isoform-probe interactions were disrupted by using a 50% formamide in aqueous solution. Calibration curves were obtained for each DNA probe by obtaining triplicates measurement of different target dilutions from standards of known concentration. The mean and the standard deviation (SD) of each concentration were plotted versus the target concentration and fitted to a curve.

3.7.5 Data analysis.

The data were collected using Origin 8.0 software (OriginLab, Northampton, MA). The experimental detection limit (LOD) was defined as the target concentration giving a ΔR (%) or ΔΦ (rad) in the hybridization signal at least three times higher than that of the standard deviation of the DNA/RNA control signal. Limit of quantification (LOQ) was defined as the target concentration giving ΔR (%) or ΔΦ (rad) in the hybridization signal at least ten times higher than that of the standard deviation of the DNA control or the RNA control signal. The coefficients of variation were obtained as the ratio of the standard deviation to the mean, expressed in percentages (*%CV*). Individual assay variation was calculated after analysis of three replicates of the target at different concentrations. Inter-assays variations were calculated gathering together all three replicates from the individual assays obtained from two different operators. Percentages of cross-hybridization were calculated by dividing the average signal intensity of the off-targets into the average signal intensity of the complementary isoform. Agreement between RT-qPCR and SPR was assessed by applying the Bland-Altman model for replicate measurements.

Chapter 4·Profiling micro-RNA levels by amplification-free and label-free biosensing

The importance of micro-RNA profiling in cancer diagnosis is highlighted in this chapter. Current methodologies for micro-RNA detection are reviewed, taking special attention to biosensors as emerging platforms for their study due to their high sensitivity and fast detection. Different approaches are evaluated in SPR and BiMW biosensors for direct and label-free detection of circulating micro-RNAs. The specific detection of the micro-RNA sequence of interest is accomplished after an exhaustive optimization to avoid cross-hybridization of homologous sequences. The feasibility of the methodologies is eventually confirmed by the analysis of clinical urine samples from cancer patients.

4. Profiling micro-RNA levels by amplification-free and label-free biosensing

4.1. Introduction

Until recently RNA has been regarded mainly as an informational intermediate between a DNA sequence (“gene”) and its encoded protein. At the same time, extensive sequences in the higher eukaryotes that do not encode proteins or cis-acting regulatory elements were thought to be simply accumulated evolutionary debris. Nonetheless, most of these supposedly inert sequences are transcribed. In recent years, it has become increasingly apparent that the non-protein-coding portion of the genome is of crucial functional importance for both normal development and physiology.[213] The modulation of gene expression by small non-coding RNAs is a recently discovered level of gene regulation in animals and plants. The functional relevance of the non-protein-coding genome is particularly evident for a class of these small non-coding RNAs called micro-RNAs (miRNAs).[7, 214]

Mature miRNAs are small and single-stranded non-coding RNAs typically containing ~19-23 nucleotides.[215-218] These short, endogenously expressed molecules are evolutionally conserved and they are present in a broad range of animals, plants, and viruses.[7, 219, 220] They play important roles in modulating several biological functions through the interaction between the miRNA sequence and mRNAs. Even though the understanding of their complex roles are not fully characterized, expression levels of specific miRNAs in tissues have already been correlated with cell fate decisions and outcome of serious diseases, such as heart diseases and various types of cancers.[66]

4.1.1. Biogenesis and functions of miRNAs

The biogenesis of miRNAs is a multiple step process and involves the activity of two RNase III proteins, Drosha and Dicer (**Figure 4.1**). MiRNAs are initially transcribed in the cell nucleus from intragenic or intergenic regions by RNA polymerase II to form primary miRNAs (pri-miRNA) with lengths of 1-3 kb.[221] They contain a local hairpin structure where miRNA sequences are embedded. These pri-miRNAs undergo several steps of maturation.[222] The maturation process is initiated by Drosha, a nuclear RNase III-type endonuclease that acts specifically on double-stranded RNA (dsRNA). This RNase together with its essential cofactor (a RNA-binding protein termed DGCR8) form a complex called Microprocessor that crops the stem-loop to release a small hairpin-shaped RNA of approximately 70-100 nucleotide-long (pre-miRNA).[223] The pre-miRNA is then transported from the nucleus to the cytoplasm by Exportin-5, where is cleaved by RNase-III enzyme Dicer, liberating a 18-24 nt-length RNA duplex (miRNA:miRNA* duplex).[224] This RNA duplex is subsequently loaded onto an argonaute (AGO) protein to form an effector complex called RNA-induced silencing complex (RISC).[225] One of the RNA strands becomes the mature miRNA guide while the complementary, the passenger strand (miRNA*), can be quickly removed by two processes: (i) cleavage,[226] when the duplex is perfectly matched or, more commonly, by (ii) unwinding,[227] in case that duplexes have a central mismatch. The miRNA biogenesis can be intrinsically regulated by several alterations in RNA sequence and/or structure that affect the maturation and turnover of miRNAs, such as single nucleotide polymorphisms[228] (SNPs), miRNA tailing,[229] RNA editing[230] or RNA methylation.[231] Furthermore, apart from the canonical miRNA biogenesis pathway described above, various alternative mechanisms can generate miRNAs or miRNA-like small RNAs.[232, 233]

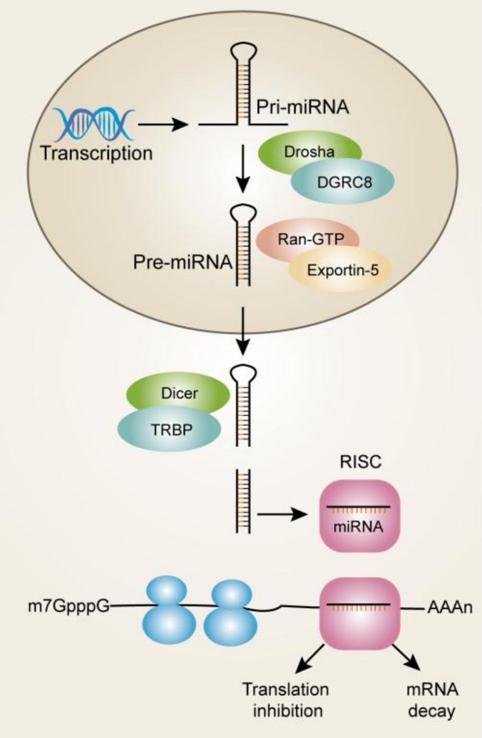

Figure 4. 1 Micro-RNA biogenesis.

MiRNA-binding sites are usually located in the 3’ *untranslated region* (UTR) of mRNAs[234] although they can also bind to the 5’-UTR[235] or the *open reading frame* (ORF)[236] of genes and, surprisingly, in some cases, they can upregulate translation.[237] The domain that spans from nucleotide position 2 to 7 at the 5’ end of miRNAs is crucial for target recognition, and it is called the “miRNA seed”. However, according to grade and localization of the complementarity, target sites have been classified into three main classes[238]: the dominant seed site targets (5’ seed-only), the 5’ dominant canonical seed site targets (5’ dominant) and the 3’ complementary seed site targets (3’ canonical). The RISC complex functions by perfectly or imperfectly matching with its complementary target mRNA, inducing target mRNA degradation or translational inhibition or sequestration of mRNA from translational machinery. As a result, a reduction of the protein level and profound consequences on cellular homeostasis can be produced.

MiRNA biology is a complex and highly orchestrated regulation network. Over 1000 miRNAs have been identified in humans,[219] whereas the number of mRNAs is estimated at approximately 30000. There are few developmental processes absolutely dependent on single miRNA.[239] A single gene can be regulated by multiple miRNAs, and likewise, a single miRNA may regulate more than one target due to the imperfectly matching between the miRNA and its target. In fact, miRNAs are estimated to regulate the translation of more than 60% of protein-coding genes. There is an increasing evidence that miRNAs play critical regulatory roles in almost every biological process, including early development, cellular differentiation, proliferation, apoptosis, developmental timing, hematopoiesis, etc.[240, 241] In addition, miRNAs are involved in diverse cellular activities, such as immune response,[242] insulin secretion,[243] neurotransmitter synthesis,[244] circadian rhythm,[245] and viral replication.[246]

4.1.2. MiRNAs as a cancer biomarker

Since miRNA function is involved in regulating crucial biological processes, disrupted expression of miRNAs has been linked with a number of diseases. Aberrant microRNA expression has shown to be associated with the initiation and development of human diseases, genetic disorders, and altered immune system function. Furthermore, miRNAs can act as both oncogenes and tumor suppressors, highlighting their influence in human cancer.[247, 248]

In diagnosis, the establishment of miRNA-pattern panels to provide detailed information for specific miRNAs or for determining the type of cancer and its stage of development (early or late stage, metastasis…) is gaining more and more interest. Genome-wide profiling has shown that miRNA expression signatures (miRNome) can be used to discriminate with a high grade of accuracy different types of cancer[249] and to identify the tissue of origin of poorly differentiated tumors.[250]

One advantage of miRNAs is that they are more stable than long mRNAs due to their small size, allowing their expression profiling from fixed tissues or other biological material like blood (whole blood, plasma or serum),[251] circulating exosomes,[252] urine,[253] saliva[254] and even sputum.[255] The profile of circulating miRNAs reflects the patterns observed in the tumor tissues, suggesting the attractive possibility of using circulating miRNAs as easily detectable tumor biomarkers, especially for early diagnosis.[256] Moreover, it is possible to use miRNAs in gene therapy for reestablishing genetic disorders either as a drug or as potential drug targets.[15-18]

4.1.3. State-of-the-art in miRNA analysis

As the miRNA field continues evolving, an essential step is to develop efficient and reliable detection strategies toward understanding the functions of miRNAs in regulatory pathways. This knowledge can bring on the development of extremely accurate diagnostic tools and the development of miRNA-based therapies at molecular level as well as their use as new targets in drug discovery.[221] Using miRNAs as analytical indicators holds many advantages over the traditional protein biomarkers since there are far fewer miRNAs species compared to proteins.[257]

Northern blot and reverse-transcription real-time polymerase chain reaction (RT-qPCR) techniques are considered the benchmark methods for miRNA detection.[258, 259] For example, several novel miRNAs have been identified by Northern blotting analyses. However, this method has a poor sensitivity requiring large amounts of sample input, i.e. hundreds of micrograms as starting material and is relatively time-consuming. On the other hand, although RT-qPCR can cover a broad dynamic range of miRNA concentrations with a relatively high sensitivity, it requires highly purified samples. The lack of standardized protocols for miRNA extraction can introduce a high variability, leading to inaccurate analyses. In addition to these methods, microarray technology has been applied to the parallel detection of multiple miRNAs.[260] However, the complexity of miRNA labeling and narrow dynamic range of miRNA microarrays together with the difficulties for standardization, limit their routine use in centralized laboratories.

Although methods for the detection of nucleic acids are well established, accurate and reliable quantification of miRNAs still remains a challenging task. Only a small fraction of the mass in total RNA samples (~0.01%)[221] represents miRNA content. In addition, expression levels of miRNAs vary by as much as four orders of magnitude from a few copies to over 50000 copies per cell, requiring techniques with a wide dynamic range. Another issue is the sequence similarity among some miRNA-family members whose presence may distort the final analysis.

Taken together all these difficulties, it is clear that there is an unmeet need for rapid and highly sensitive and selective miRNA analysis methods that can effectively profile miRNA in minimal amounts of sample. Many biosensor methods have been proposed as alternative approaches to detect miRNAs for disease diagnose.[221, 261] Biosensors represent promising tools for the detection of miRNAs due to the advantages of preamplification-free analysis, limit of detections at the femtomolar (fM)- attomolar (aM) range, short time-to-results, multiplexing capability, and minimal sample preparation requirement, thus avoiding the introduction of measurement bias.

In this Chapter we explored different approaches for the development of highly sensitive optical biosensors for miRNA analysis. Different strategies were investigated for obtaining suitable LODs with the objective to cover the wide dynamic range of concentrations found in the miRNA expression levels in real situations. To that, we exploited the use of both the SPR and the BiMW biosensors. In addition, we took the advantages offered by the ultra-low fouling monolayer developed in **Chapter 2** for human samples evaluation.

4.2. miRNA-181a detection in SPR biosensor

4.2.1. miRNA-181a as biomarker

MiRNA-181a-5p (miR-181a) belongs to the miR-181 family which includes four highly conserved mature miRNAs (miR-181a, b, c, and d) derived independently from six precursors located on three different chromosomes. In particular, miR-181a is known to participate actively in reprograming cancer cell metabolism. The metabolism of cancer cells is significantly different from the normally differentiated cells. In order to grow and proliferate rapidly, cancer cells rely on aerobic glycolysis to generate energy instead of the oxidation of pyruvate in the mitochondria, which is the typical pathway to generate energy for cellular physiology.[262] Recent studies in cancer cells proved that miR-181a is directly involved in metabolic shift. MiR-181a targets *PTEN*, a gene codifying the phosphatase and tensin homolog (PTEN), an inhibitor of the glycolysis, through the miR-181a/PTEN/AKT cascade.[263] Overexpression of miR-181a suppresses *PTEN* expression by targeting its 3'-UTR region, resulting in increased AKT kinase phosphorylation.[264] AKT kinase promotes the metabolic shift to glycolysis favoring cell proliferation. On the other hand, inhibition of miR-181a expression have been proven to attenuate cell proliferation and, therefore, mitigate tumor progression.[263] Thus, miR-181a can be considered as an oncomiR that promotes the continuous proliferation of tumor cells and cancer development.

Aberrant expression of miR-181a has been reported in several types of cancer and appears to be significantly associated with the clinical outcome of cancer patients. Overexpression of miR-181a has been demonstrated in colon[263] and breast cancer,[265] hepatocellular carcinoma,[266] human gastric[267] and bladder cancer[268, 269] tissues. This suggest that this miRNA might be considered as a valuable biomarker of cancer development and can also be considered as a suitable target for tumor inhibition due to the growing evidence which indicates that reprogramming cancer metabolism could provide a positive impact in therapy.[270]

4.2.2. Optimization of the selective detection of miR-181a

The four members of the human miR-181 family (a, b, c, and d) contain similar sequences that differ only in one to four nucleotides (**Table 4.1**). Although all members preserve the same seed sequence, they have in many cases distinct gene targets as in the case of leukemia inhibitory factor, which is targeted by miR-181d but not by miR181a.[271] In addition, while miR-181a and miR-181c encode almost identical mature miRNAs, the strength and functional specificity of these miRNAs may be modulated through their pre-miRNA loop nucleotides and/or by additional post-transcriptional processes.[272, 273] This highlights the non-redundant function of miR-181 family members and adds a new layer of complexity to their role in cancer development, which makes mandatory the specific differentiation of these family members for establishing a proper diagnostic tool. Furthermore, the methodology should have a high capability to discriminate between the pre- and mature miRNA to elucidate miRNA function and to facilitate the translation of miRNA detection methods into the clinical practice.

To achieve the most selective detection of miR-181a against its homologous, we design an ss-DNA probe (miR-181a probe) complementary to the region containing all the nucleotide differences of the homologous, i.e. the homologous mismatches (see **Table 4.1**). MiR-181a would have a perfect match with such probe in contrast with the impaired nucleotides from the homologous, providing *a priori* some advantage to detect miR-181a over the other family members.

We employed the SPR biosensor for the optimization of the label-free and selective detection of miRNA-181a. We *in-situ* immobilized miR-181a probe with the optimized conditions described in **Chapter 2** for the SH-PEG antifouling monolayer (1 μM DNA probe and 1 μM SH-PEG CO_2H/NH_2) to avoid non-specific adsorption from real samples in future studies. We evaluated the hybridization efficiency of the four miRNAs at 50 nM in 5xSSC buffer to test the degree of cross-hybridization from each homologous sequence. **Figure 4.2** shows the specific sensor response for each miRNA family member. Despite the mismatches, most of the homologous showed equal or higher hybridization efficiencies than miR-181a.

Concretely, miR-181c, with only one nucleotide difference in its sequence compared to miR-181a, showed the higher signal, with 164% cross-hybridization. MiR-181d was the one with the lowest response, whereas miR-181b showed the same hybridization efficiency than miR-181a.

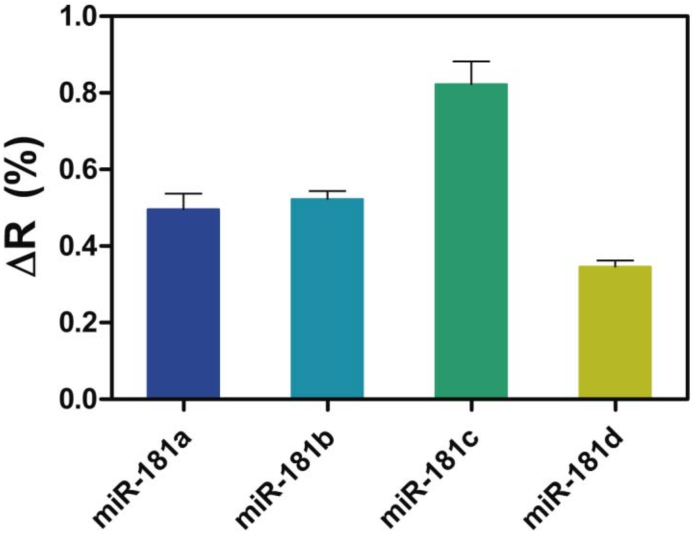

Figure 4. 2 Sensor responses of the miR-181s family members at 50 nM concentration during hybridization with miR-181a probe anchored at the SPR sensor surface.

In order to improve the selectivity and decrease the hybridization efficiency of the homologous sequences, the effect of different base-pairing destabilizers was studied. It is known that some compounds can exert some effects on the duplex stability by weakening the bonding of some particular nucleotides. By studying the effect of such additives taking into account the nucleotide content of the matching sequence, we can leverage the hybridization efficiency of the homologous over the specific target.

Tetramethylamonium chloride (TMAC) and glycine betaine have been reported to be isostabilizing agents, altering the melting temperature and making the hybridization solely dependent on oligonucleotide length independently of their GC content.[274-276] The destabilizing effect of such compounds increases with increasing GC content, with almost no effect on poly(dAdT). On the other hand, sodium perchlorate ($NaClO_4$) is a denaturing agent that acts to imperfectly matched targets. Some other components such as urea[276] promote discrimination during hybridization by decreasing the strength of AT/U more than GC base pairs.

To take advantage of such additives, we studied the nucleotide content of the different miRNAs in their matching sequences. **Table 4.1** shows the number of mismatches and AU/GC base pairing of the different miRNA family members with miR-181a probe. As can be appreciated, miR-181c has the highest complementarity (93%) compared to the rest of homologous and is expected to present the highest level of cross-hybridization. On the other hand, miR181d presents the most divergent sequence and is supposed to have less affinity to miR-181a probe. Most of the homologous had a high degree of GC base pairing. Therefore, their matches with the probe were most likely to rely on these types of bonds. On the other hand, AU base pairing was decreased in most of the cases in comparison with miR-181a. Thus, we endeavored to decrease the GC interaction strength by employing those additives that preferable favor their weakening such as TMAC and $NaClO_4$.

Table 4. 1 Matching sequences and complementarity of miR-181a and its homologous.

Name	Matching sequence	Nº mismatches	Nº AU base pairing	Nº GC base pairing	Complementarity (%)
miR-181a	ACGCUGUCGGUGAGU	0	6	9	100
miR-181b	UUGCUGUCGGUGGGU	3	3	8	80
miR-181c	AC-CUGUCGGUGAGU	1	6	8	93
miR-181d	UUGUUGUCGGUGGGU	4	4	7	73

In addition, the effect of a high percentage of FA (40%) was also evaluated since we demonstrated its remarkably positive effect in the hybridization efficiency and in the discrimination of homologous sequences in **Chapter 3**. As can be appreciated in **Figure 4.3**, all additives contributed to the increment in specificity of the miR-181a probe towards its target sequence in contrast to the decreasing signals of the homologous sequences. MiR-181a increased its affinity to the DNA probe in all cases. The highest response was achieved with the solution containing FA 40%, with an increment in the hybridization efficiency of 220%. The effect of FA also favored the discrimination of the homologous, decreasing the cross-hybridization in 29%, 60% and 71% for miR-181b, c and d, respectively. On the other hand, the presence of TMAC and $NaClO_4$ in the hybridization buffer also helped to reduce the hybridization efficiency of the homologous. Surprisingly for miR-181c, which shares a 93% of the sequence with miR-181a, such decrease in the SPR signal was particularly remarkable, reducing the cross-hybridization in 40% with respect to the solution without additives. These results evidence the possibility of reducing the hybridization efficiencies of miRNA sequences by altering the duplex formation with regard to oligonucleotide length and independently of GC content. Therefore, a high selectivity can be achieved by promoting the hybridization of the complementary sequence while decreasing the homologous ones by addition of such compounds.

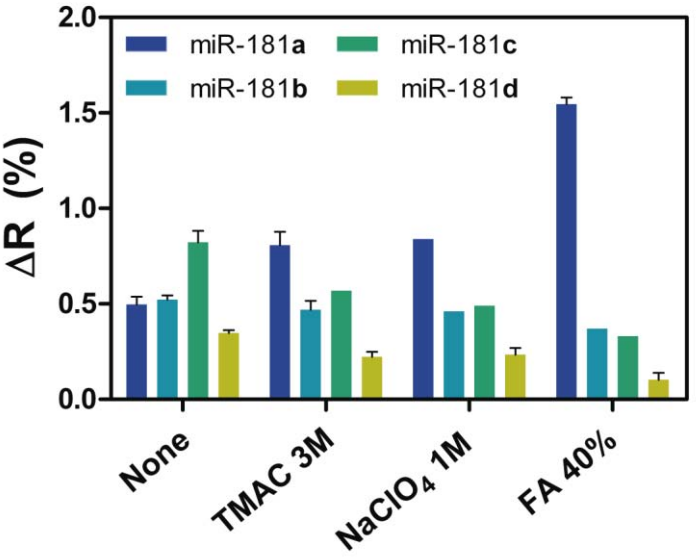

Figure 4. 3 Effect of the additives in the hybridization efficiencies with the miR-181a probe for the different miR-181s family members.

Due to the positive effect of such compounds in homologous discrimination, we tested the combination of the FA with the rest of additives in order to find the most appropriate buffer composition to achieve a total selectivity. As can be deduced from **Figure 4.4**, the combination of FA 40% with the different additives produced a decrease in the homologous miRNA signals as compared with the solution containing only FA 40%. MiR-181a signals showed no alteration among the different conditions tested. Combination of FA 40% with 3M TMAC produced the most selective detection of miR-181a, greatly reducing the non-specific hybridizations to negligible levels while maintaining a high specificity for miR-181a. Therefore, we used such cocktail for further analysis of miR-181a.

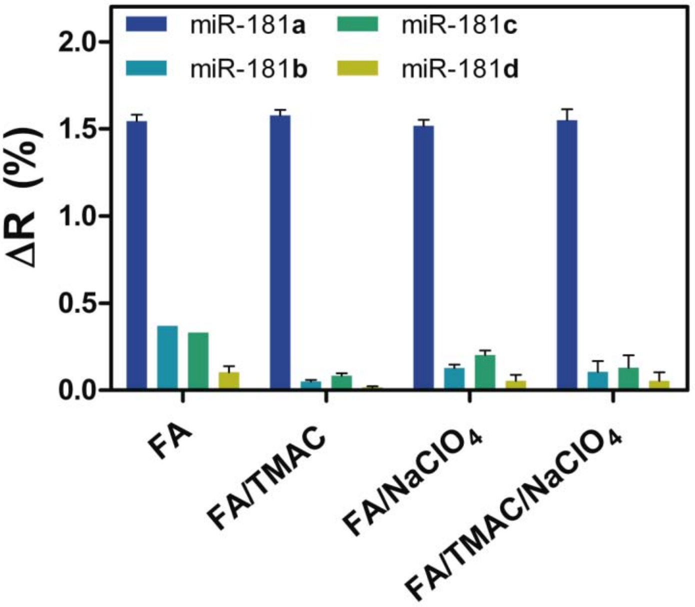

Figure 4. 4 Effect of the different additives in the hybridization efficiency of the miR-181s family members with the miR-181a probe in combination with FA 40%.

Finally, we tested the possibility of hybridization of the miR-181a precursor. Pre-miR-181a shares the same sequence than miR-181a and could fully match with the immobilized DNA probe. The interaction of this precursor with miR-181a probe may shade the detection of miR-181a, leading to an inaccurate analysis. Nevertheless, pre-miRNAs form a hairpin structure that may prevent from hybridization with the probe sequence at the sensor surface and which could have hindered the interaction of pre-miR-181a with the DNA probes at the sensor surface (**Figure 4.5A**). To demonstrate the discrimination of the pre-miR-181a with the developed methodology, we tested the SPR response after the injection of 50 nM of DNA-mimics of the pre-miR-181a sequence with the optimized hybridization solution. **Figure 4.5B** shows the sensor response for both pre-miR and miR-181a. As can be appreciated, the signal from pre-miR-181a drops until the baseline level, indicating that no-hybridization took place. Such results evidenced the specificity of the methodology for miR-181a detection and the discriminating effect over the pre-miR-181a.

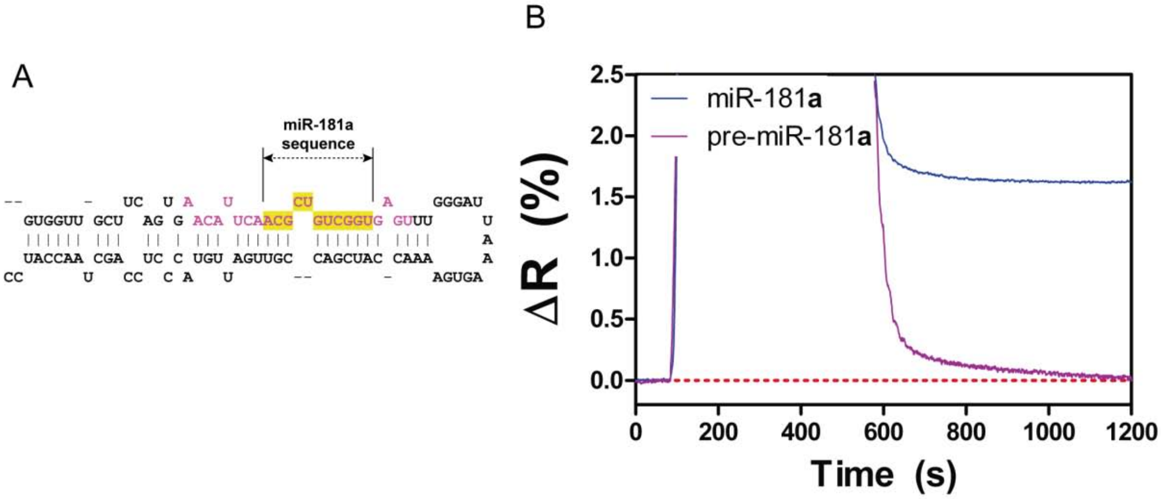

Figure 4. 5 Study of the hybridization selectivity of pre-miR-181a with miR-181a probe. (**A**) Sequence and secondary structure of pre-miR-181a. (**B**) SPR biosensor response to 50 nM of miR-181a and pre-miR-181a.

Once demonstrated the selectivity of the biosensor for miR-181a with respect to the rest of the family members and its precursor, a calibration curve was established. We employed the equilibrium values of the sensor response at different standard concentrations of this miRNA using the optimized hybridization conditions (5x SSC/ FA40%/ 3M TMAC) (**Figure 4.6**). The values were adjusted to a fitting curve and the LOD was determined.

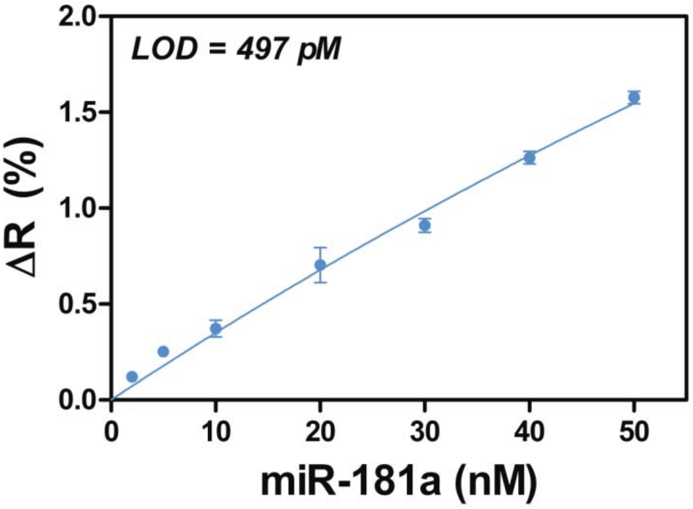

Figure 4. 6 Calibration curve of the specific detection of miR-181a by SPR. Solid line corresponds to the non-linear fit of the calibration curve. All data show mean ± SD of triplicate measurements.

As can be appreciated, we obtained a **LOD** of **497 pM** which was in the expected range for detection of short oligonucleotides by SPR biosensors.[60] Values at all tested concentrations showed %CV under the recommended values (≤ 13%) and the monolayers stood up to 60 cycles of hybridization/regeneration with no apparent loss in hybridization efficiency (2% CV). However, although the SPR biosensor sensitivity was in the pM/nM range, we had to take into account all the challenges encountered in the detection of miR-181a. The mandatory employment of a highly stringent hybridization buffer for the selective detection of such miRNA forced us to dilute the sample two-times which, in turn, affected negatively to the LOD. Therefore, in order to apply the SPR biosensor for real samples analysis an enhancement of the sensitivity is required.

4.2.3. SPR Antibody-DNA-RNA signal amplification

Due to the intrinsic sensitivity limitation of the SPR biosensor for the direct detection of small biomolecules, we could not cover the whole range of miRNA concentrations present in human samples (aM-nM). We decided then to add a signal-amplification step to obtain a more suitable detection limit.

One of most commonly employed amplification strategies for miRNA detection is the use of a specific antibody directed to DNA/RNA hybrids (i.e. anti-DNA-RNA antibody). This monoclonal antibody is generated against a bacteriophage-derived synthetic DNA–RNA antigen in mouse and recognizes RNA-DNA hybrids of various lengths.[277] It has high specificity and affinity for DNA-RNA hybrids and does not cross-react with single-stranded DNA or double-stranded DNA and RNA. Its amplification capabilities have been demonstrated in SPR[278] biosensor and in silicon microring resonator[279] based biosensor for the analysis of miRNAs in complex media. Both approaches showed a fast time to result achieving LODs in the pM-(sub)pM range. Due to the easy implementation and the high specificity and amplification achieved by the anti-DNA-RNA antibody, we decided to employ such strategy to obtain a higher sensitivity in the detection of miR-181a.

The strategy consisted in two recognition steps, as depicted in **Figure 4.7**. The first step corresponded to the capture of miR-181a by the specifically designed miR-181a probe at the optimized conditions, which will give rise to a signal proportional to the concentration of the miRNA. Secondly, a certain concentration of the anti-DNA-RNA antibody will contact the hybridized monolayer. The antibody will bind to the DNA-RNA duplexes leading to a signal proportional to the concentration of hybridized miRNA. Thus, at very low miRNA concentrations which signals may not be possible to directly monitor by the SPR biosensor, we could obtain an amplified signal by the antibody in the second step. It would allow for the quantification of miRNA concentrations out of the range of the detection limit of the SPR biosensor.

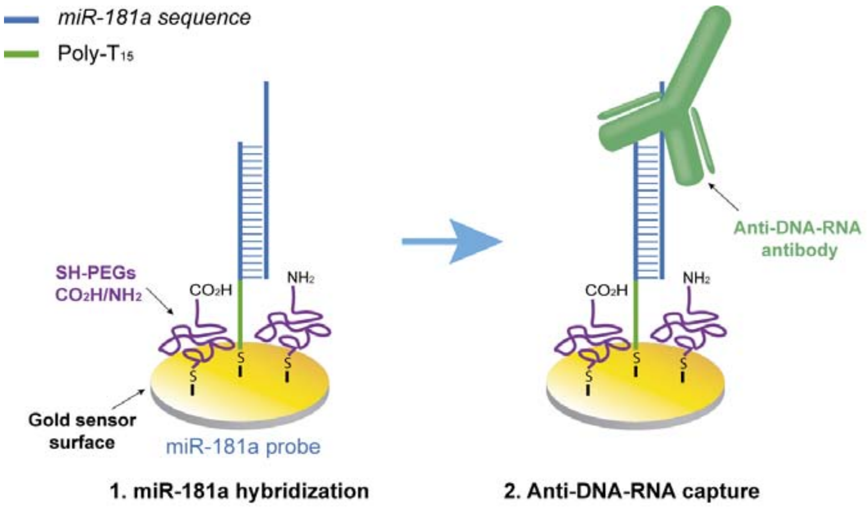

Figure 4. 7 Schematic representation of the antibody-based amplification SPR approach for miRNA-detection.

First, an optimization of the anti-DNA-RNA concentration to be employed in the second recognition step was performed to get a maximum amplification signal. The most suitable concentration of antibody would produce a signal close to the saturation level in order to achieve the maximum signal with the minimum quantity of antibody. In the first recognition step, 50 nM of miR-181a were hybridized at the optimized conditions described above. Subsequently, different antibody concentrations (0.5, 1, 2 and 3 µg/mL) diluted in Tris_{Mg} buffer[278] were tested. **Figure 4.8** shows the results for all the antibody concentrations. A saturation signal of the antibody (ΔR (%) = 1.3) was observed at concentrations equal or higher than 2 µg/mL. Therefore, for the antibody recognition step, we employed a concentration of 2 µg/mL, which will guarantee the maximum signal possible.

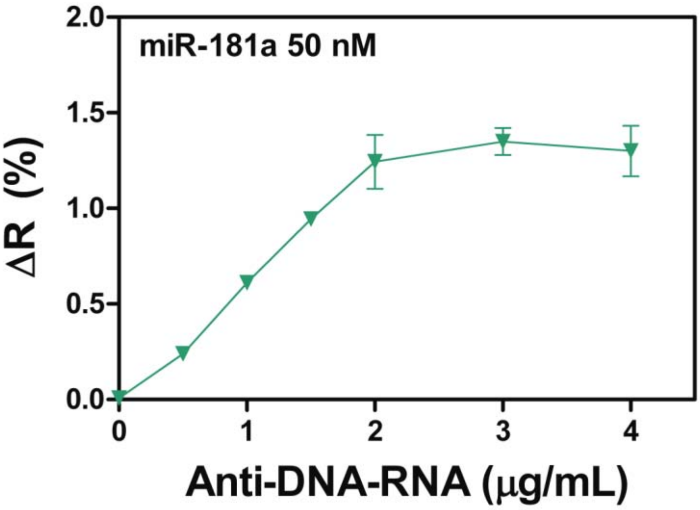

Figure 4. 8 Evaluation of anti-DNA-RNA antibody concentrations for the optimization of the signal amplification step.

Next, the efficiency of the antibody capture was optimized. For that purpose we employed three different buffer solutions at different saline concentrations and evaluated the antibody response. As can be observed in **Figure 4.9**, all buffers showed the same antibody response at 1x concentration and it decreased with increasing or decreasing saline concentrations. However, 0.5x SSC buffer greatly increased the antibody response by 80% compared to the other buffer solutions. Because of the strong antibody binding facilitated by 0.5x SSC buffer, it was used in further experiments. This increment in antibody response would enhance the final LOD obtained after the application of the second amplification step.

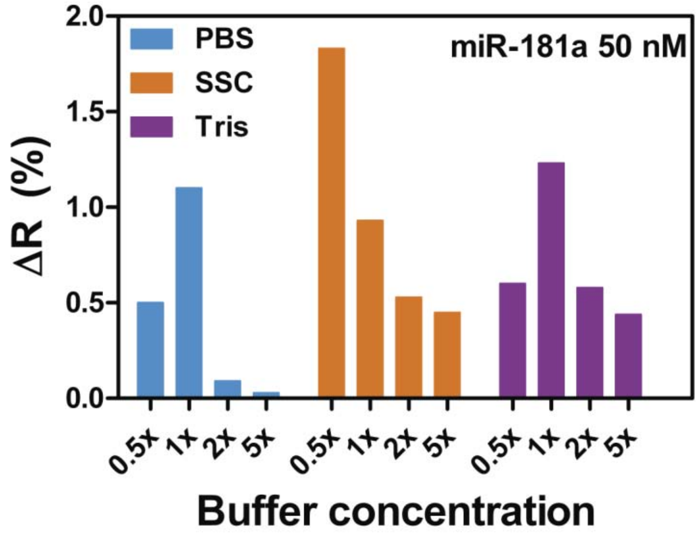

Figure 4. 9 Effect in antibody capture efficiency after hybridization of 50nM miR-181a in different buffers (PBS, SSC and Tris) at several concentrations (0.5, 1, 2 and 5x).

Finally, an evaluation of the sensitivity during the amplification step was addressed. To that, we tested the possible nonspecific binding of the anti-DNA-RNA antibody in two different scenarios: (i) when using a nonspecific miRNA as target analyte (e.g. miR-194), and (ii) when employing a DNA mimic of miR-181a (miDNA-181a). The latter test determines the specificity of the antibody to DNA-RNA duplexes. The sensor responses are presented in **Figure 4.10**. As can be observed, only the samples containing the target sequence miR-181a gave positive shift in the sensor for both detection steps. In contrast, injection of a nonspecific miRNA (black line) did not induce any response, indicating that no hybridization took place. After that, injection of the antibody also resulted in null signal. This demonstrated the absence of nonspecific adsorption of the antibody onto the sensor surface. On the other hand, injection of miDNA-181a resulted in an expected capture by the miR-181a probes, showing a similar signal to the specific target miR-181a. However, antibody amplification step resulted in negligible signal, proving the specificity of the antibody in DNA-RNA hybrid recognition.

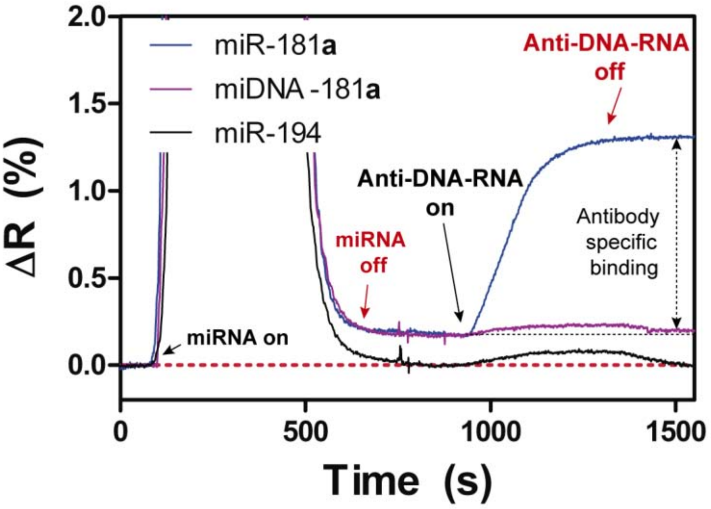

Figure 4. 10 Antibody specificity test by SPR real-time evaluation.

Due to the different nature of the bond established between the antibody and the hybrid, the regeneration with FA35% was also evaluated in order to assure a complete removal of both molecules from the monolayer for repeated uses of the same sensor chip. *A priori* it was expected that FA would destabilize the duplex formed between the miRNA and the DNA probe which, therefore, would induce the break of the bond between the antibody and the hybrid. We evaluated the sensor response after various regeneration processes with FA35%. Regeneration signals provided negative shifts in the baseline level comparable to the sum of the positive shifts given by both the miRNA binding and the antibody binding, as shown in **Figure 4.11**. These results demonstrated that the FA 35% solution is an adequate regeneration solution for this methodology as we previously hypothesized.

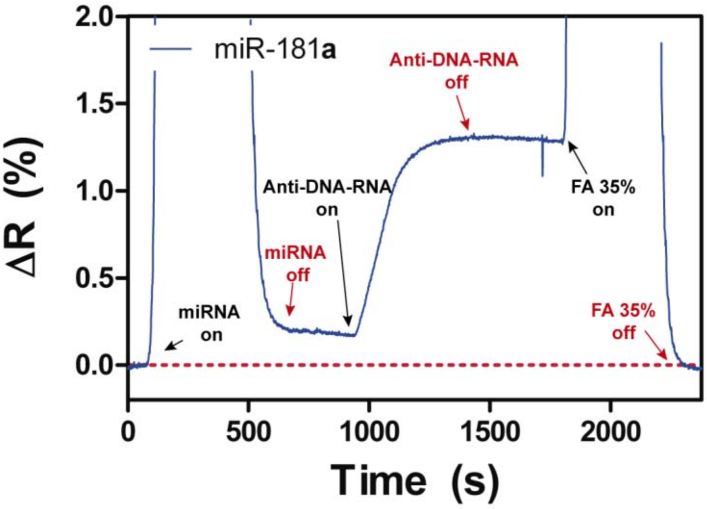

Figure 4. 11 SPR test for the surface regeneration efficiency of FA 35% after the miRNA/antibody recognition.

Finally, after optimization of the amplification conditions, the enhancement of the biosensor sensitivity was evaluated. Detailed sensor response to antibody amplification for low concentrations is displayed in **Figure 4.12A**. The concentrations were too low to produce detectable sensor response upon hybridization in the first step of detection. However, after injection of the antibody, a clear sensor signal could be observed for miR-181a concentrations equal or higher than 10 pM. The antibody significantly enhanced the sensitivity of miR-181a detection, giving a signal directly proportional to the concentration of DNA:RNA hybrids formed in the first step. **Figure 4.12B** represents the calibration curve obtained from miR-181a concentrations ranged from 10 pM to 10 nM (CV ≤ 9%). As shown in the figure, the LOD for antibody-amplified detection was **1.7 pM** ($R^2 = 0.99$) and the lowest quantifiable signal (LOQ) was 5.7 pM. The second amplification step resulted in a detection limit of nearly 300-fold better than the achieved with no amplification, allowing for the detection of this miRNA in the low-pM/nM range. These results are in good agreement with other studies, where the capability of measuring miRNAs by an SPR biosensor through antibody-amplification was demonstrated.[278]

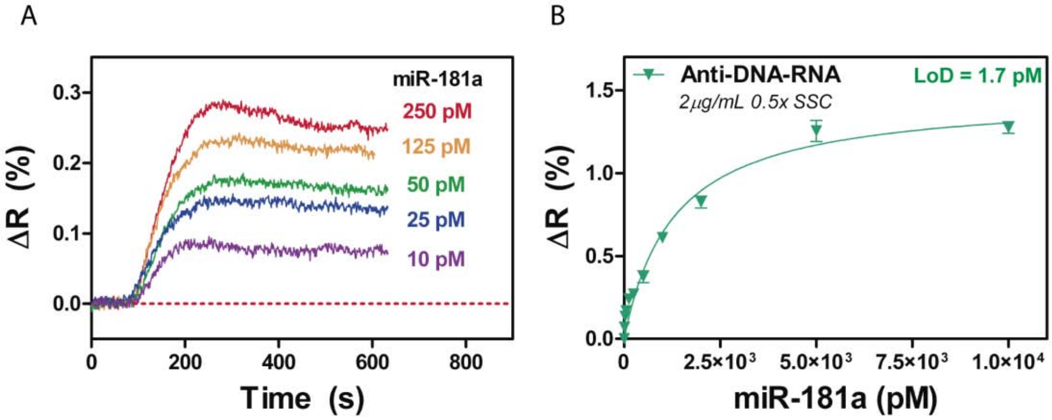

Figure 4. 12 Antibody amplification to non-detectable signals of miR-181a by SPR biosensor. (**A**) Sensograms for the antibody-amplified signals at low concentrations of miR-181a (from 10 to 250 pM). (**B**) Calibration curve obtained for the antibody amplification after hybridization of different

concentrations of miR-181a at the optimized conditions. Solid line corresponds to the non-linear fit of the calibration curve. All data show mean ± SD of triplicate measurements.

4.2.4. Detection of miR-181a in biological samples by SPR

In order to demonstrate the capabilities of the SPR biosensor, the analysis of real human samples was addressed. As described previously in **section 4.2.1**, miR-181a is involved in the development and proliferation of various types of cancers and its overexpression has been demonstrated in both circulating biofluids and tumor tissues. Among the different cancer types, we selected bladder cancer for a preliminary evaluation of the biosensor strategy as a rapid and non-invasive diagnostic tool. Bladder cancer is the fifth most common malignancy occurring worldwide and a major cause of cancer morbidity and mortality.[280] Current standard methods used to detect and monitor bladder cancer are invasive or have low sensitivity. Cytoscopy and cytology are the standard methods used so far in bladder cancer diagnosis. The former one has a high sensitivity, but constitute an invasive technique, while the latter one is non-invasive but lacks sensitivity, especially for low-grade disease.[281] These limitations of the current diagnostic methods have prompted a search for more reliable non-invasive tools. For example, an accurate urinary test to detect bladder cancer would improve patients quality of life and outcome. Currently, less-invasive methods based in urine tests have been commercialized but even though most of them are more sensitive, urine cytology continues to be more specific. Using microRNA profiling in urine samples to develop a non-invasive test for bladder cancer is of great interest. In addition, their stability in human urine supports their biomarker potential.[282] MiRNA screening in urine has demonstrated detectable miRNA species in such biofluid and differences in the miRNA spectra suggests the possibility that changes in the miRNA composition in urine can be used to identify physiopathological conditions.[283]

Prior to analyze patient samples, an evaluation of the miRNA detection in the urine matrix was carried out. The different salinity, pH or protein content of the urine samples may influence on the specific recognition of miR-181a. Different concentrations of synthetic miR-181a were spiked in control urine samples from a healthy donor. We diluted 1:1 the urine samples with the developed hybridization buffer to provide the required specificity for miR-181a detection. A calibration curve was obtained and the LOD was determined for miR-181a detection in urine samples (**Figure 4.13**). The detection limit achieved in spiked-in urine samples was **538 pM**, very similar to the one obtained in buffer (497 pM), suggesting that miR-181a detection was not affected by the presence of urine in the samples. In addition, sensor signals were very reproducible with %CV < 13% over more than 43 hybridization/regeneration cycles, which denotes the strong resistance of the monolayer against the harsh conditions caused by the urine.

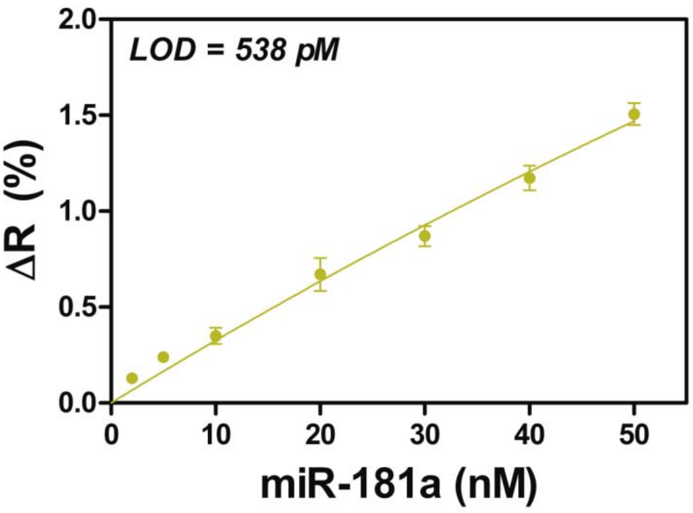

Figure 4. 13 Calibration curve obtained in urine with the developed methodology for the specific detection of miR-181a. Solid line corresponds to the non-linear fit of the calibration curves. All data show mean ± SD of triplicate measurements.

To demonstrate the utility of the label-free detection method, the methodology was employed to quantify the miR-181a levels in total RNA directly from urine samples from both, healthy donors (control samples S1 and S2) and two bladder cancer patients (samples S3 and S4). Since the specific values of miR-181a are expected to be too low to be directly quantifiable by SPR, we employed the post-amplification method through the anti-DNA-RNA antibody. First, urine samples were preheated at 90 ºC for 1 min. In contrast with the spiked-in miRNAs, endogenous miRNAs are normally associated with proteins, which may difficult their detection. A preheat step may induce the precipitation of this proteins and, therefore, the dissociation from the miRNAs.

As can be appreciated from **Figure 4.14**, no significant difference was observed between baseline levels in the healthy donor samples after injection of the antibody, indicating that the concentration of miR-181a in the sample was lower than the limit of detection of the biosensor (1.7 pM). On the other hand, antibody amplifications gave rise to small changes in the biosensor response in S3 and S4 samples, indicating that a low quantity of miR-181a hybridized in the first recognition step. By employing the calibration curve for the antibody recognition and by applying the pertinent dilution factor, the concentration obtained for miR-181a in S3 and S4 were 12.49 pM and 13.48 pM, respectively.

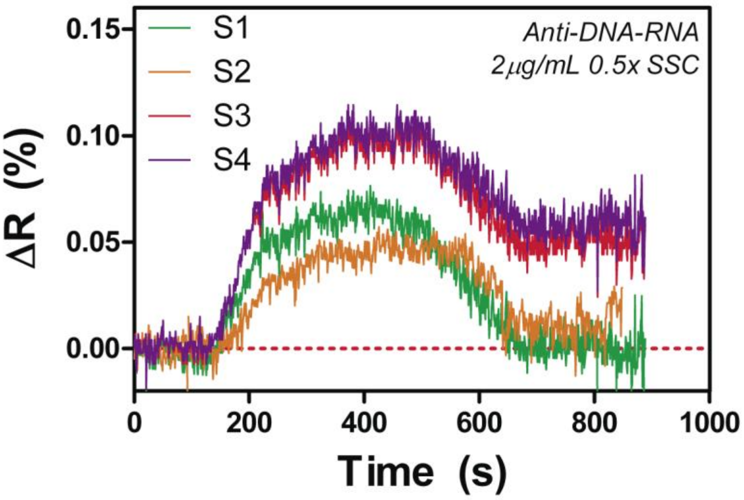

Figure 4. 14 Real-time sensograms for different urine samples from healthy donors (S1 and S2) and bladder cancer patients (S3 and S4).

These results evidence the difference in miR-181a concentration between healthy and bladder cancer urine samples. However, despite the signal amplification step by the Anti-DNA-RNA capture, the SPR biosensor sensitivity did not achieve the expected values for a more precise diagnosis. Therefore, new strategies should be explored to improve the sensitivity, such as the employment of the BiMW biosensor.

4.2.5. Conclusions

We have developed a protocol in the SPR biosensor for the selective detection of miRNAs in human fluids. We have chosen miR-181a as an example of a miRNA biomarker for cancer diagnose due to its direct implication in cancer cell metabolism. We addressed two of the main challenges in miRNA detection: (i) the selectivity by discrimination of the miR-181a family members and (ii) the high sensitivity required (i.e. aM – pM level). Selective detection of miR-181a was achieved by the implementation of a specific hybridization buffer that allowed for the discrimination of its three homologous miRNAs, which presented differences even at the single-nucleotide mismatch, and its pre-miRNA. Due to the narrow-range of concentrations affordable in a direct analysis, a signal-amplification step was optimized by the employment of an anti-DNA-RNA antibody. We have optimized the methodology to achieve the maximum efficiency from the post-amplification step and we have lowered the limit of detection in one order of magnitude, greatly increasing the dynamic range of the methodology. Finally, the feasibility of the methodology was demonstrated by detection of miR-181a in urine samples from healthy donor and bladder cancer patients. A small increment was noticed in miR-181a concentration between control and bladder cancer patient's samples, which demonstrated its different expression and suggested a possible important role of this miRNA in the onset of such disease. Despite the excellent results achieved by this methodology, we could not be able to guaranty the expression levels of miR-181a from the healthy donor due to the insufficient limit of detection of the SPR methodology, making difficult the determination of a cut-off for bladder cancer prediction.

4.3. BiMW: highly sensitive detection of miRNAs

Although a strong effort has been focused in the detection of miRNAs with biosensors very few works have shown sensitivity levels covering the required aM-nM range of miRNA concentrations without amplification processes and labeling. Recently, a technology based on localized surface plasmon resonance (LSPR) using highly sensitive nanostructures (gold nanoprisms) achieved the direct detection of miRNAs at a LOD 92 aM in complex media avoiding the need for an amplification step.[284] However, it required very long hybridization/regeneration times (≈14h) which resulted in a slow analysis for a single miRNA.

In addition, as mentioned before, a single gene can be simultaneously regulated by multiple miRNAs, which requires methods to detect multiple miRNA to fully understand the important and complex function of these tiny regulators. Considerable effort is continuously devoted to explore high-throughput analysis strategies of multiplexed miRNA gene expression. However, despite these advances, these techniques have not shown a rapid detection of miRNAs with high sensitivities in a single reaction with the capability of multiplexing yet, which is a main requirement for routine clinical applications due to the limited sample quantity, low abundance of target molecules, and complexity of the sample composition.

Integrated interferometric biosensors as BiMW devices constitute highly sensitive analytical platforms with a miniaturized size that allow multiplexed format. They represent an ideal platform for the direct and multiple miRNA analysis in complex samples avoiding pre- and post-amplification steps and with minimal sample input, thus saving time and resources. Recently, a novel integrated optical biosensor based on a slot waveguide Mach-Zehnder interferometer (MZI) configuration has been developed for miRNA detection.[285] It allowed a rapid, accurate, and multiplexed detection of miRNAs in human urine samples in a single reaction. Nevertheless, despite of its advantages presented, sensitivity levels (≤1nM) were still far from reach the required ones. For that reason, BiMW device constitutes a valuable alternative for miRNA detection due to its high sensitivity and its capability to incorporate different biorecognition elements for multiplexed analyses.

4.3.1. miR-181a specific detection by BiMW

Due to the great advantages offered by the BiMW device, we transferred the biosensing strategy previously developed with the SPR sensor and evaluated the analytical performance for the direct detection of miR-181a. We functionalized the BiMW biosensor surface following the described silanization protocol optimized in **Chapter 2**. The BiMW chip was placed into the microfluidic cell and a solution of SH-miR-181a probes with SH-PEG NH_2/CO_2H was injected. The sensor signal gave an increment in the sensor response of $\Delta\Phi$ (rad) = 60, which is in good agreement with other *in-situ* immobilization processes previously performed with the same biofunctionalization protocol. For detection assays, we also took into account the previously optimized conditions with the SPR biosensor (i.e. hybridization buffer: 5x SSC/ FA40%/ 3M

TMAC). In this case, we employed the hybridization buffer also as the running buffer to avoid excessive bulk refractive index change due to the high sensitivity of the BiMW biosensor.

We tested the selectivity by monitoring the biosensor response after the injection of the different homologous as well as the pre-miR-181a at a 100 pM concentration.. As can be seen in the sensogram depicted in **Figure 4.15**, all non-specific sequences returned to the baseline after the replacement with the running buffer, while miR-181a produced a clearly appreciable positive shift in the biosensor response (ΔΦ (rad) = 2.8), confirming the selective detection of miR-181a and the total discrimination of homologous sequences.

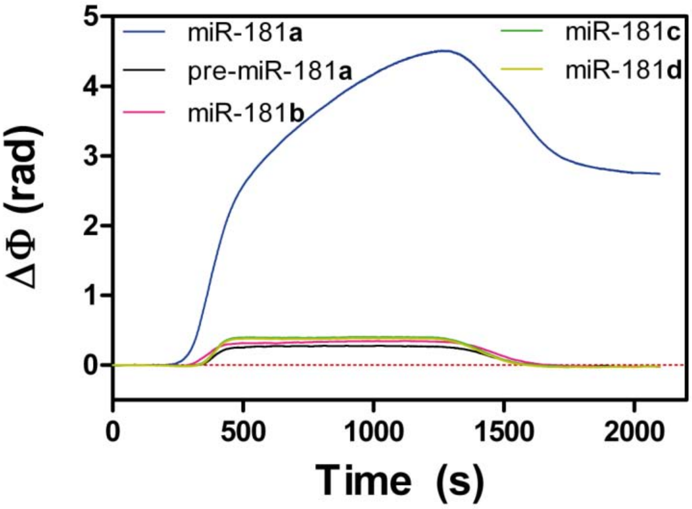

Figure 4. 15 BiMW sensogram demonstrating the specificity of the developed methodology.

In order to assess the sensitivity of the BiMW biosensor, we performed a calibration curve for the direct analysis of miR-181a in buffer conditions. We employed different concentrations of miR-181a from standard solutions covering a wide range of concentrations, from 10 aM to 10 pM, and fitted the signals to a dose-response curve. As can be observed in **Figure 4.16A**, the BiMW device was able to clearly detect a wide range of miR-181a concentrations achieving an ultra-low LOD of **20 aM** (R^2 = 0.99). The obtained LOD was 1 million times better than the one achieved with the previously described miR-181a antibody-based SPR detection and 4 times more sensitive than the miRNA LSPR-based detection (92 aM) previously published.[284] Our biosensor was capable to clearly monitor miR-181a interactions at concentrations as low as 100 aM directly without pre- or post- amplification processes as shown in the sensogram (**Figure 4.16B**).

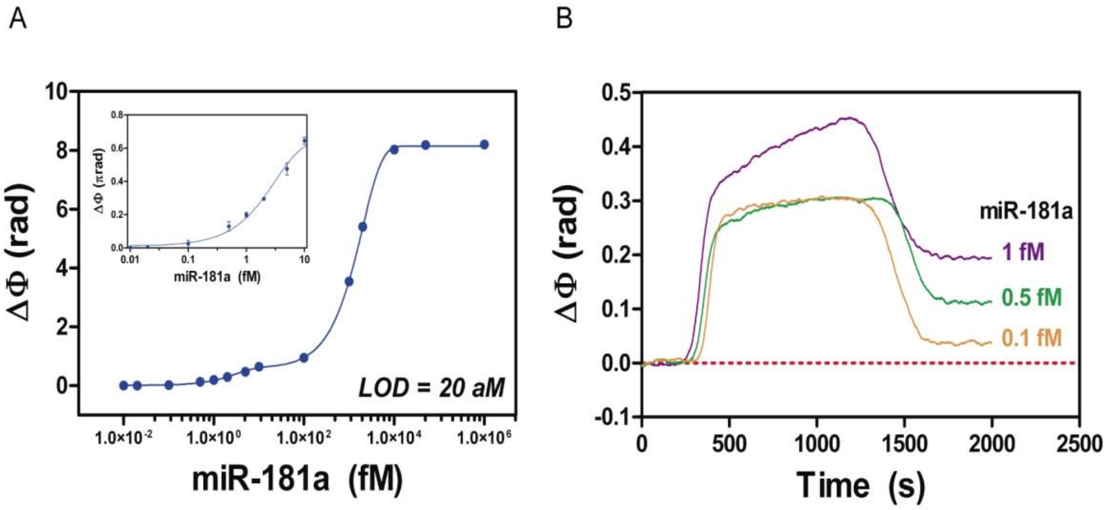

Figure 4. 16 Detection of miR-181a by the BiMW biosensor. (**A**) Calibration curve obtained by employing different concentrations of miR-181a standard solutions. Solid line correspond to the exponential fit of the calibration curve. All data show mean ± SD of triplicate measurements. (**B**) Sensograms obtained for the lowest concentrations experimentally measured by the BiMW biosensor.

The biosensor showed signal stability up to 45 hybridization/regeneration cycles (%CV ≤ 7%), evidencing a very competent half-life of the biosurface and procuring a robust biosensor platform for several analyses with the same monolayer.

4.3.2. Detection of circulating miR-181a in urine samples by BiMW

Next, the analysis in real human urine samples was addressed. In order to ensure the anti-fouling properties of the monolayer, a urine sample from healthy individual was first flowed over the BiMW interferometer modified only with a 100% SH-PEG NH_2/CO_2H at a 1 μM concentration. Such monolayer would help to assess the anti-fouling properties. We also analyzed the response of the monolayer containing the complementary probe for miR-181a. The samples were diluted 1:1 in the highly selective, anti-fouling hybridization buffer and injected in the flow delivery system. Variations in BiMW response were monitored in real time. As can be appreciated in **Figure 4.17**, the control monolayer did not show any increment in the signal at the equilibrium after the injection of the urine sample. On the other hand, an increment of ΔΦ (πrad) = 1.69 was appreciated in the monolayer modified with the specific probe for miR-181a. These results confirmed that the methodology was highly specific toward the target miRNA and manifested that in case we obtained a positive signal in the BiMW biosensor, it would presumably come from the specific hybridization of miR-181a to the immobilized probe at the biosensor surface.

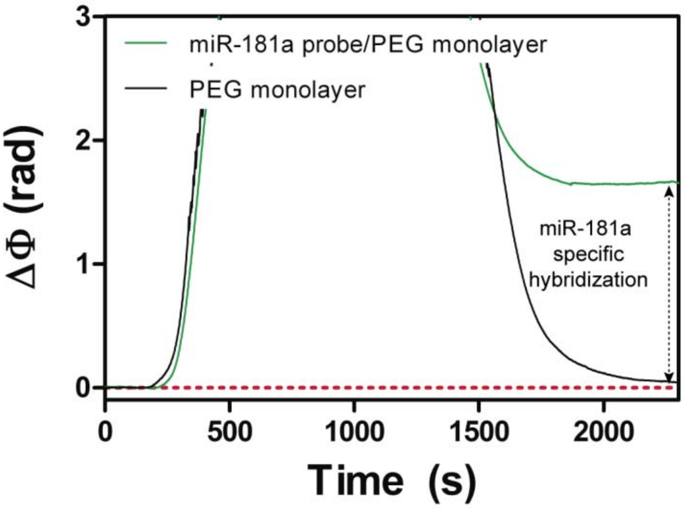

Figure 4. 17 BiMW biosensor assessment of the anti-fouling properties of the employed methodology.

We decided to test the viability of our BiMW biosensor for the diagnosis of bladder cancer as we did with the SPR biosensor. We analyzed the four urine clinical samples from both healthy donors (S1 and S2) and bladder cancer patients (S3 and S4). According to the SPR results described above, bladder cancer samples were expected to be above 10 pM concentration, which was already in the saturation region of the calibration curve obtained for the BiMW biosensor. Therefore, to avoid saturating signals and to perform an accurate analysis, samples were diluted 1:10 with the hybridization buffer to obtain a suitable concentration for their interpolation. The signals obtained for each sample were converted into the corresponding concentrations using the calibration curve derived for miR-181a and corrected by the dilution factor (**Figure 4.18**). Both healthy donors showed similar miR-181a expression (0.63 and 0.58 pM for S1 and S2, respectively). BiMW biosensor results indicated that miR-181a levels were higher in bladder cancer patients (15.1 and 18.3 pM for S3 and S4, respectively) compared to healthy control subjects, showing a 28 fold-change. These results indicated a clear differently expression of miR-181a between healthy individuals and bladder cancer patients, which suggested a possible direct implication of such miRNA in the onset of this malignancy. The miRNA can be quantified with high accuracy using the BiMW biosensor in a wide range of concentrations without the need of any modification, amplification, or labeling. Additionally, the results for bladder cancer patient samples corroborated the results previously obtained with the SPR biosensor for bladder cancer patients (**Table 4.2**), showing a good agreement in their quantification. Differences between the two biosensors performances can be explained due to their sensitivity differences.

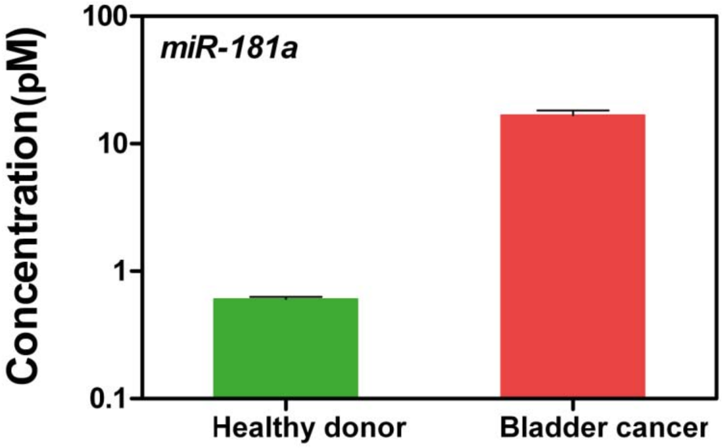

Figure 4. 18 Concentrations of miR-181a in urine samples quantified by the BiMW biosensor.

Table 4. 2 MiR-181a concentration values determined in four different urine samples by SPR and BiMW biosensors.

Sample name	**Description**	**Concentration (pM)**	
		SPR	**BiMW**
S1	Healthy donor	N/D	0.63
S2	Healthy donor	N/D	0.58
S3	Bladder cancer	12.5	15.1
S4	Bladder cancer	13.5	18.3

4.3.3. Conclusions and future perspectives

We have applied for the first time the BiMW biosensor for the specific detection of miRNAs. We have demonstrated its specificity for miR-181a and the excellent discrimination of pre-miR-181a and homologous miRNAs even with a single nucleotide mismatch. We also corroborated its specificity by employing a different miRNA (miR-194). The methodology showed a **LOD** of **20 aM**, which represents the most sensitive approach for miRNA detection so far described for direct detection and quantification of miRNA levels without amplification or labeling steps. We proved that our biosensor could be regenerated through several detection cycles without compromising its sensitivity and selectivity, which represents a simple and cost-effective tool for the early detection of miRNAs and can facilitate the diagnosis of various types of cancers. The BiMW biosensor can be implemented for the simultaneous detection of other miRNAs permitting the multiplex detection of a set of miRNAs at once.

The anti-fouling monolayer generated at the sensor surface allowed for direct measurement of urine samples without purification steps with apparently non-specific adsorptions. Moreover, we have demonstrated overexpression of miR-181a in bladder cancer patients as compared to control individuals, suggesting for the first time the direct implication of this miRNA in the outcome of this type of cancer. The results were in good agreement with the analysis performed with the SPR biosensor for bladder cancer samples. Further studies should be done to confirm the implication of this miRNA in bladder cancer through metabolic shift and to establish a proper cut-off for the early determination of cancer onset.

4.4. Materials and Methods

4.4.1. miRNA sequences.

MiRNA sequences for probes and target design were obtained from the miRNA data base miRBase, (http://www.mirbase.org). All DNA probes and RNA synthetic targets are summarized in **Table 4.3.** DNA probe sequences incorporate a SH- functional group at the 5'-end to enable coupling with gold surfaces and PDITC-activated monolayer in Si_3N_4 surfaces. *Oligo Analyzer* software and RNA fold webserver have been employed for secondary structure and self-annealing prediction of the probe and targets.

Table 4. 3 Sequences for probes and DNA/RNA synthetic targets employed in this Thesis.

Name	Sequence
miR-181a probe	5'-PolyT$_{15}$-ACTCACCGACAGCGT 3'
Pre-miR-181a	5'GUGGUUGCUUCAGUGAACAUUCAACGCUGUCGGUGAGUUUGGGAUUAAAGUGAAAACCAUCGACCGUUGAUUGUACCCUCCAGCUAACCAUCC 3'
miR-181a	5'AACAUUCAACGCUGUCGGUGAGU 3'
miR-181b	5'AACAUUCAUUGCUGUCGGUGGGU 3'
miR-181c	5'AACAUUCAACCUGUCGGUGAGU 3'
miR-181d	5'AACAUUCAUUGUUGUCGGUGGGU 3'
miR-194	5'UGUAACAGCAACUCCAUGUGGA 3'

4.4.2. SH-MiR-181a probe immobilization.

DNA-probe/SH-PEGs mixed monolayers at different molar ratios (0:1 and 1:1) (2 µM) in PBS 50 mM (pH 7) were *in-situ* immobilized on the bare gold sensor chip and PDITC-activated BiMW surface (silanization protocol described in **Chapter 2**) at 12 µL/min rate.

4.4.3. Detection conditions.

miRNA target detection was performed by injection of 250µL of the samples into the biosensors at a 15 µL/min rate and subsequent hybridization with their complementary DNA probes immobilized on the sensor surface. These samples were dissolved in 5xSSC (0.75 M in NaCl, 0.075 M in sodium citrate) with several additives, such as 40% FA and 3M TMAC for improving specificity. Finally, target-probe interactions were disrupted by employing 35% FA. Calibration curves were obtained by triplicate measurement of different dilutions from standards of known concentration. The mean and the standard deviation (SD) of each concentration were plotted versus the target concentration and fitted to a curve. The best fitting was employed in each case. For SPR, measurements were fitted to a one-site specific binding curve while for miRNA detection in BiMW an exponential fitting was employed due to the wide-dynamic range of concentration covered.

4.4.4. Urine samples.

For miR-181a detection study, the urine samples were kindly provided by the Group of Dr. M. Sánchez-Carbayo from the Center for Cooperative Research in Biosciences (CIC Biogune), Bizkaia (Spain). Samples were collected from bladder cancer patients and healthy donors and stored in a volume of 500 µL at -80ºC until their use. For their analysis, samples were unfrozen and diluted 1:10 in the highly stringent hybridization buffer for BiMW analysis and 1:1 for SPR measurements.

Chapter 5·DNA methylation profiling for cancer diagnosis

In this chapter, the analysis of DNA methylation is presented as one of the most important Epigenetic marks due to its direct implication in cancer development. A proof-of-principle for DNA methylation profiling through optical biosensors is described. SPR biosensor is employed for the direct detection of methyl-cytosines in the DNA sequence without requiring complicated processes and with minimal sample manipulation. The main advantages and limitations of the methodology are discussed, and different alternatives to improve the performance are proposed.

5. DNA methylation profiling for cancer diagnosis

5.1. Introduction

During development, most cells in higher eukaryotes differentiate without detectable changes in DNA sequence. However, the differentiation of a given cell type is associated with activation of particular set of genes and inactivation of other sets. Chromatin structure plays an important role in the regulation of such genes, changing its structure to a more loose (referred to as euchromatin) or packaged states (i.e. heterochromatin) to promote or repress gene transcription, respectively. Heterochromatic regions of the genome are generally characterized by increased chromatin condensation and decreased access to regulatory proteins.[286] Such genome regions are stably inherited and thus must contain one or more epigenetic marks to direct its maintenance during cell division. One of such marks has been under intense scrutiny: the methylation of the genomic DNA.[287]

5.1.1. DNA methylation mechanism

DNA methylation takes place at the cytosine bases of eukaryotic DNA by the covalent post-replicative addition of a methyl group (–CH_3) onto the 5-carbon of the cytosine ring[288] by DNA methyltransferase (DNMT) enzymes. Usually, the altered cytosine residues are immediately adjacent to a guanine nucleotide. It results in two-methylated cytosine residues placed diagonally to each other on the opposing DNA strands. Different members of the DNMT family of enzymes act either as de novo DNMTs, establishing the initial pattern of methyl groups in place on the DNA sequence, or as maintenance DNMTs, copying the methylation from an existing DNA strand to the newly replicated partner. Briefly, this mechanism involves DNMT binding to the DNA, eversion of the target nucleotide to project out of the double helix (“base flipping”), and transfer of the methyl group from *S*-adenosyl- l-methionine (AdoMet) to the activated cytosine C5[289] (**Figure 5.1**). In mammals, methylation is found sparsely but globally, distributed in definite CpG sequences throughout the entire genome, with the exception of CpG islands, or certain stretches (approximately 1 kilobase in length) where high CpG contents are found.

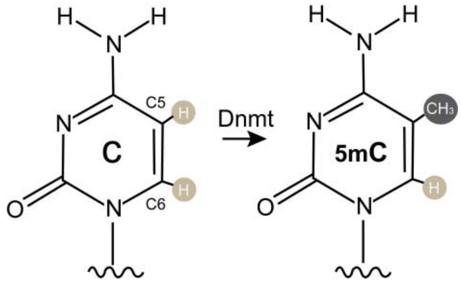

Figure 5. 1 DNA cytosine methylation.

For many years, methylation was believed to play a crucial role in repressing gene expression, probably by blocking the promoters and impeding the binding of activating transcription factors. Presently, it is known that it plays an essential role in cell differentiation and embryonic development. Moreover, methylation is crucial in gene expression. Thus, during cell development, despite of presenting invariable genetic information, a cell can show different epigenomes along its life.

Approximately, 60% of human promoters are characterized by a high CpG content.[290] However, the determinant factor in gene expression does not rely on the CpG density, but in the methylation process itself. Normally, these islands are unmethylated in genes transcriptionally active, whereas silenced genes show to be methylated in their promoter region (i.e. tissue-specific or developmental genes). This process can be reverted, giving the cell the capability of self-regulating along its growth and development.

5.1.2. DNA methylation and cancer

Aberrant DNA methylation was the first epigenetic mark to be associated with cancer as a consequence of the alteration in normal gene regulation.[291] While overall methylation levels and completeness of methylation of particular promoters are similar in individual humans, there are significant differences in overall and specific methylation levels between different tissue types and between normal cells and cancer cells from the same tissue. These alterations can be of three types: (i) DNA hypermethylation, i.e. the gain of methylation at specific sites that are normally unmethylated; (ii) DNA hypomethylation, mainly associated with losses of DNA methylation; and (iii) loss of imprinting, referring to the loss of parental allele-specific monoallelic expression of genes due to aberrant hypomethylation profiles at one of the two parental alleles. Any of these alterations in the methylation pattern, i.e. methylome, can cause the origin of cancer (**Figure 5.2**).

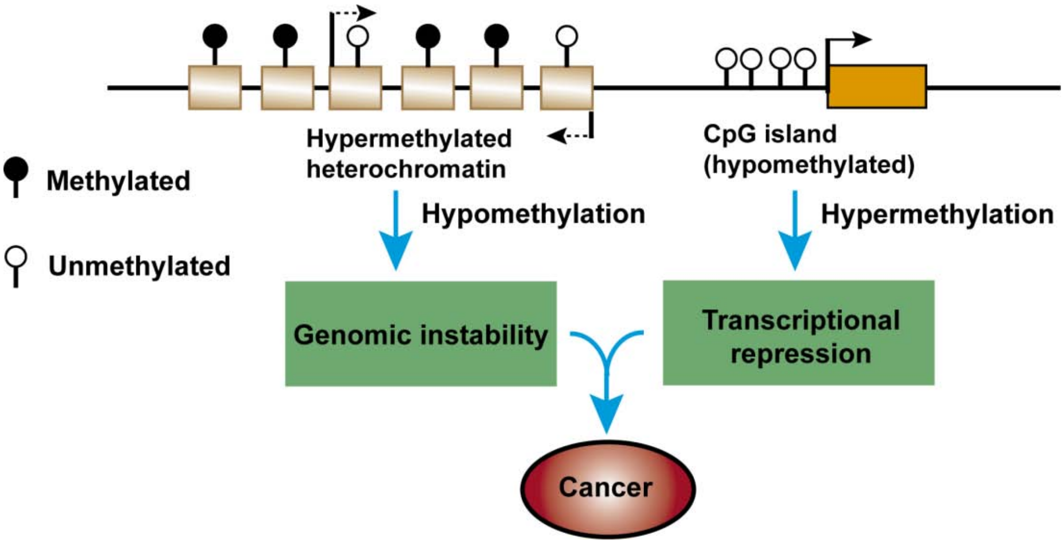
Methylated
Unmethylated
Hypermethylated heterochromatin
CpG island (hypomethylated)
Hypomethylation
Hypermethylation
Genomic instability
Transcriptional repression
Cancer

Figure 5. 2 DNA methylation and cancer.

Tumor cells are characterized by presenting a different methylome in comparison to normal cells. Genome-wide hypomethylation gives rise to genomic instability[292] and, in a much less extent, to the activation of oncogenes that may be silenced.[293-296] On the other hand, hypermethylation in certain gene promoters results in gene transcription suppression by either preventing transcription factors from binding to the gene or altering chromatin structure, leading to inactivation of tumor suppressor genes.[297] Such changes do not occur randomly but there are many kind of cancers with unique methylation profiles. Aberrant cytosine methylation is known to play decisive role in the development of several cancers, such as colorectal,[298, 299] lung,[300, 301] liver[302] and breast cancer.[303] Therefore, CpG methylation analysis can be useful in detecting the progression of tumor, classification, diagnosis and prognosis of a cancer.

5.1.3. Determining the cancer DNA Methylome

The importance of DNA methylation alterations in tumorigenesis has encouraged decoding the human epigenome. The production of a database of DNA methylation fingerprints for tumors can be crucial to resolve an important clinical issue by identifying the tumor type of unknown primary origin. This study will help in predicting the site of further dissemination for each tumor type improving prognostic evaluations.

DNA methylation markers are thought to play a role as predictive factors. They may be useful for determining not only the outcome of the disease but also the individual response to chemotherapy. There are some agents capable of restoring the normal cell DNA methylation pattern. Among them, there are some strategies that use drug to inactivate DNMTs.[12, 13] Another strategy consists of developing antisense oligonucleotides that can inhibit the DNMT at the translational level. Monitoring DNA methylation profiles after treatment of curative surgery may yield evidence concerning the efficiency of the applied therapy or to detect disease recurrence.

The application of epigenomic techniques for DNA methylation profiling will help to identify new epigenetic biomarkers that are predictors of response to particular chemotherapeutic agents. There are three basic approaches to assess methylation levels of 5-methylcytosines based on: (1) Bisulfite conversion of DNA, (2) methyl-sensitive restriction enzymes, or (3) chromatin immunoprecipitacion (ChIP) assays. Bisulfite treatment of DNA converts only unmethylated cytosines to uracil, whereas methylated nucleotides stay unchanged since they are less reactive. Afterward, methylation-specific PCR with specific primers complementary either to the originally methylated or to the unmethylated product can be performed to define the methylation pattern.[304] However, some other cytosine modifications such as hydroxymethylation (hmC) are also resistant to bisulfite conversion, implying that a proportion of genomic loci identified as methylated may actually be hydroxymethylated, giving rise to a wrong assessment. Another approach consists of using specific restriction enzymes that can digest the target sequence only if it is not methylated, which is very useful for a global DNA methylation status evaluation but rather limited, since this kind of strategy is restricted to those CpGs that are localized within the enzyme restriction site. The use of specific antibodies against methyl-CpG-binding (MBD) proteins which specifically recognize 5-methylcytosines can be employed by the combination of the ChIP method with the hybridization of DNA in microarray platforms.[305] It provides information about large-scale methylation status.

The recent interest for employing this epigenetic marks as tumor biomarkers have prompt the development of biosensor methodologies for the detection of methyl-cytosine residues in the genome. Thus, bisulfite treated DNA has been detected by SPR biosensor after sample amplification through molecular inversion probe based amplification method.[306] However, the need for bisulfite conversion and amplification steps makes this detection time-consuming and susceptible to error. On the other hand, another SPR approach consisted on the recognition of methylated DNA through MBD proteins in a two-step detection. This strategy avoids the use of any sample bisulfite treatment, but the need for methylated probes at different positions difficult the process.[307] Also, a sensitive DNA methylation detection have been achieved by a nanowire-transistor based biosensor employing methyl-specific antibody, although it required an off-chip procedure employing magnetic beads which may complicate the sample manipulation.[308]

In this Chapter we present the proof-of-principle results for the determination of the methylation status of the tumor suppressor gene *PAX-5* using the SPR biosensor. It does not require complicated bisulfite treatment or methylation-sensitive restriction digestion. The presented methodology is intended for quantification of the number of methyl-cytosines in *PAX-5* promoter region without the need for bisulfite modification and DNA-amplification steps.

5.2. Assessment of CpG island quantification in *PAX-5* gene promoter

PAX-5 gene plays an important role in cell differentiation and embryologic development. It is located in Chromosome 9p13,[309] a locus frequently associated with chromosomal translocation which contains two different promoters, leading to two alternative exons (α y β) in the 5'-end,[310] generating two different proteins that work as cellular transcription factors. It has been demonstrated that both promoters show aberrant hypermethylation in tumoral cell lines as well as in primary tumors of breast and lung cancer. They are methylated in approximately a 65% of the cases. Studies confirm that such methylation is produced only in tumor and adjacent tissues or, in rare cases, in normal epithelial cells.[311] Therefore, the assessment of the grade of methylation of such promoter region is very interesting for the diagnosis of this type of cancer.

In order to develop a biosensor methodology capable of capture the DNA fragment of interest containing the *PAX-5* gene promoter region and to quantify the number of methylated cytosine residues, we designed a process consisting of a double recognition process: (i) the capture of a ds-DNA fragment generated by restriction enzymes by oligonucleotide probe hybridization, and (ii) the determination of the sequence methylation profile by specific protein binding for such quantity of genomic DNA (**Figure 5.3**).

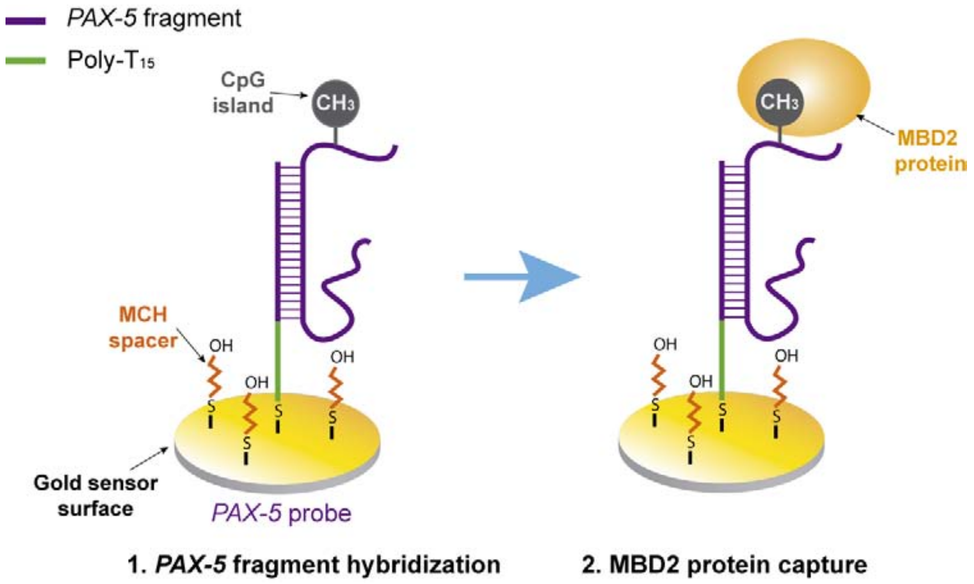

Figure 5. 3 Scheme of the two-step DNA methylation recognition methodology.

In a first attempt, we performed a proof-of-principle in the SPR biosensor to assess the possibility of the evaluation of CpG islands. To optimize the methodology for the determination of the grade of methylation, we employed synthetic ss-DNA sequences corresponding to a region of the *PAX-5* promoter (**Table 5.1**). This fragment contains 66 nucleotides with 5 possible CpG islands.

We designed a specific SH-DNA probe to capture that concrete fragment. For that, an evaluation of the whole sequence of interest was carried out. We designed the specific probe containing the minimum CG content and with the lesser possible number of secondary structures. Promoter sequences have a high CG content which makes difficult the design of an adequate probe for hybridization assays. Therefore, we studied the likelihood of secondary structures formation by self-complementarity of such fragment. The proposed *PAX-5* probe sequence (**Table 5.1**) presented the lowest number of secondary structures. However, it presented a high degree of CG content (76%), out of the recommended range (40-60%). In addition, it contained some possible secondary structures that may difficult the capture of the target. However, loop formation with ΔG energy higher than -4 kCal/mol is considered low enough to allow the hybridization of the complementary strands,[312] while the probes self-annealing can be rather solved by an appropriate monolayer optimization employing lateral spacers impeding such interactions.

Once defined our capturing probe, we optimized the monolayer for the specific detection of the *PAX-5* fragment. Different molar ratios of *PAX-5*-probe/MCH were employed for the optimization of the capture (1:0, 1:1, 1:4, 4:1). We evaluated the capture efficiency by employing 50 nM of *PAX-5* fragment. As can be observed in **Figure 6.4A**, a molar ratio of 4:1 generated the monolayer with the better hybridization efficiency compared to the rest of ratios. Due to the presence of possible formation of loops in the probes as well as their self-annealing, we assessed the formamide effect in the hybridization efficiency of the *PAX-5* fragment. We tested different concentrations of formamide from zero to 45% in the 5x SSC hybridization buffer. As can be observed in **Figure 5.4B**, 25% FA improved the detection signal in a 25%.

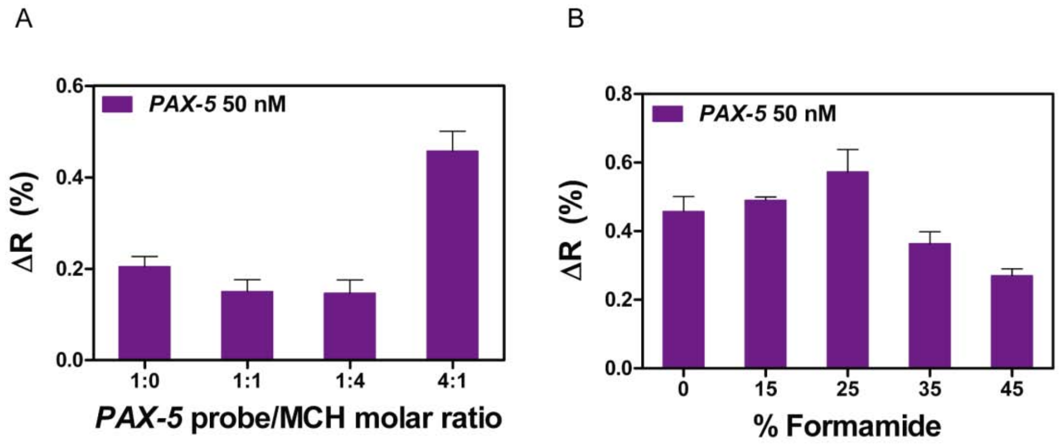

Figure 5. 4 Optimization of the *PAX-5* fragment detection conditions. (**A**) *PAX-5* probe/MCH molar ratio optimization. (**B**) Optimization of the %Formamide in the hybridization buffer.

After finding the most suitable conditions for *PAX-5* fragment detection, we obtained a calibration curve by employing different concentrations of *PAX-5* (from 5 to 50 nM), as shown in **Figure 5.5**.

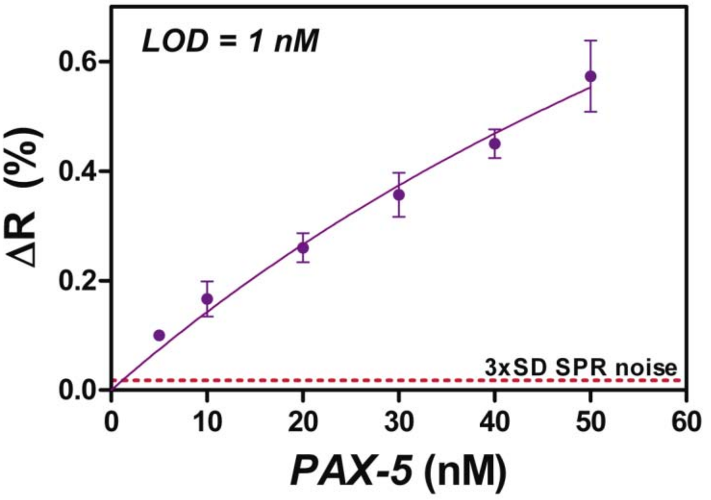

Figure 5. 5 Calibration curve for the *PAX-5* fragment (R^2 = 0.96) evaluation using the optimized hybridization conditions. Solid line corresponds to the non-linear fit of the calibration curve. Red dashed line corresponds to 3xSD SPR noise, which is the limit for the minimum signal detectable. All data show mean ± SD of triplicate measurements.

Next, we studied the CpG detection. For that, we employed an unmethylated *PAX-5* fragment and another with one methyl cytosine. We performed the second capture by taking advantage of the MBD proteins. As previously described, MBD proteins are a family of proteins intimately related to the DNA methylation process. Namely, MBD2 appear to bind with high specificity to methylated DNA.[313] Previous studies exploited such interactions for CpG island detection.[307, 314] We monitored the DNA hybridization and MBD interaction sequentially in real time by the SPR biosensor. As can be observed in the sensogram of **Figure 6.6A**, both targets produced the same increment in the reflectivity, showing the same hybridization efficiency despite of the methyl-cytosine content. However, when evaluating the MBD2 binding, only the sequence containing the methyl-modification gave rise to a positive signal, indicating that such protein was specific for methylated fragments. In fact, the MBD2 signal increased with increasing DNA concentration (**Figure 5.6B**), which indicated that this capture was concentration-dependent, and that the degree of methylation can be quantified by this methodology.

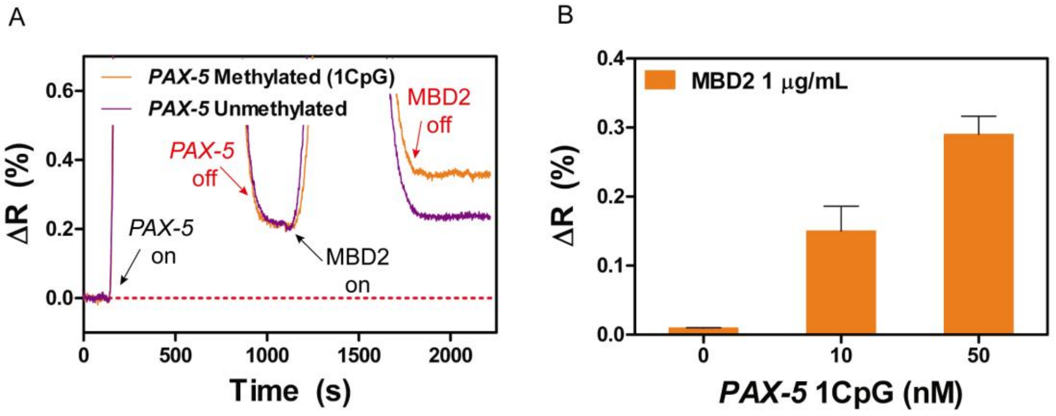

Figure 5. 6 Optimization of the detection of methyl-cytosine residues in *PAX-5* fragment. (**A**) MBD2 binding specificity assessment. (**B**) Concentration-dependence of MBD2 binding.

Next, we studied different methylation profiles by employing *PAX-5* fragments with different methylated CpGs: unmethylated fragment, one CpG island in different positions (cytosines 6 and 17) and a fragment with 5 methylations. As can be observed in **Figure 5.7**, no difference in MBD2 signal was noticed between the one-CpG fragments, indicating that the position of the methyl group did not affected to the MBD2 binding. However, when analyzing the CpG content of the 5-CpG fragments, no difference in SPR signal was perceived compared to the 1-CpG fragments. It may be due to the possible secondary structure formation in the sequence that may conceal the MBD-methyl-group recognition, making difficult the accessibility of the protein. As can be observed in **Figure 5.8**, this sequence contains strong secondary structures that can limit the accessibility of the MBD2 to the CpGs. In addition, MBD proteins are known to bind preferentially to symmetrically methylated CpG sites[315, 316] which will be only achieved by capturing ds-DNA.

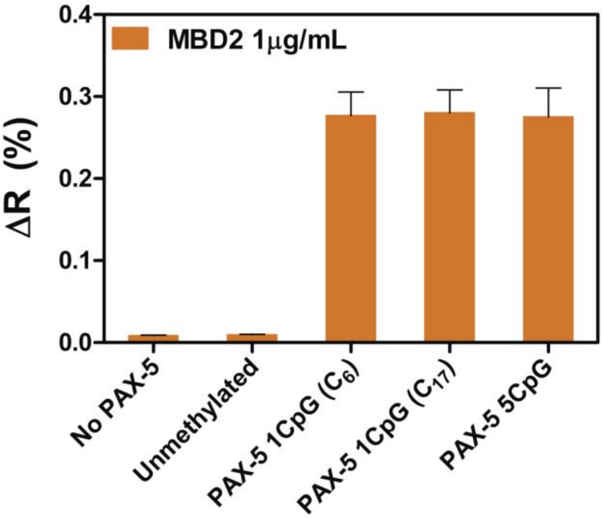

Figure 5. 7 Determination of the methylation profile of *PAX-5* fragment.

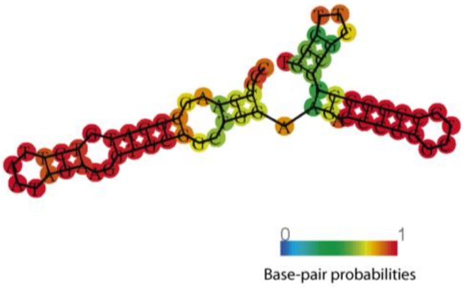

Figure 5. 8 Secondary structure prediction in the *PAX-5* fragment.

Although we could identify methylated sequences from non-methylated ones in this first proof of concept, further work should be done. Future work should focus on the capture of double-stranded *PAX-5* gene fragments in order to improve the methyl-group recognition through MBD2 second-step capture to determine the grade of methylation for DNA-methylation profiling.

5.3. Conclusions and future perspectives

We have designed a biosensor methodology for the determination of the degree of methylation of the promoter region of the *PAX-5* gene. We have optimized the hybridization efficiency of this fragment on a self-assembled monolayer by the employment of lateral spacers and a certain percentage of formamide. We have demonstrated the specificity of the MBD protein towards methyl-groups at the CpG, and its signal dependence in increasing concentrations of DNA. Furthermore, we have found that MBD binding efficiency is independent of the position of the CpG islands in the genomic fragment.

However, when trying to assess the CpG content in the same DNA fragment we were not able to discern between different degrees of methylation. It was probably due to the presence of strong secondary structures that may hinder the MBD2 accessibility to the CpGs. Moreover, the MBD capture conditions should be further optimized to find the optimal conditions for its interaction with the DNA fragment. Also, the preferential binding of MBD proteins to symmetrically methylated CpG sites makes the capture of ds-DNA more appropriate. Future experiments will be focus on:

- The capture of ds-DNA fragments. For that, different approaches can be employed as the use of oligonucleotide/PNA-assisted affinity capture (OPAC), based on selective tagging of a DNA duplex by oligodeoxyribonucleotide (ODN) through formation of a so-called PD-loop.[317] The required homopyrimidine nature of PNA “openers” makes this approach suitable for their interaction with cytosine nucleotides in the promoters, highly enriched in these sequences. Also, triplex-forming oligonucleotides (TFOs) are gaining much interest due to their capability for the detection of double-stranded DNA by targeting homopurine or homopyrimidine tracks in the sequences of interest. Such approach would improve the target capture and would avoid the presence of secondary structures.
- Establishing better conditions for MBD2 protein binding by determining the saturating concentration and exploring different buffer compositions that may lead to improved methyl-cytosine recognition as in the case of the anti-DNA-RNA antibody recognition described in **Chapter 4**.
- Defining the restriction map and enzymes required for obtaining the genomic DNA fragment of interest taking special care in preserving intact the target sequence.
- Utilizing the BiMW biosensor to achieve better sensitivities for a direct assay without the need of pre-amplification steps due to the need for preserving the initial methylation status of the fragment for MBD2-protein recognition step. Also, taking advantage of the high sensitivity of the BiMW, it could be of interest to study the differences in the sensor responses to the same fragment showing different methylation profiles and determine whether we can identify the number of cytosines due to the signal differences produced for the presence of methyl-residues. This approach would allow for the direct profiling of the degree of methylation from a determined quantity of genomic DNA without the need for the second recognition step by the MBD2 capture.
- Demonstrating the feasibility of methodology by the analysis of different cell lineages presenting different methylome of *PAX-5* gene.

5.4. Materials and Methods

5.4.1. DNA sequences

DNA synthetic targets and probe are summarized in **Table 5.1**

Table 5. 1 Sequences for probes and DNA synthetic targets employed in this thesis.

Name	**Sequence**
Pax5 probe	5’-PolyT$_{15}$-GAAGCGGAGCCCGGGAG 3’
Pax-5 Unmeth	5’CCCCCAAGCGCATGTCTTAATAGAAGGTGCGGCTGGAAGACCCGGGCTCCCGGGCTCCGCTTCGGT 3’
Pax-5 1CmG$_1$	5’CCCCCAAGC$_m$GCATGTCTTAATAGAAGGTGCGGCTGGAAGACCCGGGCTCCCGGGCTCCGCTTCGGT 3’
Pax-5 1CmG$_2$	5’CCCCCAAGCGCATGTCTTAATAGAAGGTGCGGCTGGAAGACCCGGGCTCCC$_m$GGGCTCCGCTTCGGT 3’
Pax-5 5CmG	5’CCCCCAAGC$_m$GCATGTCTTAATAGAAGGTGC$_m$GGCTGGAAGACCC$_m$GGGCTCCC$_m$GGGCTCC$_m$GCTTCGGT 3’

5.4.2. SH-*PAX-5* probe immobilization

Formation of mixed self-assembled monolayers (SAMs) of SH-*PAX-5* probe/MCH (1 µM) was carried out *in-situ* on the gold sensor chip by flowing 250 µL of the mix in PBS 50 mM (pH 7) at 12 µL/min rate. Different DNA-probe/MCH molar ratios (1:0, 1:1 1:4 and 4:1) were employed.

5.4.3. Target hybridization

PAX-5 fragment detection was performed by injection of 250 µL of the samples into the SPR biosensor at a 16 µL/min rate and subsequent hybridization with their complementary DNA probes immobilized on the sensor surface. These samples were dissolved in 5x SSC mixed with different percentages of FA (0, 15, 25, 35, 45%) to improve hybridization efficiency.

5.4.4. MBD capture

MBD protein 1 µg/mL was diluted in 1x MBD2 buffer for methyl-cytosine residues recognition in methylated DNA. Finally, target-probe interactions were disrupted by either employing H_2O (100ºC), FA35% or HCl 2mM.

General Conclusions and Future Perspectives

This PhD Thesis demonstrates the unique properties provided by nanophotonic biosensors for the fast and accurate analysis of gene regulating pathways, revealing their potential value in cancer diagnosis. The highly sensitive detection and identification of specific biomarkers directly related to genetic and epigenetic disorders in human cancers offers an attractive opportunity for the early diagnosis of cancer as well as for the real-time evaluation of novel therapies. This multidisciplinary study has involved the combination of state-of-the-art nanotechnology devices together with the recent discoveries in biotechnology and molecular biology, especially in the epigenetics field, which has permitted the development of innovative and very competent analytical methodologies as brand-new strategies to identify cancer signatures with great prognostic and diagnostic potential.

The work in this PhD Thesis involved the design and development of different biosensor strategies for the monitoring of relevant gene regulating pathways such as the RNA alternative splicing, the aberrant expression of microRNAs or the DNA methylation. We have employed two optical biosensors, the well-known SPR biosensor and the recently developed BiMW interferometer, both of them fully developed in our Group. These platforms represent promising tools for the analysis of such routes offering simple, label-free and highly sensitive detection in a few minutes and with minimal sample treatment. In particular, the BiMW biosensor has showed exceptional capabilities for the integration in Lab-on-a-chip platforms and its use at the point of care. The rigorous optimization and assessment of the biofunctionalization and biodetection processes have allowed the reliable monitoring at sensitivity and selectivity levels comparable to the current gold-standard analytical methodologies. Furthermore, the analysis of clinical samples has further demonstrated the viability of the proposed methodologies for their implementation in the biomedical and clinical field.

The main general conclusions that can be drawn from this work are the following:

- Several biofunctionalization strategies have been developed for both gold and silicon-based sensor chips for the direct detection of nucleic acids in human biofluids. To that, we have exploited different surface modification procedures including the highly stable thiol chemisorption, a novel technique based on the affinity of poly-Adenine tails for gold, and an improved silanization strategy. The in-depth optimization of surface chemistry protocols together with the employment of antifouling compounds (PEGylated compounds) provided an exceptional enhancement of the analytical features of the biosensors in terms of sensitivity, selectivity and reproducibility, while preventing from undesired nonspecific adsorptions coming from complex samples, such as serum or urine. Furthermore, the versatility and robustness of the different functionalization strategies facilitates their application for the development of multiplexed biosensors and their integration in PoC devices.
- A novel methodology for the evaluation of mRNA alternative splicing events in real-time have been developed. The designed strategy differentiates specific mRNA isoform ratios generated during the gene expression, involving minimal sample manipulation and avoiding the use of labels or pre-amplification steps. Strictly discrimination against the non-complementary isoforms at the pM-nM range has been achieved in direct

analysis with the SPR biosensor. The feasibility of the methodology was assessed in HeLa cells and showed an excellent correlation with RT-qPCR data. We also demonstrated its robustness and reproducibility for long-term use. The methodology has also been easily reproduced with the same efficiency when it is applied to a different gene, highlighting it as a suitable and general tool for the monitoring of alternative splicing events of different genes and within different biological and eventually pathological contexts. Finally, the methodology has been successfully applied to the BiMW interferometer, improving the overall sensitivity in 3 orders of magnitude (**LOD in the fM range**) with respect to the SPR biosensor. On-going work focuses on the validation of the strategy for the direct detection of RNA alternative splicing in human tissues and circulating blood. This biosensor may signify a unique tool for both the early identification of tumor processes and for the design of efficient and personalized cancer therapies.

- We have developed an efficient and sensitive strategy for the detection of cancer-associated miRNAs directly in human fluids. The methodology has been deeply optimized employing the conventional SPR biosensor in order to ensure selective detection of miR-181a. Discrimination between different homologous miRNAs at the single-nucleotide mismatch level has been achieved. The introduction of an amplification step employing a specific anti-DNA-RNA antibody increased the analytical sensitivity, improving the limit of detection to **580 fM**. Finally, the feasibility of the methodology was demonstrated by the detection of miR-181a in urine samples from healthy donor and bladder cancer patients. The methodology has been also applied to the BiMW biosensor reaching in this case a **LOD of 20 aM**, which represents the most sensitive miRNA detection so far described in a direct detection and quantification of miRNA levels without amplification or labeling steps. Moreover, we have demonstrated overexpression of miR-181a in bladder cancer patients compared to control individuals, which were in good agreement with the analysis done with the SPR biosensor for bladder cancer samples. Further studies should be performed to confirm the implication of this miRNA in bladder cancer through metabolic shift and to establish a proper cut-off for the early determination of cancer onset. Overall, the proposed biosensor constitutes an extraordinary opportunity for the development of multiplexed platforms that provide simultaneous detection of specific miRNA panels in human fluids with high sensitivity. The implementation of such PoC biosensors may drastically improve not only cancer diagnosis and prognosis but can also contribute to increase treatment and recovery probabilities.
- We have proposed a biosensor methodology for the real-time profiling of DNA methylation, an epigenetic disorder strongly related with cancer appearance and progression. We have evaluated the strategy for the tumor-suppressor gene *PAX-5* employing the SPR biosensor. The approach takes advantage of a specific protein that selectively binds to methyl groups at the CpG regions (i.e. MBD2), which has demonstrated a high binding efficiency, independently of the position of the CpG islands in the genomic fragment. On-going work in the Group focuses on the optimization of the methodology in order to ensure direct and reliable quantification of the DNA methylation level. For that purpose, different strategies have been proposed using restriction enzymes and the transfer to the BiMW biosensor platform. The DNA methyloma analysis can be useful for the determination of the tumor progression, classification of diseases, and for the diagnosis and prognosis of cancer.

This PhD Thesis has therefore exposed the extraordinary importance of developing new analytical tools for the study of gene regulating pathways. The demonstration of simple and rapid techniques for the evaluation of gene regulation pathways paves the way for the achievement of an efficient diagnosis and potential individualized therapy where the simultaneous detection of the alteration of the different processes could be of great help.

Future perspectives may be directed toward the generation of complete genomic and epigenomic biomarker panels by using the biosensor methodologies developed in this work.

The BiMW biosensor represents an exceptional opportunity due to its unique capabilities demonstrated for multiplexed and highly sensitive detection of nucleic acids. The BiMW technology has been granted with patents at international level and it has been recently licensed to the company Promax Electronica, S.L. This positions our new nanotechnology device a step closer for its commercialization and paves the route for the implementation of the developed methodologies in research and clinical settings.

This PhD thesis represent a significant contribution to the progress in nucleic acid analysis and open the door for the routine use of these gene regulating routes as biomarkers for diagnosis and patient follow-ups during therapy, providing a more informative, specific and accurate analysis for cancer research and eradication, largely contributing to improve global health care.

Annex·Sensitive and Label-Free Detection of miRNA-145 by Triplex Formation

The exploration of new probe modalities for hybridization efficiency enhancement is the main focus of this Annex. Particularly, the formation of a triplex structure between the probe and the target sequence for micro-RNA detection is demonstrated. The performance of this new probe format is evaluated and compared with conventional probes in terms of sensitivity. Finally, the advantages and limitations of the triplex-forming probe are highlighted.

A. Sensitive and Label-Free Detection of miRNA-145 by Triplex Formation

A.1. Introduction

Biosensor sensitivity is an important factor in the development of a suitable methodology for direct miRNA detection. An approach to improve it can be the employment of different DNA probe formats that can increase the efficiency of target capture, improving the overall performance of the biosensor. All the previously described methods in this thesis for miRNA analysis relied on duplex formats between the target and the complementary probe. However, alternative formats can also be employed. An example is the use of a DNA-probe modality based on *triple-helix* formation. While DNA structures are more likely to be duplexes with full complementarity between two strands, RNA structures tend to fold into complex secondary structures involving not only hairpins and loops, but also more complex structures such as triplexes[318] and quadruplexes.[319] This self-structuring is in part due to the extra oxygen in the RNA surgar (ribose) which increases the tendency for hydrogen bonding in the nucleic acid backbone. The presence of the secondary structures can hinder the hybridization of the RNA target with the probe employed for detection and constitutes one of the main difficulties for RNA analysis. However, previous studies demonstrated that triple-helix target sites are widespread within the human genome, especially at promoter regions,[320-322] reporting such type of hybridization as an interesting approach for efficient target capture. Taking advantage of that natural phenomenon, we have implemented a novel detection method based on the miRNA recognition through the formation of a triplex helix. The clamp structure formed in the probe sequence by Hoogsteen base-pairing is able to capture the target sequence by Watson-Crick duplex formation, therefore establishing a triplex structure (**Figure A.1**).

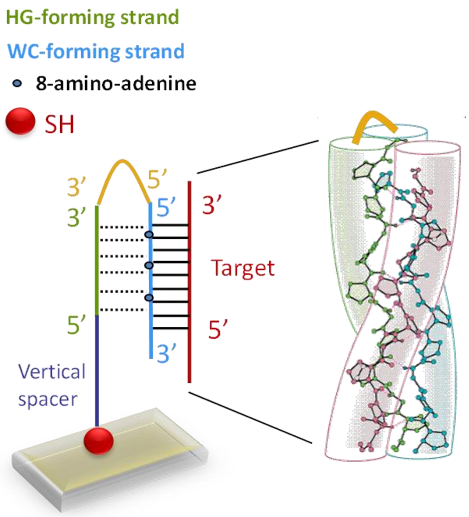

Figure A. 1 Scheme of the triplex capture.

Triple-helix can only be formed when nucleic acids meet certain characteristics, i.e. specific polypurine-polypyrimidine sequences. Previously, the triplex-stabilizing properties of

8-aminopurines[323, 324] and the use of parallel and antiparallel tail clamps to increase the efficiency of triplex formation with structured DNA and RNA targets[325] was reported. All this knowledge was applied to develop a new affinity capture technique based on the stability of triplex by using tail-clamps carrying 8-aminopurines as bioreceptor.[326] Recently, our Group applied the triplex affinity capture strategy to a novel biosensor method using an SPR biosensor for the detection of the Listeria mRNA.[327]

On the basis of such findings, we have developed a new strategy to capture and detect miRNAs based on the formation of stable triplex structures. The efficiency in target capture of the developed probe has been tested by the SPR biosensor by comparison with ordinary duplex formats. Different probe controls have also been tested to guarantee the triple-helix formation of parallel clamps and miR-145.

A.2. SPR detection of miRNA-145 using parallel clamps

In previous studies, the capability of triplex hybridization was successfully demonstrated by the detection of structured and long RNAs such as mRNA of Listeria.[327] This triplex format relied on the formation of a hairpin based on a homopurine sequence that hybridized by Watson-Crick base-pairing with the targeted sequence while, at the same time, hybridized with a second portion of homopiridine in the probe sequence by Hoogsteen base-pairing forming a clamp structure. The pyrimidine track of the tail clamps contained 12 nucleotides which provide stable triplex structures. An even better stability of the triplex structure was demonstrated after introducing 8-aminoA modifications in the homopyridine portion. This triplex format was more stable, providing a better target capture and improved LOD. Thus, for the miRNA capture with the triplex format, the recognition sequence must possess a portion of homopyrimidines in order to obtain a perfectly stable triple-helix between the probe and the target miRNA. The probe would contain a homopurine portion in order to hybridize the target with Watson-Crick interactions and the inverted homopyrimidine portion of the clamps should form a triplex by Hoogsteen hydrogen bonding.

We selected miR-145, whose sequence has a portion of homopyrimidines, which ensures the proper formation of the triplex. MiR-145 has shown to function in tumor suppression, as in most of the human cancer cell lines, a clear reduction of the expression of this miRNA has been observed. In particular, low expression in human colon or gastric cancer cells has been reported,[328] with a clear relationship between the low expression of miR-145 and the clinicopathological findings in human colorectal tumors. We designed and synthesized parallel clamps (PT Clamp, 3AG PT Clamp, **Figure A.2A**) targeting a 7-homopyrimidine sequence of miRNA-145 to assess their capacity to form triple helices. Base-pairing scheme of the triads that forms the triplex structures is showed in **Figure A.2B**.

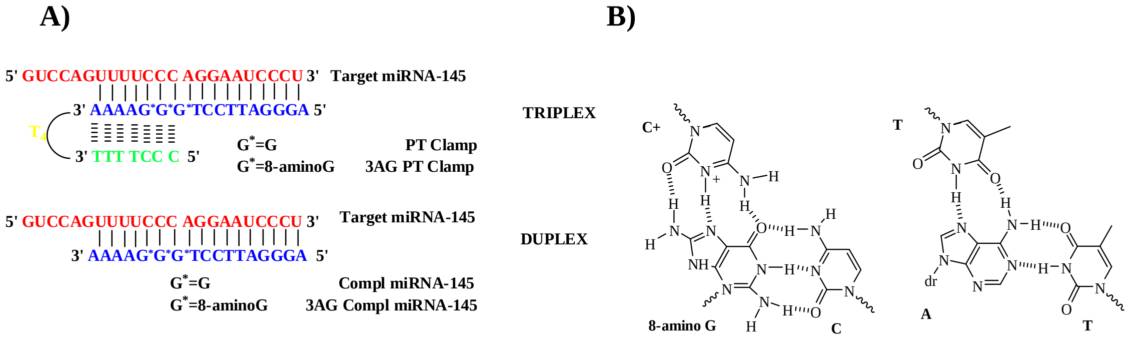
A)
5' GUCCAGUUUUCCC AGGAAUCCCU 3' Target miRNA-145
3' AAAAG*G*G*TCCTTAGGGA 5'
T4
3' TTT TCC C 5'
G*=G PT Clamp
G*=8-aminoG 3AG PT Clamp
5' GUCCAGUUUUCCC AGGAAUCCCU 3' Target miRNA-145
3' AAAAG*G*G*TCCTTAGGGA 5'
G*=G Compl miRNA-145
G*=8-aminoG 3AG Compl miRNA-145
B)
TRIPLEX
DUPLEX
C+
T
8-amino G
C
A
T
dr

Figure A. 2 Triplex and duplex hybridization of miR-145. (**A**) Scheme showing the binding of tail-clamps and complementary sequences to miRNA-145 yielding triplex and duplex structures respectively. (**B**) Scheme showing the triads that forms triplex structures C^{+} -8-aminoG - C and T-A-T.

3AG PT Clamp contained three consecutive 8-aminoguanines (8-aminoGs). The 7-base polypyrimidine track of the miRNA-145 is shorter than the 12-bases employed in previous studies.[327] MiRNAs are small RNA molecules and the Hoogsteen polypyrimidine tracks (HG tracks) should be shorter which might affect the stability of the clamp and the hybridization efficiency to form triplexes. To overcome this problem and to improve the triplex formation, we decided to use 8-aminoG modifications instead of 8-aminoA due to their improved triplex formation efficacy.[323]

To assess the advantage of this new triplex structure to capture miRNAs, we employed the SPR biosensor. We designed two PT clamp probes, one modified 8-aminoG (3AG Clamp) and other with no 8-aminoG modifications (PT Clamp). For comparison purposes, we also assayed duplex formation capture in which complementary sequences to miR-145 were prepared with and without 8-aminoG (3AG Compl. miR-145 and Compl. miR-145, respectively). In addition, we analyzed tail clamp controls that included incorrect polypyrimidine sequence in which the triplex was unable to form properly (3AG Control Clamp and Control Clamp). Schematic representations of all the employed probe formats are shown in **Figure A.3**. MiR-145 target and probe sequences are gathered in **Table A.2**.

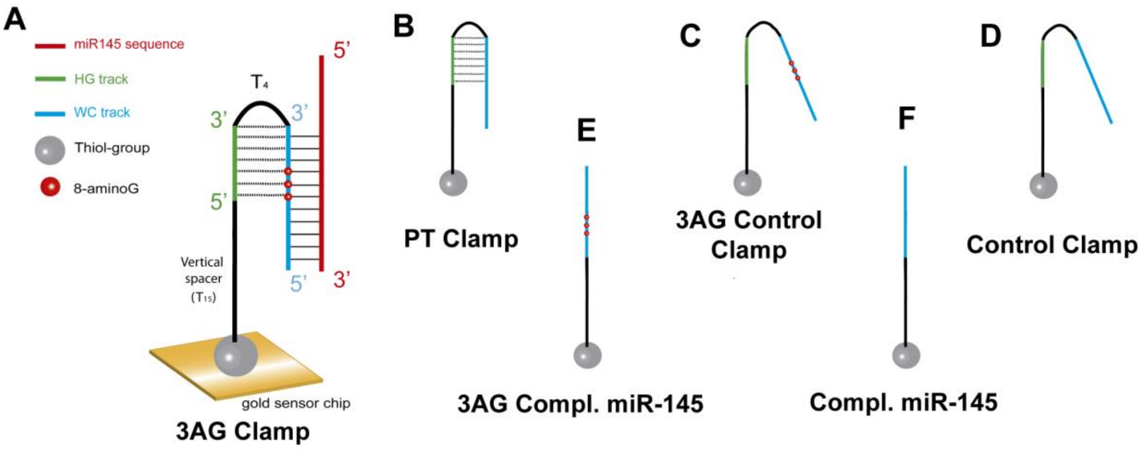
A
miR145 sequence
HG track
WC track
Thiol-group
8-aminoG
T4
3'
3'
5'
5'
5'
3'
Vertical spacer (T15)
gold sensor chip
3AG Clamp
B
PT Clamp
C
3AG Control Clamp
D
Control Clamp
E
3AG Compl. miR-145
F
Compl. miR-145

Figure A. 3 Scheme of the different probe for miR-145 capture. (**A**) 3AG PT Clamp bioreceptor. (**B**) PT Clamp. (**C**) 3AG Control Clamp. (**D**) Control Clamp. (**E**) 3AG Compl. miR-145. (**F**) Compl. miR-145.

Gold sensor chips were coated *ex situ* with the immobilization solutions (1µM probe with 50 nM MCH in PB buffered solution). Then, the chips were placed in the sensor and evaluated in real-time. We evaluated the efficiency of all the probes by monitoring their response to standard solutions at different miR-145 concentrations ranged from 2 nM to 30 nM. Results of SPR detection of miRNA-145 with all the probes are displayed in **Figure A.4**. Triplicate measurements of each miR-145 concentration were obtained and calibration curves for each probe were represented (**Figure A.4A**). As can be appreciated in **Figure A.4B**, the sensor response for 3AG Clamp probe showed the higher hybridization efficiency (ΔR(%) = 0.45) for 30 nM of miR-145 compared with the other probe formats. The LOD obtained for each probe format has been calculated and listed in **Table A.1**.

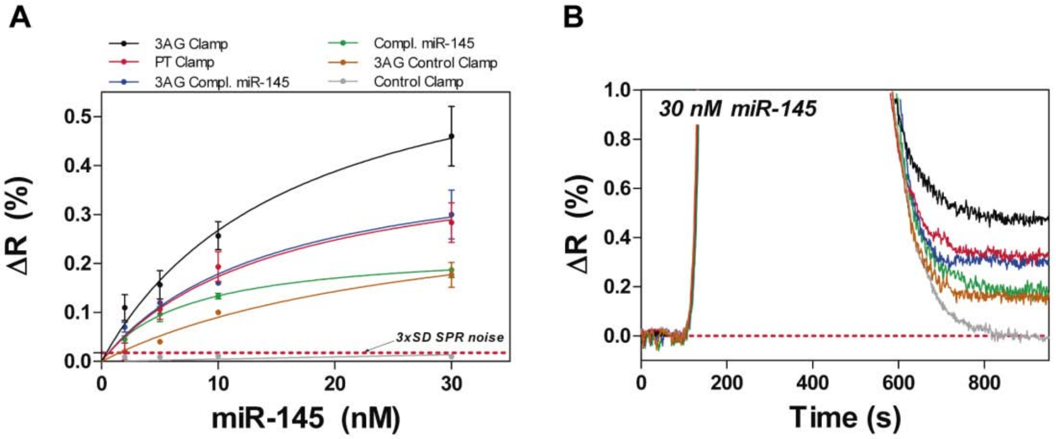

Figure A. 4 SPR results for the detection of miR-145 with the different probe formats. (**A**) SPR calibration curves of the detection of miR-145 with the different probe formats. The sensitivity for each bioreceptor was considered as three times the baseline noise standard deviation (discontinuous red line). (**B**) Real-time sensograms of 30 nM miRNA-145 using the different probe variants.

Table A. 1 LODs calculated for each probe modality.

Probe	LOD (nM)
3AG Clamp	1
PT Clamp	1.5
3AG Compl. miR-145	1.6
Compl. miR-145	2.43
3AG Control Clamp	3

Real-time sensograms of miR-145 at 30 nM with each probe showed an increase in the sensor response of miR-145 for the PT clamp probes compared with the duplex ones. In addition, their sensitivities were improved exhibiting more than 1.5 times better LODs. On the other hand, 8-aminoG modifications seem to largely stabilize the hybridization, obtaining higher signals with probes containing them as compared with the non-modified ones. The duplex detection approach is favored when the complementary probe is modified with 8-aminoG. Furthermore, the introduction of these modifications in the PT Clamp probe promoted the stabilization of the triplex as they showed the maximum biosensor response, leading to an enhancement of the sensitivity. A LOD of **1 nM** was determined for 3AG Clamp probe, rendering in a LOD 2.43 times better as compared to the standard duplex probe. Surfaces biofunctionalized with unmodified PT Clamp probes generated a LOD of **1.65 nM**, very similar to the one obtained for the duplex-forming 3AG Compl. bioreceptor (**1.60 nM**). This result suggests that under our experimental conditions, a triplex structure is only formed with 8-aminoG-modified parallel tail-clamps.

A.3. Conclusions and future perspectives

We have demonstrated for the first time a new and sensitive approach for label-free detection of miRNAs using a triplex-based probe format. A stable triplex structure was formed at neutral pH by using parallel tail-clamps probes modified with 8-aminoguanine derivatives with a short polypyrimidine track. This modified tail-clamp was more efficient for target detection than the conventional duplex formats. The introduction of 8-aminoG in both triplex- and duplex-capture probes was found to stabilize the hybridization, improving the LODs in more than 1.5 times.
This novel approach offers great potential for miRNA detection or for any other RNA structure; in this case the requirement was only to contain seven pyrimidines in the sequence in order to design an appropriate tail-clamp probe. Further work is still needed to extend this study to the detection of miRNA containing pyrimidine tracks with small number of polypyrimidine tracks or to miRNA having interruptions in the polypurine-polypyrimidine track.

Our results are an exceptional advance toward the detection of miRNA for diagnostic purposes. It could also be applied with the BiMW biosensor to highly improve the detection limit. The application of the anti-fouling monolayer developed in this Thesis and proven previously for miR-181a would also allow for the direct detection of miR-145 in real samples.

A.4. Materials & Methods.

A.4.1. Synthesis of Oligonucleotides

Oligonucleotide sequences listed in **Table A.2** were synthesized by the Group of Prof. R. Eritja from the Department of Chemical and Biomolecular Nanotechnology Group at the Institute of Advanced Chemistry of Catalonia (IQAC), CSIC (Spain). Sequences were prepared on an Applied Biosystems 3400 synthesizer using polystyrene solid supports (LV200) according to the protocols of the manufacturer. Thermal UV denaturation and CD studies were carried out to assess the triplex structure.

Table A. 2. MiR-145 target and probe sequences.

Name	Sequence
miRNA-145	5' GUCCAGUUUUCCCAGGAAUCCCU 3'
Compl miRNA-145	3' AAAAGGGTCCTTAGGGA 5'
3AG Compl miRNA-145	3' AAAAG*G*G*TCCTTAGGGA 5'
PT Clamp	3' AAAAGGGTCCTTAGGGA 5' T_4 3' TTT TCC C 5'
3AG PT Clamp	3' AAAA**G*****G*****G***TCCTTAGGGA 5' T_4 3' TTT TCC C 5'
Control Clamp	3' AAAAGGGTCCTTAGGGA 5' T_4 3' CTCCTTT 5'
3AGControl Clamp	3' AAAA**G*****G*****G***TCCTTAGGGA 5' T_4 3' CTCCTTT 5'

A.4.2. Experimental Procedure for Detection Using the SPR Biosensor

Experimental procedure was carried with the SPR biosensor employed in this Thesis.The different bioreceptors were tested in independent assays. Clean gold sensor chips were coated *ex-situ* by 100 mL of immobilization solutions (1µM DNA receptor with 50 nM Mercaptohexanol (MCH) (Sigma Aldrich, Steinhem –Germany-) in PB buffered solution (50 mM Phosphate buffer- 0.75 mM NaCl, pH 7)) and kept in a humid chamber for 3 h. Then, they were rinsed in DEPC treated H_2O, dried under N2 flux and placed in the sensor device.

Detection was done *in situ* at room temperature (RT) by flowing different concentrations of miRNA-145 over the sensor surface for their hybridization with the different immobilized bioreceptors at a 16 µL/min constant rate. These samples were dissolved in 5x SSC solution (0.75 M in NaCl, 0.075 M in sodium citrate, pH 7). Regeneration after hybridization was achieved by injecting a 35% formamide solution, allowing the analysis of a high number of interactions using the same bioreceptor monolayer.

Publications

Journal Articles:

Sensitive and Label-Free Detection of miRNA-145 by Triplex Formation
A. Aviñó, C. S. Huertas, L. M. Lechuga, R. Eritja
2016 *Analytical and Bioanalytical Chemistry* 408 885-125

Quantitative evaluation of alternatively spliced mRNA isoforms by label-free real-time plasmonic biosensing
C. S. Huertas, L. G. Carrascosa, S. Bonnal, J. Valcárcel and L. M. Lechuga
2016 *Biosensors and Bioelectronics* 78 118-125

Prospects of optical biosensors for emerging label-free RNA analysis
L. G. Carrascosa, C. S. Huertas and L.M. Lechuga
2016 *Trends in Analytical Chemistry* (In press)

Direct and label-free quantitation of microRNAs at attomolar level in complex media using a multiplexing nanophotonic biosensor
C. S. Huertas and L.M. Lechuga
2016 *ACS sensors* (Submitted)

Site-specific immobilization of DNA for the development of Silicon-based multiplexing optical biosensors
C. S. Huertas and L.M. Lechuga
(In preparation)

Analysis of circulating alternative spliced isoforms using a multiplexing nanophotonic biosensor for the diagnosis and monitoring of malignant diseases
C. S. Huertas and L.M. Lechuga
(In preparation)

Comparative study of DNA and RNA hybridization in optical label-free biosensors
C. S. Huertas and L.M. Lechuga
(In preparation)

Conferences:

Direct and label-free biosensing detection of alternative splicing events in FAS gene - Poster
L.G. Carrascosa, C. S. Huertas, A. B. González, S. Bonnal, J. Valcárcel and L. M. Lechuga
April 1st- 4th 2012 *Europtrode XI Conference on Optical Chemical Sensors and Biosensors*, Barcelona (Spain)

Rapid and sensitive label-free detection of alternative splicing Fas gene RNA isoforms- Poster
L.G. Carrascosa, C. S. Huertas, A. B. González, S. Bonnal, J. Valcárcel and L. M. Lechuga
June 5th 2012 *First Workshop on Nanomedicine UAB*, Barcelona (Spain)

Direct and label-free biosensing detection of alternative splicing events in FAS gene- Poster
L.G. Carrascosa, C. S. Huertas, A. B. González, S. Bonnal, J. Valcárcel and L. M. Lechuga.
November 19th- 20th 2012 *VI Annual Conference CIBER-BBN*, Madrid (Spain)

Plasmonic Biosensors for the study of regulation pathways in cancer-related genes- Oral presentation
C. S. Huertas.
May 13th- 14th 2013 *1st Student Scientific Meeting ICMAB-ICN2*, UAB Barcelona (Spain)

Rapid and sensitive label-free detection of alternative splicing Fas gene RNA isoforms- Poster
C. S. Huertas, L. G. Carrascosa, S. Bonnal, J. Valcárcel and L. M. Lechuga
September 17th 2013 *Workshop "Biosensors for a better environment"*, Barcelona (Spain)

Direct and label free detection of miRNAs for the monitoring of cancer development using nanobiosensing platforms - Poster
C. S. Huertas, M. Álvarez and L. M. Lechuga
November 21st- 22nd 2013 *Barcelona conference on epigenetics and cancer. Challenges, opportunities and perspectives*, Barcelona (Spain)

Analysis of miRNA biomarkers related to thyroid cancer using a bimodal waveguide interferometric- Poster
S. Dante, D. Duval, C. S. Huertas, and L. M. Lechuga
April 13th-16th 2014 *Europtrode XII Conference on Optical Chemical Sensors and Biosensors*, Athens (Greece)

List of Figures

Chapter 1· Introduction

Figure 1. 1 Central Dogma of Molecular Biology. 9
Figure 1. 2 Scheme of the different alterations in gene regulation pathways which can take place inside the cell. 10
Figure 1. 3 Interplay between gene regulating pathways inside the cell. 11
Figure 1. 4 Schematic representation of a biosensor including the heterogeneous sample, the specific biological receptor, the transducer, the data processing system and the final signal. 13
Figure 1. 5 Main types of biosensors depending on the biorecognition element: (A) enzymatic biosensor (catalytic), (B) immunosensor (affinity) and (C) DNA biosensor (affinity). 14
Figure 1. 6 DNA backbone scheme. 14
Figure 1. 7 Evanescent wave sensor configurations for conventional dielectric waveguides (*left*) and surface plasmon (*right*). 17
Figure 1. 8 Schematics of a SPP at the interface of a metal and a dielectric showing: (A) the collective charge oscillation at the surface and (B) the transversal evanescent field distribution. 18
Figure 1. 9 Schematics of a SPR biosensor employing a Kretschmann configuration. 19
Figure 1. 10 Representative SPR curves for (A) λ-interrogated and (B) θ-SPR sensors, together with their corresponding real-time tracking of curve displacements via the monitoring of (C) shifts of the resonance wavelength, λ_{SPP}, and (D) changes of the reflectivity, R. 21
Figure 1. 11 SPR biosensor. (A) SENSIA SPR Biosensor device. (B) Schematic representation of the sensor module of the SENSIA SPR Biosensor. 22
Figure 1. 12 Scheme of an asymmetric slab waveguide. 23
Figure 1. 13 Propagation of (A) TE and (B) TM modes in an asymmetric planar waveguide. 24
Figure 1. 14 Main types of 3D-waveguides: (A) raised strip waveguide, (B) embedded and strip and (C) rib waveguide. 24
Figure 1. 15 Dual-path interferometric biosensors: (A) Mach-Zehnder[98] and (B) Young.[99] (C) Typical interference signal originated by interferometric biosensors. 25
Figure 1. 16 BiMW device. (A) Photograph of a processed 4-inches wafer with 12 BiMW chips, resulting in a total of 192 sensors. (B) BiMW chip containing 16 sensors. (C) Scheme of the working principle of a Bimodal Waveguide interferometer. Light is injected in the single-mode input waveguide and after a modal splitter two modes are excited and propagate until the device output. 26
Figure 1. 17 Bimodal Waveguide interferometers cross section (A) and longitudinal view (B). 27
Figure 1. 18 Photograph of the BiMW set-up. 27
Figure 1. 19 Sensing principle of a BiMW biosensor. 28
Figure 1. 20 Typical BiMW sensor signals. (A) Acquired I_{up} and I_{down} signals and (B) corresponding S_R during the detection of a refractive index change $\Delta n = 9 \cdot 10^{-4}$. 29
Figure 1. 21 Schematic comparison of standard monochromatic approach with sinusoidal output (*up*) and wavelength modulated sensor with linear phase read-out (*down*). 30
Figure 1. 22 Array of Nanophotonic sensors incorporating grating couplers for light source coupling, optical readout and control electronic, integrated on chip for Point-of-care development. 31

Chapter 2· DNA-functionalization of the sensor surface

Figure 2. 1 Standard ss-DNA probe employed as bioreceptor in biosensors. 36
Figure 2. 2 Different DNA secondary structures that can be formed in single stranded nucleic acids. 37
Figure 2. 3 SAM formation on gold surfaces. 39
Figure 2. 4 Scheme of the target accessibility at different gold sensor surface coverages. (A) Low DNA-probe coverage with poor SAM packaging and bad DNA-probe orientation. (B) High DNA-probe coverage with high steric hindrance forces leading to poor probe accessibility that prevent target hybridization. (C) Lateral spacing by blocking agents providing good probe orientation and optimum accessibility. 40
Figure 2. 5 Typical sensogram for *in-situ* immobilization of SH-DNA probes and their subsequent hybridization/regeneration cycle. 41
Figure 2. 6 SPR responses of different DNA probe concentrations. 42
Figure 2. 7 Target hybridization efficiency for different probe densities. 42
Figure 2. 8 MCH effect in target hybridization efficiency with different DNA probes. 43
Figure 2. 9 Surface regeneration for the SPR biosensor. 44
Figure 2. 10 Detection cycles after consecutive interactions of t-DNA_1 (20 nM) with its specific probe (SH-DNA_1) and subsequent surface regenerations with FA35%. 45
Figure 2. 11 Scheme (A) and real-time SPR sensogram (B) of the covalent immobilization of NH_2-DNA probes in a MHDA SAM mediated by EDC/NHS activation. 46
Figure 2. 12 Immobilization signals of 1 μM NH2-DNA_1 on different MHDA/MUOH monolayers. 47
Figure 2. 13 Target hybridization SPR signals for the different MHDA/MUOH monolayers. ..47
Figure 2. 14 Effect on the hybridization efficiency after the employment of different molar ratios of NH_2-DNA_1/AH during the immobilization. 48
Figure 2. 15 General composition of the most commonly used human clinical samples for diagnostics: blood and serum. 49
Figure 2. 16 Structure of PLL-PEG molecule. 50
Figure 2. 17 Non-specific adsorption of commercial serum 100% over the two different thiol-chemistry based approaches with and without PLL-PEG passivation 51
Figure 2. 18 Antifouling effect by the employment of different additives to the hybridization buffer: (A) Tween 20 and (B) CHAPS. 52
Figure 2. 19 Study of the hybridization efficiency of the target after applying the antifouling buffer. 52
Figure 2. 20 Antifouling effects produced by different gold surface coatings. 53
Figure 2. 21 Antifouling effect of the SH-PEG CO_2H/NH_2 monolayer before and after adding 2% commercial serum in the continuous buffer. 54
Figure 2. 22 Hybridization efficiency study of t-$miRNA_1$ hybridization in diluted serum samples. (A) Hybridization efficiency in different dilutions of serum samples. (B) Sensogram monitoring the specific hybridization of t-$miRNA_1$ in serum 75%. 55
Figure 2. 23 General composition of human urine samples. 55
Figure 2. 24 Hybridization efficiency study of t-$miRNA_1$ in undiluted urine samples. (A) Sensogram monitoring the specific hybridization of different concentrations of t-$miRNA_1$ spiked in undiluted urine samples. (B) Comparison of the hybridization efficiency between buffer and undiluted urine conditions. 56
Figure 2. 25 Proposed mechanism for adenine adsorption on gold surfaces. Major interaction is attributed to coordination to the metal by the N atoms of the amine group and by the N_7 atom.57

Figure 2. 26 DNA probes immobilized on gold sensor surface in L-shaped conformation. 57
Figure 2. 27 Immobilization signals for both polyA-DNA and SH-DNA probes. 58
Figure 2. 28 Hybridization signals of t-DNA$_1$ at different polyA$_7$/polyA$_{15}$ DNA-probe molar ratio monolayers. 59
Figure 2. 29 Comparison of the non-specific adsorption of serum 100% over polyA-based monolayers with different surface coatings. 60
Figure 2. 30 Poly-A monolayer recycling assay monitored by the SPR biosensor. 61
Figure 2. 31 Scheme of the formation of an organosilane monolayer onto silicon-based surfaces. 63
Figure 2. 32 Schematic representation of the versatile derivatization of APTES monolayers. (A) Dimethylsuberimidiate (DMS). (B) 1,4-phenylene diisothiocyanate (PDITC). (C) N-succinimidyl-3-maleimidopropionate (SMP). (D) N-succinimidyl-3-(2-pyridyldithio) propionate. (E) N-succinimidyl (4-iodoacetyl) aminobenzoate (SIAB). 64
Figure 2. 33 XPS analysis of the Binding energy for Si 2p bonds in untreated (*red line*) and APTES-modified Si_3N_4 surfaces (*black line*). 66
Figure 2. 34 XPS analysis of the Binding energy for C1s bonds in untreated (A) and APTES-modified Si_3N_4 surfaces (B). 66
Figure 2. 35 Scheme of the heterobifunctional crosslinker sulfo-GMBS. 67
Figure 2. 36 Surface characterization of the biofunctionalization process by fluorescence. (A) Scheme of the protocol. (B) Fluorescent signals for each biofunctionalization step. 68
Figure 2. 37 Fluorescent signals after the incubation of the SH-DNA probe with different sulfo-GMBS crosslinker concentrations: *(a)* 5, *(b)* 10 and *(c)* 20 μM previously to surface biofunctionalization. 69
Figure 2. 38 Scheme of the homobifunctional crosslinker PDITC. 69
Figure 2. 39 Fluorescent signals of the PDITC biofunctionalization approach for (A) PDITC-activated surface; (B) Complementary DNA-probe functionalized surface; and (C) Non-complementary DNA-probe functionalized surface. 70
Figure 2. 40 SPR evaluation of the optimized PDITC biofunctionalization. (A) Immobilization on different surface coverages. (B) Sensogram of hybridization/regeneration cycle of t-DNA$_1$ in PDITC activated PEG-NH$_2$ surface. 71
Figure 2. 41 BiMW biosensor response for the immobilization of SH-DNA$_1$ over a PDITC-activated APTES monolayer. 72
Figure 2. 42 Real-time sensogram of the specific hybridization of t-DNA1 with the immobilized probe in the BiMW biosensor. 73
Figure 2. 43 Fluorescent signals given by the non-specific adsorption of the t-Cy3-DNA onto APTES monolayers 74
Figure 2. 44 Fluorescent emissions after incubation with fluorescent target in recycled Si_3N_4 surfaces at different intervals*: (a)* 1, *(b)* 2, *(c)* 3 and *(d)* 4 min. 74
Figure 2. 45 Fluorescent emission after a second silanization process in recycled Si_3N_4 surfaces at different intervals*: (a)* 1, *(b)* 2, *(c)* 3 and *(d)* 4 min. 75
Figure 2. 46 BiMW sensograms for two different biofunctionalization processes performed on the same chip: (A) SH-DNA probe immobilization signals (B) DNA target hybridization signals 75

Chapter 3· Quantitative evaluation of alternatively spliced mRNA isoforms by label-free real-time biosensing

Figure 3. 1 Regular splicing process. 85
Figure 3. 2 Types of alternative splicing: (A) Cassette-exon inclusion or skipping. (B) Alternative 3′ splice-site selection. (C) Alternative 5′ splice-site selection and (D) Intron retention. 86
Figure 3. 3 Schematic representation of the different RNA and protein isoforms generated by alternative splicing of *Fas* gene/*CD95*. 89
Figure 3. 4 Strategy 1 design. 90
Figure 3. 5 Strategy 1 optimization: (A) *Fas57* and *Fas567* isoforms signals. (B) T-*Exon6* signal. 90
Figure 3. 6 (A) MCH spacing effect in the 1:1 monolayer. (B) Calibration curves for independently analyzed isoforms. 91
Figure 3. 7 (A) T-*Exon6* capture at different concentrations of MCH. (B) Sensogram of the *Fas567* isoform and subsequent capture of the T-*Exon6* probe 92
Figure 3. 8 Design of Strategy 2. 93
Figure 3. 9 (A) *Fas57*-probe/MCH ratio study. (B) *FasExon6*-probe/MCH ratio study. 93
Figure 3. 10 Formamide effect on the *Fas567* isoform hybridization with *FasExon6* probe. 94
Figure 3. 11 SPR Strategy 3 for the quantitative evaluation of *Fas* gene alternatively spliced mRNA isoforms. 95
Figure 3. 12 Detection signals obtained by employing different concentration of MCH in the immobilization of *Fas57* (A) and *Fas56* (B) probes, respectively. 95
Figure 3. 13 Formamide effect in the cross-hybridization response of *Fas57* (A) and *Fas56* (B) probes. 96
Figure 3. 14 Effect of the change in the ionic strength of the hybridization buffer on isoform specificity for (A) *Fas57* probe and (B) *Fas56* probe. 96
Figure 3. 15 SPR calibration plots for *Fas57* (A) (R^2= 0.99) and *Fas56* (B) (R^2=0.99) probes using the optimized hybridization and detection conditions. Solid lines (blue and pink) correspond to the non-linear fit of the calibration curves. Red dashed line corresponds to 3xSD SPR noise, which is the limit for the minimum signal detectable. All data show mean ± SD of triplicate measurements. 97
Figure 3. 16 Schematic representation of the different RNA and protein isoforms generated by alternative splicing of *BCL-X gene*. 99
Figure 3. 17 SPR calibration plots for the detection of $BCL\text{-}X_L$ (A) (R^2= 0.99) and $BCL\text{-}X_S$ (B) (R^2= 0.99) synthetic isoforms based on the previously optimized detection conditions of *Fas* gene isoforms. Solid lines (purple and orange) correspond to the non-linear fit of the calibration curves. Red dashed line corresponds to 3xSD SPR noise, which is the limit for the minimum signal detectable. All data show mean ± SD of triplicate measurements. 99
Figure 3. 18 SPR sensograms of the detection of 20 ng/ µL of total HeLa cell RNA for the minigene-expression in both *Fas567* probe (A) and *Fas57* probe (B). 101
Figure 3. 19 Acrylamide gel electrophoresis fractionation of RT-PCR products obtained from RNA isolated from HeLa cells transfected with a *Fas* minigene expressing genomic sequences from exons 5 to 7, with or without overexpression of PTB. Vector-specific PCR primers were used for detecting specifically minigene-derived transcripts (A), while primers outside of the *Fas* genomic sequences included in the vector were used for detecting endogenous *Fas* expression (B). 101

Figure 3. 20 Demonstration of agreement between SPR biosensor and RT-qPCR technique for minigene expressed isoforms. (A) Line of equality plots and (B) difference against mean plots (Almant-Bland model for replicated measurements) 102
Figure 3. 21 Agarose electrophoresis analysis of HeLa cells total RNA fragmentation after different incubation times in alkaline buffer. 103
Figure 3. 22 Scheme of the RNase H test. Binding sites of DNA probes 428 and 429 for RNA cleavage and of *Fas* exon 5 sense primer and *Fas* exon 7 antisense primer for PCR amplification are indicated. 104
Figure 3. 23 Agarose electrophoresis analysis of HeLa cells total RNA fragmentation after different RNase H cleavage conditions. Lanes and conditions employed are indicated for each of the lanes. 105
Figure 3. 24 SPR signal for each of the conditions tested. 106
Figure 3. 25 Scheme of the strategy followed for the optimization of the RNase H activity... 107
Figure 3. 26 RNase H buffer concentration test. 107
Figure 3. 27 RNase H concentration test. 108
Figure 3. 28 Temperature test for RNase H reaction. 108
Figure 3. 29 SPR sensograms of the detection of 20 ng/ µL of total HeLa cell RNA for the endogenous expression of the two isoforms in both *Fas567* probe (A) and *Fas57* probe (B) after applying RNA hydrolysis (Δ), RNase H cleavage and without any treatment (0). 109
Figure 3. 30 Demonstration of the agreement between the SPR biosensor and the RT-qPCR technique for all HeLa cell lines in both fragmentation procedures. (A) Line of equality plot for alkaline hydrolysis. (B) Difference against mean plots (Almant-Bland model for replicated measurements) for alkaline hydrolysis. (C) Line of equality plot for RNase H cleavage. (D) Difference against mean plots (Bland-Altman model for replicated measurements) for RNase H cleavage. 110
Figure 3. 31 Demonstration of the agreement between the SPR biosensor and the RT-qPCR technique for isoform ratios in both fragmentation procedures. (A) Line of equality plot for alkaline hydrolysis. (B) Difference against mean plots (Almant-Bland model for replicated measurements) for alkaline hydrolysis. (C) Line of equality plot for RNase H cleavage. (D) Difference against mean plots (Bland-Altman model for replicated measurements) for RNase H cleavage. 111
Figure 3. 32 BiMW real-time sensograms of *Fas* isoforms for (A) *Fas57* probe and (B) *Fas56* probe. 113
Figure 3. 33 BiMW calibration curves for (A) *Fas57* probe and (B) *Fas56* probe. Solid lines (blue and pink) correspond to the non-linear fit of the calibration curves. Red dashed line corresponds to 3xSD SPR noise, which is the limit for the minimum signal detectable. All data show mean ± SD of triplicate measurements 114

Chapter 4· Profiling micro-RNA levels by amplification-free and label-free biosensing

Figure 4. 1 Micro-RNA biogenesis 122
Figure 4. 2 Sensor responses of the miR-181s family members at 50 nM concentration during hybridization with miR-181a probe anchored at the SPR sensor surface 126
Figure 4. 3 Effect of the additives in the hybridization efficiencies with the miR-181a probe for the different miR-181s family members. 128
Figure 4. 4 Effect of the different additives in the hybridization efficiency of the miR-181s family members with the miR-181a probe in combination with FA 40%. 129

Figure 4. 5 Study of the hybridization selectivity of pre-miR-181a with miR-181a probe. (A) Sequence and secondary structure of pre-miR-181a. (B) SPR biosensor response to 50 nM of miR-181a and pre-miR-181a. 129

Figure 4. 6 Calibration curve of the specific detection of miR-181a by SPR. Solid line corresponds to the non-linear fit of the calibration curve. All data show mean ± SD of triplicate measurements. 130

Figure 4. 7 Schematic representation of the antibody-based amplification SPR approach for miRNA-detection. 131

Figure 4. 8 Evaluation of anti-DNA-RNA antibody concentrations for the optimization of the signal amplification step 132

Figure 4. 9 Effect in antibody capture efficiency after hybridization of 50nM miR-181a in different buffers (PBS, SSC and Tris) at several concentrations (0.5, 1, 2 and 5x). 132

Figure 4. 10 Antibody specificity test by SPR real-time evaluation. 133

Figure 4. 11 SPR test for the surface regeneration efficiency of FA 35% after the miRNA/antibody recognition. 134

Figure 4. 12 Antibody amplification to non-detectable signals of miR-181a by SPR biosensor. (A) Sensograms for the antibody-amplified signals at low concentrations of miR-181a (from 10 to 250 pM). (B) Calibration curve obtained for the antibody amplification after hybridization of different concentrations of miR-181a at the optimized conditions. Solid line corresponds to the non-linear fit of the calibration curve. All data show mean ± SD of triplicate measurements. 134

Figure 4. 13 Calibration curve obtained in urine with the developed methodology for the specific detection of miR-181a. Solid line corresponds to the non-linear fit of the calibration curves. All data show mean ± SD of triplicate measurements. 136

Figure 4. 14 Real-time sensograms for different urine samples from healthy donors (S1 and S2) and bladder cancer patients (S3 and S4). 137

Figure 4. 15 BiMW sensogram demonstrating the specificity of the developed methodology. 139

Figure 4. 16 Detection of miR-181a by the BiMW biosensor. (A) Calibration curve obtained by employing different concentrations of miR-181a standard solutions. Solid line correspond to the exponential fit of the calibration curve. All data show mean ± SD of triplicate measurements. (B) Sensograms obtained for the lowest concentrations experimentally measured by the BiMW biosensor 140

Figure 4. 17 BiMW biosensor assessment of the anti-fouling properties of the employed methodology 141

Figure 4. 18 Concentrations of miR-181a in urine samples quantified by the BiMW biosensor. 142

Chapter 5· DNA methylation profiling for cancer diagnosis

Figure 5. 1 DNA cytosine methylation. 147

Figure 5. 2 DNA methylation and cancer. 148

Figure 5. 3 Scheme of the two-step DNA methylation recognition methodology. 151

Figure 5. 4 Optimization of the *PAX-5* fragment detection conditions. (A) *PAX-5* probe/MCH molar ratio optimization. (B) Optimization of the %Formamide in the hybridization buffer... 152

Figure 5. 5 Calibration curve for the *PAX-5* fragment ($R^2 = 0.96$) evaluation using the optimized hybridization conditions. Solid line corresponds to the non-linear fit of the calibration curve.

Red dashed line corresponds to 3xSD SPR noise, which is the limit for the minimum signal detectable. All data show mean ± SD of triplicate measurements. 152

Figure 5. 6 Optimization of the detection of methyl-cytosine residues in *PAX-5* fragment. (A) MBD2 binding specificity assessment. (B) Concentration-dependence of MBD2 binding. 153

Figure 5. 7 Determination of the methylation profile of *PAX-5* fragment. 154

Figure 5. 8 Secondary structure prediction in the *PAX-5* fragment. 154

Annex· Sensitive and Label-Free Detection of miRNA-145 by Triplex Formation

Figure A. 1 Scheme of the triplex capture. 163

Figure A. 2 Triplex and duplex hybridization of miR-145. (A) Scheme showing the binding of tail-clamps and complementary sequences to miRNA-145 yielding triplex and duplex structures respectively. (B) Scheme showing the triads that forms triplex structures C^+ -8-aminoG - C and T-A-T. 165

Figure A. 3 Scheme of the different probe for miR-145 capture. (A) 3AG PT Clamp bioreceptor. (B) PT Clamp. (C) 3AG Control Clamp. (D) Control Clamp. (E) 3AG Compl. miR-145. (F) Compl. miR-145. 166

Figure A. 4 SPR results for the detection of miR-145 with the different probe formats. (A) SPR calibration curves of the detection of miR-145 with the different probe formats. The sensitivity for each bioreceptor was considered as three times the baseline noise standard deviation (discontinuous red line). (B) Real-time sensograms of 30 nM miRNA-145 using the different probe variants 166

List of Tables

Chapter 1· Introduction

Table 1. 1 Integrated optical biosensors compared in terms of architecture and detection limits 30

Chapter 2· DNA-functionalization of the sensor surface

Table 2. 1 Contact angle values of the different steps during APTES-modification of Si_3N_4 surfaces. 65
Table 2. 2 Contact angle values for PDITC-modified and DNA functionalized Si_3N_4 surfaces. 71
Table 2. 3 Sequences for probes and DNA/RNA synthetic targets employed in this thesis. 78

Chapter 3· Quantitative evaluation of alternatively spliced mRNA isoforms by label-free real-time biosensing

Table 3. 1 Variability of the SPR sensor response for *Fas* isoforms in intra- and inter-assays performed by different operators. All Pvalues indicated not significant variation between the measurements (*P>0.05*, one-way ANOVA test). 98
Table 3. 2 Variability of the SPR sensor signal for *BCL-X* isoforms intra-assays performed by different operators. The Mean ± SD are from 3 replicates performed in the same biofunctionalized sensor chip. All Pvalues indicated not significant variation between the data (*P>0.05*, one-way ANOVA test). 100
Table 3. 3 RT-qPCR and SPR comparison of the isoform content analysis from HeLa cells endogenous expression and minigene-induced overexpression. Isoform concentration in nM for SPR was calculated through the calibration curves obtained for each receptor according to their ΔR(%). 102
Table 3. 4 Conditions employed for the RNase cleavage test. 104
Table 3. 5 SPR results after application of RNase H cleavage to HeLa cell endogenous level samples. 106
Table 3. 6 RT-PCR and SPR comparison of the isoform content analysis from HeLa cells endogenous expression. Isoform concentration in nM for SPR was calculated through the calibration curves obtained for each receptor according to their ΔR(%). Data used for ratio determination in SPR was calculated from 2 independent measurements of each sample type with each receptor. 110
Table 3. 7 Sequences for probes and DNA/RNA synthetic targets employed in this thesis. 115
Table 3. 8 DNA probes for RNase H cleavage and *Fas* mRNA fragments generated. 117

Chapter 4· Profiling micro-RNA levels by amplification-free and label-free biosensing

Table 4. 1 Matching sequences and complementarity of miR-181a and its homologous. 127
Table 4. 2 MiR-181a concentration values determined in four different urine samples by SPR and BiMW biosensors. 142
Table 4. 3 Sequences for probes and DNA/RNA synthetic targets employed in this Thesis. . 143

Chapter 5·DNA methylation profiling for cancer diagnosis

Table 5. 1 Sequences for probes and DNA synthetic targets employed in this thesis. 156

Annex· Sensitive and Label-Free Detection of miRNA-145 by Triplex Formation

Table A. 1 LODs calculated for each probe modality. 167
Table A. 2. MiR-145 target and probe sequences. 168

Bibliography

1. Crick, F. Central dogma of molecular biology. *Nature* **227**, 561-563 (1970).
2. Mattick, J.S. Deconstructing the Dogma A New View of the Evolution and Genetic Programming of Complex Organisms *Natural Genetic Engineering and Natural Genome Editing: Ann. N.Y. Acad. Sci.* **1178**, 29-46 (2009).
3. Darwin, C. (John Murray, London, 1859).
4. Goldberg, A.D., Allis, C.D. & Bernstein, E. Epigenetics: a landscape takes shape. *Cell* **128**, 635-638 (2007).
5. Fuks, F. DNA methylation and histone modifications: teaming up to silence genes. *Current opinion in genetics & development* **15**, 490-495 (2005).
6. Liu, H., He, L. & Tang, L. Alternative splicing regulation and cell lineage differentiation. *Current stem cell research & therapy* **7**, 400-406 (2012).
7. He, L. & Hannon, G.J. MicroRNAs: small RNAs with a big role in gene regulation. *Nature Reviews Genetics* **5**, 522-531 (2004).
8. Esteller, M. Aberrant DNA methylation as a cancer-inducing mechanism. *Annu. Rev. Pharmacol. Toxicol.* **45**, 629-656 (2005).
9. Oltean, S. & Bates, D. Hallmarks of alternative splicing in cancer. *Oncogene* **33**, 5311-5318 (2014).
10. Jansson, M.D. & Lund, A.H. MicroRNA and cancer. *Molecular oncology* **6**, 590-610 (2012).
11. Murr, R. Interplay between different epigenetic modifications and mechanisms. *Advances in genetics* **70**, 101-141 (2009).
12. Christman, J.K. 5-Azacytidine and 5-aza-2'-deoxycytidine as inhibitors of DNA methylation: mechanistic studies and their implications for cancer therapy. *Oncogene* **21**, 5483-5495 (2002).
13. Zhou, L. et al. Zebularine: a novel DNA methylation inhibitor that forms a covalent complex with DNA methyltransferases. *Journal of molecular biology* **321**, 591-599 (2002).
14. Spitali, P. & Aartsma-Rus, A. Splice Modulating Therapies for Human Disease. *Cell* **148**, 1085-1088 (2012).
15. Ling, H., Fabbri, M. & Calin, G.A. MicroRNAs and other non-coding RNAs as targets for anticancer drug development. *Nature reviews Drug discovery* **12**, 847-865 (2013).
16. Bertino, J.R., Banerjee, D. & Mishra, P.J. Pharmacogenomics of microRNA: a miRSNP towards individualized therapy. (2007).
17. Esau, C.C. & Monia, B.P. Therapeutic potential for microRNAs. *Advanced drug delivery reviews* **59**, 101-114 (2007).
18. Bader, A.G. & Lammers, P. The therapeutic potential of microRNAs. *Innovations in Pharmaceutical Technology*, 52-55 (2011).
19. Gingeras, T.R., Higuchi, R., Kricka, L.J., Lo, Y.D. & Wittwer, C.T. Fifty years of molecular (DNA/RNA) diagnostics. *Clinical chemistry* **51**, 661-671 (2005).
20. Saiki, R.K., Walsh, P.S., Levenson, C.H. & Erlich, H.A. Genetic analysis of amplified DNA with immobilized sequence-specific oligonucleotide probes. *Proceedings of the National Academy of Sciences* **86**, 6230-6234 (1989).
21. Gooding, J.J. Biosensor technology for detecting biological warfare agents: Recent progress and future trends. *Analytica Chimica Acta* **559**, 137-151 (2006).
22. Sobrino, B., Brión, M. & Carracedo, A. SNPs in forensic genetics: a review on SNP typing methodologies. *Forensic science international* **154**, 181-194 (2005).

23. Herring, A., Inglis, N., Ojeh, C., Snodgrass, D.a. & Menzies, J. Rapid diagnosis of rotavirus infection by direct detection of viral nucleic acid in silver-stained polyacrylamide gels. *Journal of Clinical Microbiology* **16**, 473-477 (1982).
24. Dubeau, L., Chandler, L.A., Gralow, J.R., Nichols, P.W. & Jones, P.A. Southern blot analysis of DNA extracted from formalin-fixed pathology specimens. *Cancer Research* **46**, 2964-2969 (1986).
25. Várallyay, E., Burgyán, J. & Havelda, Z. MicroRNA detection by northern blotting using locked nucleic acid probes. *Nature protocols* **3**, 190-196 (2008).
26. Desforges, J.F. & Eisenstein, B.I. The polymerase chain reaction: a new method of using molecular genetics for medical diagnosis. *New England Journal of Medicine* **322**, 178-183 (1990).
27. Espy, M. et al. Real-time PCR in clinical microbiology: applications for routine laboratory testing. *Clinical microbiology reviews* **19**, 165-256 (2006).
28. Bertucci, F. et al. Gene expression profiling of colon cancer by DNA microarrays and correlation with histoclinical parameters. *Oncogene* **23**, 1377-1391 (2004).
29. Shendure, J. & Ji, H. Next-generation DNA sequencing. *Nature biotechnology* **26**, 1135-1145 (2008).
30. Tiwari, I. & Singh, M. Advances in Sensors' Nanotechnology. *Advanced Sensor and Detection Materials*, 1 (2014).
31. Hahn, S., Mergenthaler, S., Zimmermann, B. & Holzgreve, W. Nucleic acid based biosensors: the desires of the user. *Bioelectrochemistry* **67**, 151-154 (2005).
32. Sagadevan, S. & Periasamy, M. Recent trends in nanobiosensors and their applications - A review. *Reviews of Advanced Materia Science* **36**, 62-69 (2014).
33. Ahn, C.H. et al. Disposable smart lab on a chip for point-of-care clinical diagnostics. *Proceedings of the IEEE* **92**, 154-173 (2004).
34. Kumar, S. et al. Microfluidic-integrated biosensors: Prospects for point-of-care diagnostics. *Biotechnology journal* **8**, 1267-1279 (2013).
35. Wang, J. et al. DNA electrochemical biosensors for environmental monitoring. A review. *Analytica Chimica Acta* **347**, 1-8 (1997).
36. Wang, J. DNA biosensors based on peptide nucleic acid (PNA) recognition layers. A review. *Biosensors and Bioelectronics* **13**, 757-762 (1998).
37. Aguado, G.P., Rúa, F., Branchadell, V., Nielsen, P.E. & Ortuño, R.M. Cyclobutyl-carbonyl substituted PNA: synthesis and study of a novel PNA derivative. *Tetrahedron: Asymmetry* **17**, 2499-2503 (2006).
38. Kaur, H., Babu, B.R. & Maiti, S. Perspectives on chemistry and therapeutic applications of locked nucleic acid (LNA). *Chemical Reviews* **107**, 4672-4697 (2007).
39. Carrascosa, L.G. et al. Sensitive and label-free biosensing of RNA with predicted secondary structures by a triplex affinity capture method. *Nucleic Acids Research* **40**, e56 (2012).
40. Liu, J., Cao, Z. & Lu, Y. Functional nucleic acid sensors. *Chemical Reviews* **109**, 1948-1998 (2009).
41. McKeague, M. & DeRosa, M.C. Challenges and opportunities for small molecule aptamer development. *Journal of nucleic acids* **2012** (2012).
42. Bora, U., Sett, A. & Singh, D. Nucleic Acid Based Biosensors for Clinical Applications. *Biosens J* **1**, 104 (2013).
43. Ronkainen, N.J., Halsall, H.B. & Heineman, W.R. Electrochemical biosensors. *Chemical Society Reviews* **39**, 1747-1763 (2010).
44. Tamayo, J., Kosaka, P.M., Ruz, J.J., San Paulo, Á. & Calleja, M. Biosensors based on nanomechanical systems. *Chemical Society Reviews* **42**, 1287-1311 (2013).
45. Ferreira, G.N., da-Silva, A.-C. & Tomé, B. Acoustic wave biosensors: physical models and biological applications of quartz crystal microbalance. *Trends in biotechnology* **27**, 689-697 (2009).

46. Tombelli, S., Mascini, M., Braccini, L., Anichini, M. & Turner, A.P. Coupling of a DNA piezoelectric biosensor and polymerase chain reaction to detect apolipoprotein E polymorphisms. *Biosensors and Bioelectronics* **15**, 363-370 (2000).
47. Dell'Atti, D. et al. Development of combined DNA-based piezoelectric biosensors for the simultaneous detection and genotyping of high risk Human Papilloma Virus strains. *Clinica chimica acta* **383**, 140-146 (2007).
48. Carrascosa, L.G., Moreno, M., Álvarez, M. & Lechuga, L.M. Nanomechanical biosensors: a new sensing tool. *TrAC Trends in Analytical Chemistry* **25**, 196-206 (2006).
49. Arlett, J., Myers, E. & Roukes, M. Comparative advantages of mechanical biosensors. *Nature nanotechnology* **6**, 203-215 (2011).
50. McKendry, R. et al. Multiple label-free biodetection and quantitative DNA-binding assays on a nanomechanical cantilever array. *Proceedings of the National Academy of Sciences* **99**, 9783-9788 (2002).
51. Alvarez, M. & Lechuga, L.M. Microcantilever-based platforms as biosensing tools. *Analyst* **135**, 827-836 (2010).
52. Ligler, F.S. & Taitt, C.R. Optical biosensors: today and tomorrow. (Elsevier, 2011).
53. Narayanaswamy, R. & Wolfbeis, O.S. Optical sensors: industrial, environmental and diagnostic applications, Vol. 1. (Springer, 2004).
54. Piunno, P.A., Krull, U.J., Hudson, R.H., Damha, M.J. & Cohen, H. Fiber-optic DNA sensor for fluorometric nucleic acid determination. *Analytical chemistry* **67**, 2635-2643 (1995).
55. Yao, G., Fang, X., Yokota, H., Yanagida, T. & Tan, W. Monitoring molecular beacon DNA probe hybridization at the single-molecule level. *Chemistry-A European Journal* **9**, 5686-5692 (2003).
56. Chen, N. et al. Quantum dot probes for observation of single molecule DNA and a synthetic polyelectrolyte higher-order structure. *Soft Matter* **6**, 2834-2841 (2010).
57. Fan, X. et al. Sensitive optical biosensors for unlabeled targets: A review. *Analytica Chimica Acta* **620**, 8-26 (2008).
58. Daghestani, H.N. & Day, B.W. Theory and applications of surface plasmon resonance, resonant mirror, resonant waveguide grating, and dual polarization interferometry biosensors. *Sensors* **10**, 9630-9646 (2010).
59. Passaro, V., Dell'Olio, F., Casamassima, B. & De Leonardis, F. Guided-wave optical biosensors. *Sensors* **7**, 508-536 (2007).
60. Šípová, H. & Homola, J. Surface plasmon resonance sensing of nucleic acids: a review. *Analytica chimica acta* **773**, 9-23 (2013).
61. Homola, J. Surface plasmon resonance sensors for detection of chemical and biological species. *Chemical Reviews* **108**, 462-493 (2008).
62. Vaisocherová, H. et al. Investigating oligonucleotide hybridization at subnanomolar level by surface plasmon resonance biosensor method. *Biomolecules at Surfaces* **82**, 394 - 398 (2005).
63. Li, Y.-J., Xiang, J. & Zhou, F. Sensitive and Label-Free Detection of DNA by Surface Plasmon Resonance. *Plasmonics* **2**, 79-87 (2007).
64. Carrascosa, L.G., Calle, A. & Lechuga, L.M. Label-free detection of DNA mutations by SPR: application to the early detection of inherited breast cancer. *Anal Bioanal Chem* **393**, 1173-1182 (2009).
65. Nasheri, N. et al. An enzyme-linked assay for the rapid quantification of microRNAs based on the viral suppressor of RNA silencing protein p19. *Anal Biochem.* **412**, 165-172 (2011).
66. Sipova, H. et al. Surface Plasmon Resonance Biosensor for Rapid Label-Free Detection of Microribonucleic Acid at Subfemtomole Level *Analytical Chemistry Article ASAP* (2010).

67. Lee, H., Wark, A. & Corn, R. Enhanced bioaffinity sensing using surface plasmons, surface enzyme reactions, nanoparticles and diffraction gratings. *Analyst.* **133**, 596-601 (2008).
68. Zhou, W., Chen, Y. & Corn, R. Ultrasensitive microarray detection of short RNA sequences with enzymatically modified nanoparticles and surface plasmon resonance imaging measurements. *Anal Chem* **83**, 3897-3902 (2011).
69. Nelson, B., Liles, M., Frederick, K., Corn, R. & Goodman, R. Label-free detection of 16S ribosomal RNA hybridization on reusable DNA arrays using surface plasmon resonance imaging. *Environ Microbiol.* **4**, 735-743 (2002).
70. Joung, H. et al. High sensitivity detection of 16s rRNA using peptide nucleic acid probes and a surface plasmon resonance biosensor. *Anal Chim Acta.* **630**, 168-173 (2008).
71. Boucard, D., Toulmé, J. & Di Primo, C. Bimodal loop-loop interactions increase the affinity of RNA aptamers for HIV-1 RNA structures. *Biochemistry* **45**, 1518-1524 (2006).
72. Nair, T.M., Myszka, D.G. & Davis, D.R. Surface plasmon resonance kinetic studies of the HIV TAR RNA kissing hairpin complex and its stabilization by 2-thiouridine modification. *Nucleic Acids Res.* **28**, 1935-1940 (2000).
73. Mandir, J.B. et al. Rapid Determination of RNA Accessible Sites by Surface Plasmon Resonance Detection of Hybridization to DNA arrays. *Anal Chem.* **81**, 8949-8956 (2009).
74. Homola, J. Surface plasmon resonance based sensors, Vol. 4. (Springer, 2006).
75. Raether, H. Surface plasmons on gratings. *Surface Plasmons on Smooth and Rough Surfaces and on Gratings*, 91-116 (1988).
76. Dowling, D., Donnelly, K., McConnell, M., Eloy, R. & Arnaud, M. Deposition of anti-bacterial silver coatings on polymeric substrates. *Thin Solid Films* **398**, 602-606 (2001).
77. Nagata, K. & Handa, H. Real-time analysis of biomolecular interactions. (Springer, 2000).
78. Estevez, M.-C., Otte, M.A., Sepulveda, B. & Lechuga, L.M. Trends and challenges of refractometric nanoplasmonic biosensors: A review. *Analytica chimica acta* **806**, 55-73 (2014).
79. Lofas, S., Choulier, L. & Altschuh, D. Surface Plasmon Resonance. *Biophysical Approaches Determining Ligand Binding to Biomolecular Targets: Detection, Measurement and Modelling*, 136 (2011).
80. Baird, C.L. & Myszka, D.G. Current and emerging commercial optical biosensors. *Journal of molecular recognition* **14**, 261-268 (2001).
81. www.biacore.com.
82. www.ti.com.
83. www.xantec.com.
84. www.horiba.com.
85. www.biosuplar.de.
86. www.sensia.es.
87. McDonnell, J.M. Surface plasmon resonance: towards an understanding of the mechanisms of biological molecular recognition. *Current Opinion in Chemical Biology* **5**, 572-577 (2001).
88. Rich, R.L. & Myszka, D.G. Advances in surface plasmon resonance biosensor analysis. *Current opinion in biotechnology* **11**, 54-61 (2000).
89. Bolduc, O.R., Live, L.S. & Masson, J.-F. High-resolution surface plasmon resonance sensors based on a dove prism. *Talanta* **77**, 1680-1687 (2009).
90. Tamir, T. Guided-wave optoelectronics, Vol. 26. (Springer, 1988).
91. Nellen, P.M., Tiefenthaler, K. & Lukosz, W. Integrated optical input grating couplers as biochemical sensors. *Sensors and Actuators* **15**, 285-295 (1988).

92. Iqbal, M. et al. Label-free biosensor arrays based on silicon ring resonators and high-speed optical scanning instrumentation. *Selected Topics in Quantum Electronics, IEEE Journal of* **16**, 654-661 (2010).
93. Kozma, P., Kehl, F., Ehrentreich-Förster, E., Stamm, C. & Bier, F.F. Integrated planar optical waveguide interferometer biosensors: A comparative review. *Biosensors and Bioelectronics* **58**, 287-307 (2014).
94. Prieto, F. et al. An integrated optical interferometric nanodevice based on silicon technology for biosensor applications. *Nanotechnology* **14**, 907 (2003).
95. Densmore, A. et al. Silicon photonic wire biosensor array for multiplexed real-time and label-free molecular detection. *Optics letters* **34**, 3598-3600 (2009).
96. Brandenburg, A. & Henninger, R. Integrated optical Young interferometer. *Applied optics* **33**, 5941-5947 (1994).
97. Ymeti, A., Kanger, J.S., Wijn, R., Lambeck, P.V. & Greve, J. Development of a multichannel integrated interferometer immunosensor. *Sensors and Actuators B: Chemical* **83**, 1-7 (2002).
98. Sepulveda, B. et al. Optical biosensor microsystems based on the integration of highly sensitive Mach–Zehnder interferometer devices. *Journal of Optics A: Pure and Applied Optics* **8**, S561 (2006).
99. Mulder, H.K., Ymeti, A., Subramaniam, V. & Kanger, J.S. Size-selective detection in integrated optical interferometric biosensors. *Optics express* **20**, 20934-20950 (2012).
100. Zinoviev, K., Gonzalez Guerrero, A., Dominguez, C. & Lechuga, L. Integrated Bimodal Waveguide Interferometric Biosensor for Label-Free Analysis. *Journal of Lightwave Technology* **29**, 1926-1930 (2011).
101. Vogt, M. & Hauptmann, R. Plasma-deposited passivation layers for moisture and water protection. *Surface and Coatings Technology* **74**, 676-681 (1995).
102. Dante, S. et al. All-optical phase modulation for integrated interferometric biosensors. *Optics express* **20**, 7195-7205 (2012).
103. Duval, D. & Lechuga, L.M. Breakthroughs in photonics 2012: 2012 breakthroughs in lab-on-a-chip and optical biosensors. (Institute of Electrical and Electronics Engineers, 2013).
104. WO2009010624-Interferometer and sensor based on bimodal optical waveguide and SENSING method. EP2017602; PCT/ES08/070142; US20100271634 (Granted).
105. Dante, S., Duval, D., Fariña, D., González-Guerrero, A.B. & Lechuga, L.M. Linear readout of integrated interferometric biosensors using a periodic wavelength modulation. *Laser & Photonics Reviews* **9**, 248-255 (2015).
106. Zourob, M. Recognition receptors in biosensors. (Springer, 2010).
107. Rabe, M., Verdes, D. & Seeger, S. Understanding protein adsorption phenomena at solid surfaces. *Advances in colloid and interface science* **162**, 87-106 (2011).
108. Bünemann, H., Westhoff, P. & Herrmann, R.G. Immobilization of denatured DNA to macroporous supports: I. Efficiency of different coupling procedures. *Nucleic Acids Research* **10**, 7163-7180 (1982).
109. Peterson, A.W., Heaton, R.J. & Georgiadis, R.M. The effect of surface probe density on DNA hybridization. *Nucleic Acids Research* **29**, 5163-5168 (2001).
110. Steel, A., Levicky, R., Herne, T. & Tarlov, M.J. Immobilization of nucleic acids at solid surfaces: effect of oligonucleotide length on layer assembly. *Biophysical journal* **79**, 975-981 (2000).
111. Opdahl, A., Petrovykh, D.Y., Kimura-Suda, H., Tarlov, M.J. & Whitman, L.J. Independent control of grafting density and conformation of single-stranded DNA brushes. *Proceedings of the National Academy of Sciences* **104**, 9-14 (2007).
112. Ermini, M. et al. A rational approach in probe design for nucleic acid-based biosensing. *Biosensors and Bioelectronics* **26**, 4785-4790 (2011).

113. Hormeno, S. et al. Mechanical Properties of High-G· C Content DNA with A-Type Base-Stacking. *Biophysical journal* **100**, 1996-2005 (2011).
114. Herne, T.M. & Tarlov, M.J. Characterization of DNA probes immobilized on gold surfaces. *Journal of the American Chemical Society* **119**, 8916-8920 (1997).
115. Burgener, M., Sänger, M. & Candrian, U. Synthesis of a stable and specific surface plasmon resonance biosensor surface employing covalently immobilized peptide nucleic acids. *Bioconjugate chemistry* **11**, 749-754 (2000).
116. Mir, M., Alvarez, M., Azzaroni, O. & Knoll, W. Comparison of different supramolecular architectures for oligonucleotide biosensing. *Langmuir* **24**, 13001-13006 (2008).
117. Schreiner, S.M. et al. Controlled and efficient hybridization achieved with DNA probes immobilized solely through preferential DNA-substrate interactions. *Analytical chemistry* **82**, 2803-2810 (2010).
118. Sakao, Y., Nakamura, F., Ueno, N. & Hara, M. Hybridization of oligonucleotide by using DNA self-assembled monolayer. *Colloids and Surfaces B: Biointerfaces* **40**, 149-152 (2005).
119. Ulman, A. Formation and structure of self-assembled monolayers. *Chemical reviews* **96**, 1533-1554 (1996).
120. Vericat, C., Vela, M., Benitez, G., Carro, P. & Salvarezza, R. Self-assembled monolayers of thiols and dithiols on gold: new challenges for a well-known system. *Chemical Society Reviews* **39**, 1805-1834 (2010).
121. Peeters, S. et al. Impact of spacers on the hybridization efficiency of mixed self-assembled DNA/alkanethiol films. *Biosensors and Bioelectronics* **24**, 72-77 (2008).
122. Gong, P., Lee, C.-Y., Gamble, L.J., Castner, D.G. & Grainger, D.W. Hybridization behavior of mixed DNA/alkylthiol monolayers on gold: characterization by surface plasmon resonance and 32P radiometric assay. *Analytical chemistry* **78**, 3326-3334 (2006).
123. Xia, H., Hou, Y., Ngai, T. & Zhang, G. pH induced DNA folding at interface. *The Journal of Physical Chemistry B* **114**, 775-779 (2009).
124. Satjapipat, M., Sanedrin, R. & Zhou, F. Selective desorption of alkanethiols in mixed self-assembled monolayers for subsequent oligonucleotide attachment and DNA hybridization. *Langmuir* **17**, 7637-7644 (2001).
125. Lee, C.-Y., Gamble, L.J., Grainger, D.W. & Castner, D.G. Mixed DNA/oligo (ethylene glycol) functionalized gold surfaces improve DNA hybridization in complex media. *Biointerphases* **1**, 82-92 (2006).
126. Carrascosa, L.G., Martínez, L., Huttel, Y., Román, E. & Lechuga, L.M. Understanding the role of thiol and disulfide self-assembled DNA receptor monolayers for biosensing applications. *European Biophysics Journal* **39**, 1433-1444 (2010).
127. Fuchs, J. et al. Effects of formamide on the thermal stability of DNA duplexes on biochips. *Analytical biochemistry* **397**, 132-134 (2010).
128. Hutton, J.R. Renaturation kinetics and thermal stability of DNA in aqueous solutions of formamide and urea. *Nucleic acids research* **4**, 3537-3555 (1977).
129. Ulianas, A. et al. A regenerable screen-printed DNA biosensor based on acrylic microsphere–gold nanoparticle composite for genetically modified soybean determination. *Sensors and Actuators B: Chemical* **190**, 694-701 (2014).
130. Tombelli, S., Mascini, M., Sacco, C. & Turner, A.P. A DNA piezoelectric biosensor assay coupled with a polymerase chain reaction for bacterial toxicity determination in environmental samples. *Analytica chimica acta* **418**, 1-9 (2000).
131. Wood, R. How to validate analytical methods. *TrAC Trends in Analytical Chemistry* **18**, 624-632 (1999).
132. Lee, C.-Y., Nguyen, P.-C.T., Grainger, D.W., Gamble, L.J. & Castner, D.G. Structure and DNA hybridization properties of mixed nucleic acid/maleimide-ethylene glycol monolayers. *Analytical chemistry* **79**, 4390-4400 (2007).

133. Brockman, J.M., Frutos, A.G. & Corn, R.M. A multistep chemical modification procedure to create DNA arrays on gold surfaces for the study of protein-DNA interactions with surface plasmon resonance imaging. *Journal of the American Chemical Society* **121**, 8044-8051 (1999).
134. Yang, N., Su, X., Tjong, V. & Knoll, W. Evaluation of two-and three-dimensional streptavidin binding platforms for surface plasmon resonance spectroscopy studies of DNA hybridization and protein–DNA binding. *Biosensors and Bioelectronics* **22**, 2700-2706 (2007).
135. Beier, M. & Hoheisel, J.D. Versatile derivatisation of solid support media for covalent bonding on DNA-microchips. *Nucleic acids research* **27**, 1970-1977 (1999).
136. Dugas, V., Depret, G., Chevalier, Y., Nesme, X. & Souteyrand, É. Immobilization of single-stranded DNA fragments to solid surfaces and their repeatable specific hybridization: covalent binding or adsorption? *Sensors and Actuators B: Chemical* **101**, 112-121 (2004).
137. Vaisocherová, H., Brynda, E. & Homola, J. Functionalizable low-fouling coatings for label-free biosensing in complex biological media: advances and applications. *Analytical and bioanalytical chemistry* **407**, 3927-3953 (2015).
138. Vaisocherova, H. et al. Ultralow fouling and functionalizable surface chemistry based on a zwitterionic polymer enabling sensitive and specific protein detection in undiluted blood plasma. *Analytical chemistry* **80**, 7894-7901 (2008).
139. Vaisocherová, H. et al. Functionalized ultra-low fouling carboxy-and hydroxy-functional surface platforms: functionalization capacity, biorecognition capability and resistance to fouling from undiluted biological media. *Biosensors and Bioelectronics* **51**, 150-157 (2014).
140. Blättler, T.M., Pasche, S., Textor, M. & Griesser, H.J. High salt stability and protein resistance of poly (L-lysine)-g-poly (ethylene glycol) copolymers covalently immobilized via aldehyde plasma polymer interlayers on inorganic and polymeric substrates. *Langmuir* **22**, 5760-5769 (2006).
141. Soler, M. et al. Direct detection of protein biomarkers in human fluids using site-specific antibody immobilization strategies. *Sensors* **14**, 2239-2258 (2014).
142. Rodriguez-Emmenegger, C. et al. Polymer Brushes Showing Non-Fouling in Blood Plasma Challenge the Currently Accepted Design of Protein Resistant Surfaces. *Macromolecular rapid communications* **32**, 952-957 (2011).
143. Marie, R., Dahlin, A.B., Tegenfeldt, J.O. & Höök, F. Generic surface modification strategy for sensing applications based on Au/SiO2 nanostructures. *Biointerphases* **2**, 49-55 (2007).
144. Schreiner, S.M. et al. Impact of DNA–surface interactions on the stability of DNA hybrids. *Analytical chemistry* **83**, 4288-4295 (2011).
145. Kimura-Suda, H., Petrovykh, D.Y., Tarlov, M.J. & Whitman, L.J. Base-dependent competitive adsorption of single-stranded DNA on gold. *Journal of the American Chemical Society* **125**, 9014-9015 (2003).
146. Rueda, M., Prieto, F., Álvarez-Malmagro, J. & Rodes, A. Evidences of adenine–thymine Interactions at gold electrodes interfaces as provided by in-situ infrared spectroscopy. *Electrochemistry Communications* **35**, 53-56 (2013).
147. Rodes, A. et al. Adenine Adsorption at Single Crystal and Thin-Film Gold Electrodes: An In Situ Infrared Spectroscopy Study. *The Journal of Physical Chemistry C* **113**, 18784-18794 (2009).
148. Hu, W., Hu, Q., Li, L., Kong, J. & Zhang, X. Detection of sequence-specific DNA with a morpholino-functionalized silicon chip. *Analytical Methods* **7**, 2406-2412 (2015).
149. Brzoska, J., Azouz, I.B. & Rondelez, F. Silanization of solid substrates: a step toward reproducibility. *Langmuir* **10**, 4367-4373 (1994).
150. Vashist, S.K., Lam, E., Hrapovic, S., Male, K.B. & Luong, J.H. Immobilization of antibodies and enzymes on 3-aminopropyltriethoxysilane-functionalized

bioanalytical platforms for biosensors and diagnostics. *Chemical reviews* **114**, 11083-11130 (2014).

151. Diao, J., Ren, D., Engstrom, J.R. & Lee, K.H. A surface modification strategy on silicon nitride for developing biosensors. *Analytical biochemistry* **343**, 322-328 (2005).
152. Fernandez, R.E., Bhattacharya, E. & Chadha, A. Covalent immobilization of Pseudomonas cepacia lipase on semiconducting materials. *Applied Surface Science* **254**, 4512-4519 (2008).
153. Wang, Y.-P. et al. Preparation and characterization of poly (N-isopropylacrylamide) films on a modified glass surface via surface initiated redox polymerization. *Materials Letters* **59**, 1736-1740 (2005).
154. Giesbers, M., Marcelis, A.T. & Zuilhof, H. Simulation of XPS C1s spectra of organic monolayers by quantum chemical methods. *Langmuir* **29**, 4782-4788 (2013).
155. Escorihuela, J., Bañuls, M.-J., Puchades, R. & Maquieira, Á. Site-specific immobilization of DNA on silicon surfaces by using the thiol–yne reaction. *Journal of Materials Chemistry B* **2**, 8510-8517 (2014).
156. Manning, M., Harvey, S., Galvin, P. & Redmond, G. A versatile multi-platform biochip surface attachment chemistry. *Materials Science and Engineering: C* **23**, 347-351 (2003).
157. Gokmen, M.T., Brassinne, J., Prasath, R.A. & Du Prez, F.E. Revealing the nature of thio-click reactions on the solid phase. *Chemical Communications* **47**, 4652-4654 (2011).
158. Luppa, P.B., Sokoll, L.J. & Chan, D.W. Immunosensors—principles and applications to clinical chemistry. *Clinica Chimica Acta* **314**, 1-26 (2001).
159. Hunt, H.K. & Armani, A.M. Recycling microcavity optical biosensors. *Optics letters* **36**, 1092-1094 (2011).
160. Baker, M. Plasma cleaning and the removal of carbon from metal surfaces. *Thin Solid Films* **69**, 359-368 (1980).
161. Pan, Q., Shai, O., Lee, L.J., Frey, B.J. & Blencowe, B.J. Deep surveying of alternative splicing complexity in the human transcriptome by high-throughput sequencing. *Nature genetics* **40**, 1413-1415 (2008).
162. Wang, E.T. et al. Alternative isoform regulation in human tissue transcriptomes. *Nature* **456**, 470-476 (2008).
163. Nilsen, T.W. & Graveley, B.R. Expansion of the eukaryotic proteome by alternative splicing. *Nature* **463**, 457-463 (2010).
164. Black, D.L. Mechanisms of alternative pre-messenger RNA splicing. *Annual review of biochemistry* **72**, 291-336 (2003).
165. Maniatis, T. & Tasic, B. Alternative pre-mRNA splicing and proteome expansion in metazoans. *Nature* **418**, 236-243 (2002).
166. Soares, L.M.M. & Valcárcel, J. The expanding transcriptome: the genome as the 'Book of Sand'. *The EMBO Journal* **25**, 923-931 (2006).
167. Taliaferro, J.M., Alvarez, N., Green, R.E., Blanchette, M. & Rio, D.C. Evolution of a tissue-specific splicing network. *Genes & development* **25**, 608-620 (2011).
168. Mallory, M.J. et al. Signal-and development-dependent alternative splicing of LEF1 in T cells is controlled by CELF2. *Molecular and cellular biology* **31**, 2184-2195 (2011).
169. Wakamatsu, A., Imai, J.-i., Watanabe, S. & Isogai, T. Alternative splicing of genes during neuronal differentiation of NT2 pluripotential human embryonal carcinoma cells. *FEBS letters* **584**, 4041-4047 (2010).
170. Vilardell, J. & Valcárcel, J. Powering a two-stroke RNA engine. *Nature structural & molecular biology* **14**, 574-576 (2007).
171. Behzadnia, N. et al. Composition and three-dimensional EM structure of double affinity-purified, human prespliceosomal A complexes. *The EMBO Journal* **26**, 1737-1748 (2007).

172. Montes, M., Becerra, S., Sánchez-Álvarez, M. & Suñé, C. Functional coupling of transcription and splicing. *Gene* **501**, 104-117 (2012).
173. Stamm, S. et al. Function of alternative splicing. *Gene* **344**, 1-20 (2005).
174. Hnilicová, J. et al. Histone deacetylase activity modulates alternative splicing. *PloS one* **6** (2011).
175. Loomis, R.J. et al. Chromatin binding of SRp20 and ASF/SF2 and dissociation from mitotic chromosomes is modulated by histone H3 serine 10 phosphorylation. *Molecular cell* **33**, 450-461 (2009).
176. Sims, R.J. et al. Recognition of trimethylated histone H3 lysine 4 facilitates the recruitment of transcription postinitiation factors and pre-mRNA splicing. *Molecular cell* **28**, 665-676 (2007).
177. Lyko, F. et al. The honey bee epigenomes: differential methylation of brain DNA in queens and workers. *PLoS biology* **8**, 2834 (2010).
178. Meseguer, S., Mudduluru, G., Escamilla, J.M., Allgayer, H. & Barettino, D. MicroRNAs-10a and-10b contribute to retinoic acid-induced differentiation of neuroblastoma cells and target the alternative splicing regulatory factor SFRS1 (SF2/ASF). *Journal of Biological Chemistry* **286**, 4150-4164 (2011).
179. Makeyev, E.V., Zhang, J., Carrasco, M.A. & Maniatis, T. The MicroRNA miR-124 promotes neuronal differentiation by triggering brain-specific alternative pre-mRNA splicing. *Molecular cell* **27**, 435-448 (2007).
180. Verduci, L. et al. MicroRNA (miRNA)-mediated interaction between leukemia/lymphoma-related factor (LRF) and alternative splicing factor/splicing factor 2 (ASF/SF2) affects mouse embryonic fibroblast senescence and apoptosis. *Journal of Biological Chemistry* **285**, 39551-39563 (2010).
181. Tripathi, V. et al. The nuclear-retained noncoding RNA MALAT1 regulates alternative splicing by modulating SR splicing factor phosphorylation. *Molecular cell* **39**, 925-938 (2010).
182. Kishore, S. et al. The snoRNA MBII-52 (SNORD 115) is processed into smaller RNAs and regulates alternative splicing. *Human molecular genetics* **19**, 1153-1164 (2010).
183. Lewis, B.P., Green, R.E. & Brenner, S.E. Evidence for the widespread coupling of alternative splicing and nonsense-mediated mRNA decay in humans. *Proceedings of the National Academy of Sciences* **100**, 189-192 (2003).
184. Pan, Q. et al. Quantitative microarray profiling provides evidence against widespread coupling of alternative splicing with nonsense-mediated mRNA decay to control gene expression. *Genes & development* **20**, 153-158 (2006).
185. Tazi, J., Bakkour, N. & Stamm, S. Alternative splicing and disease. *Biochimica et Biophysica Acta (BBA)-Molecular Basis of Disease* **1792**, 14-26 (2009).
186. Padgett, R.A. New connections between splicing and human disease. *Trends in Genetics* **28**, 147-154 (2012).
187. Ghigna, C., Valacca, C. & Biamonti, G. Alternative splicing and tumor progression. *Current genomics* **9**, 556 (2008).
188. David, C.J. & Manley, J.L. Alternative pre-mRNA splicing regulation in cancer: pathways and programs unhinged. *Genes & development* **24**, 2343-2364 (2010).
189. Zhang, Z., Pal, S., Bi, Y., Tchou, J. & Davuluri, R.V. Isoform level expression profiles provide better cancer signatures than gene level expression profiles. *Genome Med* **5**, 33 (2013).
190. Wu, Y.-M., Kung, S.-S. & Chow, W.-Y. Determination of relative abundance of splicing variants of Oreochromis glutamate receptors by quantitative reverse-transcriptase PCR. *FEBS letters* **390**, 157-160 (1996).
191. Xing, Y. et al. MADS: a new and improved method for analysis of differential alternative splicing by exon-tiling microarrays. *Rna* **14**, 1470-1479 (2008).
192. Lee, K., Cui, Y., Lee, L.P. & Irudayaraj, J. Quantitative imaging of single mRNA splice variants in living cells. *Nature nanotechnology* **9**, 474-480 (2014).

193. Krammer, P.H. CD95's deadly mission in the immune system. *Nature* **407**, 789-795 (2000).
194. Cheng, J. et al. Protection from Fas-mediated apoptosis by a soluble form of the Fas molecule. *Science* **263**, 1759-1762 (1994).
195. Cascino, I., Fiucci, G., Papoff, G. & Ruberti, G. Three functional soluble forms of the human apoptosis-inducing Fas molecule are produced by alternative splicing. *The Journal of Immunology* **154**, 2706-2713 (1995).
196. Owen-Schaub, L., Chan, H., Cusack, J., Roth, J. & Hill, L. Fas and Fas ligand interactions in malignant disease. *International journal of oncology* **17**, 5-17 (2000).
197. Owen-Schaub, L.B., van Golen, K.L., Hill, L.L. & Price, J.E. Fas and Fas ligand interactions suppress melanoma lung metastasis. *The Journal of experimental medicine* **188**, 1717-1723 (1998).
198. Boroumand-Noughabi, S. et al. Soluble Fas might serve as a diagnostic tool for gastric adenocarcinoma. *BMC cancer* **10**, 275 (2010).
199. Gong, P. & Levicky, R. DNA surface hybridization regimes. *Proceedings of the National Academy of Sciences* **105**, 5301-5306 (2008).
200. Špringer, T., Šípová, H., Vaisocherová, H., Štěpánek, J. & Homola, J. Shielding effect of monovalent and divalent cations on solid-phase DNA hybridization: surface plasmon resonance biosensor study. *Nucleic acids research*, gkq577 (2010).
201. Lee, J. et al. Identification of a novel cis-element that regulates alternative splicing of Bcl-x pre-mRNA. *Biochemical and biophysical research communications* **420**, 467-472 (2012).
202. Akgul, C., Moulding, D. & Edwards, S. Alternative splicing of Bcl-2-related genes: functional consequences and potential therapeutic applications. *Cellular and Molecular Life Sciences CMLS* **61**, 2189-2199 (2004).
203. Izquierdo, J.M. et al. Regulation of Fas alternative splicing by antagonistic effects of TIA-1 and PTB on exon definition. *Molecular cell* **19**, 475-484 (2005).
204. Förch, P. et al. The apoptosis-promoting factor TIA-1 is a regulator of alternative pre-mRNA splicing. *Molecular cell* **6**, 1089-1098 (2000).
205. Sasi, M.S., Mlitan, A.M. & Alkherraz, A.M. Comparing Spontaneous Hydrolysis Rates of Activated Models of DNA and RNA. *Agricultural and Biosystems Engineering* **1** (2014).
206. Elliott, D. & Ladomery, M. Molecular biology of RNA. (Oxford University Press, 2011).
207. Cerritelli, S.M. & Crouch, R.J. Ribonuclease H: the enzymes in eukaryotes. *FEBS journal* **276**, 1494-1505 (2009).
208. Wan, Y., Qu, K., Ouyang, Z. & Chang, H.Y. Genome-wide mapping of RNA structure using nuclease digestion and high-throughput sequencing. *Nature protocols* **8**, 849-869 (2013).
209. Uyeno, Y., Sekiguchi, Y., Sunaga, A., Yoshida, H. & Kamagata, Y. Sequence-specific cleavage of small-subunit (SSU) rRNA with oligonucleotides and RNase H: a rapid and simple approach to SSU rRNA-based quantitative detection of microorganisms. *Applied and environmental microbiology* **70**, 3650-3663 (2004).
210. Sulej, A.A., Tuszynska, I., Skowronek, K.J., Nowotny, M. & Bujnicki, J.M. Sequence-specific cleavage of the RNA strand in DNA–RNA hybrids by the fusion of ribonuclease H with a zinc finger. *Nucleic acids research*, gks885 (2012).
211. Joshi, G.K. et al. Highly specific plasmonic biosensors for ultrasensitive microRNA detection in plasma from pancreatic cancer patients. *Nano letters* **14**, 6955-6963 (2014).
212. Hasselmann, D.O. et al. Detection of tumor-associated circulating mRNA in serum, plasma and blood cells from patients with disseminated malignant melanoma. *Oncology reports* **8**, 115-123 (2001).

213. Mercer, T.R., Dinger, M.E. & Mattick, J.S. Long non-coding RNAs: insights into functions. *Nature Reviews Genetics* **10**, 155-159 (2009).
214. Mendell, J.T. MicroRNAs: critical regulators of development, cellular physiology and malignancy. *Cell cycle* **4**, 1179-1184 (2005).
215. Ambros, V. The functions of animal microRNAs. *Nature* **431**, 350-355 (2004).
216. Ambros, V. microRNAs: tiny regulators with great potential. *Cell* **107**, 823-826 (2001).
217. Lim, L.P. et al. Microarray analysis shows that some microRNAs downregulate large numbers of target mRNAs. *Nature* **433**, 769-773 (2005).
218. Carrington, J.C. & Ambros, V. Role of microRNAs in plant and animal development. *Science* **301**, 336-338 (2003).
219. Bartel, D.P. MicroRNAs: genomics, biogenesis, mechanism, and function. *Cell* **116**, 281-297 (2004).
220. Griffiths-Jones, S., Saini, H.K., van Dongen, S. & Enright, A.J. miRBase: tools for microRNA genomics. *Nucleic acids research* **36**, D154-D158 (2008).
221. Dong, H. et al. MicroRNA: function, detection, and bioanalysis. *Chemical reviews* **113**, 6207-6233 (2013).
222. Lee, Y., Jeon, K., Lee, J.T., Kim, S. & Kim, V.N. MicroRNA maturation: stepwise processing and subcellular localization. *The EMBO Journal* **21**, 4663-4670 (2002).
223. Lee, Y. et al. The nuclear RNase III Drosha initiates microRNA processing. *Nature* **425**, 415-419 (2003).
224. Bernstein, E., Caudy, A.A., Hammond, S.M. & Hannon, G.J. Role for a bidentate ribonuclease in the initiation step of RNA interference. *Nature* **409**, 363-366 (2001).
225. Hammond, S.M., Boettcher, S., Caudy, A.A., Kobayashi, R. & Hannon, G.J. Argonaute2, a link between genetic and biochemical analyses of RNAi. *Science* **293**, 1146-1150 (2001).
226. Leuschner, P.J., Ameres, S.L., Kueng, S. & Martinez, J. Cleavage of the siRNA passenger strand during RISC assembly in human cells. *EMBO reports* **7**, 314-320 (2006).
227. Kawamata, T., Seitz, H. & Tomari, Y. Structural determinants of miRNAs for RISC loading and slicer-independent unwinding. *Nature structural & molecular biology* **16**, 953-960 (2009).
228. Ryan, B.M., Robles, A.I. & Harris, C.C. Genetic variation in microRNA networks: the implications for cancer research. *Nature Reviews Cancer* **10**, 389-402 (2010).
229. Ameres, S.L. & Zamore, P.D. Diversifying microRNA sequence and function. *Nature reviews Molecular cell biology* **14**, 475-488 (2013).
230. Yang, W. et al. Modulation of microRNA processing and expression through RNA editing by ADAR deaminases. *Nature structural & molecular biology* **13**, 13-21 (2006).
231. Xhemalce, B., Robson, S.C. & Kouzarides, T. Human RNA methyltransferase BCDIN3D regulates microRNA processing. *Cell* **151**, 278-288 (2012).
232. Yang, J.-S. & Lai, E.C. Alternative miRNA biogenesis pathways and the interpretation of core miRNA pathway mutants. *Molecular cell* **43**, 892-903 (2011).
233. Xie, M. & Steitz, J.A. Versatile microRNA biogenesis in animals and their viruses. *RNA biology* **11**, 673-681 (2014).
234. Bartel, D.P. MicroRNAs: target recognition and regulatory functions. *Cell* **136**, 215-233 (2009).
235. Lytle, J.R., Yario, T.A. & Steitz, J.A. Target mRNAs are repressed as efficiently by microRNA-binding sites in the 5′ UTR as in the 3′ UTR. *Proceedings of the National Academy of Sciences* **104**, 9667-9672 (2007).
236. Moretti, F., Thermann, R. & Hentze, M.W. Mechanism of translational regulation by miR-2 from sites in the 5′ untranslated region or the open reading frame. *Rna* **16**, 2493-2502 (2010).

237. Vasudevan, S., Tong, Y. & Steitz, J.A. Switching from repression to activation: microRNAs can up-regulate translation. *Science* **318**, 1931-1934 (2007).
238. Brennecke, J., Stark, A., Russell, R.B. & Cohen, S.M. Principles of microRNA-target recognition. *PLoS Biol* **3**, e85 (2005).
239. Liu, N. & Olson, E.N. MicroRNA regulatory networks in cardiovascular development. *Developmental cell* **18**, 510-525 (2010).
240. Bushati, N. & Cohen, S.M. microRNA functions. *Annu. Rev. Cell Dev. Biol.* **23**, 175-205 (2007).
241. Fiore, R., Siegel, G. & Schratt, G. MicroRNA function in neuronal development, plasticity and disease. *Biochimica et Biophysica Acta (BBA)-Gene Regulatory Mechanisms* **1779**, 471-478 (2008).
242. Baltimore, D., Boldin, M.P., O'Connell, R.M., Rao, D.S. & Taganov, K.D. MicroRNAs: new regulators of immune cell development and function. *Nature immunology* **9**, 839-845 (2008).
243. Frost, R.J. & Olson, E.N. Control of glucose homeostasis and insulin sensitivity by the Let-7 family of microRNAs. *Proceedings of the National Academy of Sciences* **108**, 21075-21080 (2011).
244. Greco, S.J. & Rameshwar, P. MicroRNAs regulate synthesis of the neurotransmitter substance P in human mesenchymal stem cell-derived neuronal cells. *Proceedings of the National Academy of Sciences* **104**, 15484-15489 (2007).
245. Liu, K. & Wang, R. MicroRNA-mediated regulation in the mammalian circadian rhythm. *Journal of theoretical biology* **304**, 103-110 (2012).
246. Lei, X. et al. Regulation of NF-κB inhibitor IκBα and viral replication by a KSHV microRNA. *Nature cell biology* **12**, 193-199 (2010).
247. Iorio, M.V. & Croce, C.M. MicroRNA dysregulation in cancer: diagnostics, monitoring and therapeutics. A comprehensive review. *EMBO molecular medicine* **4**, 143-159 (2012).
248. Lee, Y.S. & Dutta, A. MicroRNAs in cancer. *Annual review of pathology* **4**, 199 (2009).
249. Lu, J. et al. MicroRNA expression profiles classify human cancers. *Nature* **435**, 834-838 (2005).
250. Rosenfeld, N. et al. MicroRNAs accurately identify cancer tissue origin. *Nature biotechnology* **26**, 462-469 (2008).
251. Schwarzenbach, H., Hoon, D.S. & Pantel, K. Cell-free nucleic acids as biomarkers in cancer patients. *Nature Reviews Cancer* **11**, 426-437 (2011).
252. Taylor, D.D. & Gercel-Taylor, C. MicroRNA signatures of tumor-derived exosomes as diagnostic biomarkers of ovarian cancer. *Gynecologic oncology* **110**, 13-21 (2008).
253. Elsevier, S. Urologic Oncology: Seminars and Original Investigations. 收錄起迄年*: 1995-Present* (2009).
254. Michael, A. et al. Exosomes from human saliva as a source of microRNA biomarkers. *Oral diseases* **16**, 34-38 (2010).
255. Xie, Y. et al. Altered miRNA expression in sputum for diagnosis of non-small cell lung cancer. *Lung cancer* **67**, 170-176 (2010).
256. Heneghan, H.M. et al. Circulating microRNAs as novel minimally invasive biomarkers for breast cancer. *Annals of surgery* **251**, 499-505 (2010).
257. Vaisocherová, H. et al. Rapid and sensitive detection of multiple microRNAs in cell lysate by low-fouling surface plasmon resonance biosensor. *Biosensors and Bioelectronics* **70**, 226-231 (2015).
258. Lagos-Quintana, M. et al. Identification of tissue-specific microRNAs from mouse. *Current Biology* **12**, 735-739 (2002).
259. Benes, V. & Castoldi, M. Expression profiling of microRNA using real-time quantitative PCR, how to use it and what is available. *Methods* **50**, 244-249 (2010).

260. Thomson, J.M., Parker, J., Perou, C.M. & Hammond, S.M. A custom microarray platform for analysis of microRNA gene expression. *Nature methods* **1**, 47-53 (2004).

261. Hamidi-Asl, E., Palchetti, I., Hasheminejad, E. & Mascini, M. A review on the electrochemical biosensors for determination of microRNAs. *Talanta* **115**, 74-83 (2013).

262. Vander Heiden, M.G., Cantley, L.C. & Thompson, C.B. Understanding the Warburg effect: the metabolic requirements of cell proliferation. *Science* **324**, 1029-1033 (2009).

263. Wei, Z., Cui, L., Mei, Z., Liu, M. & Zhang, D. miR-181a mediates metabolic shift in colon cancer cells via the PTEN/AKT pathway. *FEBS letters* **588**, 1773-1779 (2014).

264. Hagiwara, A. et al. Hepatic mTORC2 activates glycolysis and lipogenesis through Akt, glucokinase, and SREBP1c. *Cell metabolism* **15**, 725-738 (2012).

265. Jiao, X. et al. MiR-181a enhances drug sensitivity in mitoxantone-resistant breast cancer cells by targeting breast cancer resistance protein (BCRP/ABCG2). *Breast cancer research and treatment* **139**, 717-730 (2013).

266. Ji, J., Yamashita, T. & Wang, X.W. Wnt/beta-catenin signaling activates microRNA-181 expression in hepatocellular carcinoma. *Cell Biosci* **1** (2011).

267. Zhang, X. et al. MicroRNA-181a promotes gastric cancer by negatively regulating tumor suppressor KLF6. *Tumor Biology* **33**, 1589-1597 (2012).

268. Puzio-Kuter, A.M. et al. Inactivation of p53 and Pten promotes invasive bladder cancer. *Genes & development* **23**, 675-680 (2009).

269. Song, T. et al. Differential miRNA expression profiles in bladder urothelial carcinomas. *Asian Pac J Cancer Prev* **11**, 905-911 (2010).

270. Kroemer, G. & Pouyssegur, J. Tumor cell metabolism: cancer's Achilles' heel. *Cancer cell* **13**, 472-482 (2008).

271. Belkaya, S. et al. Dynamic modulation of thymic microRNAs in response to stress. *PloS one* **6**, e27580 (2011).

272. Liu, G., Min, H., Yue, S. & Chen, C.-Z. Pre-miRNA loop nucleotides control the distinct activities of mir-181a-1 and mir-181c in early T cell development. *PloS one* **3**, e3592-e3592 (2008).

273. Kuchen, S. et al. Regulation of microRNA expression and abundance during lymphopoiesis. *Immunity* **32**, 828-839 (2010).

274. Napolitano, N.M., Rohlfs, E.M. & Heim, R.A. Simultaneous Detection of Multiple Point Mutations Using Allele-Specific Oligonucleotides. *Current Protocols in Human Genetics*, 9.4. 1-9.4. 10 (2004).

275. Duby, A., Jacobs, K.A. & Celeste, A. Using synthetic oligonucleotides as probes. *Current Protocols in Molecular Biology*, 6.4. 1-6.4. 10 (2001).

276. Schwinefus, J.J. et al. Human telomerase RNA pseudoknot and hairpin thermal stability with glycine betaine and urea: Preferential interactions with RNA secondary and tertiary structures. *Biochemistry* **46**, 9068-9079 (2007).

277. Boguslawski, S.J. et al. Characterization of monoclonal antibody to DNA· RNA and its application to immunodetection of hybrids. *Journal of immunological methods* **89**, 123-130 (1986).

278. Šípová, H. et al. Surface plasmon resonance biosensor for rapid label-free detection of microribonucleic acid at subfemtomole level. *Analytical chemistry* **82**, 10110-10115 (2010).

279. Qavi, A.J., Kindt, J.T., Gleeson, M.A. & Bailey, R.C. Anti-DNA: RNA antibodies and silicon photonic microring resonators: increased sensitivity for multiplexed microRNA detection. *Analytical chemistry* **83**, 5949-5956 (2011).

280. Jemal, A. et al. Cancer statistics, 2005. *CA: a cancer journal for clinicians* **55**, 10-30 (2005).

281. Mengual, L. et al. Using microRNA profiling in urine samples to develop a non-invasive test for bladder cancer. *International Journal of Cancer* **133**, 2631-2641 (2013).
282. Mall, C., Rocke, D.M., Durbin-Johnson, B. & Weiss, R.H. Stability of miRNA in human urine supports its biomarker potential. *Biomarkers in medicine* **7**, 623-631 (2013).
283. Weber, J.A. et al. The microRNA spectrum in 12 body fluids. *Clinical chemistry* **56**, 1733-1741 (2010).
284. Joshi, G.K. et al. Label-Free Nanoplasmonic-Based Short Noncoding RNA Sensing at Attomolar Concentrations Allows for Quantitative and Highly Specific Assay of MicroRNA-10b in Biological Fluids and Circulating Exosomes. *ACS nano* (2015).
285. Liu, Q. et al. Mach–Zehnder interferometer (MZI) point-of-care system for rapid multiplexed detection of microRNAs in human urine specimens. *Biosensors and Bioelectronics* **71**, 365-372 (2015).
286. Richards, E.J. & Elgin, S.C. Epigenetic codes for heterochromatin formation and silencing: rounding up the usual suspects. *Cell* **108**, 489-500 (2002).
287. Bird, A. DNA methylation patterns and epigenetic memory. *Genes & development* **16**, 6-21 (2002).
288. Kundu, T.K. & Rao, M. CpG islands in chromatin organization and gene expression. *Journal of biochemistry* **125**, 217-222 (1999).
289. Tollefsbol, T. Handbook of epigenetics: the new molecular and medical genetics. (Academic Press, 2010).
290. Saxonov, S., Berg, P. & Brutlag, D.L. A genome-wide analysis of CpG dinucleotides in the human genome distinguishes two distinct classes of promoters. *Proceedings of the National Academy of Sciences of the United States of America* **103**, 1412-1417 (2006).
291. Feinberg, A.P. & Vogelstein, B. Hypomethylation distinguishes genes of some human cancers from their normal counterparts. *Nature* **301**, 89-92 (1983).
292. Rodriguez, J. et al. Chromosomal instability correlates with genome-wide DNA demethylation in human primary colorectal cancers. *Cancer research* **66**, 8462-9468 (2006).
293. Bera, T.K. et al. Defective retrovirus insertion activates c-Ha-ras proto-oncogene in an MNU-induced rat mammary carcinoma. *Biochemical and biophysical research communications* **248**, 835-840 (1998).
294. Alves, G., Tatro, A. & Fanning, T. Differential methylation of human LINE-1 retrotransposons in malignant cells. *Gene* **176**, 39-44 (1996).
295. Costa, F.F. et al. SATR-1 hypomethylation is a common and early event in breast cancer. *Cancer genetics and cytogenetics* **165**, 135-143 (2006).
296. Narayan, A. et al. Hypomethylation of pericentromeric DNA in breast adenocarcinomas. *International Journal of Cancer* **77**, 833-838 (1998).
297. Reik, W., Dean, W. & Walter, J. Epigenetic reprogramming in mammalian development. *Science* **293**, 1089-1093 (2001).
298. Samowitz, W.S. The CpG island methylator phenotype in colorectal cancer. *The Journal of Molecular Diagnostics* **9**, 281-283 (2007).
299. Hughes, L.A. et al. The CpG island methylator phenotype in colorectal cancer: progress and problems. *Biochimica et Biophysica Acta (BBA)-Reviews on Cancer* **1825**, 77-85 (2012).
300. Marsit, C.J. et al. Examination of a CpG island methylator phenotype and implications of methylation profiles in solid tumors. *Cancer research* **66**, 10621-10629 (2006).
301. Suzuki, M. et al. Exclusive mutation in epidermal growth factor receptor gene, HER-2, and KRAS, and synchronous methylation of nonsmall cell lung cancer. *Cancer* **106**, 2200-2207 (2006).

302. Shen, L. et al. DNA methylation and environmental exposures in human hepatocellular carcinoma. *Journal of the National Cancer Institute* **94**, 755-761 (2002).

303. Fang, F. et al. Breast cancer methylomes establish an epigenomic foundation for metastasis. *Science translational medicine* **3**, 75ra25-75ra25 (2011).

304. Licchesi, J.D. & Herman, J.G. in DNA Methylation 305-323 (Springer, 2009).

305. Weber, M. et al. Chromosome-wide and promoter-specific analyses identify sites of differential DNA methylation in normal and transformed human cells. *Nature genetics* **37**, 853-862 (2005).

306. Carrascosa, L.G. et al. Molecular inversion probe-based SPR biosensing for specific, label-free and real-time detection of regional DNA methylation. *Chemical Communications* **50**, 3585-3588 (2014).

307. Pan, S. et al. Double recognition of oligonucleotide and protein in the detection of DNA methylation with surface plasmon resonance biosensors. *Biosensors and Bioelectronics* **26**, 850-853 (2010).

308. Maki, W.C. et al. Nanowire-transistor based ultra-sensitive DNA methylation detection. *Biosensors and Bioelectronics* **23**, 780-787 (2008).

309. Lieberman, P., Hardwick, J., Sample, J., Hayward, G. & Hayward, S. The zta transactivator involved in induction of lytic cycle gene expression in Epstein-Barr virus-infected lymphocytes binds to both AP-1 and ZRE sites in target promoter and enhancer regions. *Journal of virology* **64**, 1143-1155 (1990).

310. Quinlivan, E.B. et al. Direct BRLF1 binding is required for cooperative BZLF1/BRLF1 activation of the Epstein-Barr virus early promoter, BMRF1. *Nucleic acids research* **21**, 1999-2007 (1993).

311. Raver, R.M., Panfil, A.R., Hagemeier, S.R. & Kenney, S.C. The B-cell-specific transcription factor and master regulator Pax5 promotes Epstein-Barr virus latency by negatively regulating the viral immediate early protein BZLF1. *Journal of virology* **87**, 8053-8063 (2013).

312. Thornton, B. & Basu, C. Real-time PCR (qPCR) primer design using free online software. *Biochemistry and Molecular Biology Education* **39**, 145-154 (2011).

313. Fatemi, M. & Wade, P.A. MBD family proteins: reading the epigenetic code. *Journal of cell science* **119**, 3033-3037 (2006).

314. Yu, Y. et al. Direct DNA methylation profiling using methyl binding domain proteins. *Analytical chemistry* **82**, 5012-5019 (2010).

315. Roloff, T.C., Ropers, H.H. & Nuber, U.A. Comparative study of methyl-CpG-binding domain proteins. *BMC genomics* **4**, 1 (2003).

316. Nan, X., Meehan, R.R. & Bird, A. Dissection of the methyl-CpG binding domain from the chromosomal protein MeCP2. *Nucleic acids research* **21**, 4886-4892 (1993).

317. Demidov, V.V., Bukanov, N.O. & Frank-Kamenetskii, M.D. Duplex DNA capture. *Current issues in molecular biology* **2**, 31-35 (2000).

318. Dinman, J.D. et al. The frameshift signal of HIV-1 involves a potential intramolecular triplex RNA structure. *Proceedings of the National Academy of Sciences* **99**, 5331-5336 (2002).

319. An, R. G-quadruplex in the 5'UTR of the NRAS proto-oncogene modulates translation Kumari, Sunita; Bugaut, Anthony; Huppert, Julian L.; Balasubramanian, Shankar. *Nature Chemical Biology* **3**, 218-221 (2007).

320. Morgan, A. & Wells, R. Specificity of the three-stranded complex formation between double-stranded DNA and single-stranded RNA containing repeating nucleotide sequences. *Journal of molecular biology* **37**, 63-80 (1968).

321. Goñi, J.R., De La Cruz, X. & Orozco, M. Triplex-forming oligonucleotide target sequences in the human genome. *Nucleic acids research* **32**, 354-360 (2004).

322. Goñi, J.R., Vaquerizas, J.M., Dopazo, J. & Orozco, M. Exploring the reasons for the large density of triplex-forming oligonucleotide target sequences in the human regulatory regions. *BMC genomics* **7**, 63 (2006).

323. Aviñó, A. et al. Properties of triple helices formed by parallel-stranded hairpins containing 8-aminopurines. *Nucleic acids research* **30**, 2609-2619 (2002).

324. Avino, A. et al. Parallel-stranded hairpins containing 8-aminopurines. Novel efficient probes for triple-helix formation. *Bioorganic & medicinal chemistry letters* **11**, 1761-1763 (2001).

325. Nadal, A., Eritja, R., Esteve, T. & Pla, M. "Parallel" and "Antiparallel Tail-Clamps" Increase the Efficiency of Triplex Formation with Structured DNA and RNA Targets. *ChemBioChem* **6**, 1034-1042 (2005).

326. Nadal, A. et al. Efficient Sequence-Specific Purification of Listeria innocua mRNA Species by Triplex Affinity Capture with Parallel Tail-Clamps. *ChemBioChem* **7**, 1039-1047 (2006).

327. Carrascosa, L.G. et al. Sensitive and label-free biosensing of RNA with predicted secondary structures by a triplex affinity capture method. *Nucleic acids research*, gkr1304 (2012).

328. Takagi, T. et al. Decreased expression of microRNA-143 and-145 in human gastric cancers. *Oncology* **77**, 12-21 (2009).